

Synthesis of Bio-inspired μ -oxo Heterobimetallic
Nonheme Complexes

A THESIS SUBMITTED TO THE FACULTY OF THE GRADUATE SCHOOL OF
THE UNIVERSITY OF MINNESOTA
BY

Ang Zhou

IN PARTIAL FULFILLMENT OF THE REQUIREMENTS
FOR THE DEGREE OF
DOCTOR OF PHILOSOPHY

Prof. Lawrence Que, Jr., Advisor

July 2017

Acknowledgements

Firstly, I want to express my sincere gratitude to Prof. Larry Que for his continuous support to my Ph.D. studies during the past five years. I was intrigued by his character since our first conversation in a bike ride tour in 2012, and am fortunate enough to be a member of his group. I still remember his careful revision on my writing materials, his kindness of lending me his *Time* magazine to improve my English, his comments on how to practice the chemistry intuition to be a good scientist. Equipped with the heart of curiosity and faith in rationalism, I am much more comfortable in solving unknown problems, and I attribute this to Larry. I could not have imagined having a better advisor and mentor for my Ph.D. studies.

Besides my advisor, I would like to thank the rest of my thesis committee: Prof. John Lipscomb, Prof. Ian Tonks, and Prof. Andreas Stein, not only for their insightful comments and encouragement, but also for the questions which incited me to widen my research from various perspectives.

There are many Que group alumni for me to say thank you. Dr. Katherine Van Heuvelen started the project of synthesizing μ -oxo heterobimetallic nonheme complexes. With her detailed lab notes I was able to repeat her work and explore the project. Dr. Scott Kleespies helped me from the very beginning when I first joined the group, and we shared the joy of getting the first Raman spectrum of the Fe–O–Cr species after a long time trying. Dr. Jai Prakash is an expert in both synthesis and spectroscopic techniques, and I have learned a lot from him. I greatly appreciate Dr. Greg Rohde for his help on

XRD and XAS experiments, and particularly I admire his attitude of being optimistic whatever problems are in front. Dr. Mayank Puri, who is not only an excellent scientist, but also a reliable person, has inspired me to do the right things in life. Dr. Andrew Jasniewski and I worked together for four years in 11 XAS trips, I will smile when thinking about the days and nights we stayed at the beamline. I enjoyed the collaboration experience with Dr. Wei-min Ching (Seesaw) from Taiwan. Seesaw has impressed me with his enthusiasm towards research, and I understand better of the life in Taiwan from the conversation with him. I deeply treasure the friendship with Jale Öcal, a visiting student from Turkey. We spent a long time in lab and supported with each other, I wish her all the best in her career.

I also deeply appreciate the help from the people who are still working at University of Minnesota. Waqas Rasheed is one of the most creative people I have met, and I've bothered him a lot for his suggestions on all kinds of problems in and out of the lab. Dr. Apparao Draksharapu is the Raman guy in our group, people including myself all benefit from his expertise. Dr. Johannes Klein has helped me with his deep knowledge in organic synthesis and theoretical calculations, and I wish him all the best for his new position at University of Groningen. I thank Subhasree Kal, Dr. Rahul Banerjee and Dr. Melanie Rogers for their help in doing the EPR experiment, it is my pleasure to work with you.

Last but not least, I am lucky enough to receive the support from the important people outside university in my life. I cannot get what I achieved today without my parents, they teach me to be open-minded and a person good to the society, and I have

always remembered this. I also would like to thank my fiancé Ruyue Xiao for her 2-year long-distance accompanies. It is my fortune to meet her at 2015 ICBIC in Beijing, and I am looking forward to staying with her in China.

I dedicate this thesis to my parent and my fiancé

for their constant support and unconditional love.

I love you all dearly.

Abstract

Enzymes with dinuclear metallocofactors perform versatile functions in nature. In their catalytic cycles, the two metal ions are often connected through a bridging ligand with resulting cooperative effects. Oxo-bridged heterobimetallic species stand out and act as crucial intermediates in various bimetallic active sites. For decades different approaches have been investigated to prepare synthetic μ -oxo heterobimetallic molecules. However, the synthetic strategies either have difficulties in selectively binding the two metals at specific sites while avoiding mixtures and homodinuclear side products, or require complicated unsymmetrical ligand synthesis.

This thesis explores a way of quantitatively obtaining μ -oxo heterobimetallic nonheme complexes from the inner sphere electron transfer reaction between nonheme oxoiron(IV) species and a reducing metal salt. Specifically, two types of molecules with Fe–O–Cr and Fe–O–Mn cores are prepared, and based on thorough spectroscopic characterization their structures have been identified. The effect of the Fe coordination ligand to the Fe–O–Cr core is discussed in detail. The Fe–O–Mn species are among the very few synthetic complexes with Fe/Mn bimetallic center, and their structures and reactivities have been compared with the Fe/Mn intermediates in Class Ic RNR. This research has given rise to an alternative way of synthesizing μ -oxo heterobimetallic nonheme complexes with convenience and high efficiency.

Table of Content

List of Tables	x
List of Figures	xi
Abbreviations	xxi
Compound Abbreviations by Chapter	xxiv

Chapter 1 O ₂ Activation by Bimetallic Active Sites	1
1.1 Enzymatic O ₂ Activation in Nature	2
1.2 Cytochrome <i>c</i> Oxidase	5
1.3 Ribonucleotide Reductase	9
1.3.1 Mechanism of Ribonucleotide Reduction	9
1.3.2 Structure and Function of Class Ia RNR	11
1.3.3 Structure and Function of Class Ib RNR	14
1.3.4 Structure and Function of Class Ic RNR	16
1.4 Synthetic Models for Bimetallic-Oxygen Intermediates	18
1.4.1 Synthetic Models of Bimetallic-Oxygen Species in CcO	18
1.4.2 Synthetic Models for Bimetallic-Oxygen Species in Class Ia RNR	21
1.4.3 Synthetic Models for Bimetallic-Oxygen Species in Class Ib RNR	23
1.4.4 Synthetic Models for Bimetallic-Oxygen Species in Class Ic RNR	24
1.5 Scope and Aim of Thesis	26

Chapter 2 The Two Faces of Tetramethylcyclam in Iron Chemistry: Distinct Fe–O–M Complexes Derived from [Fe ^{IV} (O _{<i>anti/syn</i>})(TMC)] ²⁺ isomers	29
2.1 Introduction	31

2.2 Experimental Details.....	33
2.2.1 Materials.....	33
2.2.2 Instrumentation.....	35
2.2.3 X-ray Absorption Spectroscopy.....	36
2.2.4 X-ray Crystallography.....	37
2.3 Results and Discussion.....	37
2.3.1 Generation of 1 and 2	37
2.3.2 ESI-MS Characterization of 1 and 2	40
2.3.3 Raman Results of 1 , 2 and 3	44
2.3.4 Mössbauer Spectroscopy of 1 and 2	47
2.3.5 XAS Analysis of 1	49
2.3.6 XAS Analysis of 2	54
2.3.7 Characterization of 4_{Cl} , 4_{OTf} and 5	58
2.3.8. O ₂ Activation Process to Generate 1	68
2.4 Conclusion.....	72

Chapter 3 Coordination Effects on Structures of (L)Fe^{III}-O-Cr^{III} species..... 74

3.1 Introduction.....	75
3.2 Experimental Details.....	77
3.2.1 Materials.....	77
3.2.2 Instrumentation.....	78
3.2.3 X-ray bsorption Spectroscopy.....	79
3.3 Results and discussion.....	79
3.3.1 Reaction between 1 and NBu ₄ X (X = NCS ⁻ , NCO ⁻).....	79
3.3.2 Generation and Characterization of 2	86
3.3.3 Generation and Characterization of 4	97
3.3.4 Generation and Characterization of 5 and 6	99
3.4 Conclusion.....	109

Chapter 4 Characterization and Reactivity Studies of a Linear Fe–O–Mn Species Obtained from Inner-Sphere Electron Transfer	113
4.1 Introduction	114
4.2 Experimental Details	117
4.2.1 Materials	117
4.2.2 Instrumentation	118
4.2.3 X-ray Absorption Spectroscopy	119
4.3 Results and discussion	121
4.3.1 Generation of 1	121
4.3.2 Resonance Raman Spectrum of 1	125
4.3.3 EPR Spectrum of 1	126
4.3.4 XAS Analysis of 1	128
4.3.5 Generation of 2	133
4.3.6 XAS Analysis of 2	136
4.3.7 Reactivity of 1	140
4.4 Conclusion	144

Chapter 5 From Linear to Nonlinear: A Synthetic Model for Class Ic Ribonucleotide Reductase	147
5.1 Introduction	148
5.2 Experimental Details	152
5.2.1 Materials	152
5.2.2 Instrumentation	153
5.2.3 X-ray Absorption Spectroscopy	153
5.3 Results and Discussion	155
5.3.1 Reaction Between and $\text{Fe}^{\text{IV}}(\text{O})(\text{TPA})(\text{OTf})_2$ and $\text{Mn}^{\text{II}}(\text{TPA})(\text{OTf})_2$	155
5.3.2 XAS Analysis of 1	157

5.3.3 Reaction Between 1 and NBU ₄ OAc.....	162
5.3.4 Reaction between 1 and H ₂ O ₂	164
5.4 Conclusion.....	171

Chapter 6 Conclusion and Perspective..... 172

6.1 Introduction	173
6.2 The Two Faces of Tetramethylcyclam in Iron Chemistry: Fe–O–M Complexes Derived from [Fe ^{IV} (O _{anti/syn})(TMC)] ²⁺ Isomers	176
6.3 Coordination Effects on Structures of (L)Fe ^{III} –O–Cr ^{III} Species.....	179
6.4 Characterization and Reactivity Studies of a Linear Fe–O–Mn Species Obtained from Inner-Sphere Electron Transfer	182
6.5 From Linear to Nonlinear: A Synthetic Model for Class 1c Ribonucleotide Reductase	184
6.6 Conclusion.....	185

References 187

Bibliography 203

List of Tables

Table 2.1 Fit parameters for complex **1**. Unfiltered data from $k = 2-12.5 \text{ \AA}^{-1}$. (52)

Table 2.2 Fit parameters for **2** based on unfiltered data from $k = 2 - 15 \text{ \AA}^{-1}$. (57)

Table 2.3 Crystallographic and structure refinement data for **4_{Cl}** (14182a in checkcif file) and **5** (14202a1 in checkcif file). (59)

Table 2.4 Select bond lengths (\AA) and angles ($^\circ$) of **4_{Cl}** and **5**. (60)

Table 2.5 Spectroscopic and structural comparisons of complexes **1 – 6**. (67)

Table 3.1 Fit parameters for **1-NCS** unfiltered data from $k = 2-12 \text{ \AA}^{-1}$. (85)

Table 3.2 Fit Parameters for **2**, unfiltered from $k = 2 - 15 \text{ \AA}^{-1}$. (92)

Table 3.3 Fit Parameters for **3**, unfiltered from $k = 2 - 15 \text{ \AA}^{-1}$. (96)

Table 3.4 Fit Parameters for **5**, unfiltered from $k = 2 - 15 \text{ \AA}^{-1}$. (108)

Table 3.5 UV-vis ϵ value, Raman shift and XAS results of Fe–O–Cr complexes in Chapter 3. (112)

Table 4.1 Fit Parameters for **1** unfiltered from $k = 2 - 15 \text{ \AA}^{-1}$. (131)

Table 4.2 Fit Parameters for **2** unfiltered from $k = 2 - 15 \text{ \AA}^{-1}$. (139)

Table 5.1 Fit Parameters for **1** unfiltered from $k = 2 - 14 \text{ \AA}^{-1}$. (161)

Table 5.2 Fit Parameters for **2** unfiltered from $k = 2 - 14 \text{ \AA}^{-1}$. (170)

List of Figures

Figure 1.1 Dioxygen activation of catechol 1,2-dioxygenase found by Osamu Hayaishi. (2)

Figure 1.2 Proposed catalytic cycle of taurine/ α -ketoglutarate dioxygenase (TauD). Reproduced with permission from ref 13. Copyright 2007 American Chemical Society. (4)

Figure 1.3 The four redox active metal sites of bovine heart CcO (*top left*). Heme *a* active site (*bottom left*). Dioxygen reduction site composed of heme a_3 and Cu_B (*bottom right*). Active site of the binuclear copper site referred to as Cu_A (*top right*). Reproduced with permission from ref 26. Copyright 2016 Springer. (6)

Figure 1.4 Coordination geometries of the peroxide unit in the fully-oxidized CcO at 2.1 Å resolution.²⁹ Copyright 2009 National Academy of Sciences. (7)

Figure 1.5 Proposed catalytic mechanism of CcO. Reproduced with permission from ref 26. Copyright 2016 Springer. (8)

Figure 1.6 Generic reaction mechanism for ribonucleotide reduction Reproduced with permission from ref 40. Copyright 2004 Wiley. (10)

Figure 1.7 Proposed radical transfer pathways in *Ec* class Ia RNR. Reproduced with permission from ref 44. Copyright 2013 American Chemical Society. (12)

Figure 1.8 (Top) Proposed O₂ activation pathway in FeFe-Y• cofactor of class Ib RNR. Reproduced with permission from ref 39. Copyright 2011 Annual Reviews. (Bottom) Proposed structure of intermediate **X**.⁵⁶ (13)

Figure 1.9 Proposed O₂ activation pathway in MnMn-Y• cofactor of class Ib RNR. Reproduced with permission from ref 39. Copyright 2011 Annual Reviews. (15)

Figure 1.10 Proposed O₂ activation pathway in FeMn cofactor of class Ic RNR. Reproduced with permission from ref 39. Copyright 2011 Annual Reviews. (18)

Figure 1.11 Structures of $[(^6\text{L})\text{Fe}^{\text{III}}\text{Cu}^{\text{II}}(\text{O}_2)]^+$,⁷⁰ $[(\text{TMP})\text{Fe}^{\text{III}}(\text{O}_2)\text{Cu}^{\text{II}}(5\text{MeTPA})]^+$,⁷¹ $[(\text{F}_8)\text{Fe}^{\text{III}}(\text{O}_2)\text{Cu}^{\text{II}}(\text{L}^{\text{Me}_2\text{N}})]^+$,⁷² $[(^2\text{L})\text{Fe}^{\text{III}}(\text{O}_2)\text{Cu}^{\text{II}}]^+$.⁷³ (20)

Figure 1.12 Crystal structures of $[\text{Fe}^{\text{III}}_2(\mu\text{-N-Et-HPTB})(\mu\text{-1,2-O}_2)(\text{Ph}_3\text{PO})_2]^{3+75}$ (left) and $[\text{Fe}^{\text{III}}_2(\mu\text{-1,2-O}_2)(\mu\text{-O}_2\text{CCH}_2\text{Ph})_2\text{-(HB(pz}^{\prime})_3)_2]^{81}$ (right). (22)

Figure 1.13 (Left) Structure of $[\text{Mn}^{\text{II}}(\text{S}^{\text{Me}_2}\text{N}_4(6\text{-MeDPEN}))]^+$ that can react with O₂. (Right) ORTEP of peroxo-bridged $[(\text{Mn}^{\text{III}}(\text{S}^{\text{Me}_2}\text{N}_4(6\text{-MeDPEN}))_2(\mu\text{-O}_2)]^{2+}$ with 50% probability ellipsoids.⁸⁵ Hydrogen atoms are omitted for clarity. (24)

Figure 1.14 (Left) Structure of $[\text{TACN}\text{Fe}^{\text{III}}\text{-O-Mn}^{\text{III}}(\text{Me}_3\text{TACN})]^{2+}$.⁸⁷ (Right) $[\text{Fe}^{\text{III}}\text{Mn}^{\text{II}}\text{BPMP}(\text{O}_2\text{CCH}_2\text{CH}_3)_2]^+$.⁸⁸ (25)

Figure 1.15 Synthesis scheme for $[(\text{F}_8\text{-TPP})\text{Fe}^{\text{III}}\text{-O-Cu}^{\text{II}}(\text{TPA})]^+$.⁸⁹ (26)

Figure 2.1 Structures of complexes **1** – **5**. An asterisk indicates that XRD data has been obtained to determine the structures of these complexes. (33)

Figure 2.2 UV-vis spectral titration of 0.45 mM $[\text{Fe}^{\text{IV}}(\text{O})(\text{TMC})(\text{NCCH}_3)]^{2+}$ in CH₃CN at -40 °C with Cr(OTf)₂. Black, 0 equiv.; red, 0.25 equiv.; blue: 0.5 equiv.; magenta, 0.75 equiv.; green, 1 equiv. Inset: titration plot. Inset: Formation of **1** vs equiv. Cr(OTf)₂ added into 0.45 mM $[\text{Fe}^{\text{IV}}(\text{O})(\text{TMC})(\text{NCCH}_3)]^{2+}$ in CH₃CN at -40 °C. (38)

Figure 2.3 UV-vis spectra of 1 mM Cr(OTf)₂ in CH₃CN before (black) and after addition of 1 equiv. PhIO (red). (39)

Figure 2.4 UV-vis absorption spectra of black: 0.35 mM **1**; red: 0.35 mM **2** in CH₃CN at -40 °C. (40)

Figure 2.5 ESI-MS spectra of **1**. (Top) positive mode spectrum, together with isotope distribution pattern of the m/z 461.1 peak simulated by $[\text{Fe}(\text{TMC})(\text{OTf})]^+$. (Bottom)

negative mode spectrum, together with isotope distribution pattern of the m/z 514.8 peak simulated by $[\text{Cr}(\text{O})(\text{OTf})_3]^+$. (41)

Figure 2.6 ESI-MS spectral features of **2**. (Top) isotope pattern for the $[(\text{TMC})\text{Fe}^{16}\text{OCr}(\text{OTf})_3]^+$ ion (m/z +827); (Bottom) isotope pattern for the $[(\text{TMC})\text{Fe}^{18}\text{OCr}(\text{OTf})_3]^+$ ion (m/z +829). (Based on the intensity ratio between the m/z +827 and +829 peaks, the latter sample contains approximately 25% of the $[(\text{TMC})\text{Fe}^{16}\text{OCr}(\text{OTf})_3]^+$ isotopomer, which may arise from incomplete ^{18}O labeling of the $2\text{-}^t\text{BuSO}_2\text{-C}_6\text{H}_4\text{I}^{18}\text{O}$ oxidant. (42)

Figure 2.7 Decay product analysis on species **1** at room temperature. Black: 0.4 mM $\text{Fe}^{\text{IV}}(\text{O})(\text{TMC})(\text{OTf})_2$; Red: 0.4 mM species **1** formed from adding 1 equiv. $\text{Cr}(\text{OTf})_2$ into 0.4 mM $\text{Fe}^{\text{IV}}(\text{O})(\text{TMC})(\text{OTf})_2$; Blue: decay of 0.4 mM species **1**; Magenta: Spectrum after adding 5 equiv. of PhIO in CH_3OH into decay of 0.4 mM species **1**. 90% (0.36 mM) of $\text{Fe}^{\text{IV}}(\text{O})(\text{TMC})(\text{OTf})_2$ was recovered based on the absorbance at 824 nm. (44)

Figure 2.8 Resonance Raman spectra of **1** in CH_3CN ($\lambda_{\text{ex}} = 568.2$ nm, 20 mW, 77 K). Black, ^{16}O ; red, ^{18}O . Asterisk denotes solvent peak. (45)

Figure 2.9 (Top) resonance Raman spectra of **2** (5 mM) in CH_3CN ($\lambda_{\text{ex}} = 514.5$ nm, 20 mW, 77 K). Black: ^{16}O ; red: ^{18}O . The residual 877-cm^{-1} peak found in ^{18}O -labeled **2** indicates the presence of ^{16}O -labeled **2**, which likely comes from residual $2\text{-}^t\text{BuSO}_2\text{-C}_6\text{H}_4\text{I}^{16}\text{O}$ in the ^{18}O -labeled oxidant used for the preparation of **2**. (Bottom) Raman spectra for **3** (12 mM) in CD_3CN obtained with $\lambda_{\text{ex}} = 515$ nm and 50-mW power at 77 K (black, pure CD_3CN ; red, ^{16}O isotopomer). Asterisks denote solvent peaks. (47)

Figure 2.10 (A) Mössbauer spectrum (black) of **1** and the corresponding fitting curve (red) with $\delta = +0.53$ mm/s, $|\Delta E_Q| = 0.87$ mm/s. (B) Mössbauer spectrum (black) of **2** and the corresponding fitting curve (red) with $\delta = +0.44$ mm/s, $|\Delta E_Q| = 0.89$ mm/s. The fit is improved with the inclusion of a 20% contribution from **1**. (49)

Figure 2.11 Pre-edge region of Fe K-edge XAS spectrum of **1** (black). Baseline fit (red), pre-edge peak 1 (blue), pre-edge peak 2 (magenta), pre-edge fit (green). (50)

Figure 2.12 (Left) Fourier-transformed Fe K-edge EXAFS data for **1** (dotted black line) and corresponding best fit (solid red line, fit #8 in Table 2.1). Inset shows unfiltered k-space data and its fit. (Right) Proposed structure for **1** (L/X = CH₃CN or OTf). (51)

Figure 2.13 Pre-edge region of the Fe K-edge XAS spectrum of **2** (black squares): rising-edge fit (red circles), pre-edge peak 1 (blue triangles pointing up, maximum at 7113.7 eV), pre-edge peak 2 (magenta triangles pointing down, maximum at 7113.0 eV), pre-edge fit (green diamonds), residuals (gray triangles pointing left). (55)

Figure 2.14 Main: Fourier-transformed Fe K-edge EXAFS data for **2** (dotted black) and the corresponding best fit (fit #6 in Table 2.2). (Inset) Unfiltered k-space data (dotted black) and its fit (solid red). (56)

Figure 2.15 (Left) ORTEP plots for (Cl)(TMC)Fe–O_{anti}–FeCl₃ (**4_{Cl}**) and [(TMC)Fe–O_{syn}–FeCl₃](OTf) (**5**) at 50% probability. H-atoms, solvent molecules and a counter ion (in **5**) have been omitted for clarity. The R₁ values for structures **4_{Cl}** and **5** are 0.023 and 0.048, respectively (CCDC numbers 1503819 and 1503820). The structure of **5** was modeled over two positions with a 90 ° rotation along the Fe–O–Fe axis. (Right) conformations of the cyclam rings in **4_{Cl}** and **5**. Red color highlights the different orientations of the two NCH₂–CH₂N bonds relative to each other in each cyclam ring (parallel in **4_{Cl}** and crossed in **5**). (58)

Figure 2.16 Structural comparison of complexes **4_{Cl}**, **5**, and **6**. (63)

Figure 2.17 ¹⁹F-NMR spectrum of A) **4_{OTf}** and B) **4_{OTf}** + 10 equiv. of Bu₄NOTf, collected in CD₃CN at 298 K. For comparison, the observed linewidth for free triflate ion under the same conditions is 5 Hz. (64)

Figure 2.18 (Top) Infrared spectroscopic data for **4_{OTf}** (black, ¹⁶O isotopomer; red, ¹⁸O isotopomer). (Bottom) Infrared spectroscopic data for **5** (black, ¹⁶O isotopomer; red, ¹⁸O isotopomer). (66)

Figure 2.19 UV-vis spectra observed in CH₃CN at -40 °C upon O₂ exposure of 1 mM Cr(OTf)₂ (red) and a mixture of 1 mM Fe(TMC)(OTf)₂ and 1 mM Cr(OTf)₂ (black). Bands with asterisks are associated with **1**. (69)

Figure 2.20 Yields of **1** based on the 558-nm peak intensity upon O₂ bubbling into Fe^{II}(TMC)(OTf)₂ + Cr^{II}(OTf)₂ solutions in CH₃CN at -40 °C with varying ratios of Fe^{II}(TMC)(OTf)₂ to Cr^{II}(OTf)₂. Cr^{II}(OTf)₂ = 1 mM. (70)

Figure 2.21 Yields of **1** based on the 558-nm peak intensity upon O₂ bubbling into Fe^{II}(TMC)(OTf)₂ + Cr^{II}(OTf)₂ solutions in CH₃CN at -40 °C with varying ratios of Cr^{II}(OTf)₂ to Fe^{II}(TMC)(OTf)₂. Fe^{II}(TMC)(OTf)₂ = 1 mM. (71)

Figure 2.22 Proposed mechanism for formation of **1** by O₂ activation. (72)

Figure 3.1 UV-vis spectra of 0.3 mM **1** (black), 1-NCO (blue), **1-NCS** (red) in CH₃CN at -40 °C. λ_{\max} (ϵ) for **1**: 398 (3800), 447 (3000), and 558 (700). λ_{\max} (ϵ_M) for **1-NCO**: 380 (6000), 438 (4200), and 560 (850). λ_{\max} (ϵ_M) for **1-NCS**: 390 (7500), 442 (6300), and 560 (1400). ϵ unit: M⁻¹ cm⁻¹. (80)

Figure 3.2 Changes in the UV-vis spectrum when NBu₄SCN was added into 0.42 mM **1** in CH₃CN at -40 °C. Black: no NCS⁻ added. Red: 0.25 eq. of NCS⁻ added. Blue: 0.5 eq. of NCS⁻ added. Pink: 0.75 eq. of NCS⁻ added. Green: 1.0 eq. of NCS⁻ added. Purple: 2.0 eq. of NCS⁻ added. Insets: UV-vis change upon titration of NCS⁻ into **1**. (81)

Figure 3.3 Changes in the UV-vis spectrum when NBu₄NCO was added into 0.4 mM **1** in CH₃CN at -40 °C. Black: no NCO⁻ added. Red: 0.5 eq. of NCO⁻ added. Blue: 1.0 eq. of NCO⁻ added. Pink: 2.0 eq. of NCO⁻ added. Inset: Absorbance change upon titration of NCO⁻ into **1**. (82)

Figure 3.4 (Left) Positive mode ESI-MS spectra for 1 mM **1** + 1 eq. NBu₄SCN. (Right) Positive mode ESI-MS spectra for 1 mM **1** + 1 eq. NBu₄SCO. (82)

Figure 3.5 Pre-edge region of Fe K-edge XAS spectrum of **1-NCS** (black). Baseline fit (red), pre-edge peak 1 (blue), pre-edge peak 2 (magenta), pre-edge fit (green). (83)

Figure 3.6 Fit 7 in Table 3.1 (red line) of the Fourier transformed unfiltered (black dots) EXAFS data of **1-NCS**. (84)

Figure 3.7 UV-vis spectra of $\text{Fe}^{\text{IV}}(\text{O})(\text{TMCPy})(\text{OTf})_2$ (black) and **2** (red) in CH_3CN at $-40\text{ }^\circ\text{C}$. ϵ ($\text{M}^{-1}\text{ cm}^{-1}$) for bands in **2**: 3800 (381 nm), 3200 (451 nm), 920 (558 nm). (87)

Figure 3.8 ESI-MS spectrum of the reaction of $\text{Fe}^{\text{IV}}(\text{O})(\text{TMC-py})(\text{OTf})_2$ with 1 eq. of $\text{Cr}^{\text{II}}(\text{OTf})_2$ at $-40\text{ }^\circ\text{C}$. (87)

Figure 3.9 Experimental and simulation isotopic patterns of $[(\text{TMC-py})\text{Fe}^{\text{III}}-\text{O}-\text{Cr}^{\text{III}}(\text{OTf})_3]^+$ (top) and $[(\text{TMC-py})\text{Fe}^{\text{III}-16/18}\text{O}-\text{Cr}^{\text{III}}(\text{OTf})_3]^+$ (bottom). (88)

Figure 3.10 Resonance Raman spectra of **2** ($\lambda_{\text{ex}} = 561\text{ nm}$, 77 K). Black, ^{16}O -labeled; red, ^{18}O -labeled. (89)

Figure 3.11 Pre-edge region of the Fe K-edge XAS spectrum of **2** (black squares): rising-edge fit (red circles), pre-edge peak (blue triangles pointing up, maximum at 7114.7 eV), pre-edge fit (green diamonds). (90)

Figure 3.12 (Top) Unfiltered k -space data of **2** (dotted black line) and its fit (solid red line). (Bottom) Fourier-transformed Fe K-edge EXAFS data for **2** (dotted black line) and corresponding best fit (solid red line, fit #5 in Table 3.2). (91)

Figure 3.13 Pre-edge region of the Fe K-edge XAS spectrum of **3** (black squares): rising-edge fit (red circles), pre-edge peak 1 (blue triangles pointing up, maximum at 7113.2 eV), pre-edge peak 2 (magenta triangles pointing down, maximum at 7115.0 eV), pre-edge fit (green diamonds). (93)

Figure 3.14 Main: Fourier-transformed Fe K-edge EXAFS data for **3** (dotted black) and the corresponding best fit (solid red, fit #6 in Table 3.3). Inset: unfiltered k -space data (dotted black) and its fit (solid red). (95)

Figure 3.15 UV-vis spectra of $0.75\text{ mM } [\text{Fe}^{\text{IV}}(\text{O})(\text{TMCdma})](\text{OTf})_2$ (black) and **4** (red) at $-40\text{ }^\circ\text{C}$ in CH_3CN . (98)

Figure 3.16 Resonance Raman spectra of **4** in CH₃CN ($\lambda_{\text{ex}} = 561 \text{ nm}$, 77 K). (99)

Figure 3.17 (Top) UV-vis spectra of Cr(OTf)₂ + [Fe^{IV}(O)(N4Py)](OTf)₂ in CH₃CN at -40 °C. (Bottom) Titration between Cr(OTf)₂ + [Fe^{IV}(O)(N4Py)](OTf)₂. (101)

Figure 3.18 Resonance Raman spectra of **5** in CH₃CN ($\lambda_{\text{ex}} = 514.5 \text{ nm}$, 77 K). Black, ¹⁶O; red, ¹⁸O. Asterisk denotes solvent peak. (102)

Figure 3.19 UV-vis spectra of 0.32 mM [(BnTPEN)Fe^{IV}(O)](OTf)₂ (black) and **6** (red) at -40 °C in CH₃CN. (103)

Figure 3.20 Resonance Raman spectra of **6** in CH₃CN ($\lambda_{\text{ex}} = 514.5 \text{ nm}$, 77 K). Black, ¹⁶O; red, ¹⁸O. Asterisk denotes solvent peak. (104)

Figure 3.21 Pre-edge region of the Fe K-edge XAS spectrum of **5** (black squares): rising-edge fit (red circles), pre-edge peak (blue triangles pointing up, maximum at 7114.9 eV), pre-edge fit (pink triangles pointing down), residue (grey diamonds). (105)

Figure 3.22 (Left) unfiltered k-space data of **5** (dotted black line) and its fit (solid red line). (Right) Fourier-transformed Fe K-edge EXAFS data for **5** (dotted black line) and corresponding best fit (solid red line, fit #8 in Table 3.4). (107)

Figure 3.23 Structures of complexes **1**, **1-NCS**, **1-NCO**, **2**, **4**, **5**, **6**. (109)

Figure 4.1 (Left) Structure of [(TACN)Fe^{III}-O-Mn^{III}(Me₃TACN)]²⁺.⁸⁷ (Middle) [Fe^{III}Mn^{II}BPMP(O₂CCH₂CH₃)₂]⁺.⁸⁸ (Right) [Fe^{III}Mn^{II}(ICIMP)(OAc)₂Cl].¹⁵³ (115)

Figure 4.2 UV-vis absorption spectral titration of 0.3 mM [Fe^{IV}(O)(N4Py)(NCCH₃)]²⁺ in CH₃CN at -40 °C with [Mn^{II}(dpaq)](OTf). Black, 0 eq.; red, 0.25 eq.; blue: 0.5 eq.; magenta, 0.75 eq.; green, 1 eq. (Inset) Absorbance at 440 nm indicating formation of **1** vs eq. [Mn^{II}(dpaq)](OTf) added into 0.3 mM [Fe^{IV}(O)(N4Py)(NCCH₃)](OTf)₂ in CH₃CN at -40 °C. (122)

Figure 4.3 (Top) ESI-MS spectrum of $m/z = 1174.0$ peak; (Bottom) Simulated peak based on $[(N4Py)FeOMn(dpaq)(OTf)_2]^+$ formula. (123)

Figure 4.4 (Top) UV-vis spectra of 1 mM $[Mn^{II}(dpaq)](OTf)$ in CH_3CN (black) and after the addition of 3 eq. PhIO dissolved in CH_3OH (red) at $-40\text{ }^\circ C$. (Bottom) ESI-MS spectrum of the reaction between $[Mn^{II}(dpaq)](OTf)$ and 3 eq. PhIO dissolved in CH_3OH . (124)

Figure 4.5 Resonance Raman spectra of **1** (0.5 mM) in CH_3CN at λ_{ex} 514.5 nm at 77 K. (Black) CH_3CN . (Red) ^{16}O -labeled **1**. (Blue) ^{18}O -labeled **1**. (126)

Figure 4.6 X-band EPR spectrum of 0.5 mM **1** in frozen CH_3CN . Conditions: $T = 30\text{ K}$; microwave power attenuation: 30 dB. Asterisks indicate hyperfine pattern. (127)

Figure 4.7 Pre-edge region of the Fe K-edge XAS spectrum of **1** (grey line): baseline fit (red dot), pre-edge peaks (red lines), pre-edge fit (blue line), Residuals (green line). (129)

Figure 4.8 Fourier-transformed Fe K-edge EXAFS data for **1** (black) and the corresponding best fit (red, fit #15 in Table 4.1). (Inset) unfiltered k -space data (black) and its fit (red). (130)

Figure 4.9 UV-vis absorption spectra of 0.3 mM $[Fe^{IV}(O)(BnTPEN)(NCCH_3)](OTf)_2$ in CH_3CN at $-40\text{ }^\circ C$ (black) with 1 eq. of $[Mn^{II}(dpaq)](OTf)$ (red). (133)

Figure 4.10 (Top) ESI-MS spectra of $m/z = 1123.0$ peak; (Bottom) Simulated peak of $m/z = 1230.2$ based on $[(BnTPEN)FeOMn(dpaq)(OTf)_2]^+$ formula. (134)

Figure 4.11 X-band EPR spectrum of 0.5 mM **2** in frozen CH_3CN . Conditions: $T = 30\text{ K}$; microwave power attenuation: 30 dB. Asterisks indicate hyperfine pattern. (135)

Figure 4.12 Pre-edge region of the Fe K-edge XAS spectrum of **2** (black): baseline fit (red), pre-edge peak (blue), pre-edge fit (magenta), Residual (green). (136)

Figure 4.13 (Top) Fourier-transformed Fe K-edge EXAFS data for **2** (black) and the corresponding best fit (red, fit #9 in Table 4.2). (Bottom) unfiltered k -space data (black) and fit (red). (138)

Figure 4.14 (Top) In 1.5 mL 0.4 mM **1** in CH₃CN at 25 °C (red), 50 uL H₂O was added (blue). (Bottom) UV-vis absorption change of the 440-nm peak. (141)

Figure 4.15 (Top) ESI-MS results on **1** +H₂O. (bottom) Proposed hydrolysis reaction between **1** and H₂O. (142)

Figure 4.16 (Left) Titration of decamethylferrocene (Fc*) into **1** at -40 °C in CH₃CN. Black: 0.5 mM **1**; Red: **1** + 0.5 eq. Fc*; Blue: **1** + 1.0 eq. Fc*. (Right) decay of 560 nm species. (143)

Figure 4.17 (Red) 560-nm intermediate. (Black) decay of 560-nm intermediate $\lambda_{\text{ex}} = 568.2$ nm, 20 mW, 77 K. (144)

Figure 4.18 Proposed structures of **1** and **2**. (145)

Figure 5.1 Structures of [Fe^{IV}(O)(TPA)(NCCH₃)]²⁺ (top left), [Fe^{III}Fe^{IV}(μ -O)₂(5-Et₃-TPA)₂]³⁺ (top right), [Fe^{IV}Fe^{IV}(μ -O)₂(3,5-Me₂-4-MeO)₃-TPA)₂]⁴⁺ (bottom). (150)

Figure 5.2 Proposed reaction between [Fe^{IV}(O)(TPA)](OTf)₂ and Mn^{II}(TPA)(OTf)₂ to generate (TPA)Fe^{III}-O-Mn^{III}(TPA) species. L represents OTf or CH₃CN. (151)

Figure 5.3 Proposed reactions between OAc⁻/H₂O₂ with **1**. (152)

Figure 5.4 (Left) UV-vis spectra of 1 mM Fe^{IV}(O)(TPA)(OTf)₂ and Mn^{II}(TPA)(OTf)₂ in CH₃CN at -40 °C. Black, 0 eq.; red, 0.25 eq.; blue: 0.5 eq.; magenta, 0.75 eq.; green, 1 eq. (Right) Titration between Fe^{IV}(O)(TPA)(OTf)₂ and Mn^{II}(TPA)(OTf)₂. (156)

Figure 5.5 X-band EPR spectrum of 0.5 mM **1** in CH₃CN. Conditions: $T = 2$ K; microwave power attenuation: 30 dB. Asterisk indicates hyperfine pattern. (157)

Figure 5.6 Pre-edge region of the Fe K-edge XAS spectrum of **1** (black line): baseline fit (pink dot), pre-edge peak (red lines), pre-edge fit (blue line). (158)

Figure 5.7 (Top) Fourier-transformed Fe K-edge EXAFS data for **1** (black) and the corresponding best fit (red, fit #7 in Table 5.1). (160)

Figure 5.8 At -40 °C in CH₃CN, UV-vis spectra of 0.5 mM **1** (red) and after the addition 1 eq. of NBu₄Ac (blue). (162)

Figure 5.9 EPR spectrum of the reaction of **1** and 1 eq. of NBu₄OAc. Conditions: *T* = 2 K; microwave power attenuation: 30 dB. (163)

Figure 5.10 Time trace of 0.75 mM **1** + 1 eq of H₂O₂ at -40 °C in CH₃CN. (165)

Figure 5.11 Reaction between 0.75 mM **1** and different eq. of H₂O₂. (166)

Figure 5.12 Pre-edge region of the Fe K-edge XAS spectrum of **1** + 4 eq. of H₂O₂ (black line): baseline fit (red line), pre-edge peak 1 (magenta line), pre-edge peak 2 (blue line), pre-edge fit (green line), residuals (gray line). (167)

Figure 5.13 Proposed reaction mechanism between **1** and H₂O₂ to form **2**. (168)

Figure 5.14 (Top) Fourier-transformed Fe K-edge EXAFS data for **2** (black) and the corresponding best fit (red, fit #7 in Table 5.2). (Bottom) Unfiltered *k*-space data (black) and its fit (red). (169)

Figure 6.1 XRD structures of **1**¹⁰⁵, **2**¹⁷⁶, **3**¹⁰³. (174)

Figure 6.2 Structural comparison between **4** and **5**. (178)

Figure 6.3 Proposed structures of **6-9**. (180)

Figure 6.4 Proposed structures of **10-11**. (183)

Abbreviations

α -KG	α -ketoglutarate
δ	isomer shift
ΔE_Q	quadrupole splitting
2- ^t BuSO ₂ -C ₆ H ₄ IO	2-(<i>tert</i> -butylsulfonyl)iodosylbenzene
BPMP	2,6-bis[(bis(2-pyridylmethyl)-amino)methyl]-4-methylphenolate
CcO	Cytochrome c oxidase
<i>Ct</i>	<i>C. trachomatis</i>
dpaq	2-[bis(pyridin-2-ylmethyl)]amino-N-quinolin-8-yl-acetamidate
DOPA	3,4-dihydroxyphenylalanine
<i>Ec</i>	<i>E. coli</i>
ENDOR	electron nuclear double resonance
EPR	electron paramagnetic resonance
ESI-MS	electrospray ionization mass spectrometry
Et ₂ O	diethyl ether
EXAFS	extended X-ray absorption fine structure
F ₈ -TPP	tetrakis(2,6-difluorophenyl)-porphyrinate
Fc*	decamethylferrocene
FT	Fourier transform
HAT	hydrogen atom transfer

HPTB	N,N,N',N'-tetrakis(2-benzylimidazolymethyl)-2-hydroxo-1,3-diaminopropane
IR	infrared
Me ₃ TACN	1,4,7-trimethyl-1,4,7-triazacyclononane
N4Py	N,N-bis(2-pyridylmethyl)-N-bis(2-pyridyl)methylamine
NMR	nuclear magnetic resonance
OEC	oxygen-evolving complex
OTf	triflate
PhIO	iodosylbenzene
PS II	photosystem II
Py	pyridine
RNR	ribonucleotide reductase
TACN	1,4,7-triazacyclononane
TauD	taurine dioxygenase
TMC	1,4,8,11-tetramethyl-1,4,8,11-tetraazacyclotetradecane
TMCdma	1,4,8-Me ₃ cyclam-11-CH ₂ C(O)NMe ₂
TMCPy	1,4,8-trimethyl-11-pyridylmethyl-1,4,8,11-tetraazacyclotetradecane
TMCS	1-mercaptoethyl-4,8,11-trimethyl-1,4,8,11-tetraaza cyclotetradecane monoanion
TMP	tetramesitylporphin dianion
TPA	tris(2-pyridylmethyl)-amine

TPP	tetraphenylporphin dianion
UV-vis	Ultraviolet–visible
VT-MCD	variable-temperaturemagnetic circular dichroism
XANES	X-ray absorption near edge structure
XAS	X-ray absorption spectroscopy
XRD	X-ray diffraction

Compound Abbreviations by Chapter

Chapter 2

- 1** $(\text{CH}_3\text{CN})(\text{TMC})\text{Fe}^{\text{III}}-\text{O}_{\text{anti}}-\text{Cr}^{\text{III}}(\text{OTf})_4(\text{NCCH}_3)$
- 2** $(\text{TMC})\text{Fe}^{\text{III}}-\text{O}_{\text{syn}}-\text{Cr}^{\text{III}}(\text{OTf})_4(\text{NCCH}_3)$
- 3** $(\text{TMC})\text{Fe}-\text{O}-\text{Sc}^{\text{III}}(\text{OTf})_4(\text{OH}_x)$
- 4_{Cl}** $(\text{Cl})(\text{TMC})\text{Fe}^{\text{III}}-\text{O}_{\text{anti}}-\text{Fe}^{\text{III}}\text{Cl}_3$
- 4_{OTf}** $(\text{OTf})(\text{TMC})\text{Fe}^{\text{III}}-\text{O}_{\text{anti}}-\text{Fe}^{\text{III}}\text{Cl}_3$
- 5** $[(\text{TMC})\text{Fe}^{\text{III}}-\text{O}_{\text{syn}}-\text{Fe}^{\text{III}}\text{Cl}_3](\text{OTf})$
- 6** $(\text{Me}_3\text{cyclam-acetate})\text{Fe}-\text{O}-\text{FeCl}_3$

Chapter 3

- 1** $(\text{CH}_3\text{CN})(\text{TMC})\text{Fe}^{\text{III}}-\text{O}_{\text{anti}}-\text{Cr}^{\text{III}}(\text{OTf})_4(\text{NCCH}_3)$
- 1-NCS** $[(\text{SCN})(\text{TMC})\text{Fe}^{\text{III}}-\text{O}_{\text{anti}}-\text{Cr}^{\text{III}}(\text{OTf})_4(\text{NCCH}_3)]^-$
- 1-NCO** $[(\text{OCN})(\text{TMC})\text{Fe}^{\text{III}}-\text{O}_{\text{anti}}-\text{Cr}^{\text{III}}(\text{OTf})_4(\text{NCCH}_3)]^-$
- 2** $(\text{TMCPy})\text{Fe}^{\text{III}}-\text{O}-\text{Cr}^{\text{III}}(\text{OTf})_4(\text{NCCH}_3)$
- 3** $[(\text{TMCPy})\text{Fe}^{\text{III}}\text{OH}]^{2+}$
- 4** $(\text{TMCdma})\text{Fe}^{\text{III}}-\text{O}-\text{Cr}^{\text{III}}(\text{OTf})_4(\text{NCCH}_3)$
- 5** $(\text{N4Py})\text{Fe}^{\text{III}}-\text{O}-\text{Cr}^{\text{III}}(\text{OTf})_4(\text{NCCH}_3)$
- 6** $(\text{BnTPEN})\text{Fe}^{\text{III}}-\text{O}-\text{Cr}^{\text{III}}(\text{OTf})_4(\text{NCCH}_3)$

Chapter 4

- 1 $[(\text{N4Py})\text{Fe}^{\text{III}}-\text{O}-\text{Mn}^{\text{III}}(\text{dpaq})]^{3+}$
- 2 $[(\text{BnTPEN})\text{Fe}^{\text{III}}-\text{O}-\text{Mn}^{\text{III}}(\text{dpaq})]^{3+}$

Chapter 5

- 1 $[(\text{TPA})\text{Fe}^{\text{III}}-\text{O}-\text{Mn}^{\text{III}}(\text{TPA})]^{4+}$
- 2 $[(\text{TPA})\text{Fe}^{\text{III}}(\text{O})(\mu-1,2\text{-peroxo})\text{Mn}^{\text{III}}(\text{TPA})]^{2+}$

Chapter 6

- 1 $[\text{Fe}^{\text{IV}}(\text{O}_{\text{anti}})(\text{TMC})(\text{NCCH}_3)](\text{OTf})_2$
- 2 $(\text{TMC})\text{Fe}-\text{O}-\text{Sc}^{\text{III}}(\text{OTf})_4(\text{OH}_x)$
- 3 $[\text{Fe}^{\text{IV}}(\text{O}_{\text{anti}})(\text{TMC})(\text{OTf})](\text{OTf})$
- 4 $(\text{CH}_3\text{CN})(\text{TMC})\text{Fe}^{\text{III}}-\text{O}_{\text{anti}}-\text{Cr}^{\text{III}}(\text{OTf})_4(\text{NCCH}_3)$
- 5 $(\text{TMC})\text{Fe}^{\text{III}}-\text{O}_{\text{syn}}-\text{Cr}^{\text{III}}(\text{OTf})_4(\text{NCCH}_3)$
- 6 $(\text{TMCPy})\text{Fe}^{\text{III}}-\text{O}-\text{Cr}^{\text{III}}(\text{OTf})_4(\text{NCCH}_3)$
- 7 $(\text{TMCdma})\text{Fe}^{\text{III}}-\text{O}-\text{Cr}^{\text{III}}(\text{OTf})_4(\text{NCCH}_3)$
- 8 $(\text{N4Py})\text{Fe}^{\text{III}}-\text{O}-\text{Cr}^{\text{III}}(\text{OTf})_4(\text{NCCH}_3)$
- 9 $(\text{BnTPEN})\text{Fe}^{\text{III}}-\text{O}-\text{Cr}^{\text{III}}(\text{OTf})_4(\text{NCCH}_3)$
- 10 $[(\text{N4Py})\text{Fe}^{\text{III}}-\text{O}-\text{Mn}^{\text{III}}(\text{dpaq})]^{3+}$
- 11 $[(\text{BnTPEN})\text{Fe}^{\text{III}}-\text{O}-\text{Mn}^{\text{III}}(\text{dpaq})]^{3+}$

Chapter 1

O₂ Activation by Bimetallic Active Sites

1.1 Enzymatic O₂ Activation in Nature

The importance of oxygen, which accounts for 20% of composition in air, can never be overestimated to living beings on earth. Molecular oxygen is quite stable due to its triplet ground state and strong O=O bond. However, nature has devised methods to activate the O₂ molecule and incorporate oxygen atoms into enzymatic substrates with high regioselectivity and stereoselectivity. Landmark research illustrating O₂ activation came from Osamu Hayaishi in 1955,¹ where the insertion of both oxygen atoms from O₂ into catechol to generate *cis,cis*-muconic acid by the enzyme catechol 1,2-dioxygenase was demonstrated (Figure 1.1). This enzyme was found to possess a monoiron center in the active site. Hayaishi's pioneering research has inspired researchers to investigate the functions of metal atoms in the oxygen activation process.²

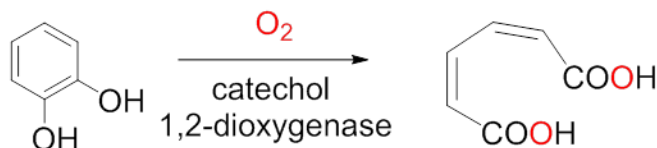


Figure 1.1 Dioxygen activation of catechol 1,2-dioxygenase found by Osamu Hayaishi.

Following this early observation, more examples of metals have been found to be involved in O₂ activation. Among these, iron stands out prominently because of its natural abundance and broad spectrum of oxidation states.³ O₂ activating iron proteins can be divided to two categories: heme and nonheme.⁴ In heme proteins, the iron center is coordinated by a large heterocyclic porphyrin ring.⁵ These iron-porphyrin structures are found in hemoglobin, myoglobin, cytochromes,^{5,6} and are critical in catalyzing a variety

of oxidation reactions, such as C–H bond hydroxylation, C=C bond epoxidation, aromatic hydroxylation and heteroatom oxidation.⁷ Unlike heme proteins, nonheme proteins do not contain a porphyrin ring coordinated to the iron center.

The 2-histidine-1-carboxylate facial coordination mode is a common motif in mononuclear nonheme proteins.⁸⁻¹⁰ Representative examples include taurine α -ketoglutarate (α -KG) dioxygenase (TauD), which catalyzes the conversion of 2-aminoethanesulfonate (taurine) to sulfite and aminoacetaldehyde, concurrent with the conversion of α -KG to succinate and CO₂.¹¹⁻¹⁴ As shown in Figure 1.2, the catalytic cycle begins with the binding of α -KG to the Fe(II) center *via* C1 carboxylate and keto oxygen atoms, thus substituting two water molecules. With the taurine molecule approaching the vicinity of the Fe(II) center, a third water molecule is released to generate a 5-coordinate Fe(II) species. The vacant axial binding site is then occupied by O₂ to form a ferric-superoxo species. The superoxide ligand subsequently carries out a nucleophilic attack on the α -carbon atom of α -KG, leading to the oxidative decarboxylation reactions and with the formation of a high-valent Fe(IV)-oxo intermediate, concomitantly with the succinate. The short-lived Fe(IV)-oxo species is thought to oxidize the taurine substrate *via* a hydrogen atom transfer (HAT) reaction, and similar intermediates have also been proposed in other α -KG dependent enzymes, such as halogenases CytC3^{15, 16} and phenylalanine hydroxylase (PheH).¹⁷ Identification and characterization of these transient species have enhanced our understanding on the role of the iron center in O₂ activation.

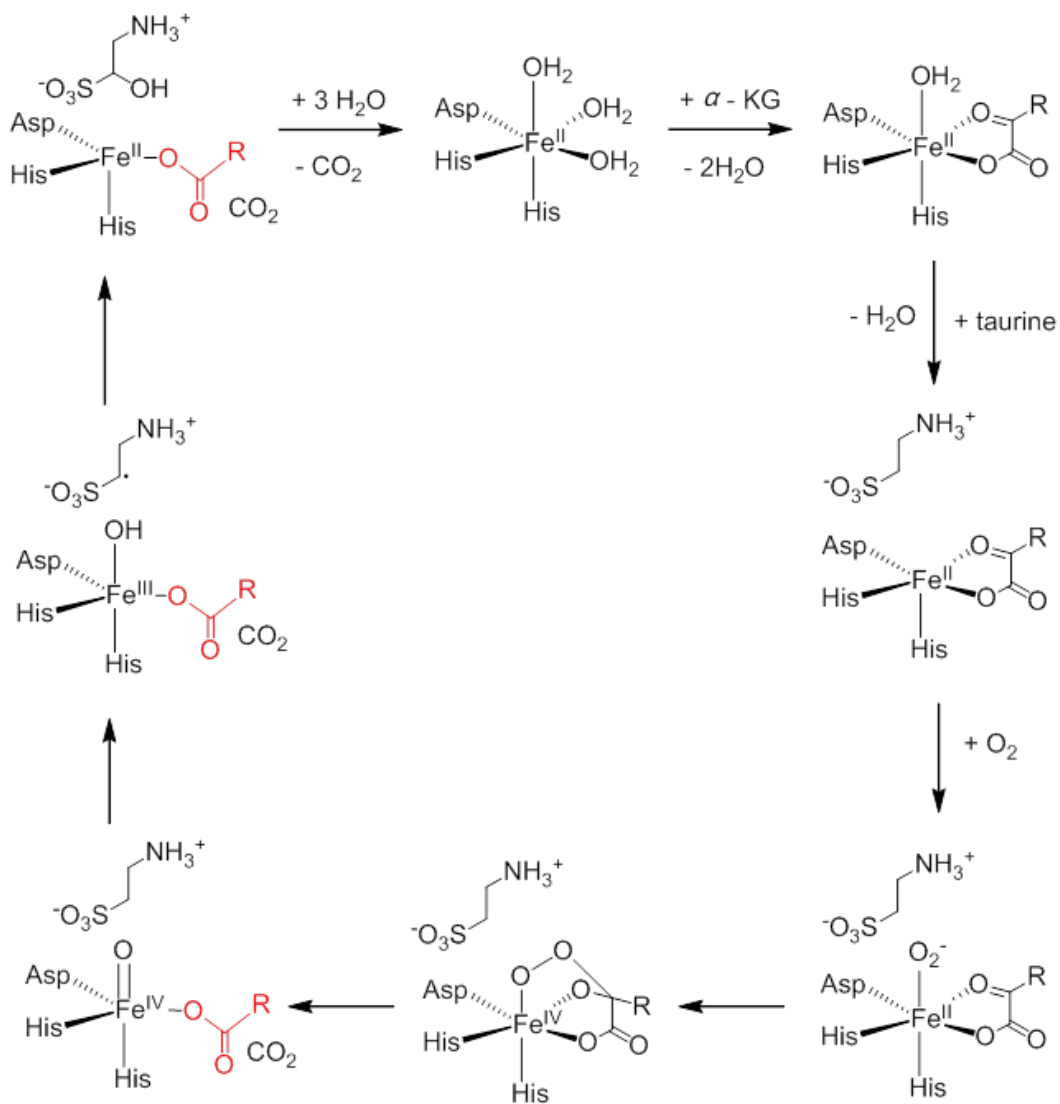


Figure 1.2 Proposed catalytic cycle of taurine/ α -ketoglutarate dioxygenase (TauD). Reproduced with permission from ref 13. Copyright 2007 American Chemical Society.

Besides O₂ activation systems with monoiron metallocofactors, the active sites may employ a second metal to work cooperatively with the iron center towards the activation of O₂. The extra metal endows an enlarged range of oxidation states, leading to

versatile bimetallic-oxygen intermediates. Based on the types of the second metal, the dimetal center can be either homobimetallic (two iron centers) or heterobimetallic (one iron center and one other center). Two examples, cytochrome c oxidase and class I ribonucleotide reductase, will be discussed to illustrate how two metals work together in O₂ activation. Next, the development of their corresponding synthetic model complexes and associated challenges will be reviewed. Finally, I will introduce the central idea of this thesis: construction of μ -oxo heterobimetallic complexes *via* inner-sphere electron transfer reactions.

1.2 Cytochrome c Oxidase

Cytochrome c oxidase (CcO) is a transmembrane protein that is essential for coupling four-electron reduction of O₂ to H₂O, with transportation of protons across the mitochondrial membrane.¹⁸⁻²⁰ CcO is widely found in bacteria and eukaryotes, and the electrochemical gradient it generates on both sides of mitochondrial membrane is important for ATP synthase activity.²¹

The crystal structure of the oxidized CcO in bovine heart revealed that thirteen different subunits constitute this large membrane protein.²² The biggest subunit is where O₂ reduction takes place, and it contains two iron heme centers and one copper center (Cu_B). The third biggest subunit contains the other copper center (Cu_A), which is also involved in O₂ activation.^{23, 24} Heme *a* has a 6-coordinate Fe center with two histidine residues binding to both axial coordination sites, while heme *a*₃ has only one histidine

binding to the axial position of the Fe center. The Cu_B site is 5.1 Å away from heme a₃, and is coordinated with three histidines. Cu_A is composed of a dicopper center coordinated with two histidines and four carboxylate amino acids (Figure 1.3).^{25, 26} These four metal centers each contribute one electron during the four electron reduction of the O₂.

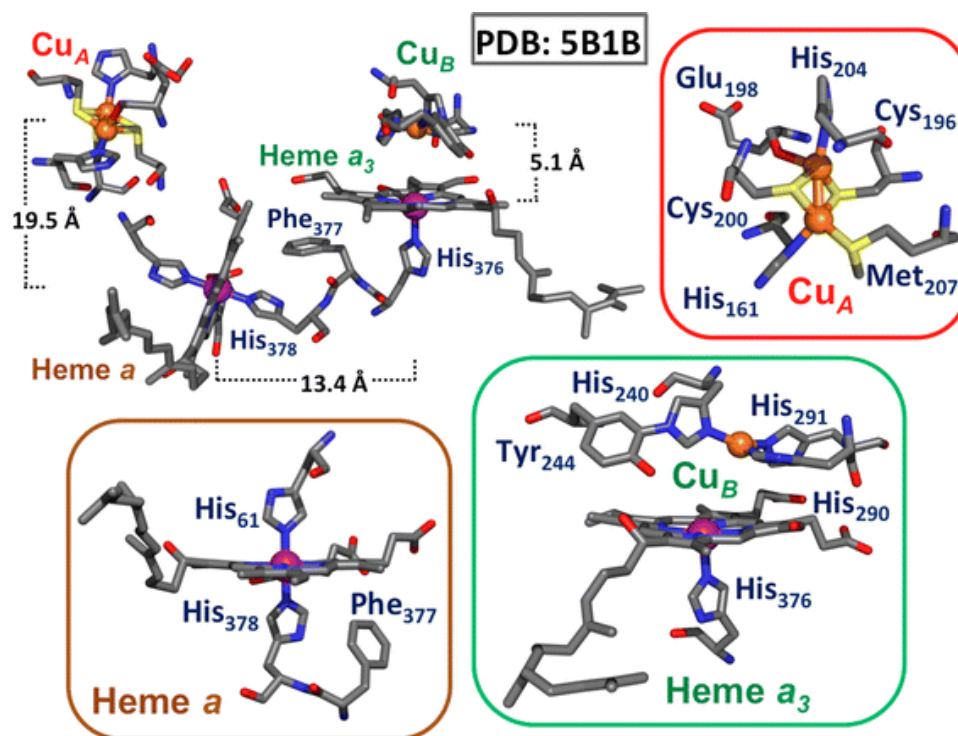


Figure 1.3 The four redox active metal sites of bovine heart CcO (*top left*). Heme *a* active site (*bottom left*). Dioxygen reduction site composed of heme a₃ and Cu_B (*bottom right*). Active site of the binuclear copper site referred to as Cu_A (*top right*). Reproduced with permission from ref 26. Copyright 2016 Springer.

In 1998, Yoshikawa's group reported the crystal structure of a fully-oxidized CcO-oxygen adduct with 2.3 Å resolution.²⁴ The two oxygen atoms are end-on bound

between the Fe_{a_3} and Cu_B centers, with $d(\text{O}-\text{O}) = 1.6 \text{ \AA}$, $d(\text{Cu}-\text{O}) = 2.2 \text{ \AA}$ and $d(\text{Fe}-\text{O}) = 2.5 \text{ \AA}$. The electron spin resonance and magnetic susceptibility experiments supported the antiferromagnetically coupling between a $S = 5/2$ Fe(III) and a $S = 1/2$ Cu(II) centers.^{27, 28} These results indicate that O_2 is reduced to a peroxide ligand bridging between Fe_{a_3} and Cu_B . In 2009, the Aoyama group reviewed this structure by limiting the X-ray dose for each exposure, and revealed a $d(\text{O}-\text{O}) = 1.70 \text{ \AA}$, $d(\text{Cu}-\text{O}) = 2.17 \text{ \AA}$ and $d(\text{Fe}-\text{O}) = 2.24 \text{ \AA}$ with 2.1 \AA resolution (Figure 1.4).²⁹ Based on the binding motif between metals and O–O moiety the author suggested O_2 is reduced by heme a_3 and Cu_B to a peroxo anion, although the O–O distance is longer than what is expected for a peroxo bond length ($1.4\text{--}1.5 \text{ \AA}$).

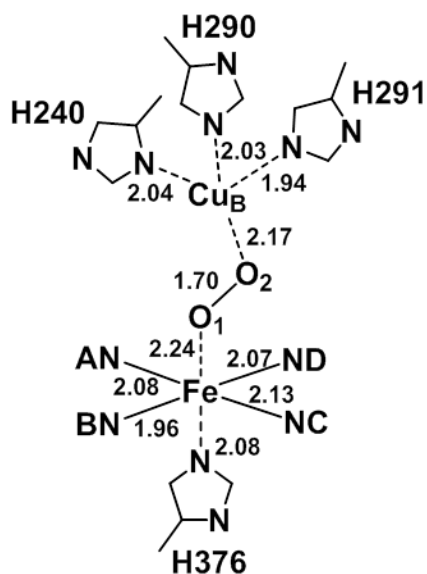


Figure 1.4 Coordination geometries of the peroxide unit in the fully-oxidized CcO at 2.1 \AA resolution.²⁹ Copyright 2009 National Academy of Sciences.

The full oxygen reduction cycle of CcO is shown in Figure 1.5.^{26, 30} The reaction is initiated by the binding of O₂ to Fe_{a3} to form an Fe_{a3}^{III}-O₂⁻ intermediate **A**, which is supported by the 571 cm⁻¹ (Fe-O₂) vibrational feature in resonance Raman spectroscopy.³¹⁻³³

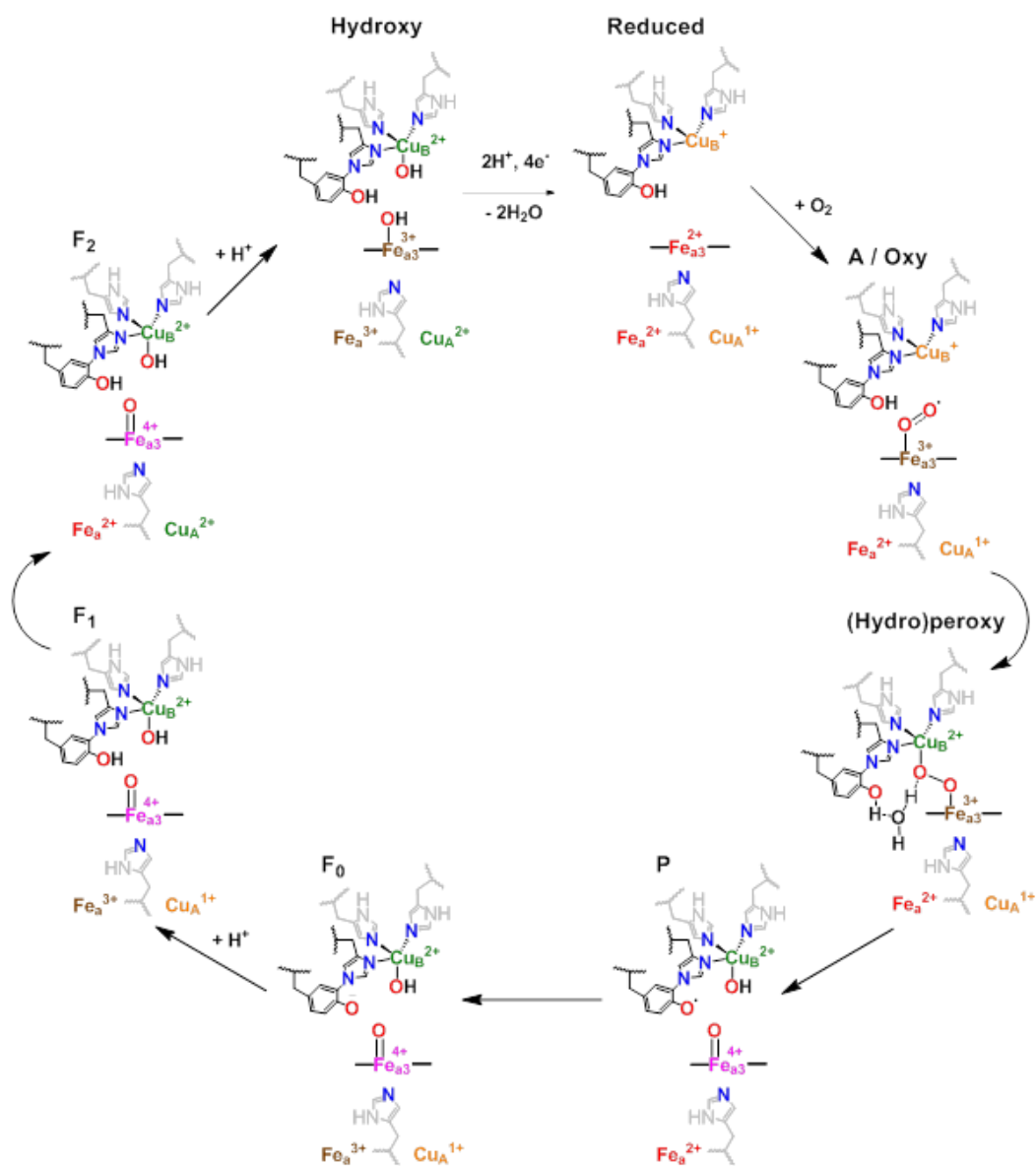


Figure 1.5 Proposed catalytic mechanism of CcO. Reproduced with permission from ref 26. Copyright 2016 Springer.

It is proposed that **A** is further reduced to form a putative $\text{Fe}_{a3}^{\text{III}}(\mu\text{-}1,2\text{-peroxo})\text{Cu}_B^{\text{II}}$ species, which has yet to be confirmed experimentally in the enzymatic systems. With the assistance of a proton from the adjacent amino acid network, the O–O bond is cleaved to sequentially generate the intermediate **P** ($\nu(\text{Fe}^{\text{IV}}=\text{O}) = 803 \text{ cm}^{-1}$) and intermediate **F** ($\nu(\text{Fe}^{\text{IV}}=\text{O}) = 785 \text{ cm}^{-1}$).^{34, 35} The formation of intermediate **F** can be further divided into three stages **F**₀, **F**₁, **F**₂ based on the oxidation state changes of heme *a* and Cu_A , as well as the protonation states in the adjacent Tyr244. Raman technique has played an important role in identifying the Fe/Cu-oxygen intermediates in the CcO catalytic cycle, and more of its applications will be reflected in identifying the correlated synthetic model complexes.

1.3 Ribonucleotide Reductase

1.3.1 Mechanism of Ribonucleotide Reduction

Ribonucleotide reductase (RNR) is an enzyme that reduces ribonucleotides (NDPs or NTPs, where N = C, U, G or A, and DP/TP means di-/tri- phosphate) to 2'-deoxynucleotides (dNDPs or dNTPs), which are the building blocks for DNA. Found in all organisms, RNR operates as the only *de novo* pathway for deoxynucleotide synthesis, irreplaceable in controlling DNA replication and repair in organisms.³⁶⁻³⁸

Studies on ribonucleotide reduction in different RNRs suggest that they all share a common free-radical mechanism (Figure 1.6).³⁹ Initiated by the abstraction of the C3 hydrogen of NDP or NTP by a cysteine thiyl radical, a radical is formed on C2 through a proton transfer from the proximal dithiol group. The second hydrogen atom is transferred from the dithiol group to reduce the radical C2 with the formation of a disulfide bridge anion radical. The C3 radical is reduced by the cysteine formed in the first step and the cysteine thiyl radical is thus recovered. Two hydrogens are transferred by redoxins to the disulfide group that restores the original configuration.

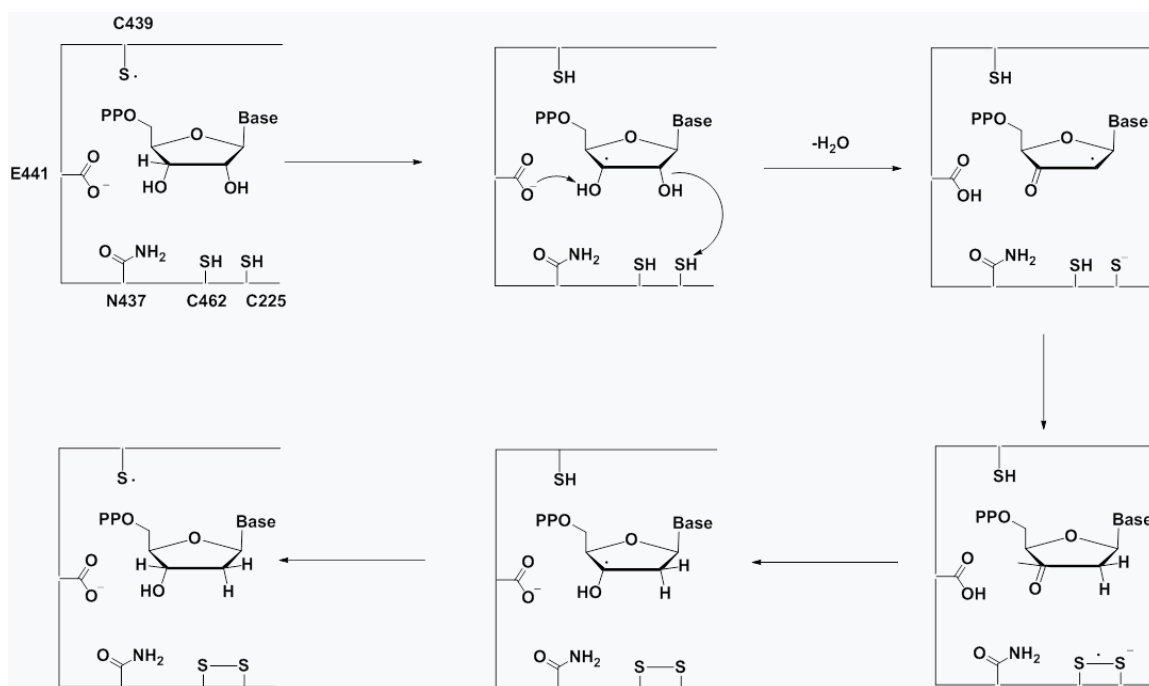


Figure 1.6 Generic reaction mechanism for ribonucleotide reduction. Reproduced with permission from ref 40. Copyright 2004 Wiley.

Based on the different mechanisms that the metallocofactors employ for cysteine thiyl radical formation, RNRs are divided into three classes: class I, class II and class III. Class I RNRs use a bimetallic active site (FeFe class Ia, MnMn class Ib, or FeMn class Ic) to generate the tyrosyl radical under aerobic conditions. Class II RNRs generate a free radical by mechanisms involving 5'-deoxyadenosyl cobalamin (coenzyme B12) under either aerobic or anaerobic conditions.^{41,42} Class III RNRs are anaerobic enzymes which generate a glycy radical with the assistance of an S-adenosyl methionine and an iron sulphur cluster under anaerobic conditions.⁴³ In the following sections attention will be focused on class I RNRs.

1.3.2 Structure and Function of Class Ia RNR

Herein class Ia RNR from *E. coli* (*Ec*) is used to illustrate the structure and function of class Ia RNR.⁴⁴ *Ec* Class Ia RNR is composed of two subunits: $\alpha 2$ and $\beta 2$. Although the crystal structure of an $\alpha 2\beta 2$ holoenzyme has not been solved, its structure is proposed based on the docking models.⁴⁵ $\alpha 2$ subunits contain the binding site of the ribonucleotide substrate, as well as two allosteric effector binding sites that govern which ribonucleotide is reduced.⁴⁵ $\beta 2$ subunits contains an Fe^{III}/Fe^{III}-tyrosyl cofactor. The tyrosine residue Y122, which is oxidized to Y \cdot upon O₂ activation in $\beta 2$, 35 Å away from the C439 site in $\alpha 2$ unit. This distance is too long for direct oxidation by a single step (Figure 1.7). The Stubbe group has proposed a radical transfer mechanism and identified key amino acids in this long-distance radical relay by site directed mutagenesis

substitution.⁴⁴ For example, when Y356 was replaced with 3,4-dihydroxyphenylalanine (DOPA), which has a 260 mV lower potential compared with Y, the reaction between Y356DOPA- β_2 and substrate led to the loss of initial tyrosyl radical concomitant with the formation of an equal amounts of DOPA \cdot .⁴⁶ This result indicates that the radical is trapped at the DOPA position, suggesting that Y356 is involved in the radical relay. Similarly, in α_2 subunits, Y730/Y731 are proposed to be involved in the radical relay.⁴⁷ These tyrosine residues between Y122 and C349 act as bridges to facilitate the long distance radical transfer.

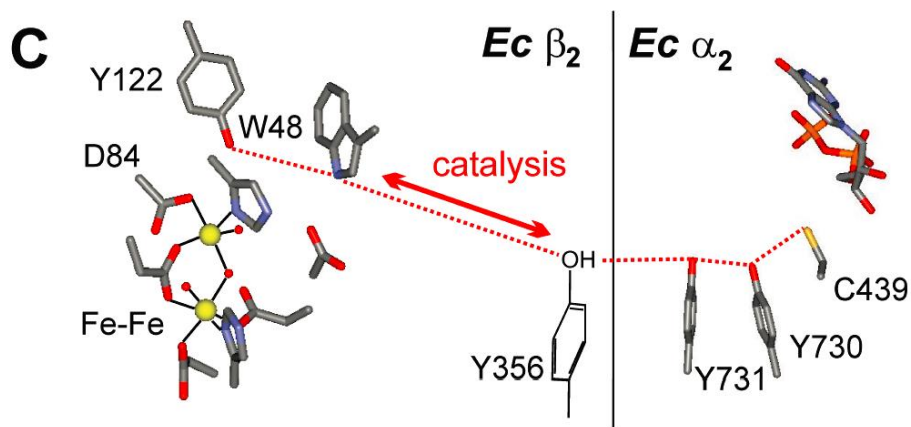


Figure 1.7 Proposed radical transfer pathways in *Ec* class Ia RNR. Reproduced with permission from ref 44. Copyright 2013 American Chemical Society.

The formation mechanism of the tyrosyl radical in the β_2 unit begins with the diiron cofactor in Figure 1.8. The diferrous cofactor located at NrdB (the β_2 subunit of the *E. coli* class Ia) first reacts with O_2 to generate a peroxodiferric intermediate.^{48, 49} This peroxodiferric species is then reduced by Trp48 to generate an Fe^{III}/Fe^{IV} species, named

intermediate **X**, which is proposed as the active oxidant for one-electron oxidation of the proximal tyrosine to tyrosyl radical.^{50, 51} Once the tyrosyl radical is formed, it initiates the long distance radical relay as illustrated in Figure 1.7. Also, A ferredoxin YfaE with the [2Fe2S] clusters is involved in reducing Trp48⁺ and diferric center, promoting the cycle to proceed smoothly.³⁹

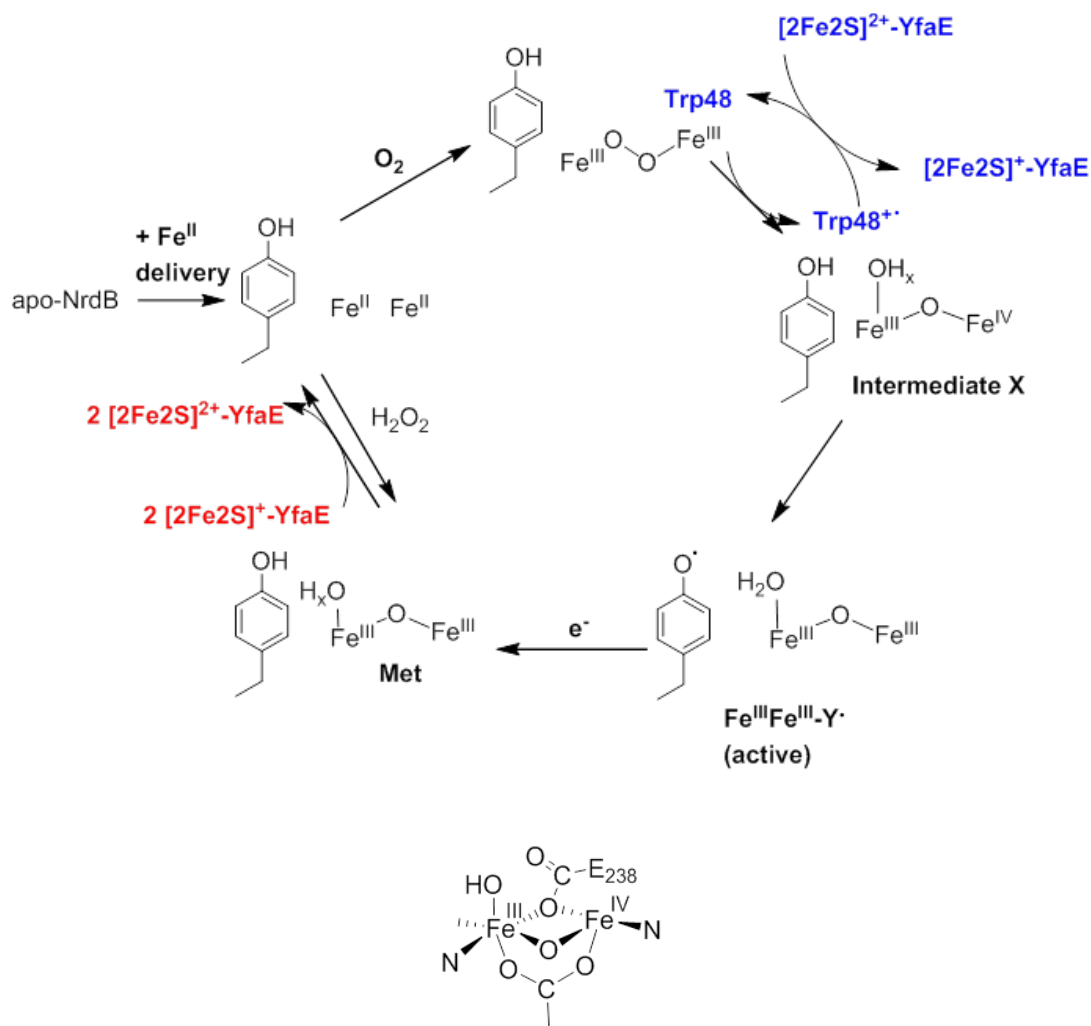


Figure 1.8 (Top) Proposed O₂ activation pathway in FeFe-Y• cofactor of class Ib RNR. Reproduced with permission from ref 39. Copyright 2011 Annual Reviews. (Bottom) Proposed structure of intermediate **X**.⁵⁶

The structure of intermediate **X** remained unclear for decades due to its instability (its decay rates is $\sim 1 \text{ s}^{-1}$ in the wild-type β and 0.2 s^{-1} in the Y122F variant at $5 \text{ }^\circ\text{C}$).^{50, 52} In 1998, the Stubbe group reported a 2.5 \AA Fe \cdots Fe vector and a 1.8 \AA Fe–O interaction in **X** based on extended X-ray absorption fine structure (EXAFS) analysis, and proposed a structure with three single-atom bridges (HO–, O₂–, and/or μ -1,1-carboxylates).⁵³ However, this short Fe \cdots Fe distance has been irreconcilable with computational models, which all predict $d(\text{Fe}\cdots\text{Fe}) \geq 2.7 \text{ \AA}$.^{54, 55} Also, no synthetic molecules with less than $2.5\text{-}\text{\AA}$ Fe \cdots Fe distance have been reported so far. In 2013, the Green group re-investigated the species **X** with a higher concentration sample, and a $2.78\text{-}\text{\AA}$ Fe \cdots Fe distance was obtained with better data quality in EXAFS analysis (Figure 1.8).⁵⁶ Two years later, the Hoffman group used the electron nuclear double resonance (ENDOR) techniques to further clarify the structure of **X**, in which one oxygen bridge is derived from O₂, while the second oxygen bridge is derived from a carboxyl in E238.⁵⁷

1.3.3 Structure and Function of Class Ib RNR

Class Ib RNRs are found in a wide range of aerobic prokaryotes.³⁹ With identical metal-binding residues to those of class Ia RNRs, class Ib RNRs have been long assumed to contain Fe^{III}Fe^{III}-Y· cofactors. It was not until 2010 when the Stubbe group provided evidence that class Ib RNR has a Mn^{III}Mn^{III}-Y· cofactor, not an Fe^{III}Fe^{III}-Y· cofactor.⁵⁸

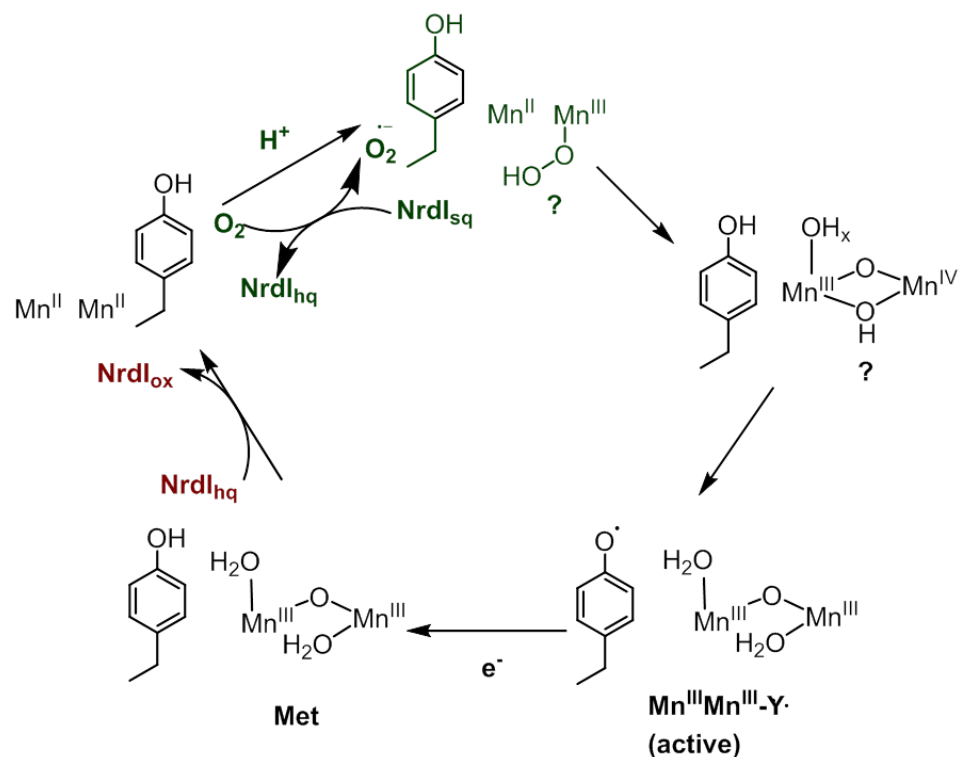


Figure 1.9 Proposed O_2 activation pathway in $MnMn-Y\cdot$ cofactor of class Ib RNR. Reproduced with permission from ref 39. Copyright 2011 Annual Reviews.

Although class Ia and class Ib RNRs are structurally homologous, the pathways of generating the tyrosyl radical upon O_2 activation are different. In the $\beta 2$ unit of class Ia RNR, it is thermodynamically favorable for the diiron site to activate O_2 . In class Ib RNR however, the dimanganese center can only activate O_2 with the assistance of a flavoprotein NrdI, which is proposed to react with O_2 first to form a superoxide radical. Sequentially a $Mn_2^{III/IV}$ species is generated to oxidize tyrosine (Figure 1.9).^{39, 59, 60}

1.3.4 Structure and Function of Class Ic RNR

In 2000, a class I RNR was isolated from pathogenic intracellular parasite *Chlamydia trachomatis* (*Ct*).⁶¹ In its crystal structure a redox-inert phenylalanine (F127) is located at the site where Y122 used to be at the proximity of diiron cofactor.⁶² Since Y122 is the radical precursor in forming cysteinyl radical in class Ia RNR, its replacement by F127 suggests a different mechanism of radical transfer.

Initially researchers hypothesized that an Fe^{IV}/Fe^{III} functionally replaced Y· in *Ct* class I RNR.⁶² Bollinger, Krebs and co-workers observed a $g = 2$ EPR signal with multiple hyperfine splitting pattern after reducing the oxidized intermediate in *Ct* $\beta 2$.⁶³ Since the ⁵⁶Fe nucleus has an $I = 0$ spin state, a metal with a nonzero I value should be involved to rationalize the hyperfine splitting pattern. They further examined the reactivity of *Ct* RNR to investigate the relationship between the metal content and enzymatic activity in the isolated $\beta 2$ subunit. When only Fe was added, the turnover number of $\beta 2$ is significantly lower than the reported value. However, when Mn and Fe were both added, the turnover number is significantly increased and maximized at a 1:1 ratio. Also, the Mn nucleus has a nuclear spin of 5/2, which can rationalize the hyperfine splitting pattern in the EPR signal that originates from electron-nucleus coupling. These observations suggest that the *Ct* $\beta 2$ employs an Fe/Mn cofactor rather than an Fe/Fe cofactor, and has later been named as class Ic RNR.

Bollinger, Krebs and co-workers further identified an Fe^{III}/Mn^{IV} intermediate in the catalytic cycle of class Ic RNR, equivalent to intermediate **X** in class Ia RNR.⁶⁴⁻⁶⁶

Due to the lack of tyrosine, the Fe^{III}/Mn^{IV} species is proposed to functionally replace the tyrosyl radical. Further analysis revealed that the Fe^{III}/Mn^{IV} intermediate is reduced from an Fe^{IV}/Mn^{IV} intermediate, which is initially formed during O₂ activation with Fe^{II}/Mn^{II} (Figure 1.10).⁶⁴ The formation pathway of Fe^{IV}/Mn^{IV} resembles the mechanism of generating the Fe^{IV}/Fe^{IV} intermediate **Q** in soluble methane monooxygenase.⁶⁷

Structures of both Fe^{III}/Mn^{IV} and Fe^{IV}/Mn^{IV} intermediates have been reported. EXAFS analysis of the Fe^{III}/Mn^{IV} complex indicates a 2.92 Å Fe···Mn distance and a 1.74 Å Mn–O bond.⁶⁸ Computational results suggest that these measurements are consistent with a μ -oxo/ μ -hydroxo/ μ -carboxylato Fe/Mn core. EXAFS analysis of the Fe^{IV}/Mn^{IV} intermediate revealed a 2.75 Å Fe···Mn distance and a 1.8 Å Fe–C/N/O interaction, from which a bis- μ -oxo/ μ -carboxylato Fe/Mn core is proposed.⁶⁹

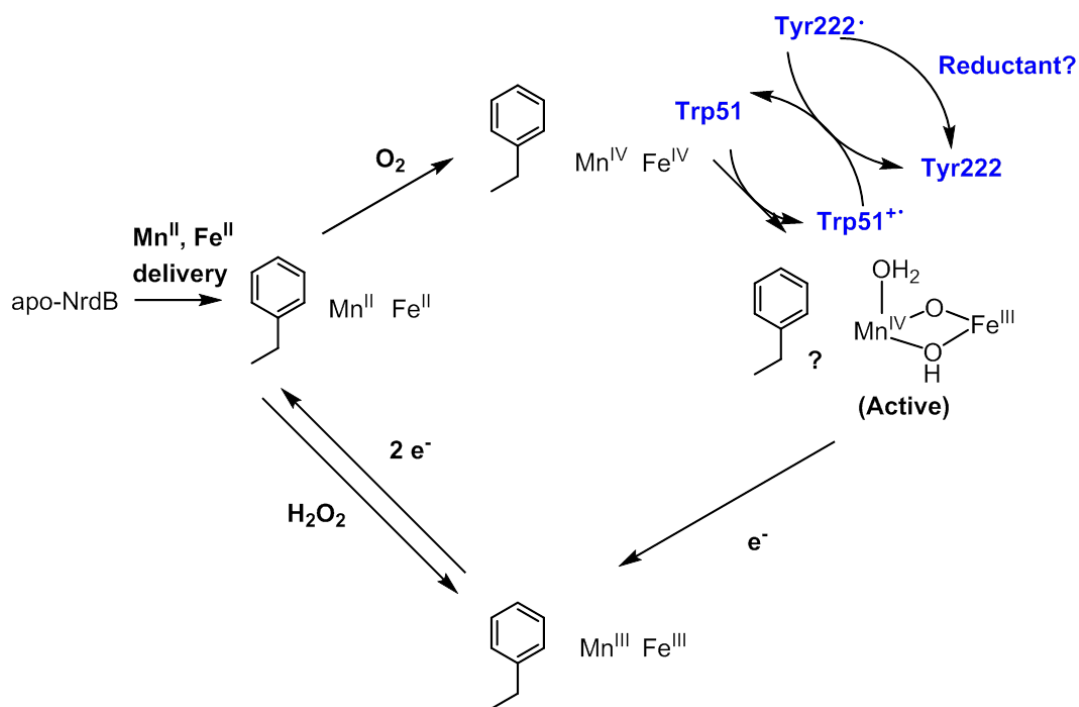


Figure 1.10 Proposed O₂ activation pathway in FeMn cofactor of class Ic RNR. Reproduced with permission from ref 39. Copyright 2011 Annual Reviews.

1.4 Synthetic Models for Bimetallic-Oxygen Intermediates

Based on the cases of CcO and class I RNR discussed above, the O₂ activation process catalyzed by bimetallic active sites can be divided into two stages: (i) binding of the O₂ to the metal atoms; (ii) cleavage of O–O bond. In CcO, O₂ is proposed to first bind with Fe_{a3} to generate an Fe_{a3}^{III}-O₂⁻ intermediate, which further converts to the proposed Fe_{a3}^{III}-(μ-1,2-peroxo)-Cu_B^{II} species. In class Ic RNR, a Fe^{IV}/Mn^{IV} species is proposed to form after O–O bond activation, and is sequentially reduced to Fe^{III}/Mn^{IV} species to oxidize the cysteine that initiates the ribonucleotide reduction. In both stages, various bimetallic-oxygen intermediates have been identified or proposed in the catalytic cycle. They have inspired synthetic chemists to prepare model complexes to better understand the structures and reactivity of their analogues in nature. In the following part, the development and associated challenges of bimetallic-oxygen synthetic complexes in the CcO and class I RNR enzymatic systems will be discussed.

1.4.1 Synthetic Models of Bimetallic-Oxygen Species in CcO

The suggestion of an Fe_{a3}^{III}(μ-1,2-peroxo)Cu_B^{II} binding mode in the crystal structure of oxidized bovine heart CcO inspired researchers to develop corresponding synthetic molecules.^{24, 29} In 1999, the Karlin group reported the activation of O₂ by

$[(^6\text{L})\text{Fe}^{\text{II}}\text{-Cu}^{\text{I}}](\text{BAr}^{\text{F}})$ (In the ^6L ligand, the triphenylporphyrin and tris(2-pyridylmethyl)-amine moieties are connected by an ether oxygen linkage).⁷⁰ The oxidized product was speculated to be $(^6\text{L})\text{Fe}^{\text{III}}(\text{peroxo})\text{Cu}^{\text{II}}$ based on the $[(^6\text{L})\text{Fe}^{\text{III}}\text{Cu}^{\text{II}}(\text{O}_2)]^+$ cluster peak observed in ESI-MS spectrum and a 787 cm^{-1} vibration ($\Delta^{16}\text{O}_2/^{18}\text{O}_2 = 43\text{ cm}^{-1}$) in the resonance Raman spectrum (Figure 1.11). However, the binding mode of the peroxo unit to the bimetallic center was not clear by that time.

In 2003 the Naruta group prepared a complex $[(\text{TMP})\text{Fe}^{\text{II}}\text{Cu}^{\text{I}}(5\text{MeTPA})]\text{BPh}_4$ (TMP-5MeTPA = 10,15,20-tris(2,4,6-trimethylphenyl)-5-(2'-bis((5''-methyl-2''-pyridylmethyl)aminomethyl)pyridine-5'-carboxyamidophenyl)-porphyrin). Upon exposure to O_2 , a new complex with similar UV-vis patterns as $[(^6\text{L})\text{Fe}^{\text{III}}(\text{O}_2)\text{Cu}^{\text{II}}]^+$ was formed.⁷¹ This new species is stable enough to allow successful recrystallization, with the XRD results of $[(\text{TMP})\text{Fe}^{\text{III}}(\text{O}_2)\text{Cu}^{\text{II}}(5\text{MeTPA})]^+$ with a $\mu\text{-}\eta^2\text{:}\eta^1$ Fe–O₂–Cu binding motif: Both oxygen atoms of the peroxo unit bind to Fe, while only one oxygen atom binds to Cu (Figure 1.11). The Raman spectrum of the complex exhibited the peroxo vibrational band at 790 cm^{-1} ($\Delta^{16}\text{O}_2/^{18}\text{O}_2 = 43\text{ cm}^{-1}$), comparable to the band of 787 cm^{-1} ($\Delta^{16}\text{O}_2/^{18}\text{O}_2 = 43\text{ cm}^{-1}$) in $[(^6\text{L})\text{Fe}^{\text{III}}(\text{O}_2)\text{Cu}^{\text{II}}]^+$. The similarity in UV-vis spectra as well as Raman vibrations suggested that $[(^6\text{L})\text{Fe}^{\text{III}}(\text{O}_2)\text{Cu}^{\text{II}}]^+$ also has a $\mu\text{-}\eta^2\text{:}\eta^1$ Fe–O₂–Cu binding motif.

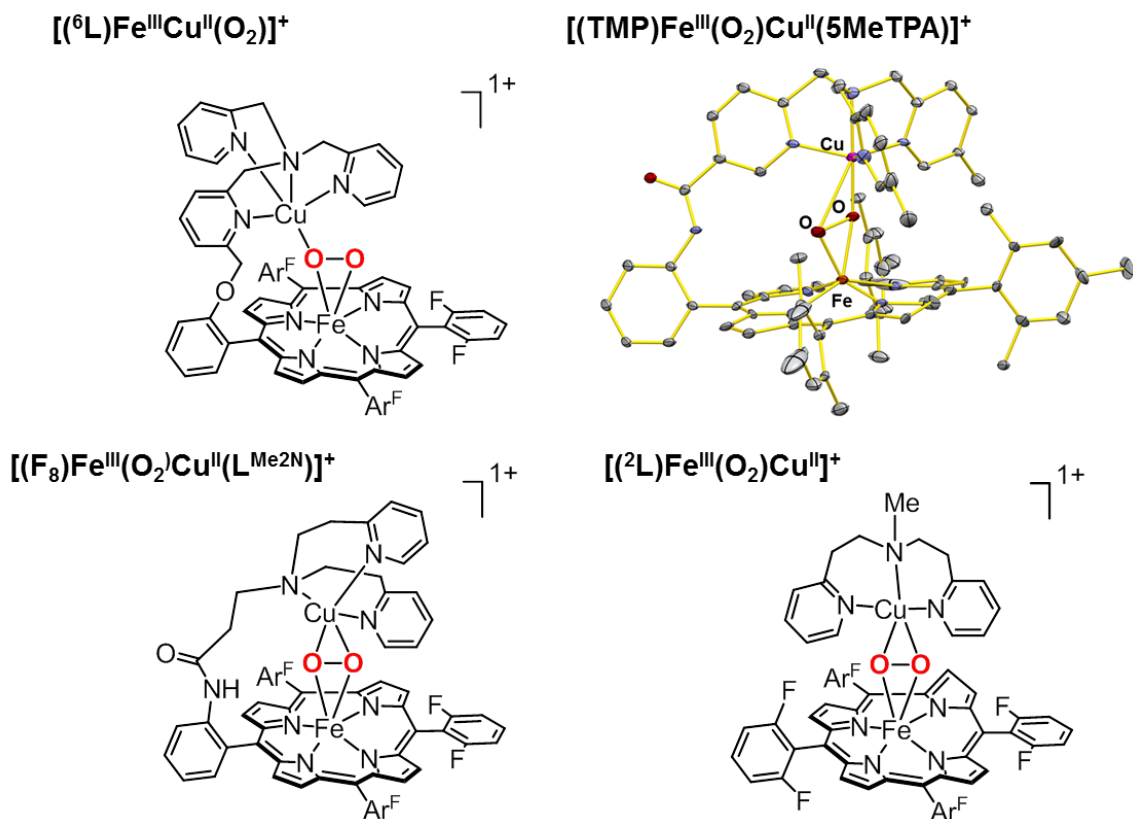


Figure 1.11 Structures of $[(^6L)Fe^{III}Cu^{II}(O_2)]^+$,⁷⁰ $[(TMP)Fe^{III}(O_2)Cu^{II}(5MeTPA)]^+$,⁷¹ $[(F_8)Fe^{III}(O_2)Cu^{II}(L^{Me2N})]^+$,⁷² and $[(^2L)Fe^{III}(O_2)Cu^{II}]^+$ complexes.⁷³

The $\mu\text{-}\eta^2\text{:}\eta^1$ Fe–O₂–Cu synthetic complexes were further elaborated with the switch from a tetradentate to a tridentate ligand on Cu site. Examples include $[(F_8)Fe^{III}(O_2)Cu^{II}(L^{Me2N})]^+$ (F_8 = tetrakis(2,6-difluorophenyl) porphyrinate, L^{Me2N} = *N,N*-bis-(2-(2-(*N',N'*-4-dimethylamino)pyridyl)ethyl)methylamine)⁷² and $[(^2L)Fe^{III}(O_2)Cu^{II}]^+$ (2L = 3-(bis(2-(pyridin-2-yl)ethyl)amino)-*N*-(2-(15-(2,6-difluorophenyl)-10,20-bis(fluoroargio)porphyrin-5yl)phenyl)propanamide)).⁷⁴ The $\nu(O-O)$ band in $[(F_8)Fe^{III}(O_2)Cu^{II}(L^{Me2N})]^+$ and $[(^2L)Fe^{III}(O_2)Cu^{II}]^+$ were 752 cm⁻¹ and 747 cm⁻¹, significantly lower than $\nu(O-O)$ in $[(^6L)Fe^{III}(O_2)Cu^{II}]^+$ and

$[(\text{TMP})\text{Fe}^{\text{III}}(\text{O}_2)\text{Cu}^{\text{II}}(5\text{MeTPA})]$ ($\sim 790\text{ cm}^{-1}$). This observation is rationalized by the change in binding mode of the peroxo ligand from $\mu\text{-}\eta^2\text{:}\eta^1$ to $\mu\text{-}\eta^2\text{:}\eta^2$ in $[(\text{F}_8)\text{Fe}^{\text{III}}(\text{O}_2)\text{Cu}^{\text{II}}(\text{L}^{\text{Me}_2\text{N}})]^+$ and $[(^2\text{L})\text{Fe}^{\text{III}}(\text{O}_2)\text{Cu}^{\text{II}}]^+$ (Figure 1.11), and was further confirmed by XAS analysis. The finding of $\mu\text{-}\eta^2\text{:}\eta^1$ and $\mu\text{-}\eta^2\text{:}\eta^2$ Fe–O₂–Cu moieties in these synthetic complexes is interesting; however these structures are not consistent with what is observed in the crystal structure of oxidized bovine heart CcO, which is proposed to have a Fe–(μ -1,2-peroxo)–Cu motif.

1.4.2 Synthetic Models for Bimetallic-Oxygen Species in Class Ia RNR

In the $\beta 2$ unit of class Ia RNR, the diferrous center first reacts with one molecule of O₂ to generate an Fe^{III}/Fe^{III}-peroxo intermediate, which subsequently converts to an Fe^{III}/Fe^{IV} species. This process can also be divided into two steps: the binding of O₂ and the cleavage of the O–O bond. Synthetic chemists have characterized a series of peroxodiferric complexes in efforts to study the mechanism of O₂ binding and breaking.

The (μ -alkoxo)(μ -carboxylato)diiron(II) compounds supported by the dinucleating ligand, HPTB (N,N,N',N'-tetrakis(2-benzylimidazolylmethyl)-2-hydroxo-1,3-diaminopropane), are among the first diiron(II) compounds to form peroxodiferric intermediate upon oxygenation.⁷⁵⁻⁷⁹ Reported by the Que group, the reaction between $[\text{Fe}^{\text{II}}_2(\mu\text{-N-Et-HPTB})(\text{Ph}_3\text{PO})_2]^{3+}$ and O₂ resulted in a species exhibiting a visible absorption band at 600 nm and resonance Raman features at 900 cm⁻¹, characteristic of a μ -1,2-peroxo species.⁸⁰ The XRD structure of one complex was solved and confirmed the

$[\text{Fe}^{\text{III}}_2(\mu\text{-N-Et-HPTB})(\mu\text{-1,2-O}_2)(\text{Ph}_3\text{PO})_2]^{3+}$ composition, in which the peroxo unit coordinates in a *cis- μ -1,2* fashion with an Fe \cdots Fe distance of 3.46 Å (Figure 1.12).⁷⁵ Another example of peroxodiferric synthetic complex is $[\text{Fe}^{\text{III}}_2(\mu\text{-1,2-O}_2)(\mu\text{-O}_2\text{CCH}_2\text{Ph})_2(\text{HB}(\text{pz}')_3)_2]$ ($\text{pz}' = 3,5\text{-bis(isopropyl)-pyrazolyl}$) reported by the Lippard group, which was generated upon exposure of the monoiron(II) precursor to O_2 .⁸¹ The peroxo unit bridges the two iron atoms also in a $\mu\text{-1,2}$ mode, and gave rise to an Fe \cdots Fe separation of 4.0 Å together with the two bridging carboxylate ligands (Figure 1.12).⁷⁸ The shorter Fe \cdots Fe distance in $[\text{Fe}^{\text{III}}_2(\mu\text{-N-Et-HPTB})(\mu\text{-1,2-O}_2)(\text{Ph}_3\text{PO})_2]^{3+}$ compared to that in $[\text{Fe}^{\text{III}}_2(\mu\text{-1,2-O}_2)(\mu\text{-O}_2\text{CCH}_2\text{Ph})_2(\text{HB}(\text{pz}')_3)_2]$ is due to the greater constraint imposed by the dinucleating ligand in the former.

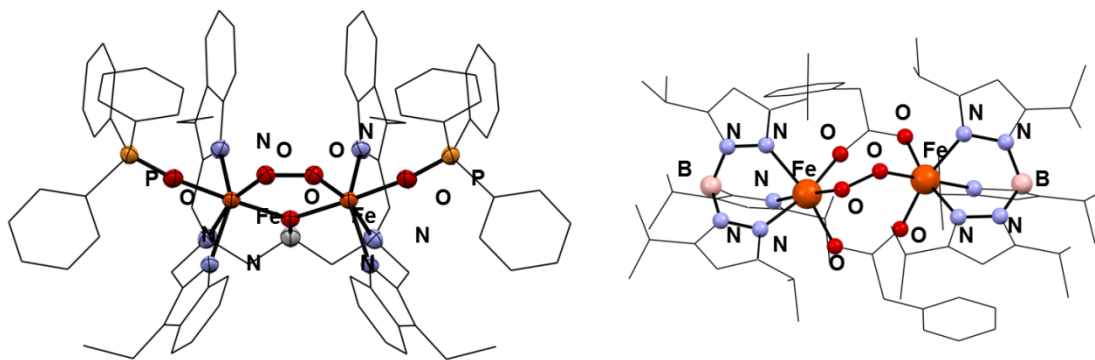


Figure 1.12 Crystal structures of $[\text{Fe}^{\text{III}}_2(\mu\text{-N-Et-HPTB})(\mu\text{-1,2-O}_2)(\text{Ph}_3\text{PO})_2]^{3+75}$ (left) and $[\text{Fe}^{\text{III}}_2(\mu\text{-1,2-O}_2)(\mu\text{-O}_2\text{CCH}_2\text{Ph})_2(\text{HB}(\text{pz}')_3)_2]^{81}$ (right).

The synthetic models of **X** formed after the cleavage of the O–O bond in the peroxodiferric complexes has also been investigated. The Que group has reported that the

reaction of $[\text{Fe}^{\text{III}}_2(\mu\text{-O})(5\text{-Me}_3\text{-TPA})_2(\text{OH})(\text{OH}_2)]^{3+}$ (5-Me₃-TPA = tris(5-methyl-2-pyridylmethyl)amine) with H₂O₂ can yield a $[\text{Fe}^{\text{III}}\text{Fe}^{\text{IV}}(\text{O})_2(5\text{-Me}_3\text{-TPA})_2]^{3+}$ species, and was determined as a paramagnetic-coupled $S = 3/2$ complex by EPR and Mössbauer spectroscopy.^{78, 79, 82} Interestingly, when 6-Me₃-TPA (6-Me₃-TPA = tris(6-methyl-2-pyridylmethyl)amine) was used as the supporting ligand, the $[\text{Fe}^{\text{III}}\text{Fe}^{\text{IV}}(\text{O})_2(6\text{-Me}_3\text{-TPA})_2]^{3+}$ species generated following the same procedure is an antiferromagnetically coupled $S = 1/2$ complex, which is also the case in intermediate **X**.⁸³

1.4.3 Synthetic Models for Bimetallic-Oxygen Species in Class Ib RNR

Synthetic dimanganese model complexes capable of O₂ activation have also been studied. The Kovacs group thoroughly investigated the O₂ activation by a series of monomanganese(II) complexes, which are supported by ligand scaffolds consisting of a thiolate and either a primary amine or N-heterocycle donors.⁸⁴ One representative complex is $[\text{Mn}^{\text{II}}(\text{S}^{\text{Me}_2}\text{N}_4(6\text{-MeDPEN}))](\text{BPh}_4)$ ($\text{S}^{\text{Me}_2}\text{N}_4(6\text{-MeDPEN}) = 3\text{-}((2\text{-}(\text{bis}((6\text{-methylpyridin-2-yl)methyl)amino)ethyl)imino)\text{-}2\text{-methylbutane-2-thiol}$) (Figure 1.13). At room temperature $[\text{Mn}^{\text{II}}(\text{S}^{\text{Me}_2}\text{N}_4(6\text{-MeDPEN}))](\text{BPh}_4)$ reacts with O₂ to form a stable Mn^{III}-O-Mn^{III} species, while at -40 °C the reaction leads to a metastable green species $[(\text{Mn}^{\text{III}}(\text{SMe}_2\text{N}_4(6\text{-MeDPEN}))_2(\mu\text{-O}_2))]^{2+}$.⁸⁵ The crystal structure of the peroxodimanganese complex exhibits a *trans*- μ -1,2 binding mode with a 1.45-Å O-O bond, and its resonance Raman spectrum exhibits $\nu_{\text{O-O}}(\Delta^{18}\text{O}) = 819(47) \text{ cm}^{-1}$ and $\nu_{\text{Mn-O}}(\Delta^{18}\text{O}) = 611(25) \text{ cm}^{-1}$. Although this peroxodimanganese complex is the first well characterized μ -1,2

Mn(III)–peroxo species with XRD structure, such species is not proposed in the O₂ activation cycle of the β2 unit in class Ib RNR. Instead, in the enzyme a hydroperoxo-Mn^{II}Mn^{III} intermediate is first proposed to form from the reaction of O₂^{•-} with the Mn^{II}Mn^{II} cluster and a proton donor (Figure 1.9).

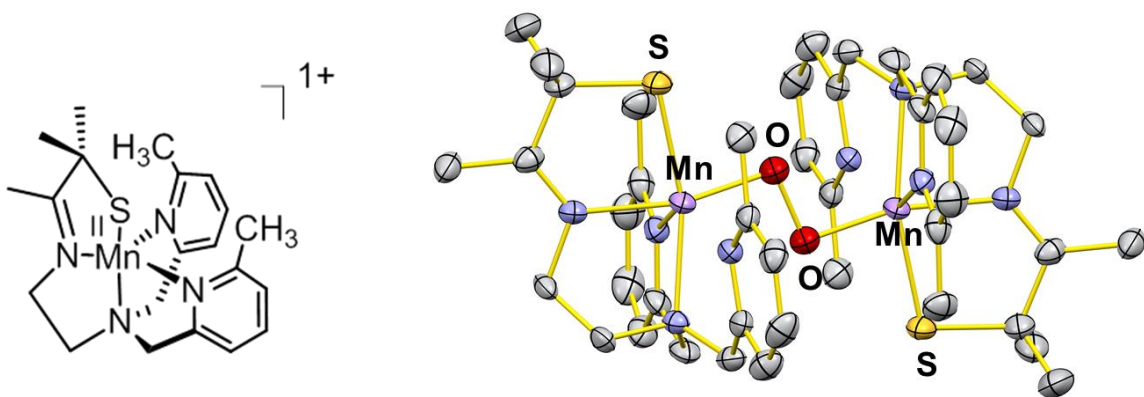


Figure 1.13 (Left) Structure of $[\text{Mn}^{\text{II}}(\text{S}^{\text{Me}_2}\text{N}_4(6\text{-MeDPEN}))]^+$ that can react with O₂. (Right) ORTEP of peroxo-bridged $[(\text{Mn}^{\text{III}}(\text{S}^{\text{Me}_2}\text{N}_4(6\text{-MeDPEN}))_2(\mu\text{-O}_2))]^{2+}$ with 50% probability ellipsoids.⁸⁵ Hydrogen atoms are omitted for clarity.

Synthetic dimanganese complexes after O–O bond cleavage have also been studied. The Jackson group have reported the conversion of $[\text{Mn}^{\text{II}}(\text{N4Py})(\text{OTf})](\text{OTf})$ to $[\text{Mn}^{\text{III}}\text{Mn}^{\text{IV}}(\mu\text{-O})_2(\text{N4Py})_2]^{3+}$ by treating the system with superoxide. However, the reactivity of the Mn^{III}Mn^{IV} species has not been reported.⁸⁶

1.4.4 Synthetic Models for Bimetallic-Oxygen Species in Class Ic RNR

Although the Fe/Mn active site in class Ic RNR was first identified in 2007,⁶³ the Fe/Mn synthetic models have a much longer history. In 1992, Wieghardt and coworkers

reported the synthesis of carboxylate-bridged $(\text{TACN})\text{Fe}^{\text{III}}-\text{O}-\text{Mn}^{\text{III}}(\text{Me}_3\text{TACN})$ complexes (TACN = 1,4,7-triazacyclononane, Me_3TACN = 1,4,7-trimethyl-1,4,7-triazacyclononane), formed *via* hydrolysis of $\text{FeCl}_3(\text{TACN})$ and $\text{MnCl}_3(\text{Me}_3\text{TACN})$ precursors, where the bridging oxygen atom is derived from H_2O .⁸⁷ In another case, the Que group prepared a $[\text{Fe}^{\text{III}}\text{Mn}^{\text{II}}\text{BPMP}(\text{O}_2\text{CCH}_2\text{CH}_3)_2](\text{BPh}_4)$ compound (BPMP is the anion of 2,6-bis[bis(2-pyridylmethyl)-amino)methyl]-4-methylphenol) by sequentially adding Fe and Mn salts into a solution of the BPMP ligand, where the Fe–O–Mn core is supported by a phenoxy bridge (Figure 1.14).⁸⁸

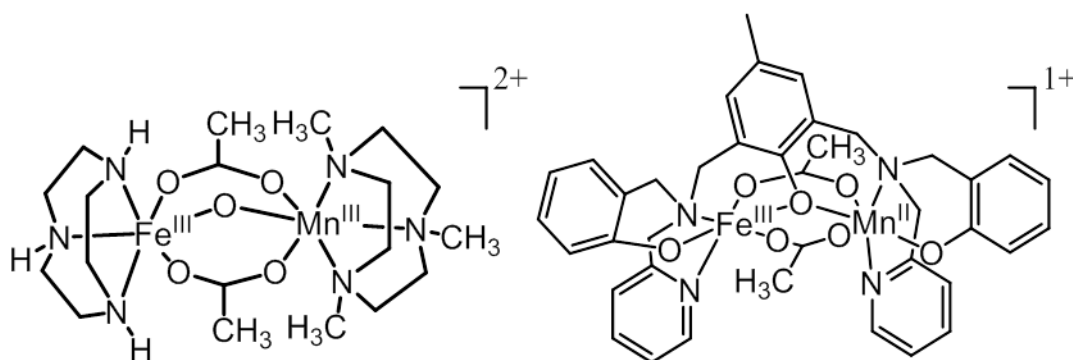


Figure 1.14 (Left) Structure of $[\text{TACN})\text{Fe}^{\text{III}}-\text{O}-\text{Mn}^{\text{III}}(\text{Me}_3\text{TACN})]^{2+}$.⁸⁷ (Right) $[\text{Fe}^{\text{III}}\text{Mn}^{\text{II}}\text{BPMP}(\text{O}_2\text{CCH}_2\text{CH}_3)_2]^+$.⁸⁸

In both cases, the synthetic Fe/Mn complexes were constructed by a spontaneous self-assembly process. However, as Fe and Mn ions are very close in size and mass, the reaction is more likely to produce a mixture of Fe–O–Fe, Fe–O–Mn and Mn–O–Mn units. The difficulty in selectively binding the two metals at specific sites while avoiding mixtures and homodinuclear side products is a problem. Additionally, in class Ic RNR, the proposed active intermediates are $\text{Fe}^{\text{III}}/\text{Mn}^{\text{IV}}$ and $\text{Fe}^{\text{IV}}/\text{Mn}^{\text{IV}}$ species, but no synthetic

$\text{Fe}^{\text{III}}/\text{Mn}^{\text{IV}}$ or $\text{Fe}^{\text{IV}}/\text{Mn}^{\text{IV}}$ complexes have been reported up to date. This has inspired me to look for an alternative approach to synthesize Fe/Mn bimetallic complexes.

1.5 Scope and Aim of Thesis

When examining the model complexes of the Fe/Cu site in CcO, I was intrigued by the synthetic design of an $\text{Fe}^{\text{III}}\text{-O-Cu}^{\text{II}}$ complex prepared by the Karlin group (Figure 1.15). The complex, $[(\text{F}_8\text{-TPP})\text{Fe}^{\text{III}}\text{-O-Cu}^{\text{II}}(\text{TPA})]^+$ ($\text{F}_8\text{-TPP}$ = tetrakis(2,6-difluorophenyl) porphyrinate, TPA = tris(2-pyridylmethyl)-amine) was generated through an acid-base reaction between $[(\text{F}_8\text{-TPP})\text{Fe}^{\text{III}}(\text{OH})]$ and $[\text{Cu}^{\text{II}}(\text{TPA})]^{2+}$ with the addition of NEt_3 , ensuring a 1:1 Fe : Cu ratio of the resulting heterobimetallic complex.⁸⁹ Inspired by this elegant system, I thought to use a similar strategy to make the Fe-O-Mn complex.

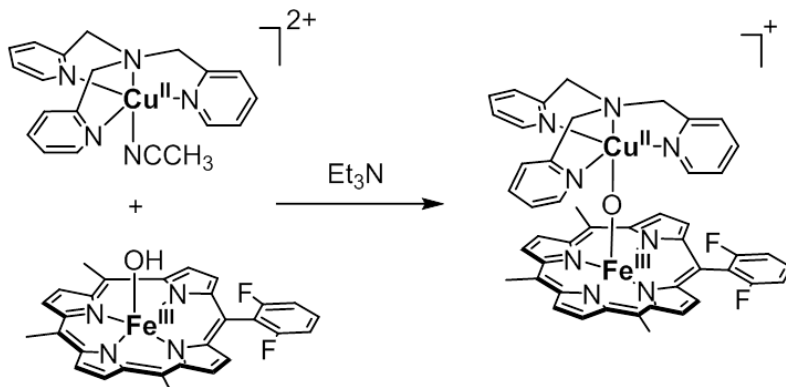


Figure 1.15 Synthesis scheme for $[(\text{F}_8\text{-TPP})\text{Fe}^{\text{III}}\text{-O-Cu}^{\text{II}}(\text{TPA})]^+$.⁸⁹

Although nonheme Fe(III)-hydroxide synthetic molecules are rare in literature,⁹⁰⁻
⁹³ there is a big pool of nonheme Fe(IV)-oxo species that have been reported and

characterized.⁹⁴ In order to build the Fe–O–Mn core, instead of an acid-base reaction between an Fe(III)-hydroxide complex and Mn salt, a complementary approach is to react an Fe(IV)-oxo complex with a reducing Mn salt *via* an inner-sphere electron transfer reaction. This process should assemble μ -oxo heterobimetallic core at a high yield.

However, there are two concerns for this strategy. Firstly, it is possible that the μ -oxo heterobimetallic may not be stable and can dissociate. For example, the Nam group reported the reaction between $[\text{Fe}^{\text{IV}}(\text{O})(\text{N4Py})](\text{OTf})_2$ (N4Py = N,N-bis(2-pyridylmethyl)-N-bis(2-pyridyl)methylamine) and $[\text{Fe}^{\text{II}}(\text{TMC})(\text{NCCH}_3)](\text{OTf})_2$ (TMC = 1,4,8,11-tetramethyl-1,4,8,11-tetraazacyclotetradecane),⁹⁵ and the final products were identified as $[\text{Fe}^{\text{II}}(\text{N4Py})](\text{OTf})_2$ and $[\text{Fe}^{\text{IV}}(\text{O})(\text{TMC})](\text{OTf})_2$. In the paper it is proposed that the reaction proceeds through a transient $(\text{TMC})\text{Fe}^{\text{III}}\text{--O--Fe}^{\text{III}}(\text{N4Py})$ species, followed by the dissociation of the μ -oxo bimetallic core. Secondly, whether the inner-sphere electron transfer is thermodynamically favorable depends on the difference in redox potential between Fe(IV)-oxo species and the Mn(II) salt. To construct the desired Fe–O–Mn species, an oxoiron(IV) complex with enough oxidizing capability and a Mn(II) salt with enough reducing capability are required.

Previously, Dr. Katherine M. Van Heuvelen in the Que group studied the reaction between $[\text{Fe}^{\text{IV}}\text{O}(\text{TMC})](\text{OTf})_2$ and CrCl_2 . What she observed are three distinct bands between 300 nm and 600 nm with the product formation. However, the product is not stable, and its structure is not clear. After repeating these experiments, I utilized $\text{Cr}(\text{OTf})_2$ instead of CrCl_2 to minimize the effect of chloride anion binding to the Fe(IV)-oxo

moiety, and was able to obtain a series of $\text{Fe}^{\text{III}}\text{-O-Cr}^{\text{III}}$ species with detailed characterization (Chapters 2 and 3).

With the success in making the $\text{Fe}^{\text{III}}\text{-O-Cr}^{\text{III}}$ complexes, I moved forward to making the model complexes for Fe/Mn active site in class Ic RNR. Two reaction systems, $[\text{Fe}^{\text{IV}}(\text{O})(\text{N4Py})](\text{OTf})_2$ with $[\text{Mn}^{\text{II}}(\text{dpaq})](\text{OTf})$ (dpaq = 2-[bis(pyridin-2-ylmethyl)]amino-N-quinolin-8-yl-acetamidate), as well as $[\text{Fe}^{\text{IV}}(\text{O})(\text{TPA})(\text{NCCH}_3)](\text{OTf})_2$ with $\text{Mn}^{\text{II}}(\text{TPA})(\text{OTf})_2$, were carried out, and the corresponding $\text{Fe}^{\text{III}}\text{-O-Mn}^{\text{III}}$ species were generated and studied with various spectroscopic techniques (Chapters 4 and 5). These Fe-O-Mn species are among the very few synthetic complexes with Fe/Mn bimetallic center, and their structures and reactivities have been compared with the Fe/Mn intermediates in Class Ic RNR. This research provides an alternative way of synthesizing μ -oxo heterobimetallic complexes with convenience and high efficiency.

Chapter 2

The Two Faces of Tetramethylcyclam in Iron Chemistry:

Distinct Fe–O–M Complexes Derived from

$[\text{Fe}^{\text{IV}}(\text{O}_{\text{anti/syn}})(\text{TMC})]^{2+}$ Isomers

Parts of this chapter were published in:

1. **Zhou, A.**; Kleespies, S.; Heuvelen, K.; Que, L. Jr. Characterization of a Heterobimetallic Nonheme Fe(III)–O–Cr(III) Species Formed by O₂ Activation. *Chem. Commun.* **2015**, *51*, 14326-14329.

2. **Zhou, A.**; Prakash, J.; Rohde, G. T.; Klein, J. E. M. N.; Kleespies, S. T.; Draksharapu, A.; Fan, R.; Guo, Y.; Cramer, C. J.; Que, L., Jr. The Two Faces of Tetramethylcyclam in Iron Chemistry: Distinct Fe–O–M Complexes Derived from [Fe^{IV}(O_{syn/anti})(TMC)]²⁺ Isomers. *Inorg. Chem.* **2017**, *56*, 518-527.

Reprinted with permission from the Royal Society of Chemistry. Copyright © 2015, Royal Society of Chemistry. & the American Chemical Society. Copyright © 2016, American Chemical Society.

2.1 Introduction

Enzymes with dinuclear metallocofactors exhibit versatile functions in nature. In their catalytic cycles, the two metal ions are often connected through a bridging ligand with resulting cooperative effects. Oxo-bridged heterobimetallic species stand out as novel examples of this class and act as crucial intermediates in various bimetallic active sites. One example is the Mn–O–Ca unit found in the oxygen-evolving complex (OEC) of photosystem II (PS II) at which the O–O bond is proposed to form.^{96,97} The other case is the Fe/Mn cofactor in Class 1c ribonucleotide reductases from *Chlamydia trachomatis*.^{98,99} The bimetallic center is proposed to react with O₂ to form an Fe^{III}–O–Mn^{IV} species that serves as the one-electron oxidant of the conserved cysteine residue required to initiate the conversion from ribonucleotides to deoxyribonucleotides.

For decades, different strategies have been investigated to prepare synthetic (μ -oxo)–heterobimetallic molecules in order to improve our understanding of the structures and chemical properties of their analogs in nature. For example, Wieghardt reported a series of carboxylate-bridged (TACN)Fe^{III}–O–M(Me₃TACN) complexes (M = Cr^{III} or Mn^{III}, TACN = 1,4,7-triazacyclononane, Me₃TACN = 1,4,7-trimethyl-1,4,7-triazacyclononane) by hydrolysis between FeCl₃(TACN) and MCl₃(Me₃TACN) precursors, where the bridging oxygen atom is derived from H₂O.⁸⁷ In another case, the Que group prepared a [Fe^{II}Mn^{II}BPMP(O₂CCH₂CH₃)₂](BPh₄) compound (BPMP is the anion of 2,6-bis[(bis(2-pyridylmethyl)-amino)methyl]-4-methylphenol) by sequentially adding Fe and Mn salt into the solution with the BPMP ligand, and the Mn–O–Fe core is supported via a phenoxy bridge.⁸⁸

In 2010, Fukuzumi and Nam reported the crystal structure of a novel [(TMC)Fe–O–Sc^{III}(OTf)₄(OH_x)] complex (**3**), which was obtained from the reaction of Sc(OTf)₃ with [Fe^{IV}(O)(TMC)(NCCH₃)]²⁺ (TMC = 1,4,8,11-tetramethyl-1,4,8,11-tetraazacyclotetradecane).¹⁰⁰ This structure sparked some controversy with respect to the iron oxidation state,¹⁰¹ which was assigned as +4 in the original report but was later revised to +3 after detailed spectroscopic characterization.¹⁰²

Inspired by this result, herein we reported the synthesis and characterization of [(CH₃CN)(TMC)Fe^{III}–O_{anti}–Cr^{III}(OTf)₄(NCCH₃)] (**1**) from reaction between [Fe^{IV}(O_{anti})(TMC)(NCCH₃)]²⁺ and 1 equiv. Cr(OTf)₂, as well as [(TMC)Fe^{III}–O_{syn}–Cr^{III}(OTf)₄(NCCH₃)] (**2**) from reaction between [Fe^{IV}(O_{syn})(TMC)(NCCH₃)]²⁺¹⁰³ and 1 equiv. of Cr(OTf)₂. The *anti* and *syn* subscripts in **1** and **2** reflect different orientations of the Fe=O unit with respect to the methyl groups of the TMC ligand. In **1** the methyl groups are presumed to be *anti* to the oxo bridge, while in **2** the methyl groups are presumed to be *syn* to the oxo bridge. UV-vis, resonance Raman, Mössbauer, and X-ray absorption spectroscopic methods, as well as electrospray mass spectrometry, were used to confirm the structures of **1** and **2**, indicating the Fe center is 6-coordinate in the former and 5-coordinate in the latter. The correlation between orientation of the TMC methyl groups and the coordination number of the metal center is further clarified with crystallographically characterized complexes (Cl)(TMC)Fe^{III}–O_{anti}–Fe^{III}Cl₃ (**4_{Cl}**) and [(TMC)Fe^{III}–O_{syn}–Fe^{III}Cl₃](OTf) (**5**). All these results provide insight into how ligand topology can affect the coordination spheres of the metal sites.

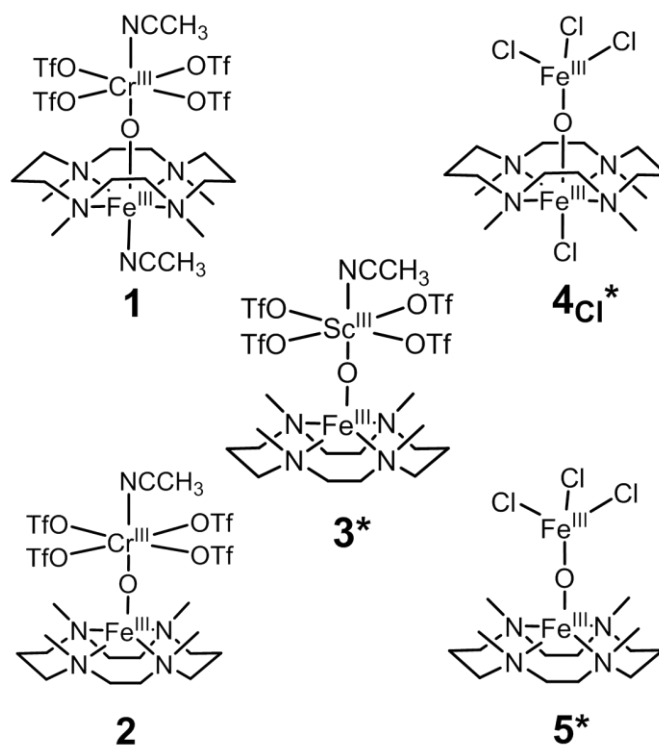


Figure 2.1 Structures of complexes **1** – **5**. An asterisk indicates that XRD data has been obtained to determine the structures of these complexes.

2.2 Experimental Details

2.2.1 Materials

All reagents and solvents were purchased from commercial sources and used as received unless specified. The preparations for $\text{Cr}(\text{OTf})_2 \cdot 2\text{CH}_3\text{CN}$,¹⁰⁴ $\text{Fe}^{\text{II}}(\text{TMC})(\text{OTf})_2$,¹⁰⁵ iodosylbenzene ($\text{C}_6\text{H}_5\text{IO}$),¹⁰⁶ 2-(*tert*-butylsulfonyl)iodosylbenzene ($2\text{-}^t\text{BuSO}_2\text{-C}_6\text{H}_4\text{IO}$)^{107, 108} were carried out following published procedures. (*Caution: An injury was recently reported while attempting to synthesize 2-^tBuSO₂-C₆H₄IO,*¹⁰⁹ so this synthetic procedure should be carried out with the appropriate safety precautions and

protective equipment).¹¹⁰ The ¹⁸O labeled isotopomer of 2-(*tert*-butylsulfonyl)iodosylbenzene was synthesized according to the published procedure.¹¹¹ All moisture- and oxygen-sensitive compounds were prepared using standard Schlenk-line techniques.

Complexes **4_{Cl}** and **4_{OTf}** were obtained by the following procedures: The oxoiron(IV) species [Fe^{IV}(O_{anti})(TMC)(NCCH₃)]²⁺ was generated by vigorously stirring an acetonitrile solution of Fe^{II}(TMC)(OTf)₂ (25 mg in 2 mL, 0.04 mmol) with 2 equiv. of solid C₆H₅IO (~ 17 mg, 0.08 mmol) at room temperature. The unreacted insoluble C₆H₅IO particles were then removed from the solution by filtration using a PTFE syringe filter. One equiv. of Et₄NFe^{III}Cl₄ (13.5 mg, 0.04 mmol, dissolved in acetonitrile) was then added to the solution, and the solution was placed in a diethyl ether bath at -20 °C for crystallization. A crystalline solid was obtained within one week in 50-60 % yield, which was used for NMR and IR analysis. Elemental analysis data obtained from this solid was consistent with its formulation as (TfO)(TMC)Fe^{III}-O_{anti}-Fe^{III}Cl₃, so this solid was designated as **4_{OTf}**. Anal. Calcd. for C₁₅H₃₂Cl₃F₃Fe₂N₄O₄S (**4_{OTf}**): C, 28.17; H, 5.04; N, 8.76; Cl, 16.63. Found: C, 28.68; H, 5.03; N, 8.74; Cl, 16.15. The ¹⁸O-labeled **4_{OTf}** was obtained in an analogous manner using C₆H₅I¹⁸O as an oxidant. However, the single crystal selected for X-ray diffraction analysis was found to possess a composition of (Cl)(TMC)Fe^{III}-O_{anti}-Fe^{III}Cl₃ and designated as **4_{Cl}**.

Complex **5** was prepared by following the same procedure except that the oxoiron(IV) species [Fe^{IV}(O_{syn})(TMC)(NCCH₃)]²⁺ was generated by adding one equiv. of 2-¹BuSO₂-C₆H₄IO (dissolved in trifluoroethanol) to the acetonitrile solution of

$\text{Fe}^{\text{II}}(\text{TMC})(\text{OTf})_2$ at room temperature. Yield = 50-60 %. Anal. Calcd. for $\text{C}_{15}\text{H}_{32}\text{Cl}_3\text{F}_3\text{Fe}_2\text{N}_4\text{O}_4\text{S}$: C, 28.17; H, 5.04; N, 8.76. Found: C, 27.72; H, 5.16; N, 8.57. ^{18}O -labeled **5** was obtained in an analogous manner using $2\text{-}^t\text{BuSO}_2\text{-C}_6\text{H}_5\text{I}^{18}\text{O}$ as an oxidant.

2.2.2 Instrumentation

Elemental analyses were carried out by Atlantic Microlab (Norcross, GA). UV-vis absorption spectra were recorded on an HP 8453A diode array spectrometer. Low-temperature visible spectra were obtained using a cryostat from UNISOKU Scientific Instruments, Japan. Electrospray mass spectrometry was performed on a Finnigan LCQ ion trap mass spectrometer. FTIR measurements were performed using Thermo Scientific (Nicolet iS5) spectrometer equipped with a diamond ATR module (iD5). Resonance Raman and Raman spectra were collected with an Acton AM-506 monochromator equipped with a Princeton LN/CCD data collection system, with 568.2-nm excitation from a Spectra-Physics model 2060 krypton-ion laser on **1**, 514.5-nm excitation from a Spectra-Physics model 2060 argon-ion laser on **2**, and 515-nm excitation from a 50 mW laser by Cobolt Lasers, Inc. on **3**. Spectra in acetonitrile were obtained at 77 K using a 135° backscattering geometry. Raman samples were prepared in cuvettes in a -40°C cold bath and quickly transferred to either a gold-plated copper cold finger in thermal contact with a Dewar flask containing liquid N_2 (**1**), or in EPR tubes and then froze (**2** and **3**). Raman bands were calibrated to indene prior to data collection. The monochromator slit

width was set for a band pass of 4 cm^{-1} for all spectra. Mössbauer spectra were recorded with home-built spectrometers using Janis Research Super-Varitemp dewars. Mössbauer spectral simulations were performed using the WMOSS software package (SEE Co., Edina, MN). Isomer shifts are quoted relative to Fe metal at 298 K. All Mössbauer figures were prepared using SpinCount software.¹¹²

2.2.3 X-ray Absorption Spectroscopy (XAS)

XAS data on **1** were collected at beamline X3B at the National Synchrotron Light Source (NSLS) of Brookhaven National Laboratory. Fe K-edge XAS data were collected for frozen solutions maintained at $\sim 30\text{ K}$ over the energy range 6.9-8.0 keV. A Fe foil spectrum was measured simultaneously for internal energy calibration using the first inflection point of the K-edge energy (7112.0 eV). Data were obtained as fluorescence excitation spectra using a solid-state germanium detector (Canberra).

XAS data on **2** were collected at Beamline 7-3 at the Stanford Synchrotron Radiation Lightsource (SSRL) of SLAC National Accelerator Laboratory. Fe K-edge XAS data were collected for frozen solutions maintained at $\sim 10\text{ K}$ over the energy range of 6.9-8.0 keV. An Fe foil spectrum was measured simultaneously for internal energy calibration using the first inflection point of the K-edge energy (7112.0 eV). Data were obtained as fluorescence excitation spectra using a solid-state germanium detector (Canberra).

Data reduction, averaging, and normalization on both **1** and **2** were performed using the program EXAFSPAK. The coordination number of a given shell was a fixed parameter and was varied iteratively in integer steps while the bond lengths (R) and mean-square deviation (σ^2) were allowed to freely float. The amplitude reduction factor was fixed at 0.9 while the edge-shift parameter E_0 was allowed to float as a single value for all shells. The pre-edge features were fitted using the Fityk program¹¹³ with pseudo-Voigt functions composed of 50:50 Gaussian/Lorentzian functions.

2.2.4 X-ray Crystallography

Selected single crystals of **4_{Cl}** or **5** were placed onto the top of a 0.1 mm diameter glass capillary and mounted on a Bruker APEX II area detector diffractometer for data collection at 173(2) K. The structures were solved and refined using the SHELXL software package and ShelXle graphical user interface.^{114, 115} Additional crystallographic details may be found in the cif files, CCDC numbers 1503819 and 1503820.

2.3 Results and Discussion

2.3.1 Generation of **1** and **2**

Firstly, we investigated the reaction of $[\text{Fe}^{\text{IV}}(\text{O}_{\text{anti}})(\text{TMC})(\text{NCCH}_3)]^{2+}$ with $\text{Cr}(\text{OTf})_2$ in CH_3CN at $-40\text{ }^\circ\text{C}$ as a more direct means of synthesizing putative species **1**. As shown in Figure 2.2, the addition of $\text{Cr}(\text{OTf})_2$ to $[\text{Fe}^{\text{IV}}(\text{O}_{\text{anti}})(\text{TMC})(\text{NCCH}_3)]^{2+}$ in

CH₃CN solution caused the instantaneous disappearance of its characteristic 824-nm peak concomitant with the growth of bands at 398, 447, and 558 nm that are assigned to **1**. Titration experiments (Figure 2.2, inset) revealed that the transformation was complete upon addition of 1 equiv. Cr(OTf)₂, strongly suggesting a 1:1 Fe:Cr stoichiometry for **1**.

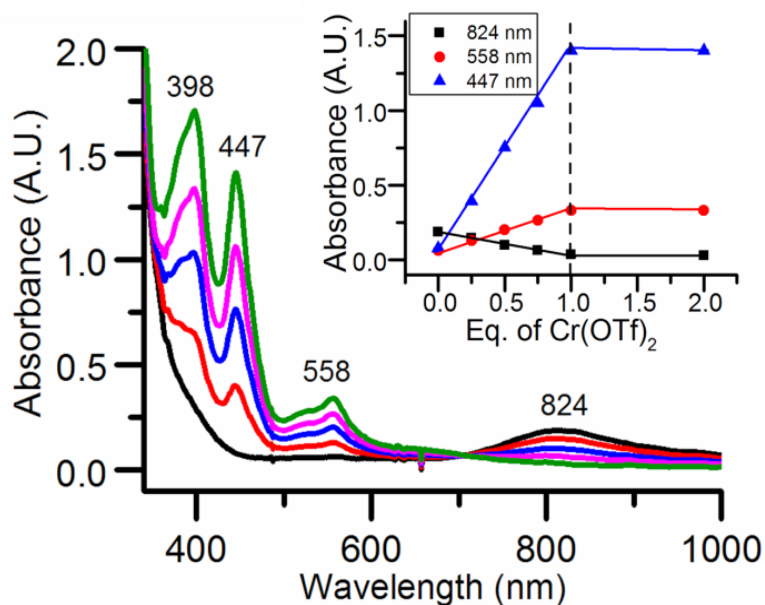


Figure 2.2 UV-vis spectral titration of 0.45 mM [Fe^{IV}(O)(TMC)(NCCH₃)₂]²⁺ in CH₃CN at -40 °C with Cr(OTf)₂. Black, 0 equiv.; red, 0.25 equiv.; blue: 0.5 equiv.; magenta, 0.75 equiv.; green, 1 equiv. Inset: titration plot. Inset: Formation of **1** vs equiv. Cr(OTf)₂ added into 0.45 mM [Fe^{IV}(O)(TMC)(NCCH₃)₂]²⁺ in CH₃CN at -40 °C.

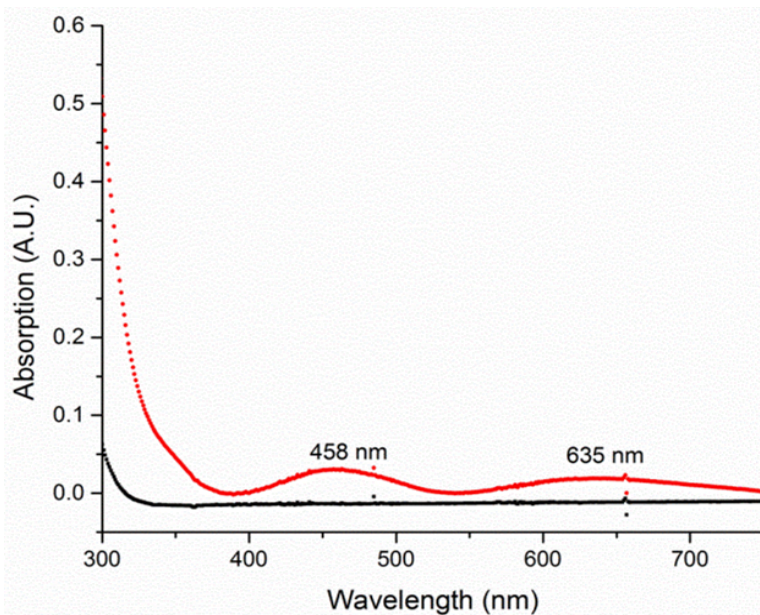


Figure 2.3 UV-vis spectra of 1 mM Cr(OTf)₂ in CH₃CN before (black) and after addition of 1 equiv. PhIO (red).

A control experiment between Cr(OTf)₂ and PhIO did not elicit the same peaks as found in **1** (Figure 2.3) suggesting that [Fe^{IV}(O)(TMC)(NCCH₃)²⁺ acts more than just an oxygen atom donor to Cr(OTf)₂. These results demonstrate that **1** can be generated by inner-sphere electron transfer from Cr(II) to oxoiron moiety.

In parallel, a 0.35 mM solution of [Fe^{IV}(O_{syn})(TMC)(NCCH₃)](OTf)₂ was first generated by adding 1 equiv. of (2-^tBuSO₂-C₆H₄IO) (dissolved in trifluoroethanol) to the acetonitrile solution of the iron(II)-precursor complex Fe^{II}(TMC)(OTf)₂ at -40 °C. The addition of 1 equiv. of Cr(OTf)₂ into the oxoiron(IV) solution resulted in the immediate disappearance of its characteristic 815-nm near-IR band, concomitant with the growth of bands at 395 nm, 446 nm, 515 nm and 560 nm, indicating the formation of a new species

(Figure 2.4). The bands at 395 nm, 446 nm and 560 nm resemble those reported for the closely related complex **1** at 397 nm, 447 nm and 558 nm, which is generated from the reaction of $[\text{Fe}^{\text{IV}}(\text{O}_{\text{anti}})(\text{TMC})(\text{NCCH}_3)](\text{OTf})_2$ with $\text{Cr}(\text{OTf})_2$, but the 515-nm band of **2** is unique. The similarity in chromophores reflects the structural similarities between **1** and **2**.

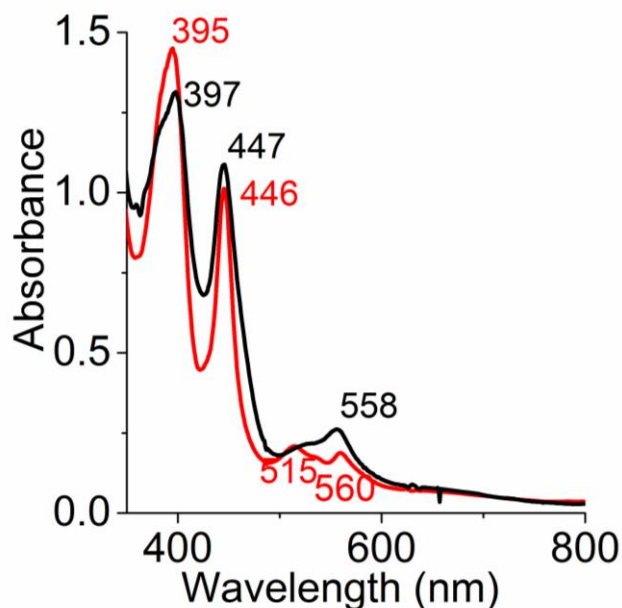


Figure 2.4 UV-vis absorption spectra of black: 0.35 mM **1**; red: 0.35 mM **2** in CH_3CN at $-40\text{ }^\circ\text{C}$.

2.3.2 ESI-MS Characterization of **1** and **2**

ESI-MS analysis of the solution of **1** at $-40\text{ }^\circ\text{C}$ revealed dominant peaks at m/z 461.2 (positive mode) and 514.8 (negative mode) (Figure 2.5). The ions observed have masses and isotope distribution patterns that correspond to $[\text{Fe}(\text{TMC})(\text{OTf})]^+$ and

$[\text{CrO}(\text{OTf})_3]^-$, respectively. Furthermore, the $[\text{CrO}(\text{OTf})_3]^-$ peak was upshifted by 2 units when $[\text{Fe}^{\text{IV}}(^{18}\text{O}_{\text{anti}})(\text{TMC})(\text{NCCH}_3)]^{2+}$ was used, showing the incorporation of an oxygen atom from oxoiron moiety (Figure 2.5). Based on these results, we tentatively assign **1** as a heterobimetallic $[(\text{TMC})\text{Fe}^{\text{III}}-\text{O}-\text{Cr}^{\text{III}}(\text{OTf})_4]$ complex, which undergoes homolysis of the Fe–O bond to give rise to the observed mass spectral features.

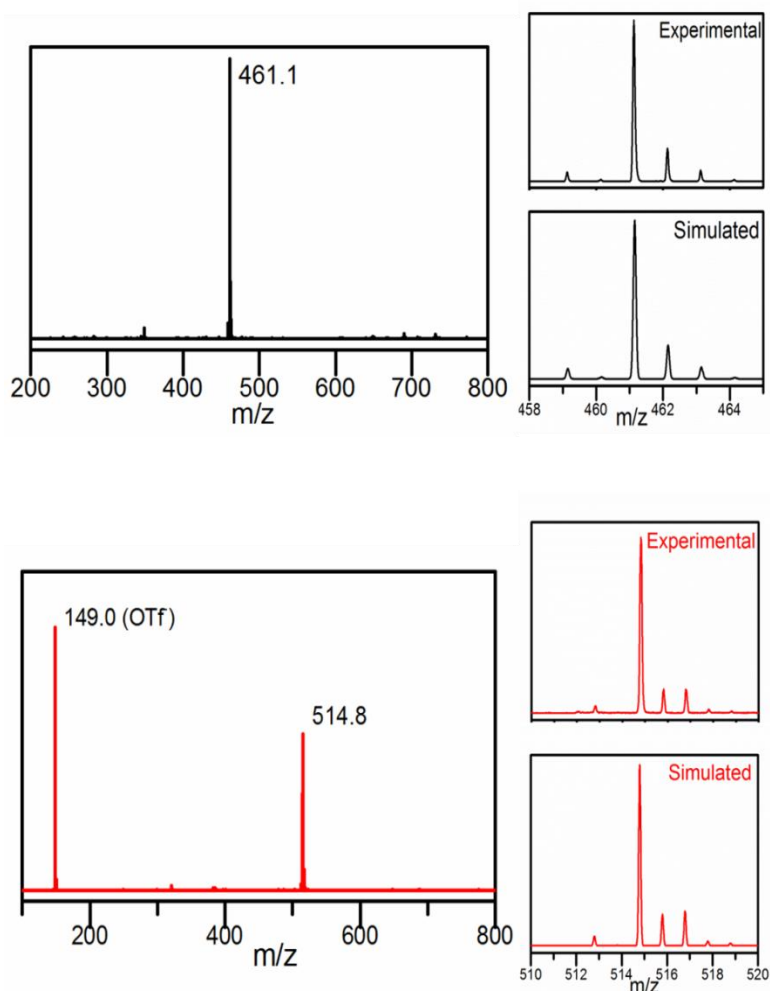


Figure 2.5 ESI-MS spectra of **1**. (Top) positive mode spectrum, together with isotope distribution pattern of the m/z 461.1 peak simulated by $[\text{Fe}(\text{TMC})(\text{OTf})]^+$. (Bottom)

negative mode spectrum, together with isotope distribution pattern of the m/z 514.8 peak simulated by $[\text{Cr}(\text{O})(\text{OTf})_3]^-$.

To test our hypothesis that **2** has an Fe–O–Cr core similar to **1**, an aliquot of a solution of **2** was subjected to analysis by electrospray ionization mass spectrometry (ESI-MS). A peak at m/z +827.0 was observed and assigned as $[(\text{TMC})\text{FeOCr}(\text{OTf})_3]^+$ based on its mass and isotope distribution pattern. This peak was shifted to m/z +829.0 when $2\text{-}^t\text{BuSO}_2\text{-C}_6\text{H}_4\text{I}^{18}\text{O}$ was used to introduce the ^{18}O isotope (Figure 2.6). The ESI-MS spectra and the isotope labeling results support the presence of an Fe–O–Cr core in **2**.

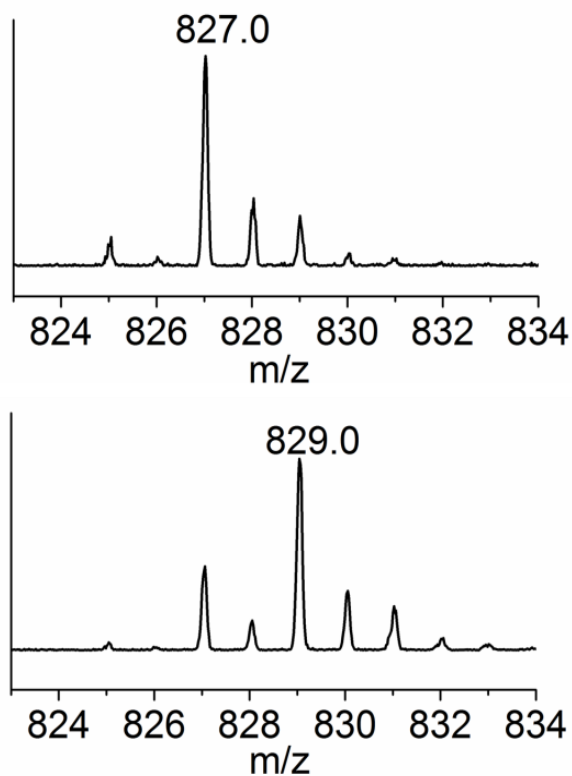


Figure 2.6 ESI-MS spectral features of **2**. (Top) isotope pattern for the $[(\text{TMC})\text{Fe}^{16}\text{OCr}(\text{OTf})_3]^+$ ion (m/z +827); (Bottom) isotope pattern for the

$[(\text{TMC})\text{Fe}^{18}\text{OCr}(\text{OTf})_3]^+$ ion (m/z +829). (Based on the intensity ratio between the m/z +827 and +829 peaks, the latter sample contains approximately 25% of the $[(\text{TMC})\text{Fe}^{16}\text{OCr}(\text{OTf})_3]^+$ isotopomer, which may arise from incomplete ^{18}O labeling of the $2\text{-}^t\text{BuSO}_2\text{-C}_6\text{H}_4\text{I}^{18}\text{O}$ oxidant.

While complex **2** is stable at room temperature, complex **1** exhibits a half-life of only 30 minutes under the same conditions. The latter observation is in agreement with the fact that in the ESI-MS spectrum of **1** only the fragment ion peaks $[\text{Fe}^{\text{II}}(\text{TMC})(\text{OTf})]^+$ and $[\text{Cr}^{\text{IV}}\text{O}(\text{OTf})_3]^-$ were found,¹⁰⁴ while the molecular ion peak $[(\text{TMC})\text{FeOCr}(\text{OTf})_3]^+$ was detected in the ESI-MS spectrum of **2**. These results suggest that the homolysis of the Fe–O bond in **1** is more facile than for **2**. To test this hypothesis, an excess of PhIO was added into the decay product of **1**, and 90% of $[\text{Fe}^{\text{IV}}(\text{O}_{\text{anti}})(\text{TMC})(\text{NCCH}_3)](\text{OTf})_2$ was recovered based on the peak growth at 824 nm (Figure 2.7), confirming that the decay product of **1** is $\text{Fe}^{\text{II}}(\text{TMC})(\text{OTf})_2$ from the homolytic dissociation of its Fe–O bond.

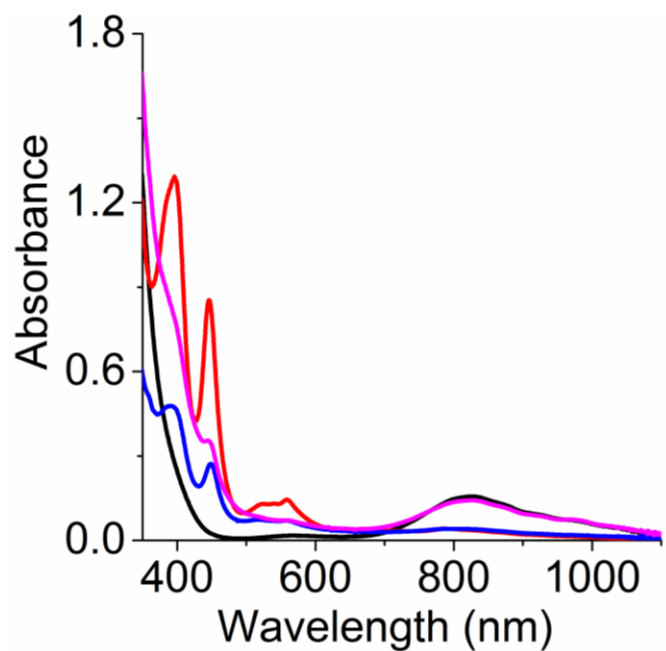


Figure 2.7 Decay product analysis on species **1** at room temperature. Black: 0.4 mM Fe^{IV}(O)(TMC)(OTf)₂; Red: 0.4 mM species **1** formed from adding 1 equiv. Cr(OTf)₂ into 0.4 mM Fe^{IV}(O)(TMC)(OTf)₂; Blue: decay of 0.4 mM species **1**; Magenta: Spectrum after adding 5 equiv. of PhIO in CH₃OH into decay of 0.4 mM species **1**. 90% (0.36 mM) of Fe^{IV}(O)(TMC)(OTf)₂ was recovered based on the absorbance at 824 nm.

2.3.3 Raman Results on **1**, **2** and **3**

The Fe–O–Cr core in both **1** and **2** was further characterized by resonance Raman spectroscopy. A resonance-enhanced vibration at 773 cm⁻¹ was observed upon excitation of **1** with 568.2-nm irradiation (Figure 2.8). This vibration falls within the 700-900 cm⁻¹ range found for the $\nu_{\text{as}}(\text{Fe–O–Fe})$ features of other oxo-bridged Fe(III) complexes.¹¹⁶ This assignment is corroborated by the observed downshift of this vibration to 730 cm⁻¹ upon substitution of ¹⁸O into the oxo bridge. Although Hooke's Law predicts a 35-cm⁻¹

¹ downshift for a diatomic Fe–O mode, the experimentally obtained ¹⁸O shift is 43 cm⁻¹. This larger than predicted shift is not unusual and has been seen for corresponding vibrations of a number of other bimetallic oxo-bridged systems.¹¹⁶ There is also a weaker feature found at 746 cm⁻¹ that exhibits an upshift of 7 cm⁻¹ upon ¹⁸O-substitution; this is an unusual observation that we cannot explain. No enhanced vibrations were obtained upon excitation with laser lines at 457.9, 514.5, or 647.1 nm, suggesting that the 558-nm absorption band can be associated with a transition of the Fe–O–Cr moiety.

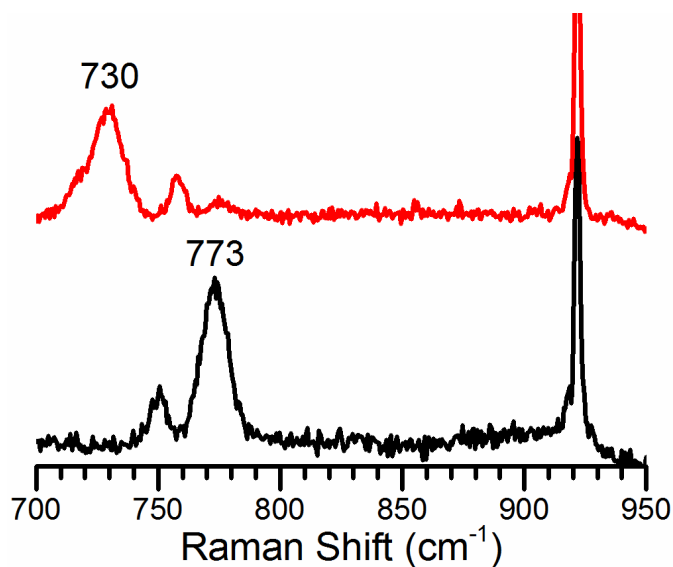


Figure 2.8 Resonance Raman spectra of **1** in CH₃CN ($\lambda_{\text{ex}} = 568.2$ nm, 20 mW, 77 K). Black, ¹⁶O; red, ¹⁸O. Asterisk denotes solvent peak.

Complex **2** was also studied by resonance Raman spectroscopy to gain insight into its Fe–O–Cr core. A resonance-enhanced peak at 877 cm^{-1} was observed upon 514.5-nm excitation (Figure 2.9). This vibration falls within the $700\text{--}900\text{ cm}^{-1}$ range typically found for the $\nu_{\text{as}}(\text{Fe–O–Fe})$ features of other oxo-bridged diiron(III) complexes.¹¹⁶ This assignment is corroborated by the observed downshift of the peak from 877 cm^{-1} to 832 cm^{-1} upon substitution of ^{18}O into the oxo bridge. The 45-cm^{-1} experimental downshift is slightly larger than the 40-cm^{-1} downshift predicted by the Hooke's Law based on a diatomic Fe–O model, but similar cases have been reported for the corresponding vibrations in several other oxo-bridged diiron(III) complexes.¹¹⁶ The $\nu_{\text{as}}(\text{Fe–O–Cr})$ of **2** is over 100 cm^{-1} higher than that of **1** at 770 cm^{-1} ,¹⁰⁴ indicating a stronger bonding interaction in the Fe–O–Cr core of **2**. Complementary to these data is the $\nu_{\text{as}}(\text{Fe–O–Sc})$ mode of **3** at 878 cm^{-1} obtained by Raman spectroscopy with 515-nm laser excitation. This frequency is essentially identical to that of **2**, suggesting that this feature derives from a common $(\text{TMC})\text{Fe}^{\text{III}}\text{--O}_{\text{syn}}\text{--M}$ unit found in complexes **2** and **3** (Figure 2.9).

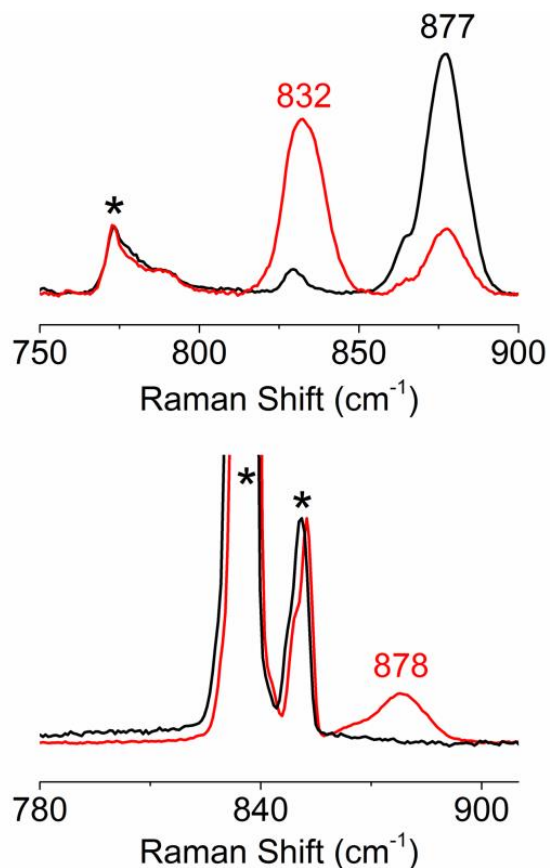


Figure 2.9 (Top) resonance Raman spectra of **2** (5 mM) in CH₃CN ($\lambda_{\text{ex}} = 514.5$ nm, 20 mW, 77 K). Black: ¹⁶O; red: ¹⁸O. The residual 877-cm⁻¹ peak found in ¹⁸O-labeled **2** indicates the presence of ¹⁶O-labeled **2**, which likely comes from residual 2-^tBuSO₂-C₆H₄I¹⁶O in the ¹⁸O-labeled oxidant used for the preparation of **2**. (Bottom) Raman spectra for **3** (12 mM) in CD₃CN obtained with $\lambda_{\text{ex}} = 515$ nm and 50-mW power at 77 K (black, pure CD₃CN; red, ¹⁶O isotopomer). Asterisks denote solvent peaks.

2.3.4 Mössbauer Spectroscopy of **1** and **2**

In order to confirm the oxidation state of iron center and the influence of the ligand conformation, we obtained the Mössbauer spectra of **1** and **2** (Figure 2.10)

showing quadrupole doublets at zero applied field for both complexes. Complex **1** has an isomer shift δ of $+0.53 \text{ mm s}^{-1}$ and a quadrupole splitting $|\Delta E_Q|$ of 0.87 mm s^{-1} , while **2** has a δ of $+0.44 \text{ mm s}^{-1}$ and a $|\Delta E_Q|$ of 0.89 mm s^{-1} . We found that the Mössbauer spectrum of **2** also contained ca. 20% of **1**, which derives from $\sim 17\%$ $[\text{Fe}^{\text{IV}}(\text{O}_{\text{anti}})(\text{TMC})(\text{NCCH}_3)](\text{OTf})_2$ contaminant present in the generation of $[\text{Fe}^{\text{IV}}(\text{O}_{\text{syn}})(\text{TMC})(\text{NCCH}_3)](\text{OTf})_2$.¹⁰³ Although the isomer shift values of **1** and **2** both fall within the range typical of high spin Fe^{III} species, the observation of quadrupole doublets for **1** and **2** at 4.2 K indicates that they both have an integer spin ground state ($S = 0, 1, 2, \dots$), presumably from coupling to the associated Cr^{III} center. Furthermore, the difference in their isomer shifts of 0.09 mm s^{-1} suggests that the iron centers in the two complexes differ somewhat in their electronic structures. More interestingly, the isomer shift found for **2** is halfway between the values for **1** and **3**.¹⁰² However, the magnitude of the coupling constant J cannot be reliably determined, because Mössbauer measurements at higher temperature (up to 180 K) show that the electronic systems of these compounds still exhibit intermediate magnetic relaxation.

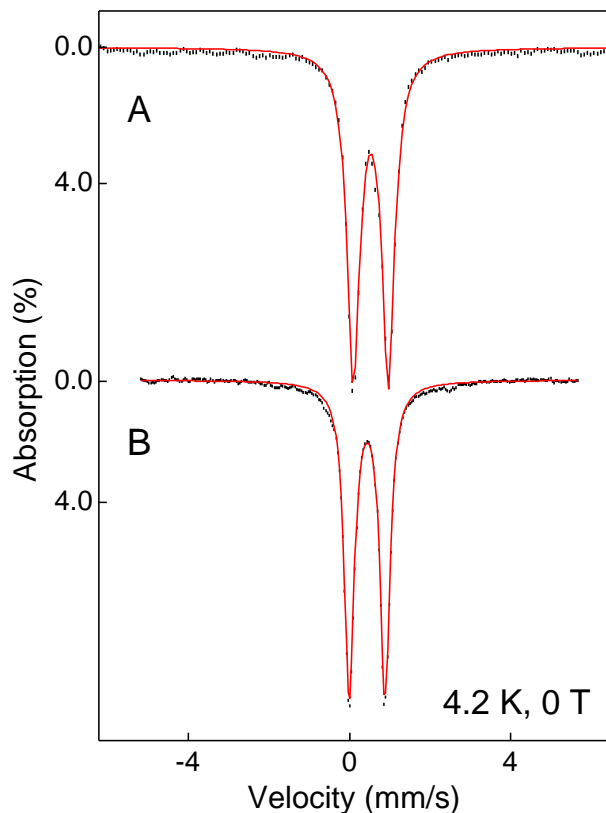


Figure 2.10 (A) Mössbauer spectrum (black) of **1** and the corresponding fitting curve (red) with $\delta = +0.53$ mm/s, $|\Delta E_Q| = 0.87$ mm/s. (B) Mössbauer spectrum (black) of **2** and the corresponding fitting curve (red) with $\delta = +0.44$ mm/s, $|\Delta E_Q| = 0.89$ mm/s. The fit is improved with the inclusion of a 20% contribution from **1**.

2.3.5 XAS Analysis of **1**

In order to obtain structural insight, Fe K-edge X-ray absorption spectroscopy studies were carried out on **1**. As shown in Figure 2.11, the Fe K-edge of **1** was found at 7124.0 eV, which is comparable to those of known Fe^{III}(TMC) and related complexes.¹¹⁷

Species **1** also exhibits a pre-edge feature that is associated with 1s-to-3d transitions with an area of 11 units.

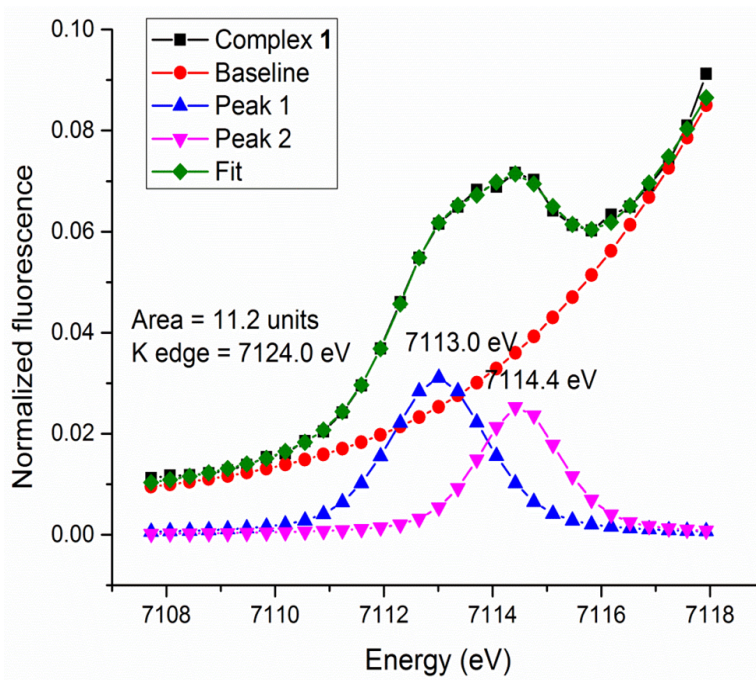


Figure 2.11 Pre-edge region of Fe K-edge XAS spectrum of **1** (black). Baseline fit (red), pre-edge peak 1 (blue), pre-edge peak 2 (magenta), pre-edge fit (green).

The Fourier-transformed EXAFS region revealed two prominent features at $R + \Delta$ ~ 1.8 Å and 3.2 Å (Figure 2.12, left). The best fit of the data (fit #8 in Table 2.1) consisted of 1 O/N scatterer at 1.81 Å, 5 O/N scatterers at 2.17 Å, 4 C scatterers at 2.91 Å and a Cr scatterer at a distance of 3.65 Å. The 2.17-Å and 2.91-Å scatterers arise from the supporting TMC ligand, while the 1.81-Å scatterer has an Fe–O distance typically found for oxo bridges in Fe^{III}–O–M^{III} complexes.¹¹⁸ The 3.2 Å feature corresponds to a Cr

scatterer at 3.65 Å; its intensity derives from multiple scattering pathways due to a linear Fe–O–Cr core. Indeed, the Fe...Cr distance is typical of the metal-metal distances found for linear Fe^{III}–O–M complexes^{100, 102, 119, 120} and exemplified by [(py)(TPP)Cr^{III}–O–Fe^{III}(TMP)] ($r(\text{Fe}\dots\text{Cr}) = 3.60 \text{ \AA}$; py = pyridine; TPP = tetraphenylporphin dianion; TMP = tetramesitylporphin dianion).¹²¹ We thus propose that **1** has the structure shown in Figure 2.12, right.

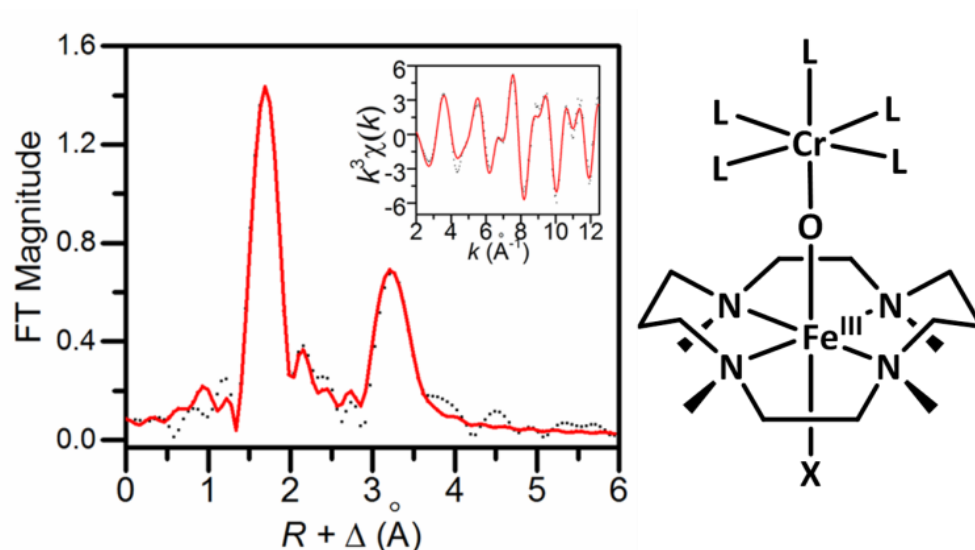


Figure 2.12 (Left) Fourier-transformed Fe K-edge EXAFS data for **1** (dotted black line) and corresponding best fit (solid red line, fit #8 in Table 2.1). Inset shows unfiltered k-space data and its fit. (Right) Proposed structure for **1** (L/X = CH₃CN or OTf).

Table 2.1 Fit parameters for complex 1. Unfiltered data from $k = 2-12.5 \text{ \AA}^{-1}$.

	Fe–N/O			Fe–N/O			Fe•••C			Fe•••Cr			E_0	F	F'
Fit	N	R (Å)	$\sigma^2 \times 10^{-3}$	N	R (Å)	$\sigma^2 \times 10^{-3}$	N	R (Å)	$\sigma^2 \times 10^{-3}$	N	R (Å)	$\sigma^2 \times 10^{-3}$			
1	4	2.17	2.10										-9.06	422	591
2	5	2.17	3.47										-8.93	440	604
3	4	2.16	2.47	1	1.82	3.60							-7.85	357	544
4	5	2.16	3.91	1	1.82	2.94							-7.97	337	529
5	5	2.17	3.56	1	1.82	3.50	4	2.90	2.76				-8.72	254	459
6	5	2.16	3.62	1	1.82	3.35	5	2.90	4.62				-8.85	262	466
7	5	2.16	4.04	1	1.81	2.74	4	2.90	6.36	1	3.72	-0.8	-9.48	54	211
8	5	2.17	4.12	1	1.81	2.55	4	2.92	6.77	1	 3.65	 1.00	-7.26	52	207

\ indicates the Fe•••Cr distance obtained from a double scattering pathway.

The proposed structure for **1** resembles that found in the crystal structures of **3**.^{100,}
¹⁰² However, they differ in several respects. Although the Fe...M distances are essentially identical for **1** and **3**, the respective Fe–O and M–O distances differ. The Fe–O distance of 1.81 Å for **1** is 0.07 Å longer than that found for **3**, while the Cr–O distance of 1.84 Å (deduced from the difference between the Fe...Cr and the Fe–O distances from the EXAFS analysis assuming $\angle\text{Fe–O–Cr} \sim 180^\circ$) is 0.07 Å shorter than the Sc–O distance of 1.91 Å observed for **3** in its crystal structures. The distinct M–O distances in **1** and **3** presumably reflect the difference between the more covalent Cr–O bond and the more ionic Sc–O bond, which also affect the corresponding Fe–O bond. Another feature distinguishing **1** from **3** is the intensity of the XAS pre-edge feature. Complex **1** exhibits a pre-edge area of 11 units, typical of a six-coordinate iron(III) center,^{122, 123} while **3** (L = NCCH₃) has a much larger pre-edge area of 32 units, reflecting the square pyramidal geometry of its iron(III) center. Lastly, the four methyl groups of the TMC ligand are shown in Figure 2.1 as being oriented *anti* with respect to the oxo bridge, opposite to the orientation found crystallographically for the methyl groups in **3**.^{100, 102} Although we do not have direct proof, our main argument to favor the *anti*-orientation over the *syn* one is the observed immediate formation of **1** upon Cr(OTf)₂ addition to a solution of [Fe^{IV}(O)(TMC)(NCCH₃)]²⁺. As the TMC methyl groups are oriented *anti* to the oxo moiety in the precursor, it seems unlikely that a change in their relative orientations could occur at -40 °C within this very short time scale.

2.3.6 XAS Analysis of **2**

Fe K-edge X-ray absorption spectroscopy (XAS) measurements were conducted in order to obtain more structural information on **2**. The Fe K-edge of **2** is observed at 7123.6 eV (Figure 2.13), which is comparable to the value found for **1** (7124.0 eV)¹⁰⁴ and within the range typical for Fe(III) species.¹²⁴ The XAS sample of **2** also exhibits a pre-edge feature at 7113.0 eV which is fitted with two peaks providing a total area of 26 units, a value that increases to 30 units when the contribution of 20% **1** in the sample is taken into account (Figure 2.10). These peaks are associated with the 1s-to-3d transitions of the Fe center, and the total area reflects the extent to which the iron center is distorted from centrosymmetry.¹²² For comparison, the pre-edge areas reported for **1** and **3** are 11 and 32, respectively.^{102, 104} The much smaller pre-edge area found for **1** is rationalized by the presence of an axial CH₃CN ligand that makes its iron(III) center 6-coordinate, while that of **3** has a much higher value because of its square pyramidal iron(III) center. Thus the comparable pre-edge areas of **2** and **3** strongly suggest that they share a common square pyramidal iron(III) center.(Figure 2.1)

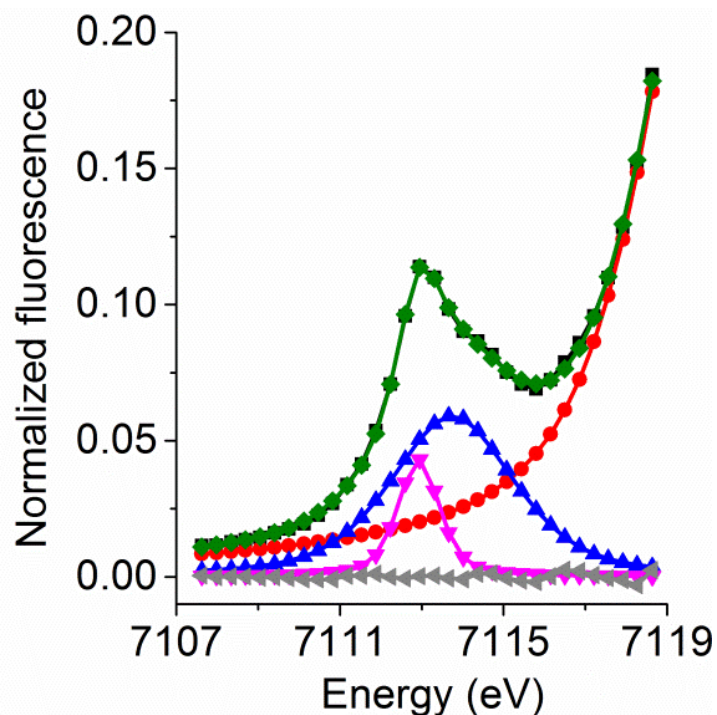


Figure 2.13 Pre-edge region of the Fe K-edge XAS spectrum of **2** (black squares): rising-edge fit (red circles), pre-edge peak 1 (blue triangles pointing up, maximum at 7113.7 eV), pre-edge peak 2 (magenta triangles pointing down, maximum at 7113.0 eV), pre-edge fit (green diamonds), residuals (gray triangles pointing left).

The Fourier-transformed extended X-ray absorption fine structure (EXAFS) region of **2** revealed two prominent features at $r' \sim 1.8 \text{ \AA}$ and 3.2 \AA (Figure 2.14). The best fit of the data consists of 1 O/N scatterer at 1.77 \AA , 4 O/N scatterers at 2.16 \AA , 4 C scatterers at 2.99 \AA and 1 Cr scatterer at 3.58 \AA (Table 2.2). In contrast, the best fit for the EXAFS data of **1** shows 1 O/N scatterer at 1.81 \AA , 5 O/N scatterers at 2.17 \AA , 4 C scatterers at 2.92 \AA and 1 Cr scatterer at 3.65 \AA .¹⁰⁴ The shorter Fe–O distance in **2** (1.77 \AA) relative to that in **1** (1.81 \AA) is consistent with the absence of an axial ligand *trans* to the oxoiron center in the former. Also, the shorter Fe–O and Fe•••Cr distances in **2** than

those in **1** indicate a stronger bonding interaction in the Fe–O–Cr core, consistent with the Raman results. In fact, the dimensions of the Fe–O–Cr core in **2** closely resemble those of the crystallographically characterized Fe–O–Sc core in **3**^{100, 102}. As **2** is generated immediately upon reaction of $[\text{Fe}^{\text{IV}}(\text{O}_{\text{syn}})(\text{TMC})(\text{NCCH}_3)](\text{OTf})_2$ with $\text{Cr}(\text{OTf})_2$, it is likely that the TMC methyl groups in **2** remain *syn* to the oxo bridge, like those found in **3** but different from those in **1**, where the TMC methyl groups are *anti* to the oxo bridge (Figure 2.1). Thus **2** and **3** would appear to be structurally quite closely related.

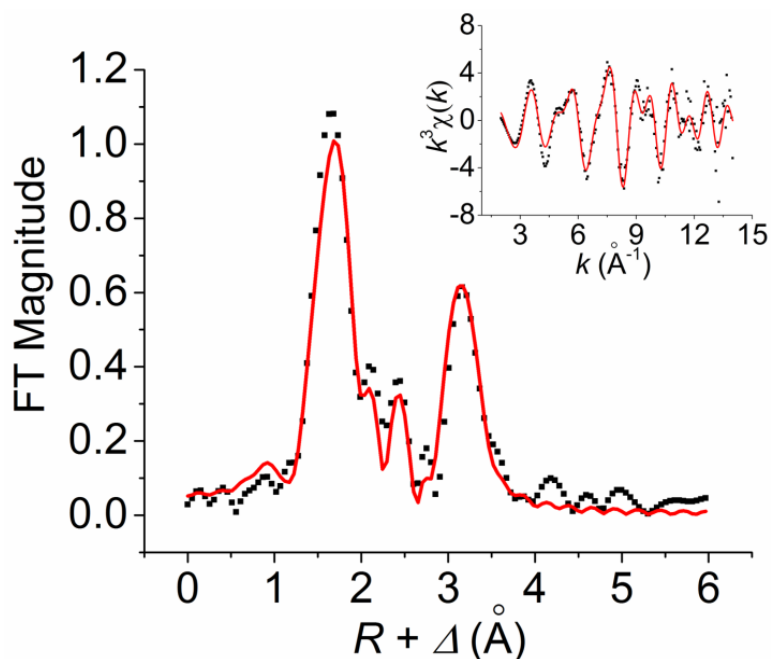


Figure 2.14 Main: Fourier-transformed Fe K-edge EXAFS data for **2** (dotted black) and the corresponding best fit (fit #6 in Table 2.2). (Inset) Unfiltered k-space data (dotted black) and its fit (solid red).

Table 2.2 Fit parameters for **2** based on unfiltered data from $k = 2 - 15 \text{ \AA}^{-1}$.

Fit	Fe-N/O			Fe-N/O			Fe•••C			Fe•••Cr			E_0	F	F'
	N	R (Å)	$\sigma^2 \times 10^{-3}$	N	R (Å)	$\sigma^2 \times 10^{-3}$	N	R (Å)	$\sigma^2 \times 10^{-3}$	N	R (Å)	$\sigma^2 \times 10^{-3}$			
1	4	2.16	3.14										-10.7	528	644
2	5	2.15	4.27										-10.6	522	640
3	4	2.16	3.16	1	1.77	3.84							-6.85	470	608
4	4	2.16	3.19	1	1.77	4.07	4	2.94	8.54				-8.25	423	576
5	4	2.15	3.14	1	1.76	4.83	4	2.94	7.99	1	3.64	-0.2	-9.69	198	394
6	4	2.16	3.28	1	1.77	4.12	4	2.99	9.36	1	 3.58	 1.33	-6.47	198	394

\ indicates the Fe•••Cr distance obtained from a double scattering pathway.

2.3.7 Characterization of 4_{Cl} , 4_{OTf} and 5

Despite our detailed characterization efforts on **1** and **2**, we were not able to obtain crystals suitable for X-ray crystallography. As an alternative, we have obtained the crystal structures of $(\text{Cl})(\text{TMC})\text{Fe}-\text{O}_{\text{anti}}-\text{FeCl}_3$ (4_{Cl}) and $[(\text{TMC})\text{Fe}-\text{O}_{\text{syn}}-\text{FeCl}_3](\text{OTf})$ (**5**), both of which are stable at room temperature. These complexes were obtained from the reactions of $[\text{Fe}^{\text{IV}}(\text{O}_{\text{anti/syn}})(\text{TMC})(\text{NCCH}_3)]^{2+}$ isomers with FeCl_4^- . Key structural parameters compared in Table 2.3, showing that the structural deductions made for the **1** / **2** pair are consistent with the crystallographic data for the 4_{Cl} / **5** pair.

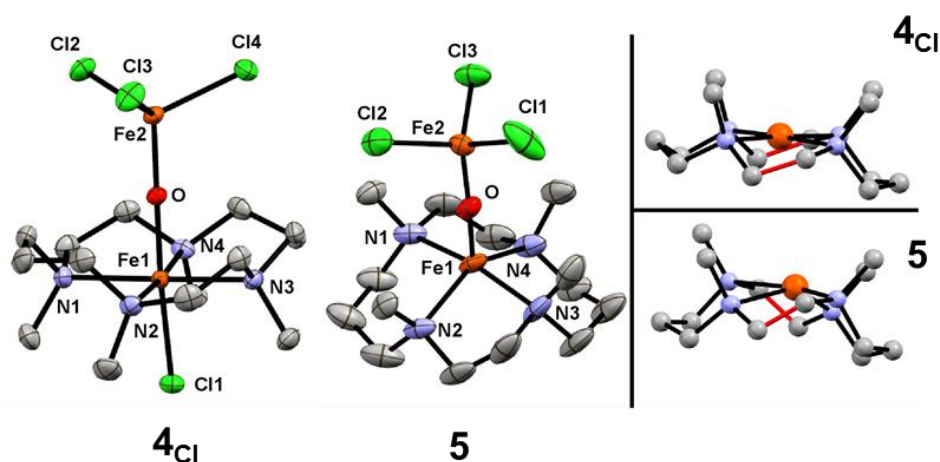


Figure 2.15 (Left) ORTEP plots for $(\text{Cl})(\text{TMC})\text{Fe}-\text{O}_{\text{anti}}-\text{FeCl}_3$ (4_{Cl}) and $[(\text{TMC})\text{Fe}-\text{O}_{\text{syn}}-\text{FeCl}_3](\text{OTf})$ (**5**) at 50% probability. H-atoms, solvent molecules and a counter ion (in **5**) have been omitted for clarity. The R_1 values for structures 4_{Cl} and **5** are 0.023 and 0.048, respectively (CCDC numbers 1503819 and 1503820). The structure of **5** was modeled over two positions with a 90° rotation along the Fe–O–Fe axis. (Right) conformations of the cyclam rings in 4_{Cl} and **5**. Red color highlights the different orientations of the two NCH₂–CH₂N bonds relative to each other in each cyclam ring (parallel in 4_{Cl} and crossed in **5**).

Table 2.3 Crystallographic and structure refinement data for **4_{Cl}**(14182a in checkcif file) and **5** (14202a1 in checkcif file)

	4_{Cl}	5
Empirical formula	C ₁₆ H ₃₅ Cl ₄ Fe ₂ N ₅ O	C ₂₀ H ₃₈ Cl ₃ F ₃ Fe ₂ N ₆ O ₄ S
Temperature (K)	173(2)	173(2)
Wavelength (Å)	0.71073	0.71073
Crystal system	Orthorhombic	Monoclinic
Space group	P2(1)2(1)2(1)	P2(1)/c
<i>a</i> (Å)	12.8738(11)	10.1776(8)
<i>b</i> (Å)	12.8805(11)	9.2395(7)
<i>c</i> (Å)	14.9102(12)	33.194(3)
α (°)	90	90
β (°)	90	91.9480(10)
γ (°)	90	90
Volume (Å ³)	2472.4(4)	3119.6(4)
<i>Z</i>	4	4
<i>F</i> (000)	1176	1488
θ max (°)	27.48	26.41
Complete	99.9%	100.0%
<i>R</i> (<i>int</i>)	0.0342	0.0376
Data	5674	6404
Restraints	0	313
Parameters	258	501

R1 ^b [I > 2σ(I)]	0.0227	0.0479
wR2 ^c	0.0517	0.1167
Goof ^d	1.020	1.043

Table 2.4 Select bond lengths (Å) and angles (°) of **4_{Cl}** and **5**.

	4_{Cl}	5^a
Fe(1)–O	1.8510(12)	1.742(3)
O–Fe(2)	1.7713(12)	1.771(3)
Fe(1)–N _{ave}	2.2064(17)	2.168(3)
Fe(2)–Cl _{ave}	2.2321(6)	2.207(2)
Fe(1)–Cl	2.3586(5)	–
Fe(1)...Fe(2)	3.6213(5)	3.4994(14)
∠Fe(1)–O–Fe(2)	177.30(9)	169.9(3)
^a distances and angles are reported for the major position of the disorder modeling (85% occupancy) of 5 . The structure of 5 was modeled over two positions with a 90 ° rotation along the Fe–O–Fe axis.		

Several points can be made based on structural comparisons among complexes **1** – **5**. (i) In the crystal structure of **4_{Cl}**, the TMC methyl groups are oriented in an *anti* fashion with respect to the oxo bridge and the Fe center is 6-coordinate, while in the crystal structure of **5** the TMC methyl groups are *syn* to the oxo bridge and the Fe center is 5-coordinate. These results confirm the correlation between the orientation of the Fe=O unit relative to the TMC methyl groups and the coordination number of the iron center found for (TMC)Fe–O–M complexes **1**, **2**, and **3**. (ii) The Fe_{TMC}–O distance in **4_{Cl}** is significantly longer (~0.1 Å) than that in **5**, which can be attributed to the presence of an axial chloride ligand in **4_{Cl}**. (iii) The Fe(III) ion bound to the TMC ligand in **5** is much farther away from the mean N4 plane of the TMC framework (0.50 Å) than that in **4_{Cl}** (0.044 Å), but comparable to that in **3** (0.53 Å). The longer Fe–N4 plane distance reflects a higher degree of distortion from centrosymmetry resulting from the square pyramidal Fe centers in **3** and **5**.

This structural pattern can also be discerned in the only two other Fe^{III}(TMC) complexes that are crystallographically characterized. The 6-coordinate (Me₃cyclam-acetate)Fe–O–FeCl₃ (**6**) reported by Wiegardt and coworkers in 2006¹²⁰ (Figure 2.16) exhibits features between those of **4_{Cl}** and **5** but closer to the former (Figure 2.16). Complex **6** has an Fe_{TMC}–O distance of 1.801 Å and an Fe–N4 plane distance of 0.196 Å. These intermediate values may be rationalized by the fact that **6** has two *syn* methyl groups and two *anti* alkyl groups (Figure 2.16), resulting in effects in between those from a fully *anti* set versus a fully *syn* set of alkyl groups. On the other hand, the Fe–N4 plane

distance for $[\text{Fe}^{\text{III}}(\eta\text{-O}_2)(\text{TMC})]^+$ is 0.644 Å,¹²⁵ so the side-on-bound peroxo ligand pulls the Fe even further away from the mean N4 plane of the TMC macrocycle.

An additional structural feature that divides the above complexes into two subsets is the relative orientation of the two $-\text{CH}_2-\text{CH}_2-$ units connecting the amine donors in the cyclam rings. The ethylene linkers in **4_{Cl}** are related to each other by a pseudo-mirror plane, while those in **3** and **5** are related by a pseudo-twofold axis (Figure 2.15, right). Interestingly, the ethylene groups of the cyclam ring in **6** are oriented parallel to each other, like those of **4_{Cl}**, while those of $[\text{Fe}^{\text{III}}(\eta\text{-O}_2)(\text{TMC})]^+$ are crossed like those found in **3** and **5**. Furthermore, the ethylene group orientations in $\text{Fe}^{\text{II}}(\text{TMC})(\text{X})$ complexes, which are all 5-coordinate, are similar to those of **3** and **5**,¹²⁶⁻¹²⁸ while the ethylene group orientations for both *syn* and *anti* isomers of $[\text{Fe}^{\text{IV}}(\text{O})(\text{TMC})(\text{L})]^{2+}$, which are both 6-coordinate, are similar to those found in **4_{Cl}**.^{103, 105} So this structural feature likely reflects the Fe–N4 plane distance and the TMC macrocycle conformation required to support this distance. Therefore the XRD results of **3**, **4_{Cl}** and **5** support the proposed structures for **1** and **2** and further illustrate how the orientation of the Fe=O unit relative to the TMC methyl groups affects the parameters of the Fe–O–M core.

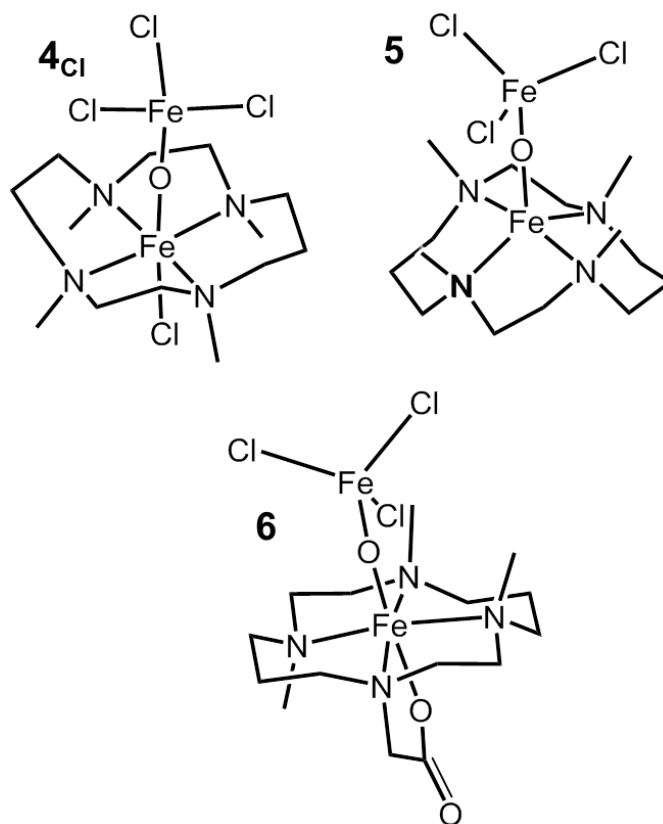


Figure 2.16 Structural comparison of complexes **4_{Cl}**, **5**, and **6**.

As noted in the experimental section, a single crystal of **4_{Cl}** was analyzed by X-ray diffraction. However, based on the elemental analysis, the bulk crystalline solid best characterized as **4_{OTf}**. To assess whether the triflate ion in **4_{OTf}** is bound as a ligand or simply a counterion, ¹⁹F-NMR studies were performed on a CD₃CN solution of the bulk crystalline solid. The ¹⁹F-NMR spectrum of **4_{OTf}** displays a signal corresponding to the presence of OTf⁻ ion in the solution with a chemical shift close to that observed for free OTf⁻ ion in the solution, but its line width was found to be 32 Hz (vs. 5 Hz for free OTf⁻ ion), suggesting that either this OTf⁻ ion is bound to the Fe center in **4_{OTf}** or is in a rapid

exchange equilibrium with CD_3CN solvent. Addition of 10 equiv. triflate ion to this solution led to the sharpening of peak from 32 Hz to 18 Hz in support of the latter scenario (Figure 2.17). We have made several attempts to obtain diffraction quality crystals of $\mathbf{4}_{\text{OTf}}$, but these efforts have thus far been unsuccessful. Clearly, the crystal of $\mathbf{4}_{\text{Cl}}$ picked out for X-ray diffraction analysis was unrepresentative of the bulk solid. Nevertheless, the obtained crystal structure of $\mathbf{4}_{\text{Cl}}$ provides the information needed for a structural comparison with $\mathbf{5}$.

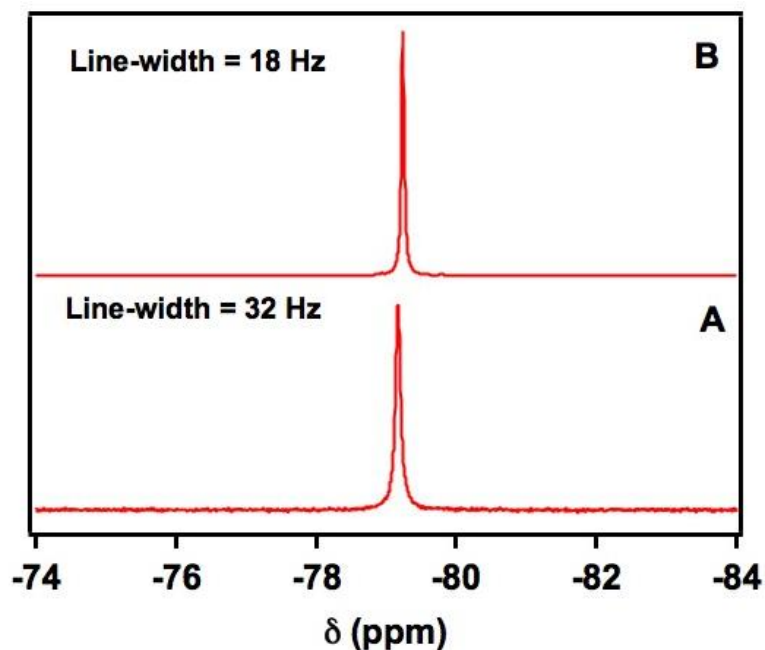


Figure 2.17 ^{19}F -NMR spectrum of A) $\mathbf{4}_{\text{OTf}}$ and B) $\mathbf{4}_{\text{OTf}}$ + 10 equiv. of Bu_4NOTf , collected in CD_3CN at 298 K. For comparison, the observed linewidth for free triflate ion under the same conditions is 5 Hz.

As additional characterization, infrared spectroscopic data was collected on solid samples of **4_{OTf}** and **5**, together with corresponding ¹⁸O isotopomers (**Figure 2.18**). Complex **4_{OTf}** exhibits a peak at 800 cm⁻¹, which shifts to 768 cm⁻¹ upon ¹⁸O-labeling of the oxo bridge, while **5** shows a peak at 888 cm⁻¹, which shifts to 839 cm⁻¹ in its ¹⁸O isotopomer. These features are analogous to those obtained from resonance Raman experiments on **1** and **2**, which reveal respective resonance enhanced vibrations at 770 and 877 cm⁻¹ assigned as $\nu_{\text{as}}(\text{Fe-O-Cr})$ modes. Due to the structural similarities between **1** and **4_{OTf}** and between **2** and **5**, the 800-cm⁻¹ peak in **4_{OTf}** and the 888-cm⁻¹ peak in **5** are both assigned as $\nu_{\text{as}}(\text{Fe-O-Fe})$ modes. The higher frequency of $\nu_{\text{as}}(\text{Fe-O-Fe})$ feature in **5** can be rationalized by the shorter (TMC)Fe-O and Fe•••Fe distances determined by XRD.

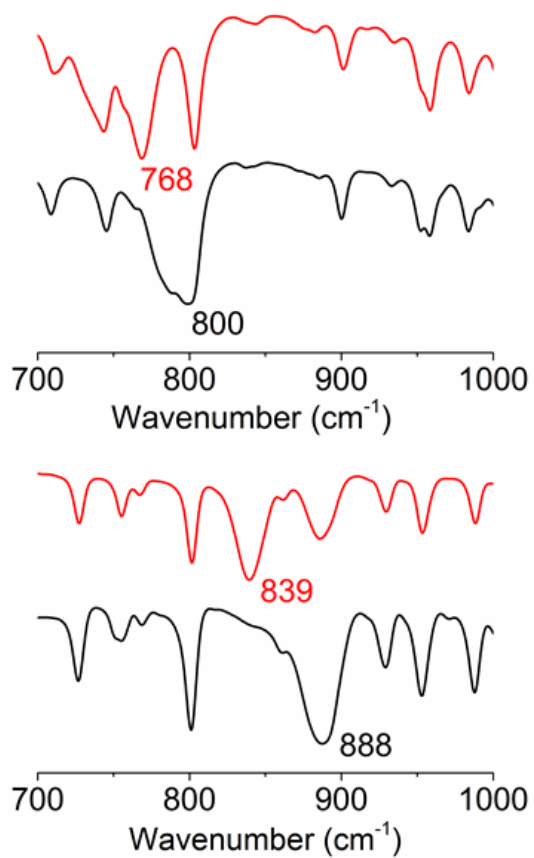


Figure 2.18 (Top) Infrared spectroscopic data for **4_{OTf}** (black, ¹⁶O isotopomer; red, ¹⁸O isotopomer). (Bottom) Infrared spectroscopic data for **5** (black, ¹⁶O isotopomer; red, ¹⁸O isotopomer).

Table 2.5 Spectroscopic and structural comparisons of complexes **1** – **6**.

	1	2	3	4_{Cl}	5	6
Orientation of the TMC methyl groups to the oxo bridge	<i>anti</i>	<i>syn</i>	<i>syn</i>	<i>anti</i>	<i>syn</i>	
Coordination number of the Fe ^{III} (TMC) site	6	5	5	6	5	6
rR or IR peak (¹⁸ O shift) (cm ⁻¹)	773 (-43)	877 (-45)	878	800 (-32) ^a	888 (-49)	N.D.
Mössbauer parameters (δ [ΔE_Q]) of the Fe(TMC) fragment (mm/s)	+0.53 [0.87] ^b	+0.44 [0.89] ^b	+0.36 [-1.02]	N.D.	N.D.	+0.44 ^d [+1.46] _d
XANES K-edge energy (eV)	7124.0	7123.6	7122.6	N.D.	N.D.	N.D.
XANES pre-edge area (units)	11	30	32	N.D.	N.D.	N.D.
Fe _{TMC} -N4 plane distance (Å)	N.D.	N.D.	0.53	0.044	0.50 ^c	0.196
Fe–O distance (Å)	1.81	1.77	1.748(5)	1.8510 (12)	1.742 (3) ^c	1.802
Fe•••M distances (Å)	3.65	3.58	3.64	3.6213 (5)	3.4994 (14) ^c	3.559

^a IR values are determined based on **4**_{OTf}. ^b The sign of ΔE_Q is not determined. ^c Distances and angles are reported for the major position of the disorder modeling (85% occupancy) of **5**. The structure of **5** was modeled over two positions with a 90 ° rotation along the Fe–O–Fe axis. ^d Mössbauer data for **6** was collected at 80 K, while Mössbauer data for **1** - **3** were collected at 4.2 K.

2.3.8. O₂ Activation Process to Generate **1**

Here is an interesting observation to end this chapter. Accidentally, I found that bubbling O₂ into a mixture of 1 mM Fe(TMC)(OTf)₂ and 1 mM Cr(OTf)₂ in CH₃CN solution at -40 °C could rapidly elicit a UV-vis spectrum with bands at 358, 398, 447 and 558 nm (Figure 2.19), suggesting the formation of a new species designated as **1**. This spectral pattern was not observed in the absence of either Fe(TMC)(OTf)₂ or Cr(OTf)₂ from the reaction mixture; Fe(TMC)(OTf)₂ simply did not react with O₂, but the reaction of Cr(OTf)₂ with O₂ gave rise to features at 358 and 445 nm (Figure 2.19), distinct from that of **1**. Species **1** had a half-life of 10 h at -40 °C and decayed upon warming to room temperature. Taken together, these observations implicate both Fe and Cr in the formation of **1**.

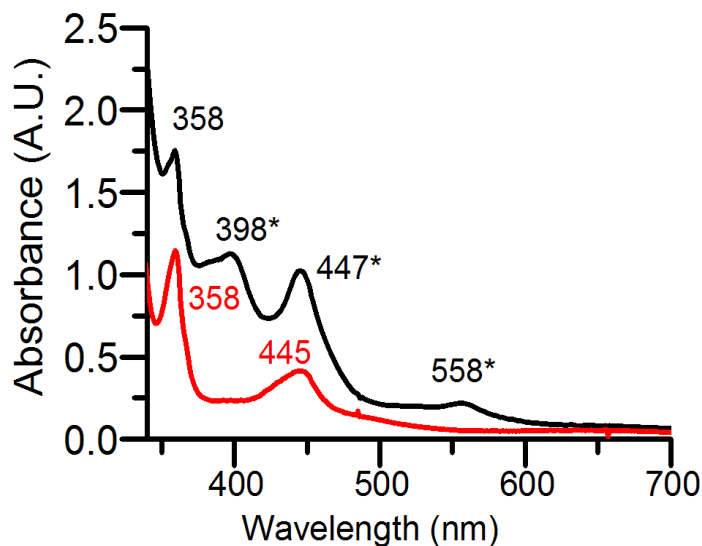


Figure 2.19 UV-vis spectra observed in CH₃CN at -40 °C upon O₂ exposure of 1 mM Cr(OTf)₂ (red) and a mixture of 1 mM Fe(TMC)(OTf)₂ and 1 mM Cr(OTf)₂ (black). Bands with asterisks are associated with **1**.

With the nature of **1** reasonably well characterized, we return to an analysis of the O₂ activation reaction results. Based on the molar extinction coefficients of **1** determined from the stoichiometric conversion of [Fe^{IV}(O_{anti})(TMC)(NCCH₃)₂]²⁺ to **1** by Cr(OTf)₂, we conclude that **1** is produced in about 30% yield from the reaction of equimolar amounts of Fe(TMC)(OTf)₂ and Cr(OTf)₂ to O₂. The yield of **1** was unchanged by increasing the Fe(TMC)(OTf)₂/Cr(OTf)₂ ratio from 1 to 10 ([Cr(OTf)₂] = 1 mM) (Figure 2.20), suggesting that Cr(OTf)₂ is the limiting reagent. In contrast, the yield of **1** increased to 95% when the concentration of Fe(TMC)(OTf)₂ was fixed at 1 mM and the Cr(OTf)₂ concentration was raised from 1 mM to 10 mM (Figure 2.21).

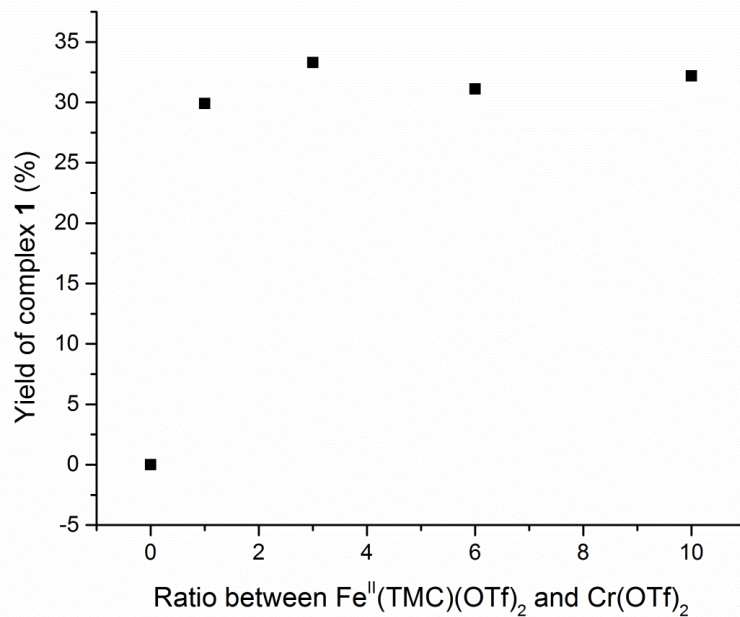


Figure 2.20 Yields of **1** based on the 558-nm peak intensity upon O₂ bubbling into Fe^{II}(TMC)(OTf)₂ + Cr^{II}(OTf)₂ solutions in CH₃CN at -40 °C with varying ratios of Fe^{II}(TMC)(OTf)₂ to Cr^{II}(OTf)₂. Cr^{II}(OTf)₂ = 1 mM.

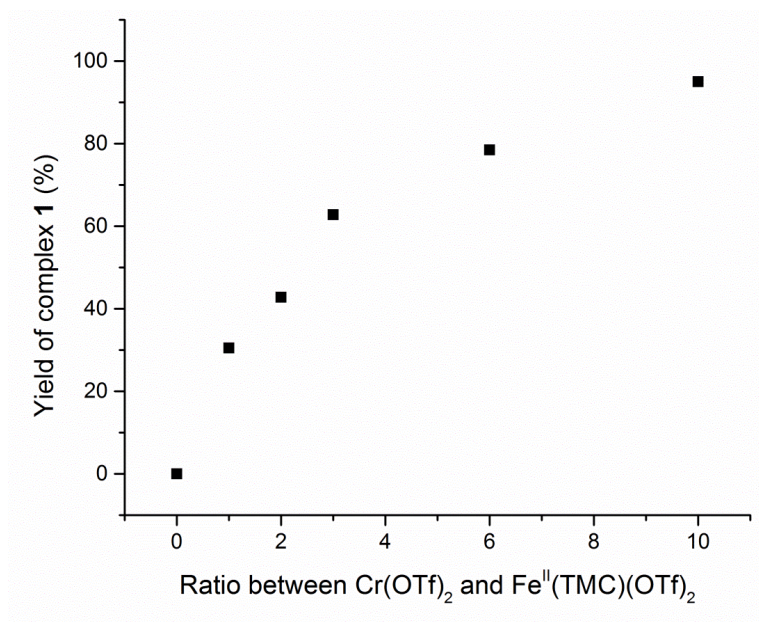


Figure 2.21 Yields of **1** based on the 558-nm peak intensity upon O₂ bubbling into Fe^{II}(TMC)(OTf)₂ + Cr^{II}(OTf)₂ solutions in CH₃CN at -40 °C with varying ratios of Cr^{II}(OTf)₂ to Fe^{II}(TMC)(OTf)₂. Fe^{II}(TMC)(OTf)₂ = 1 mM.

Therefore, the % yield of **1** is dependent on the amount of Cr(OTf)₂, but not on the amount of Fe(TMC)(OTf)₂. These results can be rationalized by the O₂ activation pathway proposed in Figure 2.22, in which the four electrons needed to reduce O₂ to the oxidation level of water are provided by 1 equiv. Fe(TMC)(OTf)₂ and 3 equiv. Cr(OTf)₂, not unlike the four redox-active centers required for O₂ activation by cytochrome oxidase.³⁶ In the present case, we postulate that O₂ initially binds to the O₂-sensitive Cr(OTf)₂ to form a transient adduct (analogous to that characterized by Nam in the reaction of [Cr^{II}(TMC)Cl]⁺ with O₂¹²⁹) that is then trapped by Fe(TMC)(OTf)₂ to generate a yet unobserved Fe^{III}-O-O-Cr^{III} peroxo-bridged intermediate. This intermediate is then reduced by another 2 equiv. Cr(OTf)₂ to form **1**. Thus the ca. 30% yield of **1** observed under limiting Cr conditions reflects the 1:3 stoichiometry of Fe(TMC)(OTf)₂/Cr(OTf)₂ needed to make **1**. On the other hand, under limiting Fe conditions, enough Cr-O₂ adduct is formed to react with all the available Fe(TMC)(OTf)₂ to convert the latter almost quantitatively to **1**, which is by far the only synthetic nonheme Fe-O-M complex (where M is a non-iron metal) has thus far been generated by O₂ activation.

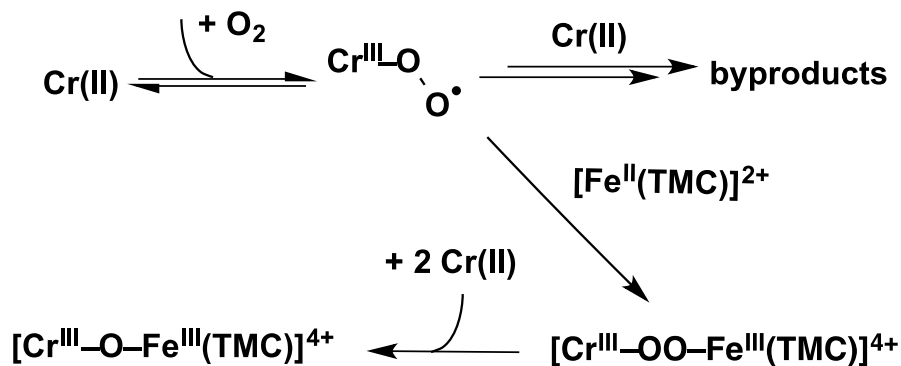


Figure 2.22 Proposed mechanism for formation of **1** by O₂ activation.

2.4 Conclusion

In conclusion, a heterobimetallic nonheme species **1** with an Fe–O–Cr core has been generated from both O₂ activation and inner-sphere electron transfer. The structure of **1** was deduced by a combination of UV-vis, resonance Raman, and X-ray absorption spectroscopic methods and ESI-MS. The O₂ activation mechanism for the formation of **1** is proposed to be analogous to that of cytochrome oxidase, where the initial O₂ adduct formed is reduced by the other three redox-active metal centers in the enzyme, demonstrating a general strategy for O₂ activation. Furthermore, **1** represents only the second example of a heterobimetallic M–O–Fe(TMC) complex, which can shed light on the effects of Lewis acidic metal centers on the redox properties of high-valent M=O species.¹³⁰ Such interactions are considered important for facilitating the oxidation of water by the CaMn₄O₅ cluster of the oxygen evolving complex in photosynthesis.¹³¹⁻¹³³ Along these lines, Lloret-Fillol and coworkers have demonstrated the formation of a

related $\text{Fe}^{\text{IV}}\text{-O-Ce}^{\text{IV}}$ intermediate in the oxidation of water by a nonheme iron catalyst using ceric ammonium nitrate as the oxidant.¹³⁴

Two pairs of oxo-bridged bimetallic complexes obtained (**1** and **2**, **4_{Cl}**/**4_{OTf}** and **5**) from the reactions of $\text{Cr}(\text{OTf})_2$ or $\text{Et}_4\text{NFe}^{\text{III}}\text{Cl}_4$ with two $(\text{TMC})\text{Fe}^{\text{IV}}(\text{O}_{\text{anti/syn}})$ isomers. Complex **1** has been assigned in a previous report as $[(\text{CH}_3\text{CN})(\text{TMC})\text{Fe}^{\text{III}}\text{-O}_{\text{anti}}\text{-Cr}^{\text{III}}(\text{OTf})_4(\text{NCCH}_3)]$ and **2** is identified in this paper as $[(\text{TMC})\text{Fe}^{\text{III}}\text{-O}_{\text{syn}}\text{-Cr}^{\text{III}}(\text{OTf})_4(\text{NCCH}_3)]$ based on UV-vis, resonance Raman, Mössbauer, and X-ray absorption spectroscopic data, as well as electrospray mass spectrometry. In addition, the structures of **4_{Cl}** ($(\text{Cl})(\text{TMC})\text{Fe-O}_{\text{anti}}\text{-FeCl}_3$) and **5** ($[(\text{TMC})\text{Fe-O}_{\text{syn}}\text{-FeCl}_3](\text{OTf})$) have been determined by X-ray crystallography. On the basis of these studies, the key factor linking the $(\text{TMC})\text{Fe-O-M}$ species listed above is the orientation of the methyl groups of the TMC framework relative to the oxo bridge. This characteristic affects three features of the $(\text{TMC})\text{Fe-O-M}$ complexes: (i) the coordination number of the Fe site, (ii) the $\text{Fe}_{\text{TMC}}\text{-O}$ distance, (iii) the Fe-N4 plane distance. When the TMC methyl groups are *syn* to the oxo bridge in the $(\text{TMC})\text{Fe-O-M}$ species, the iron center favors a square pyramidal geometry, resulting in a shorter $\text{Fe}_{\text{TMC}}\text{-O}$ distance and a longer distance of the Fe from the mean N4 plane of the TMC framework. These results emphasize the importance of the ligand topology in determining the coordination sphere of the iron center. Future work will focus on the consequences of replacing the methyl groups of the TMC ligand with other R groups such as the benzyl groups introduced by Nam¹³⁵ on the relative stabilities of the *syn* and *anti* isomers.

Chapter 3

Coordination Effects on Structures of (L)Fe^{III}-O-Cr^{III} Species

3.1 Introduction

In Chapter 2, we have discussed a pair of $\text{Fe}^{\text{III}}\text{-O-Cr}^{\text{III}}$ isomers: $[(\text{CH}_3\text{CN})(\text{TMC})\text{Fe}^{\text{III}}\text{-O}_{\text{anti}}\text{-Cr}^{\text{III}}(\text{OTf})_4(\text{NCCH}_3)]$ (1) and $[(\text{TMC})\text{Fe}^{\text{III}}\text{-O}_{\text{syn}}\text{-Cr}^{\text{III}}(\text{OTf})_4(\text{NCCH}_3)]$.^{104, 136} Structures of both complexes were assigned unambiguously based on detailed characterization from UV-vis, resonance Raman, Mössbauer, and X-ray absorption spectroscopic methods, as well as electrospray mass spectrometry. Interestingly, both species have three characteristic UV-vis bands between 350 nm to 600 nm, indicative of electronic transitions relevant to $\text{Fe}^{\text{III}}\text{-O-Cr}^{\text{III}}$ core. This is a convenient way to tell whether the inner-sphere electron transfer happens smoothly between Fe(IV)-oxo moiety and Cr(II) salt.

One advantage of studying synthetic molecules compared with its corresponding nature intermediates is that, in principle, the coordination sphere of the synthetic molecules can be systematically modulated to determine how the local coordination geometry governs electronic structure and reactivity.¹³⁷ Representative examples include $[\text{Fe}^{\text{IV}}(\text{O}_{\text{anti}})(\text{TMC})(\text{NCCH}_3)](\text{OTf})_2$, in which the axial CH_3CN coordination site is labile to be substituted by other ligand. A series of monoanionic X ligands, including OH^- , CF_3CO_2^- , N_3^- , NCS^- , NCO^- , and CN^- with the form of NBu_4X salts have been used to displace CH_3CN to make new $[\text{Fe}^{\text{IV}}(\text{O}_{\text{anti}})(\text{TMC})\text{X}]^{\text{n}+}$ species,¹³⁷ and the changes in the UV-vis spectrum caused by axial ligand substitution involve not only an energy shift, but also a redistribution of absorption intensities, implying a complicated trans-influence of X⁻ in $[\text{Fe}^{\text{IV}}(\text{O}_{\text{anti}})(\text{TMC})\text{X}]^{\text{n}+}$ species. Fitting results from Fe K-edge extended X-ray absorption fine structure (EXAFS) spectroscopy for $[\text{Fe}^{\text{IV}}(\text{O}_{\text{anti}})(\text{TMC})\text{X}]^{\text{n}+}$ (X =

CF_3CO_2^- , N_3^- , NCS^- , NCO^- , CN^-) revealed the Fe–O distances to be $1.65 \pm 0.02 \text{ \AA}$, indicating a minor influence of the axial ligands on the Fe–O bond length $[\text{Fe}^{\text{IV}}(\text{O}_{\text{anti}})(\text{TMC})\text{X}]^{\text{n+}}$ structures. The values of ν_{FeO} however, showed the decreasing trend with increasing basicity of the axial ligand ($\text{CF}_3\text{CO}_2^- < \text{CH}_3\text{CN} < \text{CN}^- \approx \text{NCO}^- \approx \text{NCS}^- < \text{N}_3^-$), indicating that a stronger *trans* donor could weaken the Fe=O bond. Intriguingly, the observed hydrogen atom abstraction reactivities among different $[\text{Fe}^{\text{IV}}(\text{O}_{\text{anti}})(\text{TMC})\text{X}]^{\text{n+}}$ did not follow the spectroscopic trend, where the ordering of X is $\text{CF}_3\text{CO}_2^- > \text{CH}_3\text{CN} > \text{N}_3^-$.¹³⁸ The lack of clear correlation could be a consequence of the relatively small number of complexes used in the reactivity study, and further experimental and theoretical studies are warranted.¹³⁹ People are also able to synthesize $[\text{Fe}^{\text{IV}}(\text{O})(\text{TMCS})](\text{OTf})_2$ (TMCS is a monoanion of 1-mercaptoethyl-4,8,11-trimethyl-1,4,8,11-tetraaza cyclotetradecane),¹⁴⁰ $[\text{Fe}^{\text{IV}}(\text{O})(\text{TMCPy})](\text{OTf})_2$ (TMCPy = 1,4,8-trimethyl-11-pyridylmethyl-1,4,8,11-tetraazacyclotetradecane),¹⁴¹ $[\text{Fe}^{\text{IV}}(\text{O})(\text{TMCdma})](\text{OTf})_2$ (TMCdma = 1,4,8-Me₃cyclam-11-CH₂C(O)NMe₂)¹⁴², by replacing a methyl group on TMC molecule with a thiolate arm, a 2-pyridylmethyl arm, and an amide arm respectively to provide the fifth donor ligand. These three oxoiron(IV) species exhibit different spectroscopic features as well as reactivities compared with the original $[\text{Fe}^{\text{IV}}(\text{O})(\text{TMC})(\text{NCCH}_3)](\text{OTf})_2$ complex.

Based on EXAFS data analysis, complex **1** possesses a labile axial ligand bound to the Fe(III) center, which endows feasibility for ligand substitution.¹⁰⁴ Reaction between **1** and NBu_4X (X = NCS^- , NCO^-) have been conducted, and the results confirmed the formation of corresponding **1-NCS** and **1-NCO**, with different spectroscopic

characters presented. Also, the success of reaction between $[\text{Fe}^{\text{IV}}(\text{O}_{\text{anti}})(\text{TMC})(\text{NCCH}_3)](\text{OTf})_2$ and $\text{Cr}(\text{OTf})_2$ suggests that other oxoiron(IV) species may also undergo inner-sphere electron transfer reaction with the Cr(II) salt. Therefore a variety of oxoiron(IV) species, including $[\text{Fe}^{\text{IV}}(\text{O})(\text{TMCPy})](\text{OTf})_2$, $[\text{Fe}^{\text{IV}}(\text{O})(\text{TMCdma})](\text{OTf})_2$, $[\text{Fe}^{\text{IV}}(\text{O})(\text{N4Py})](\text{OTf})_2$ and $[\text{Fe}^{\text{IV}}(\text{O})(\text{BnTPEN})](\text{OTf})_2$, were utilized to react with $\text{Cr}(\text{OTf})_2$ to generate corresponding $(\text{L})\text{Fe}^{\text{III}}-\text{O}-\text{Cr}^{\text{III}}$ complexes. The UV-vis spectra of all $(\text{L})\text{Fe}^{\text{III}}-\text{O}-\text{Cr}^{\text{III}}$ species show similar tri-peak patterns as what are observed in **1**. However, their $\nu_{\text{as}}(\text{Fe}^{\text{III}}-\text{O}-\text{Cr}^{\text{III}})$ in Raman spectra vary significantly. The vibrational numbers in $(\text{TMCPy})\text{Fe}^{\text{III}}-\text{O}-\text{Cr}^{\text{III}}$ (**2**) and $(\text{TMCdma})\text{Fe}^{\text{III}}-\text{O}-\text{Cr}^{\text{III}}$ (**4**) are around 770 cm^{-1} , while in $(\text{N4Py})\text{Fe}^{\text{III}}-\text{O}-\text{Cr}^{\text{III}}$ (**5**) and $(\text{BnTPEN})\text{Fe}^{\text{III}}-\text{O}-\text{Cr}^{\text{III}}$ (**6**) the vibrational numbers are around 870 cm^{-1} . In all these four complexes the Fe center is 6-coordinate, thus the 100 cm^{-1} difference in the $\nu_{\text{as}}(\text{Fe}^{\text{III}}-\text{O}-\text{Cr}^{\text{III}})$ is due to the coordination environmental effects of the supporting ligand to the Fe center. The conclusion is further supported by the relevant XAS analysis and will be discussed in detail in this chapter.

3.2 Experimental details

3.2.1 Materials

The preparations for $\text{Cr}(\text{OTf})_2 \cdot 2\text{CH}_3\text{CN}$,¹⁰⁴ $\text{Fe}^{\text{II}}(\text{TMC})(\text{OTf})_2$,¹⁰⁵ iodosylbenzene ($\text{C}_6\text{H}_5\text{IO}$),¹⁰⁶ ^{18}O -labeled iodosylbenzene ($\text{C}_6\text{H}_5\text{I}^{18}\text{O}$)¹⁴³ and the iron(II) salt $([\text{Fe}^{\text{II}}(\text{TMCPy})](\text{OTf})_2)$,¹⁴⁴ $([\text{Fe}^{\text{II}}(\text{TMCdma})](\text{OTf})_2)$,¹⁴² $([\text{Fe}^{\text{II}}(\text{N4Py})(\text{NCCH}_3)](\text{OTf})_2)$,¹⁴⁵ $([\text{Fe}^{\text{II}}(\text{BnTPEN})(\text{OTf})](\text{OTf}))$ ¹⁴⁵ were prepared following published procedures. Their

correlated oxoiron(IV) species were prepared in a universal procedure as follows: Fe(II) complex in CH₃CN was stirred with 3 eq. solid PhIO at room temperature for 30 min. The turbid liquid was kept at -40 °C for 20 mins and then filtered by the 25 mm filter plate for use. All reagents and solvents were purchased from commercial sources and used as received unless specified. All moisture- and oxygen-sensitive compounds were prepared using standard Schlenk-line techniques or in the glove box filled with N₂.

3.2.2 Instrumentation

UV-vis absorption spectra were recorded on an HP 8453A diode array spectrometer. Low-temperature visible spectra were obtained using a cryostat from UNISOKU Scientific Instruments, Japan. Electrospray mass spectrometry was performed on a Finnigan LCQ ion trap mass spectrometer. Resonance Raman spectra were collected with an Acton AM-506 monochromator equipped with a Princeton LN/CCD data collection system, with 515-nm or 561-nm excitation from 50 mW lasers by Cobolt Lasers, Inc. Spectra in acetonitrile were obtained at 77 K using a 135° backscattering geometry. Raman samples were prepared in cuvettes in a -40 °C cold bath and quickly transferred to EPR tubes and then froze in liquid N₂. Raman bands were calibrated to indene prior to data collection. The monochromator slit width was set for a band pass of 4 cm⁻¹ for all spectra.

3.2.3 X-ray Absorption Spectroscopy

XAS data were collected at beamline X3B at the National Synchrotron Light Source (NSLS) of Brookhaven National Laboratory and SSRL beam line 7-3. Fe K-edge XAS data were collected for frozen solutions maintained at ~30 K over the energy range 6.9-8.0 keV. A Fe foil spectrum was measured simultaneously for internal energy calibration using the first inflection point of the K-edge energy (7112.0 eV). Data were obtained as fluorescence excitation spectra using a solid-state germanium detector (Canberra).

Data reduction, averaging, and normalization were performed using the program EXAFSPAK. The coordination number of a given shell was a fixed parameter and was varied iteratively in integer steps while the bond lengths (R) and mean-square deviation (σ^2) were allowed to freely float. The amplitude reduction factor was fixed at 0.9 while the edge-shift parameter E_0 was allowed to float as a single value for all shells. The pre-edge features were fitted using the Fityk program¹¹³ with pseudo-Voigt functions composed of 50:50 Gaussian/Lorentzian functions.

3.3 Results and Discussion

3.3.1 Reaction Between **1** and NBu_4X ($\text{X} = \text{NCS}^-$, NCO^-)

The likelihood of a sixth ligand bound to the iron(III) center in **1** was supported by the change in its spectral features upon addition of NBu_4X ($\text{X} = \text{NCS}^-$ or NCO^-). As

shown in Figure 3.1, there are small shifts of the three bands between 350-600 nm, as well as increases in intensity upon addition of X anion. Titration experiments showed that only 1 eq. of NCS^- or NCO^- was needed to transform **1** fully into **1-NCS** (Figure 3.2) or **1-NCO** (Figure 3.3).

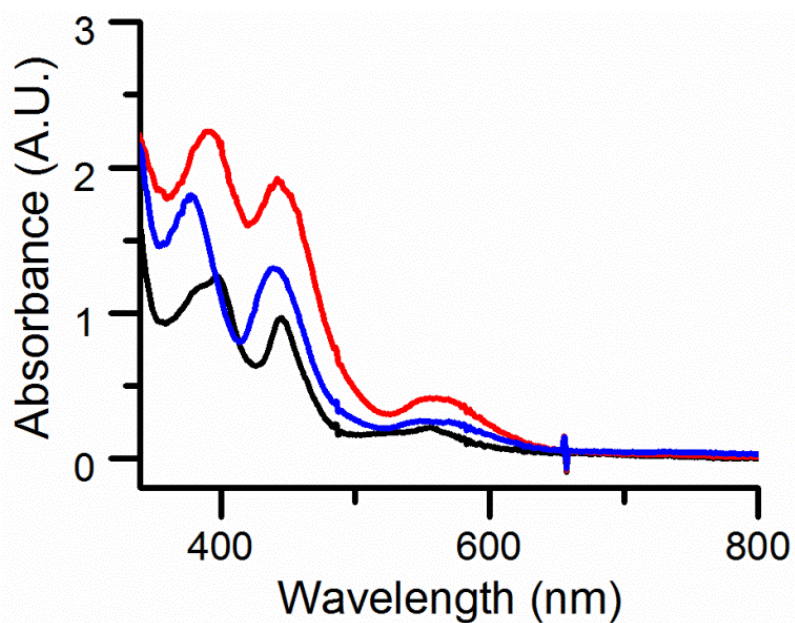


Figure 3.1 UV-vis spectra of 0.3 mM **1** (black), **1-NCO** (blue), **1-NCS** (red) in CH_3CN at $-40\text{ }^\circ\text{C}$. λ_{max} (ϵ) for **1**: 398 (3800), 447 (3000), and 558 (700). λ_{max} (ϵ_{M}) for **1-NCO**: 380 (6000), 438 (4200), and 560 (850). λ_{max} (ϵ_{M}) for **1-NCS**: 390 (7500), 442 (6300), and 560 (1400). ϵ unit: $\text{M}^{-1}\text{ cm}^{-1}$.

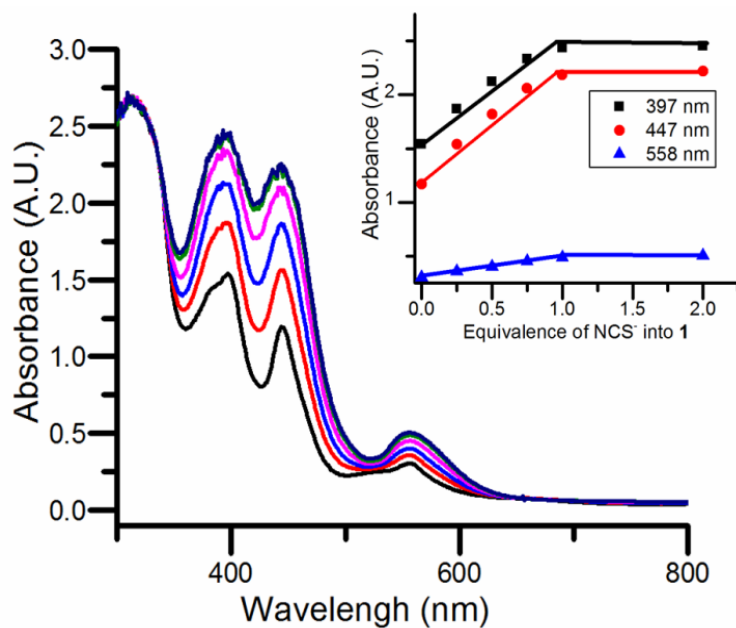


Figure 3.2 Changes in the UV-vis spectrum when NBU₄SCN was added into 0.42 mM **1** in CH₃CN at -40 °C. Black: no NCS⁻ added. Red: 0.25 eq. of NCS⁻ added. Blue: 0.5 eq. of NCS⁻ added. Pink: 0.75 eq. of NCS⁻ added. Green: 1.0 eq. of NCS⁻ added. Purple: 2.0 eq. of NCS⁻ added. Insets: UV-vis change upon titration of NCS⁻ into **1**.

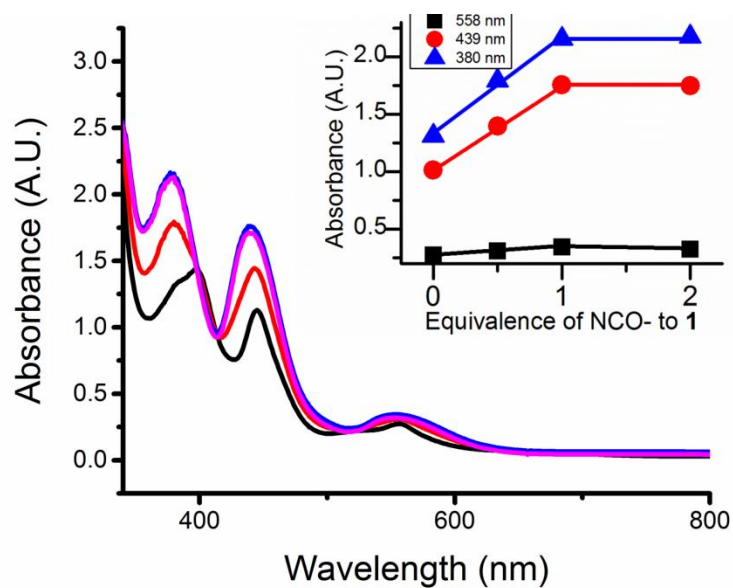


Figure 3.3 Changes in the UV-vis spectrum when NBu_4NCO was added into 0.4 mM **1** in CH_3CN at $-40\text{ }^\circ\text{C}$. Black: no NCO^- added. Red: 0.5 eq. of NCO^- added. Blue: 1.0 eq. of NCO^- added. Pink: 2.0 eq. of NCO^- added. Inset: Absorbance change upon titration of NCO^- into **1**.

ESI-MS analysis of **1-NCS** and **1-NCO** revealed respective positive mode peaks at m/z 370 and 354, corresponding to $[\text{Fe}(\text{TMC})(\text{NCS})]^+$ and $[\text{Fe}(\text{TMC})(\text{NCO})]^+$ fragment ions (Figure 3.4), suggesting the occupation of the axial position *trans* to the oxo bridge by these anions.

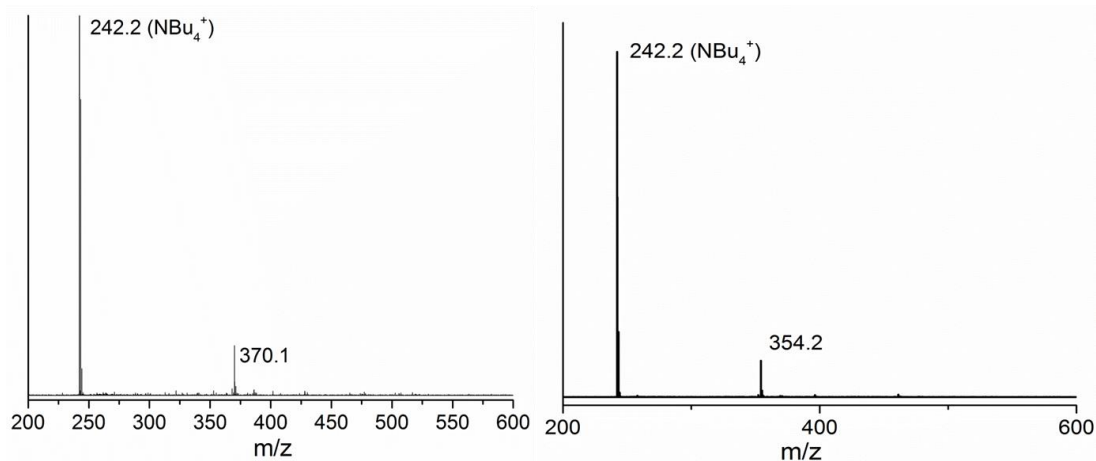


Figure 3.4 (Left) Positive mode ESI-MS spectra for 1 mM **1** + 1 eq. NBu_4SCN . (Right) Positive mode ESI-MS spectra for 1 mM **1** + 1 eq. NBu_4SCO .

Furthermore, **1-NCS** exhibits an Fe K-edge energy of 7124.3 eV, comparable to the 7124.0 eV value found for **1**. **1-NCS** also exhibits a pre-edge feature with an area of 9 units (Figure 3.5), which is close to the 11 units found for **1**, showing that a six-coordinate iron(III) center in **1-NCS** is maintained. EXAFS analysis of **1-NCS** shows the

presence of a linear Fe–O–Cr core like that in **1**, but with a 1.85 Å Fe–O bond and an Fe···Cr distance of 3.67 Å (Figure 3.6). The lengthening of the Fe–O bond can be rationalized by the axial NCS[−] binding.

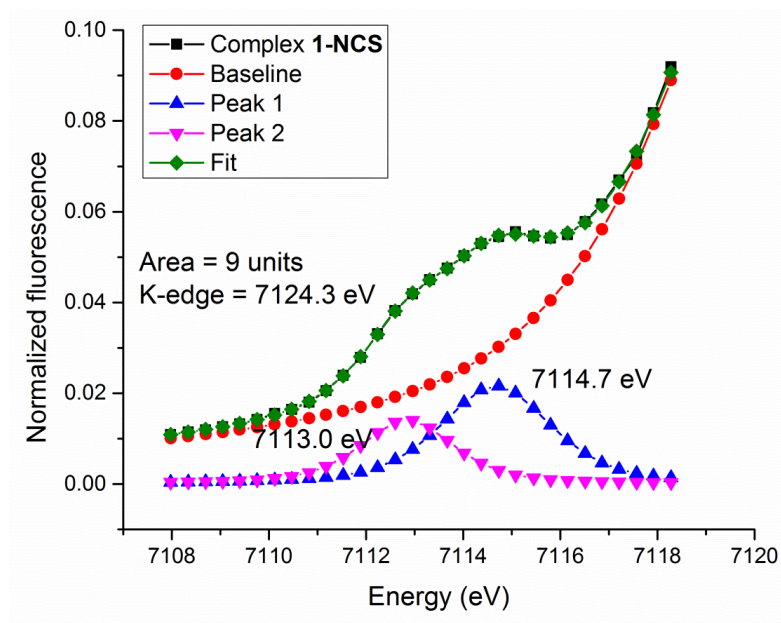


Figure 3.5 Pre-edge region of Fe K-edge XAS spectrum of **1-NCS** (black). Baseline fit (red), pre-edge peak 1 (blue), pre-edge peak 2 (magenta), pre-edge fit (green).

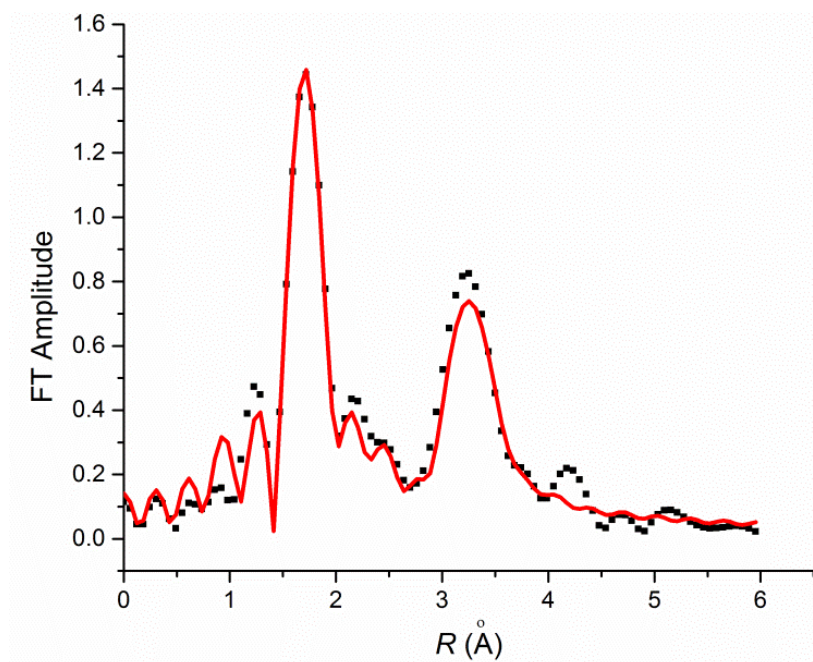


Figure 3.6 Fit 7 in Table 3.1 (red line) of the Fourier transformed unfiltered (black dots) EXAFS data of **1-NCS**

Table 3.1 Fit parameters for **1-NCS** unfiltered data from 2-12 Å⁻¹.

Fit	Fe–N/O			Fe–N/O			Fe···C			Fe···Cr			E ₀	F	F'
	N	R (Å)	σ ² ×10 ⁻³	N	R (Å)	σ ² ×10 ⁻³	N	R (Å)	σ ² ×10 ⁻³	N	R (Å)	σ ² ×10 ⁻³			
1	4	2.18	2.0										-4.58	614	672
2	5	2.18	3.6										-4.28	653	693
4	5	2.17	4.5	1	1.85	0.5							-6.24	489	600
5	5	2.16	4.3	1	1.85	0.7	4	2.90	3.8				-7.34	400	543
6	5	2.16	4.2	1	1.85	1.6	4	2.94	6.9	1	3.75	-0.2	-8.24	139	320
7	5	2.17	4.2	1	1.85	1.5	4	2.95	6.4	1	\3.67	\0.0	-6.65	76	236
8	4	2.17	2.4	1	1.85	2.9	4	2.96	6.1	1	\3.67	\0.0	-6.56	84	248

\ indicates the Fe···Cr distance obtained from a double scattering pathway.

3.3.2 Generation and Characterization of **2**

With the successful synthesis of **1**, **1-NCS** and **1-NCO**, I switched focus on different $[\text{Fe}^{\text{IV}}(\text{O})(\text{L})]^{2+}$ complexes to react with $\text{Cr}(\text{OTf})_2$ to generate $(\text{L})\text{Fe}^{\text{III}}-\text{O}-\text{Cr}^{\text{III}}$ complexes, which can further justify the coordination environmental effect of the Fe–O–Cr core. TMCPy, a TMC-derived ligand with a pyridine moiety appended to the cyclam framework, was first used.

At $-40\text{ }^\circ\text{C}$ $\text{Cr}(\text{OTf})_2$ was titrated into 0.45 mM $[(\text{TMCPy})\text{Fe}^{\text{IV}}(\text{O})](\text{OTf})_2$ in CH_3CN under anaerobic condition to form a new species (**2**). The characteristic near-IR band of oxoiron(IV) complex at 834 nm immediately decreased and accompanied with the appearance of three new bands at 381 , 451 , and 558 nm (Figure 3.7), which chromophore pattern is very close to that for **1**. Formation of **2** was further supported by the m/z peak from ESI-MS result at 903.8 , which is assigned as $[(\text{TMCPy})\text{FeOCr}(\text{OTf})_3]^+$ based on its isotope pattern (Figure 3.8). The formula was further confirmed by ^{18}O -labeled experiment, which shifted the 903.8 peak by $+2$ (Figure 3.9).

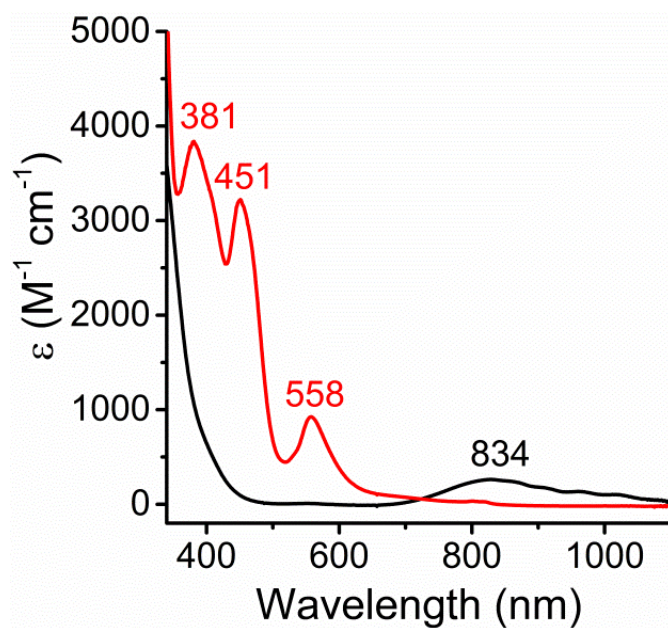


Figure 3.7 UV-vis spectra of $\text{Fe}^{\text{IV}}(\text{O})(\text{TMCPy})(\text{OTf})_2$ (black) and **2** (red) in CH_3CN at $-40\text{ }^\circ\text{C}$. ϵ ($\text{M}^{-1}\text{ cm}^{-1}$) for bands in **2**: 3800 (381 nm), 3200 (451 nm), 920 (558 nm).

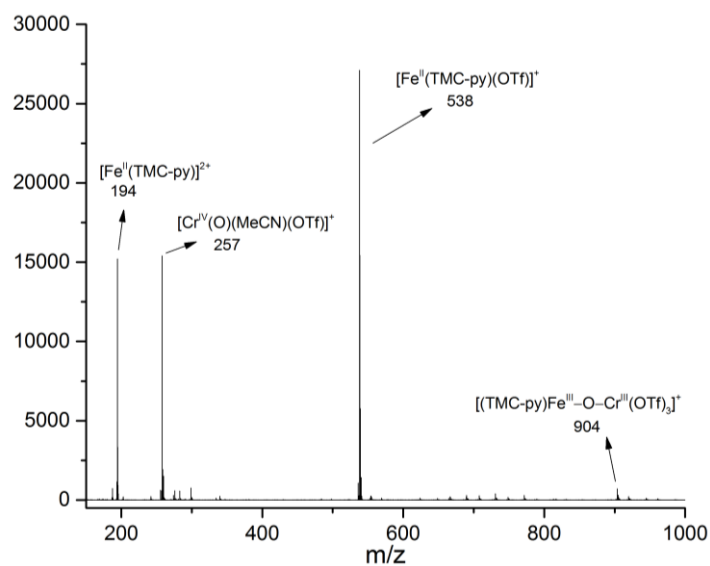


Figure 3.8 ESI-MS spectrum of the reaction of $\text{Fe}^{\text{IV}}(\text{O})(\text{TMC-py})(\text{OTf})_2$ with 1 eq. of $\text{Cr}^{\text{II}}(\text{OTf})_2$ at $-40\text{ }^\circ\text{C}$

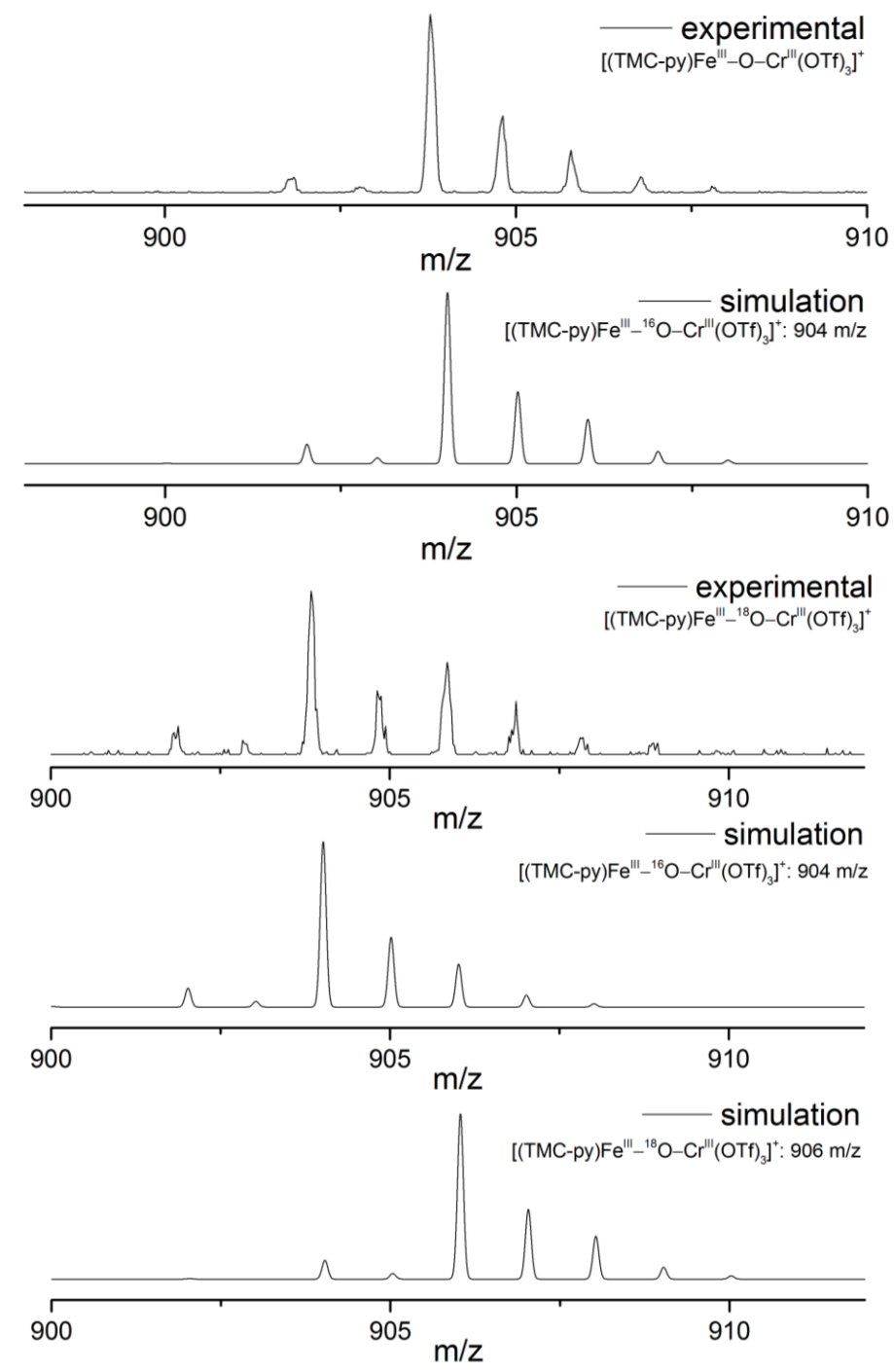


Figure 3.9 Experimental and simulation isotopic patterns of $[(\text{TMCpy})\text{Fe}^{\text{III}}\text{OCr}^{\text{III}}(\text{OTf})_3]^+$ (top), $[(\text{TMCpy})\text{Fe}^{\text{III}16/18}\text{OCr}^{\text{III}}(\text{OTf})_3]^+$ (bottom).

Resonance Raman spectrum of **2** showed three peaks at 770, 762, 749 cm^{-1} using 561 nm laser in CD_3CN , these peaks are shifted to 723, 717 cm^{-1} when ^{18}O isotope was introduced in **2** in CH_3CN (Figure 3.10). The origin for the multiple peaks in **2** is not clear, however the wavenumber of the vibration is consistent with Fe–O–M asymmetric vibration number in **1** (773 cm^{-1}), which has a 6-coordinate Fe center.

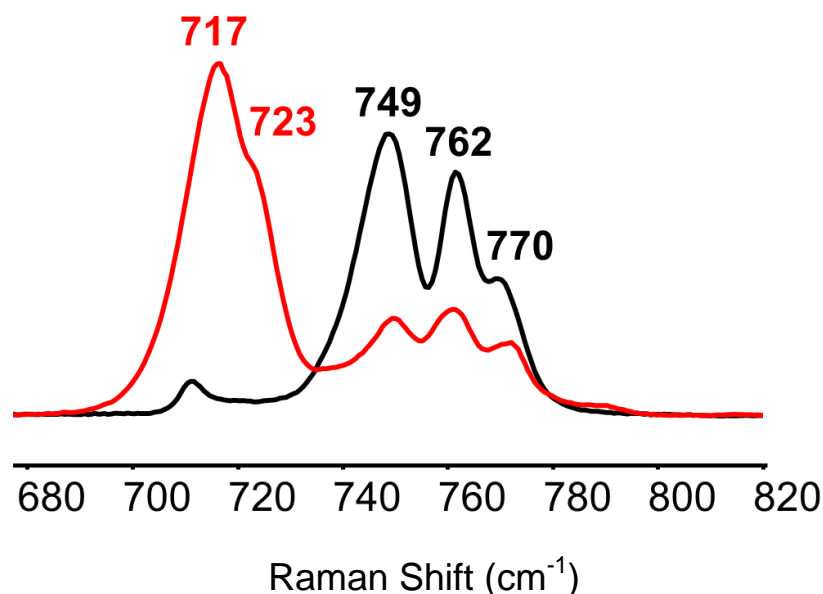


Figure 3.10 Resonance Raman spectra of **2** ($\lambda_{\text{ex}} = 561 \text{ nm}$, 77 K). Black, ^{16}O -labeled; red, ^{18}O -labeled.

The structure of **2** was further characterized by the Fe K-edge X-ray absorption spectroscopy (XAS). The Fe K-edge of **2** is 7124.2 eV, which is a little higher compared with the K-edge energy found for **1** (7124.0 eV) (Figure 3.11). **2** exhibits a pre-edge feature at 7114.7 eV fitted with one peak providing a total area of 14.8 units, comparable with that in **1** (11 units),¹⁰⁴ but much lower than that in $(\text{TMC})\text{Fe}^{\text{III}}\text{-O}_{\text{syn}}$

$\text{Cr}^{\text{III}}(\text{OTf})_4(\text{NCCH}_3)$ (30 units)¹³⁶ and $(\text{TMC})\text{Fe}^{\text{III}}\text{-O}_{\text{anti}}\text{-Sc}^{\text{III}}(\text{OTf})_4(\text{NCCH}_3)$,¹⁰² suggesting a 6-coordinating Fe center in **2**, which is consistent with the pyridine binding at the axial position.

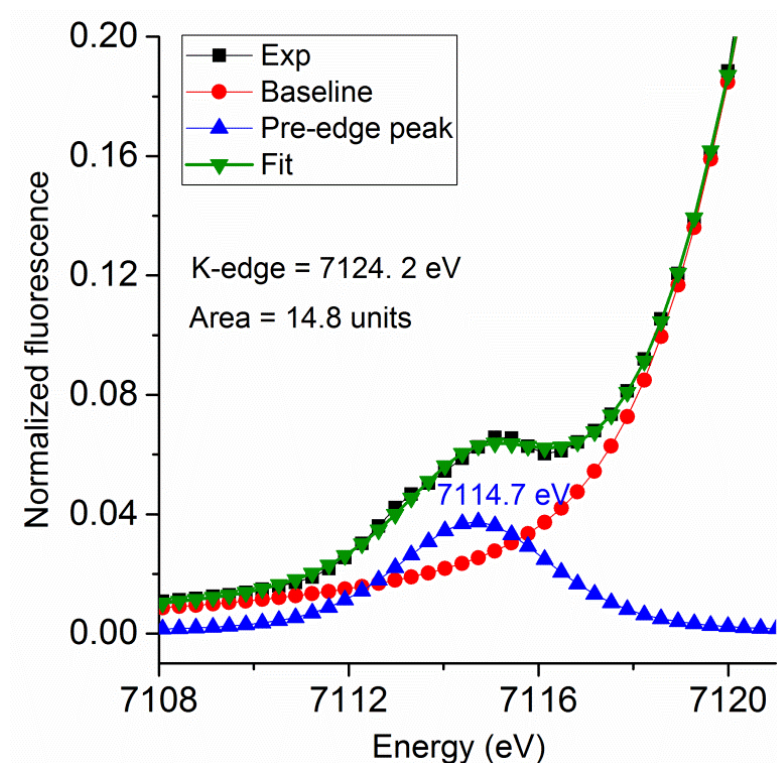


Figure 3.11 Pre-edge region of the Fe K-edge XAS spectrum of **2** (black squares): rising-edge fit (red circles), pre-edge peak (blue triangles pointing up, maximum at 7114.7 eV), pre-edge fit (green diamonds).

The best fit of the EXAFS data on **2** gives quite close results on the first two shells (1 O/N scatterer at 1.84 Å, 5 O/N scatterers at 2.16 Å), and also a multiple scattering from Cr at 3.65 Å (Figure 3.12, Table 3.2). The bond distance of $\text{Fe}^{\text{III}}\text{-O/N}$ in **2**

also falls in the range of the bond distances in iron(III) moiety with TMC-based ligand. In conclusion, the XAS data indicates a 6-coordinating Fe(III) center in **2**.

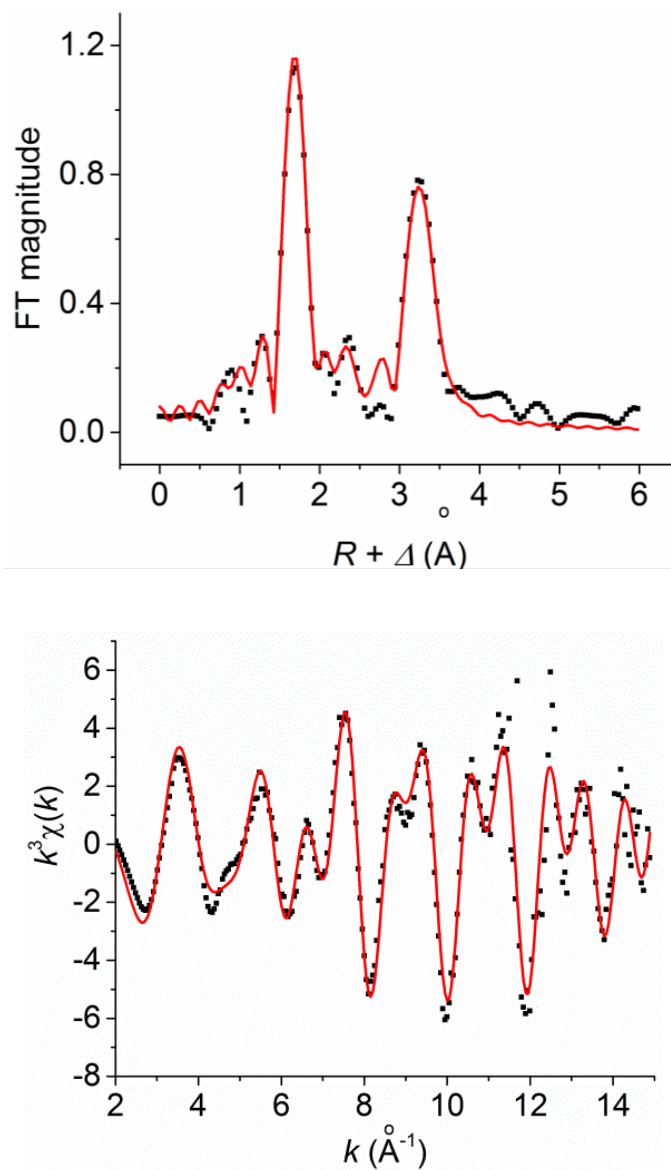


Figure 3.12 (Top) Unfiltered k -space data of **2** (dotted black line) and its fit (solid red line). (Bottom) Fourier-transformed Fe K-edge EXAFS data for **2** (dotted black line) and corresponding best fit (solid red line, fit #5 in Table 3.2).

Table 3.2 Fit Parameters for **2**, unfiltered from $k = 2 - 15 \text{ \AA}^{-1}$.

Fit	Fe–N			Fe–O			Fe•••C			Fe•••Cr			E_0	GOF	
	N	R(Å)	σ^2 (10^{-3})	N	R(Å)	σ^2 (10^{-3})	N	R(Å)	σ^2 (10^{-3})	N	R(Å)	σ^2 (10^{-3})		F	F'
1	4	2.15	3.09										-11.23	891	790
2	4	2.15	3.51	1	1.84	1.16							-10.37	682	691
3	5	2.15	4.94	1	1.84	0.94							-10.17	683	692
4	5	2.14	5.03	1	1.84	0.52	4	2.90	4.18	1	3.71	-0.07	-12.81	248	417
5	5	2.16	5.28	1	1.84	0.43	4	2.91	4.57	1	\3.65	\0.33	-9.63	192	367
6	5	2.16	4.91				4	2.91	5.20	1	\3.65	\0.55	-9.69	486	584

\ indicates the Fe•••Cr distance obtained from a double scattering pathway.

During the same time of my study on **2**, I had a nice collaboration with Seesaw, a visiting scholar from Taiwan to our lab (his name is Wei-min, Ching, but he preferred to be called differently and everyone did so in the lab). Seesaw's project is to develop synthetic models to study nonheme Fe(III)-hydroxide species, which is a biomimetic models for catalytic cycle in lipoxygenase.¹⁴⁶ He successfully synthesized [(TMCPy)Fe^{III}OH](OTf)₂ (complex **3**) from reaction between [Fe^{IV}(O)(TMCPy)](OTf)₂ and cyclohexadiene, together with a thorough characterization on this Fe(III)-hydroxide species. Inspired by his research, since H[•] acts equivalently as Cr(II) ion in reducing the oxoiron(IV) moiety to Fe(III), we conducted XAS analysis on **3** aimed to compare its structure with **2**.

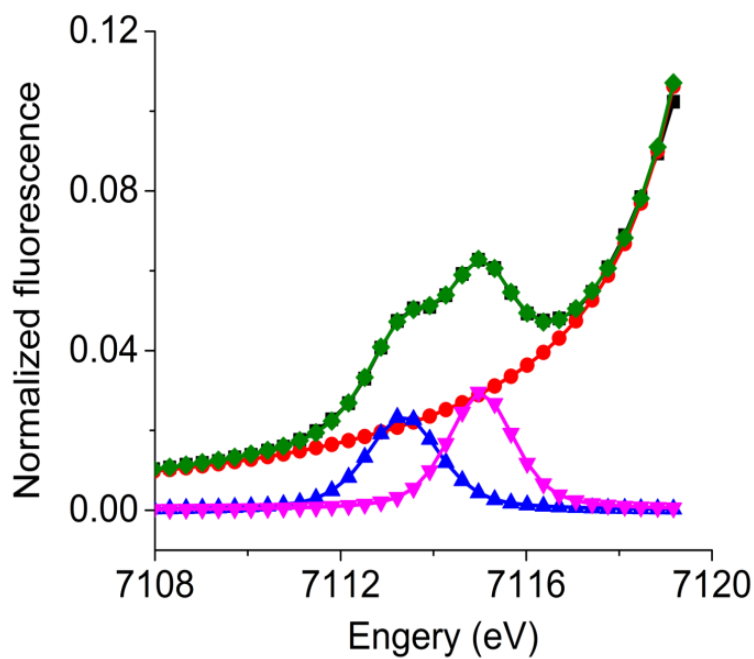


Figure 3.13 Pre-edge region of the Fe K-edge XAS spectrum of **3** (black squares): rising-edge fit (red circles), pre-edge peak 1 (blue triangles pointing up, maximum at 7113.2 eV), pre-edge peak 2 (magenta triangles pointing down, maximum at 7115.0 eV), pre-edge fit (green diamonds).

The Fe K-edge energy of **3** is 7124.8 eV, which is a little higher compared with those of **2** (7124.2 eV) and **1** (7124.0 eV) (Figure 3.13). **3** exhibits a pre-edge feature at ca. 7114 eV, which is fitted with two peaks providing a total area of 9.4 units, a value that increases to 14.8 units in **2**, consistent with a 6-coordinate Fe center as well.

The best fit for the EXAFS data of **3** consists of 1 O/N scatterer at 1.84 Å, 5 O/N scatterers at 2.17 Å, 4 C scatterers at 2.92 Å and 4 C scatterers at 3.07 Å (Figure 3.14, Table 3.3). The XAS data indicates 6-coordinate Fe(III) centers in both **2** and **3**. Interestingly, the d (Fe–O) from EXAFS fitting for **2** and **3** are identical (1.84 Å), which suggests the very close structural effect between Cr and H atom when binding to the Fe(III)–O moiety.

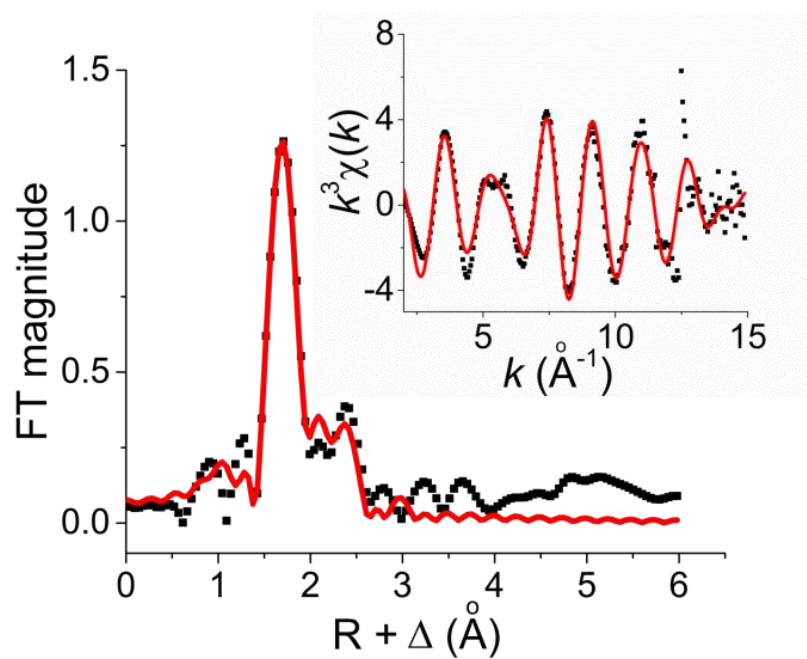


Figure 3.14 Main: Fourier-transformed Fe K-edge EXAFS data for **3** (dotted black) and the corresponding best fit (solid red, fit #6 in Table 3.3). Inset: unfiltered k-space data (dotted black) and its fit (solid red).

Table 3.3 Fit Parameters for **3**, unfiltered from $k = 2 - 15 \text{ \AA}^{-1}$.

Fit	Fe-N			Fe-O			Fe•••C			Fe•••C			E_0	GOF	
	N	R(\AA)	$\sigma^2(10^{-3})$		F	F'									
1	5	2.16	4.50										-10.91	942	813
2	4	2.15	3.09										-11.23	891	790
3	4	2.15	3.51	1	1.84	1.16							-10.38	682	691
4	5	2.15	4.94	1	1.84	0.94							-5.69	683	692
5	5	2.17	3.86	1	1.84	0.88	4	2.95	8.04				-4.64	189	392
6	5	2.17	3.91	1	1.84	0.76	4	2.91	4.02	4	3.07	6.13	-4.86	182	384
7	5	2.17	3.65				4	2.91	4.85	4	3.07	8.43	-4.96	400	570

3.3.3 Generation and Characterization of **4**

It appears that both **1** and **2** have comparable $\nu_{\text{as}}(\text{Fe}^{\text{III}}-\text{O}-\text{Cr}^{\text{III}})$ values (770 cm^{-1}). To investigate whether this value is universal for all 6-coordinate $\text{Fe}^{\text{III}}-\text{O}-\text{Cr}^{\text{III}}$ complexes, another TMC-derived oxoiron(IV) species, $[\text{Fe}^{\text{IV}}(\text{O})(\text{TMCdma})](\text{OTf})_2$, was used to react with $\text{Cr}(\text{OTf})_2$ in generating $(\text{TMCdma})\text{Fe}-\text{O}-\text{Cr}(\text{OTf})_4(\text{NCCH}_3)$ (**4**). Like TMCPy, TMCdma is also a TMC-derived ligand, with an amide moiety appended to the cyclam framework. The Fe center is coordinated with the carbonyl oxygen at the axial position.

As shown in Figure 3.15, the reaction between 0.76 mM $[\text{Fe}^{\text{IV}}(\text{O})(\text{TMCdma})](\text{OTf})_2$ and 1.5 eq. of $\text{Cr}(\text{OTf})_2$ led to a formation of new species, with the band at 544 nm ($\epsilon = 920\text{ M}^{-1}\text{ cm}^{-1}$). The 561-nm laser was then shed on the frozen solution of 3.75 mM **4**, and a vibrational peak at 780 cm^{-1} together with a minor peak at 751 cm^{-1} were observed (Figure 3.16). The 751 cm^{-1} peak may arise from the Fermi doublet, the 780 cm^{-1} wavenumber is comparable to 773 cm^{-1} in **1** and 760 cm^{-1} in **2**, reflecting the linear $\nu_{\text{as}}(\text{Fe}^{\text{III}}-\text{O}-\text{Cr}^{\text{III}})$ value. The 780 cm^{-1} peak in **4** is shifted to 736 cm^{-1} when ^{18}O isotope was introduced. All the results above indicate a 6-coordinate Fe center in $\text{Fe}^{\text{III}}-\text{O}-\text{Cr}^{\text{III}}$ core in **4**, similar as that in **1** and **2**.

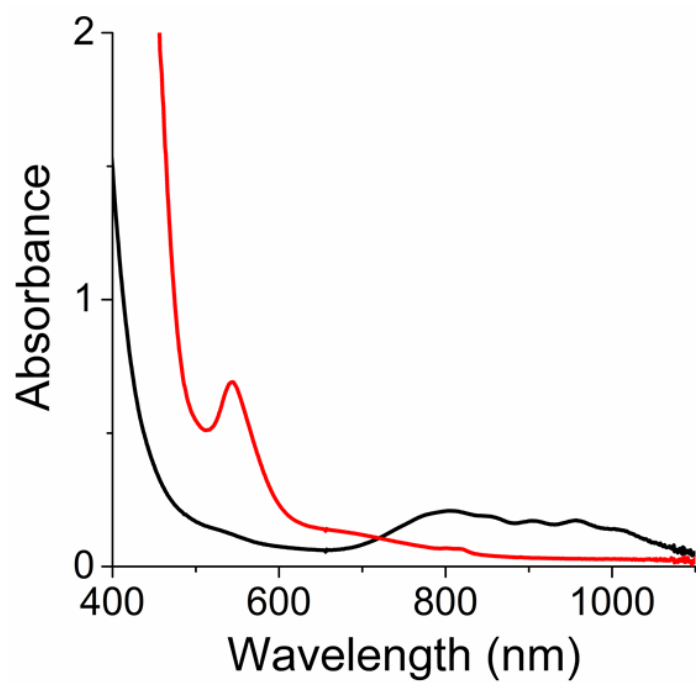


Figure 3.15 UV-vis spectra of 0.75 mM $[\text{Fe}^{\text{IV}}(\text{O})(\text{TMCdma})](\text{OTf})_2$ (black) and **4** (red) at $-40\text{ }^\circ\text{C}$ in CH_3CN .

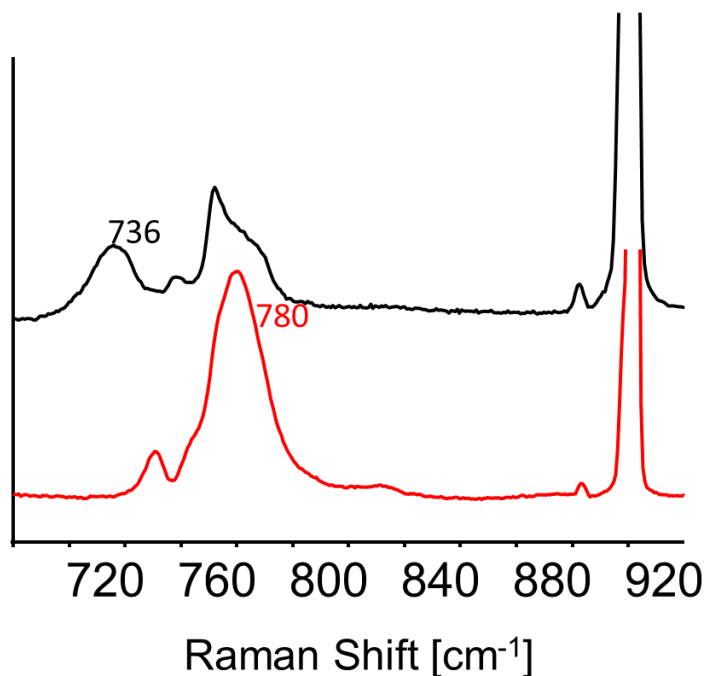


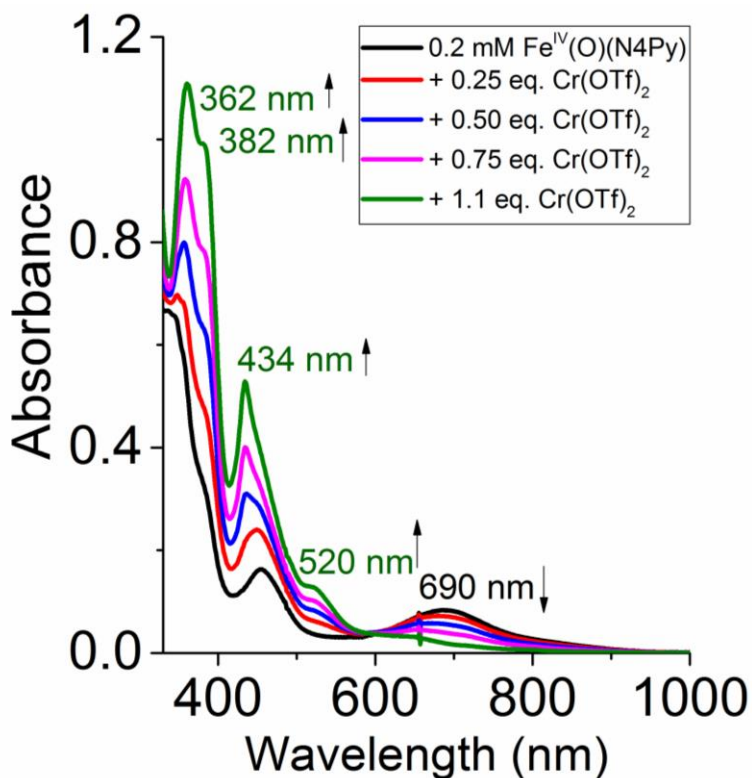
Figure 3.16 Resonance Raman spectra of **4** in CH₃CN ($\lambda_{\text{ex}} = 561$ nm, 77 K).

3.3.4 Generation and Characterization of **5** and **6**

From the research above, we have successfully synthesized and characterized a series of Fe–O–Cr complexes, in which Fe center is coordinated by TMC (**1**, **1-NCS**, **1-NCO**) or TMC derivatives (**2** and **4**). In all these complexes the Fe center is 6-coordinated, and the $\nu_{\text{as}}(\text{Fe}^{\text{III}}\text{--O--Cr}^{\text{III}})$ are all within the range of 750–770 cm^{-1} . What about the Fe–supporting ligand other than TMC derivatives? Will it have similar effect on the Fe–O–Cr structure? In order to answer this, two oxoiron(IV) complexes, $[\text{Fe}^{\text{IV}}(\text{O})(\text{N4Py})](\text{OTf})_2$ and $[\text{Fe}^{\text{IV}}(\text{O})(\text{BnTEPN})](\text{OTf})_2$, in which the support ligand framework is significantly different with TMC, were used. The purpose is to study the

corresponding spectral properties of (N4Py)Fe–O–Cr(OTf)₄(NCCH₃) (**5**) and (BnTPEN)Fe–O–Cr(OTf)₄(NCCH₃) (**6**).

0.2 mM [Fe^{IV}(O)(N4Py)](OTf)₂ was first generated from the reaction between [Fe^{II}(N4Py)(NCCH₃)](OTf)₂ and 3 eq. PhIO in CH₃CN at -40 °C. The Cr(OTf)₂ was gradually added into the oxoiron(IV) complex, 368 nm, 382 nm, 434 nm and 520 nm peaks were generated while the 690 nm peak decreased at the same time, indicating new complex (**5**) is formed. The titration suggested 1.1 eq. Cr(OTf)₂ was needed for the full reaction with [Fe^{IV}(O)(N4Py)](OTf)₂, indicating a 1:1 ratio between Cr(OTf)₂ and oxoiron(IV) (Figure 3.17).



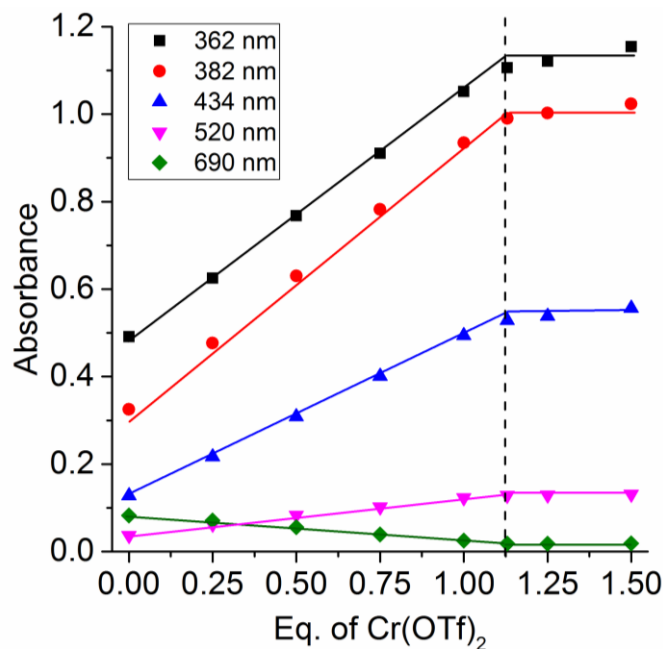


Figure 3.17 (Top) UV-vis spectra of $\text{Cr}(\text{OTf})_2 + [\text{Fe}^{\text{IV}}(\text{O})(\text{N4Py})](\text{OTf})_2$ in CH_3CN at $-40\text{ }^\circ\text{C}$. (Bottom) Titration between $\text{Cr}(\text{OTf})_2 + [\text{Fe}^{\text{IV}}(\text{O})(\text{N4Py})](\text{OTf})_2$.

The UV-vis pattern of **5** is comparable with that in **1**, **2** and **4**, suggesting that it has an Fe–O–Cr core structure. 514.5-nm laser was shot on **5** and its ^{18}O -labeled isotopomer, and their resonance Raman spectra are shown in Figure 3.18. The ^{16}O -labeled **5** exhibits a vibrational peak at 886 cm^{-1} , which is shifted to 844 cm^{-1} in its ^{18}O -labeled isotopomer. The wavenumber of 886 cm^{-1} is very close to $\nu_{\text{as}}(\text{Fe–O–Cr})$ in $(\text{TMC})\text{Fe–O}_{\text{syn}}\text{–Cr}(\text{OTf})_4(\text{NCCH}_3)$ (877 cm^{-1}),¹³⁶ $[(\text{TMC})\text{Fe–O}_{\text{syn}}\text{–FeCl}_3](\text{OTf})$ (888 cm^{-1})¹³⁶ and $(\text{TMC})\text{Fe–O}_{\text{syn}}\text{–Sc}(\text{OTf})_4(\text{NCCH}_3)$ (878 cm^{-1}),¹⁰² which all have a 5-coordinate Fe_{TMC} center. However, the 886 cm^{-1} wavenumber in **5** is about 100 cm^{-1} bigger than that in **1**, **1-NCS**, **1-NCO**, **2** and **4**, which all have a 6-coordinate Fe center.

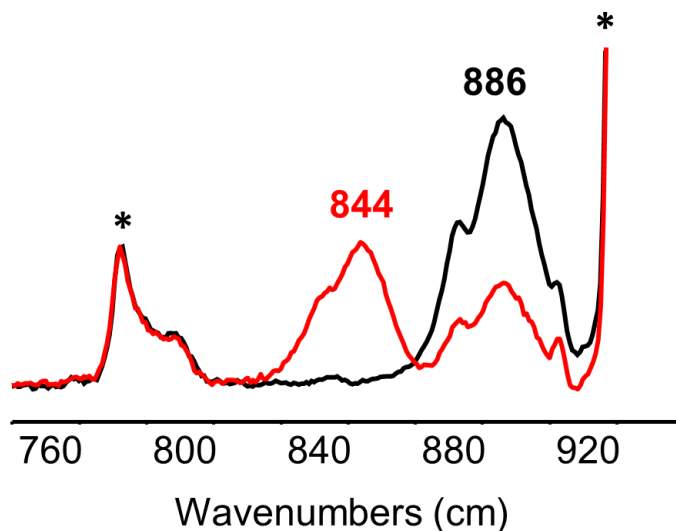


Figure 3.18 Resonance Raman spectra of **5** in CH₃CN ($\lambda_{\text{ex}} = 514.5$ nm, 77 K). Black, ¹⁶O; red, ¹⁸O. Asterisk denotes solvent peak.

In chapter 2 we concluded that the 100 cm^{-1} $\nu_{\text{as}}(\text{Fe-O-Cr})$ difference between (TMC)Fe-O_{anti}-Cr and (TMC)Fe-O_{syn}-Cr are due to the difference in the coordination number of Fe center (6-coordinate for the former and 5-coordinate for the latter). However, in this case **5** is with 6-coordinate Fe center since N4Py is a pentadentate coordinating ligand, but it has a $\nu_{\text{as}}(\text{Fe-O-Cr})$ value 100 cm^{-1} bigger than expected.

To investigate this question, [Fe^{IV}(O)(BnTPEN)](OTf)₂ was used to react with Cr(OTf)₂ in order to obtain a comparable Fe-O-Cr complex as **5**. As shown in Figure 3.19, at $-40\text{ }^{\circ}\text{C}$ 0.32 mM [Fe^{IV}(O)(BnTPEN)](OTf)₂ in CH₃CN can react with 1 eq. Cr(OTf)₂ to generate a new species (**6**) with absorbance at 376 nm, 438 nm and 538 nm, together with the disappearance of 734 nm peak, which is associated to the

$[(\text{BnTPEN})\text{Fe}^{\text{IV}}(\text{O})](\text{OTf})_2$ species. The chromophore pattern of **6** resembles that of **5**, suggesting similar Fe–O–Cr core was maintained.

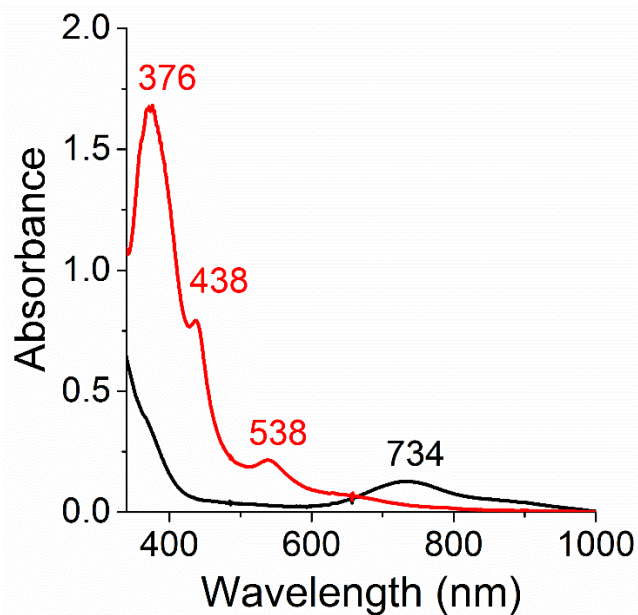


Figure 3.19 UV-vis spectra of 0.32 mM $[(\text{BnTPEN})\text{Fe}^{\text{IV}}(\text{O})](\text{OTf})_2$ (black) and **6** (red) at $-40\text{ }^{\circ}\text{C}$ in CH_3CN .

Resonance Raman experiment was conducted on **6** as well as its ^{18}O labeled isotopomer to obtain vibrational data of the Fe–O–Cr core. Raman spectrum of ^{16}O -labeled **6** exhibits a vibrational peak at 877 cm^{-1} by using a 514.5 nm excitation laser (Figure 3.20), and is shifted to 824 cm^{-1} in ^{18}O -labeled **6**. The wavenumber of 877 cm^{-1} is comparable with $\nu_{\text{as}}(\text{Fe–O–Cr})$ in **5** (886 cm^{-1}), and is also about 100 cm^{-1} bigger than that in **1**, **1-NCS**, **1-NCO**, **2** and **4**.

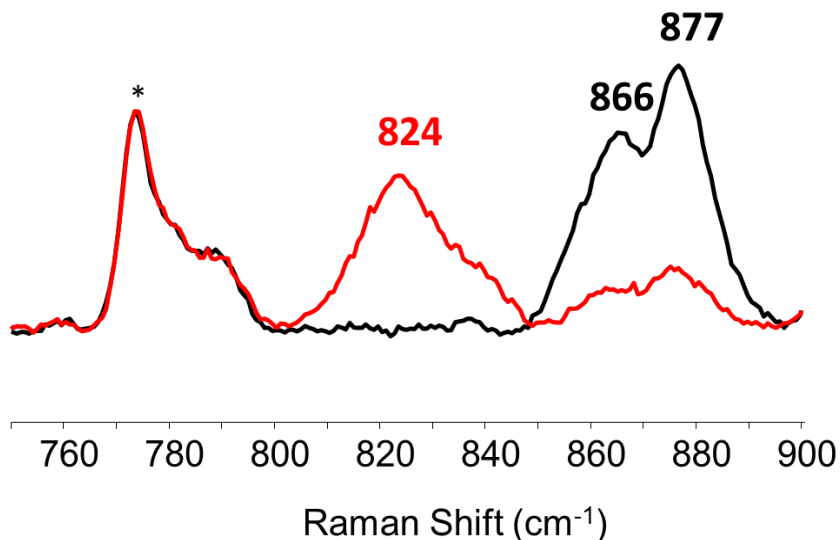


Figure 3.20 Resonance Raman spectra of **6** in CH_3CN ($\lambda_{\text{ex}} = 514.5 \text{ nm}$, 77 K). Black, ^{16}O ; red, ^{18}O . Asterisk denotes solvent peak.

The Fe K-edge XAS data of **5** was collected to clarify its structures. The Fe K-edge is 7124.0 eV, in the range of the K-edge energy for typical Fe(III) oxidation state. **5** exhibits a pre-edge feature at 7114.9 eV fitted by one peak with a total area of 13.8 units (Figure 3.21), comparable with that in **1** (11 units) and **2** (14.8 units), but much lower than that in $(\text{TMC})\text{Fe}^{\text{III}}\text{-O}_{\text{syn}}\text{-Cr}^{\text{III}}(\text{OTf})_4(\text{NCCH}_3)$ (30 units) and $(\text{TMC})\text{Fe}^{\text{III}}\text{-O}_{\text{syn}}\text{-Sc}^{\text{III}}(\text{OTf})_4(\text{NCCH}_3)$ (32 units). The pre-edge area indicates a 6-coordinating Fe center in **5**, and is consistent with the pentadentate N4Py ligand binding.

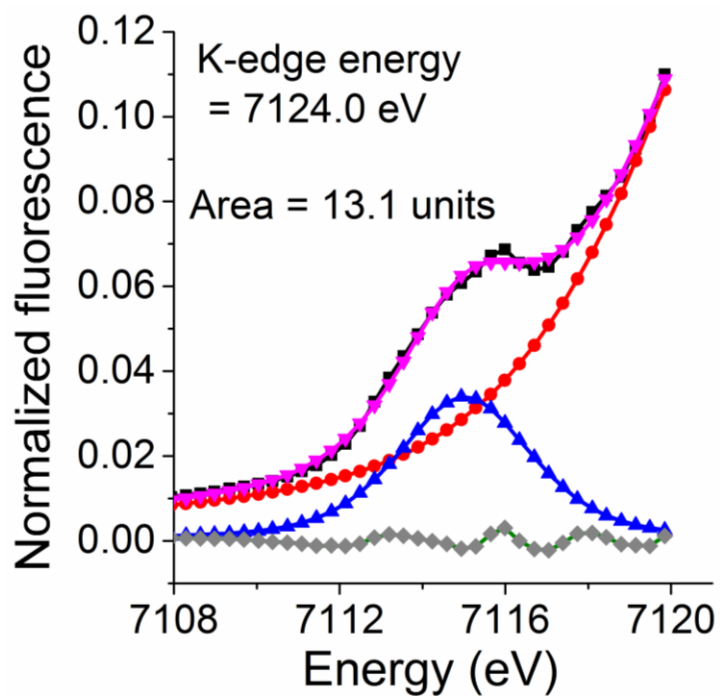


Figure 3.21 Pre-edge region of the Fe K-edge XAS spectrum of **5** (black squares): rising-edge fit (red circles), pre-edge peak (blue triangles pointing up, maximum at 7114.9 eV), pre-edge fit (pink triangles pointing down), residue (grey diamonds).

The best fit of the EXAFS data on **5** showed three single-scattering shells (1 O/N scatterer at 1.78 Å, 5 O/N scatterers at 2.15 Å, 4 O/N scatterers at 3.05 Å), and also a multiple scattering from Cr at 3.56 Å (Figure 3.22). As comparison, the EXAFS fit for **1** showed 1 O/N scatterer at 1.81 Å, 5 O/N scatterers at 2.17 Å, 4 C scatterers at 2.91 Å and a Cr scatterer at 3.65 Å. The EXAFS fit for **2** showed 1 O/N scatterer at 1.84 Å, 5 O/N scatterers at 2.16 Å, 4 C scatterers at 2.91 Å and 1 Cr scatterer at 3.65 Å. Although **5** has a 6-coordinate Fe center as that in **1** and **2**, its Fe···Cr distance is significantly shorter than that in **1** or **2**, and is consistent with the much higher $\nu_{as}(\text{Fe-O-Cr})$ in the former (886 cm⁻¹) than that in the latter two complexes (~770 cm⁻¹).

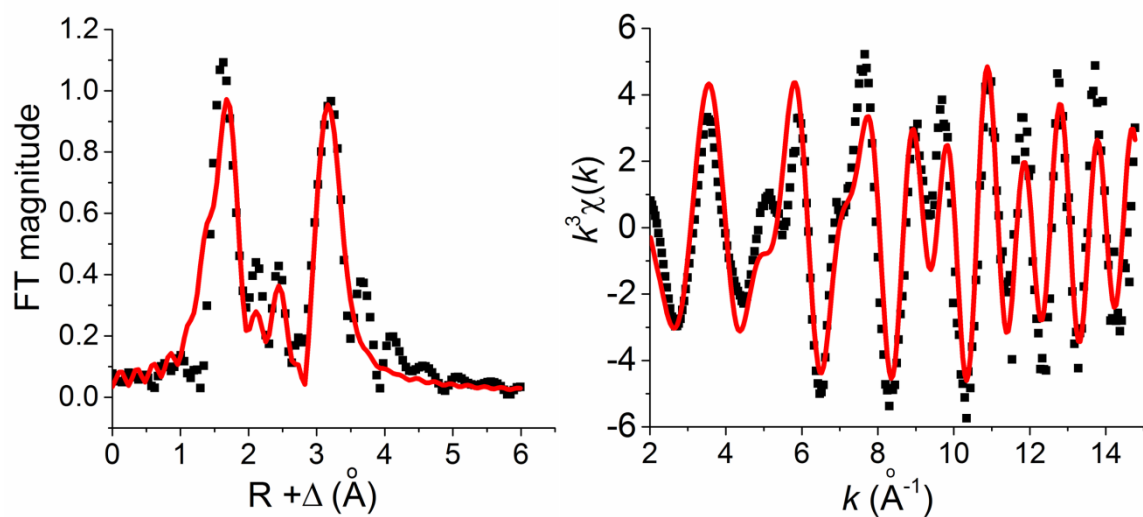


Figure 3.22 Left: unfiltered k-space data of **5** (dotted black line) and its fit (solid red line). Right: Fourier-transformed Fe K-edge EXAFS data for **5** (dotted black line) and corresponding best fit (solid red line, fit #8 in Table 3.4).

Table 3.4 Fit Parameters for **5**, unfiltered from $k = 2 - 15 \text{ \AA}^{-1}$.

Fit	Fe-N			Fe-O			Fe•••C			Fe•••Cr			E ₀	GOF	
	N	R(Å)	$\sigma^2(10^{-3})$		F	F'									
2	4	2.15	4.24										-7.88	1128	799
3	4	2.16	4.11	1	1.79	1.14							-4.70	955	735
4	5	2.15	5.41	1	1.79	1.34							-5.71	931	726
5	5	2.16	5.63	1	1.79	1.35	4	3.10	2.54				-4.18	865	700
7	5	2.14	5.20	1	1.78	1.24	4	2.99	7.95	1	3.61	-1.6	-9.71	283	400
8	5	2.15	5.27	1	1.78	1.25	4	3.05	5.10	1	3.56	-0.6	-5.57	182	321

\ indicates the Fe•••Cr distance obtained from a double scattering pathway

3.4 Conclusion

The proposed structures of Fe–O–Cr complexes **1**, **1-NCS**, **1-NCO**, **2**, **4**, **5**, **6** discussed above are shown in Figure 3.23. Their correlated UV-vis, Raman and XAS spectroscopic properties are organized in Table 3.5.

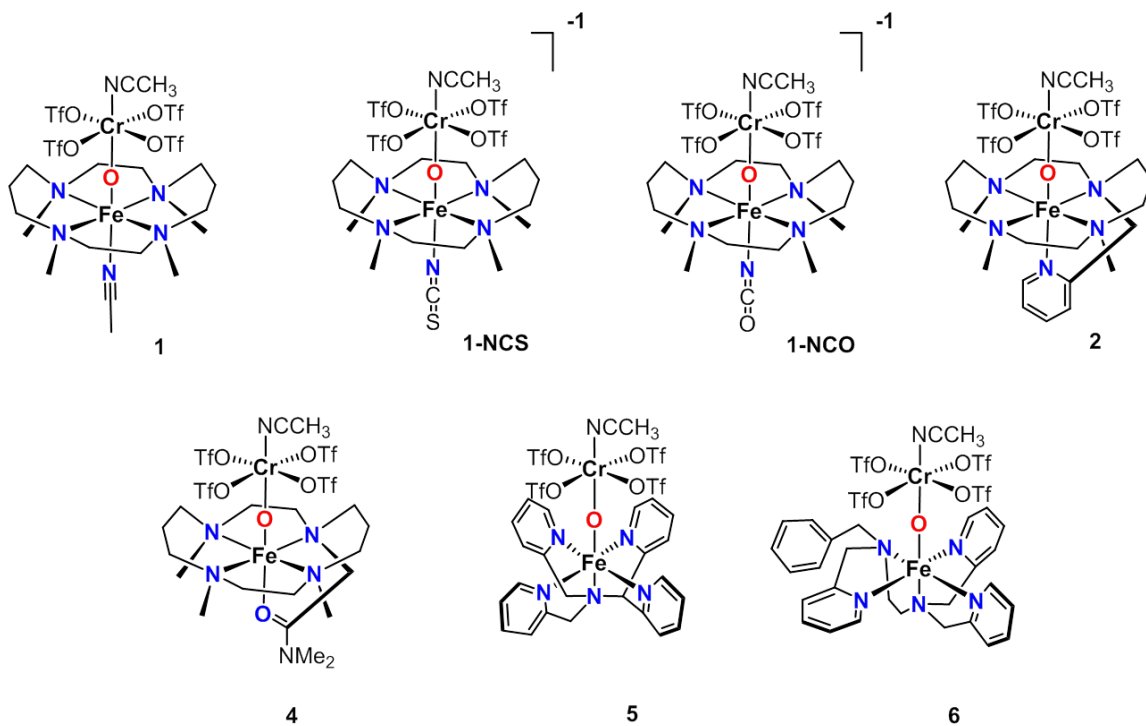


Figure 3.23 Structures of complexes **1**, **1-NCS**, **1-NCO**, **2**, **4**, **5**, **6**.

In the UV-vis spectra, all these Fe^{III}–O–Cr^{III} species possess the three-band characters between 350 nm to 600 nm. The band with the smallest wavelength (370 – 400 nm) has the largest extinction coefficient value (3700 – 6300 M⁻¹ cm⁻¹), the band in the middle (430 – 450 nm) has the modest extinction coefficient value (2000 – 3000 M⁻¹ cm⁻¹), and the band with the highest wavelength (550–570 nm) has the lowest extinction

coefficient value ($500 - 1400 \text{ M}^{-1} \text{ cm}^{-1}$). In the Raman spectra, **1**, **1-NCS**, **NCO**, **2**, **4** all have the $\nu_{\text{as}}(\text{Fe-O-Cr})$ close to 770 cm^{-1} , while **5** and **6** have $\nu_{\text{as}}(\text{Fe-O-Cr})$ close to 870 cm^{-1} . All these species have the 6-coordinate Fe center, so coordination number is not the reason to cause the 100 cm^{-1} difference in $\nu_{\text{as}}(\text{Fe-O-Cr})$, which is against the conclusion in Chapter 2.

The XAS results provide some hints to answer this question. As shown in Table 3.5, for complexes **1**, **1-NCS** and **2**, they all have a $\text{Fe-O}_{\text{bridge}}$ bond longer than 1.80 \AA and $\text{Fe}\cdots\text{Cr}$ distance longer than 3.65 \AA . For complex **5**, it has a $1.78\text{-}\text{\AA}$ $\text{Fe-O}_{\text{bridge}}$ bond and a $3.56\text{-}\text{\AA}$ $\text{Fe}\cdots\text{Cr}$ distance. The apparently shorter $\text{Fe-O}_{\text{bridge}}$ bond and $3.56\text{-}\text{\AA}$ $\text{Fe}\cdots\text{Cr}$ distance in **5** is consistent with the larger $\nu_{\text{as}}(\text{Fe-O-Cr})$ value compared with those in **1**, **1-NCS** and **2**.

Based on the XAS results, the 100 cm^{-1} $\nu_{\text{as}}(\text{Fe-O-Cr})$ difference between **1**, **1-NCS**, **1-NCO**, **2**, **4** with **5**, **6**, which all have 6-coordinate Fe center, is attributed to the ligand binding effect. In **1**, **1-NCS**, **1-NCO**, **2**, **4**, the Fe center is coordinated by four alkyl amines in the equatorial position and one ligand at the axial position. In **5**, the Fe center is coordinated by four pyridines in the equatorial position and one alkyl amine at the axial position. In **6**, the Fe center is coordinated by three pyridines, one alkyl amine in the equatorial position and one alkyl amine in the axial position. Since alkyl amine is a strong Lewis base than pyridine, the stronger electron donation effect from more alkyl amines in **1**, **1-NCS**, **1-NCO**, **2**, **4** counteracts the positive charge of the Fe center in a higher level, thus elongate the Fe-O and $\text{Fe}\cdots\text{Cr}$ distances, also lower the $\nu_{\text{as}}(\text{Fe-O-Cr})$ compared with that in **5** and **6**.

In conclusion, a series of (L)Fe–O–Cr species (**1**, **1-NCS**, **1-NCO**, **2**, **4**, **5**, **6**) supported by different L ligands have been generated by the inner-sphere electron transfer reaction between corresponding oxoiron(IV) complex and Cr(OTf)₂. Their structures are identified by a combination of UV-vis, resonance Raman, and X-ray absorption spectroscopic methods and ESI-MS. All these complexes have 6-coordinate Fe centers, however the $\nu_{\text{as}}(\text{Fe-O-Cr})$ values in **1**, **1-NCS**, **1-NCO**, **2**, **4** are around 100 cm⁻¹ smaller than those in **5** and **6**. In chapter 2 the importance of TMC ligand topology and coordination number of Fe to $\nu_{\text{as}}(\text{Fe-O-Cr})$ have been emphasized. Herein it is suggested that the different Lewis basicity of the supporting ligand maybe the reason that leads to the difference in $\nu_{\text{as}}(\text{Fe-O-Cr})$, as yet confirmed experimentally or theoretically. Future work will be focused on investigating the reactivity properties among the sets of (L)Fe–O–Cr species, especially how does L affects redox potential of the Fe^{III}–O moiety.

Table 3.5 UV-vis ϵ value, Raman shift and XAS results of Fe–O–Cr complexes in Chapter 3.

Complex	UV-vis bands nm (ϵ M⁻¹ cm⁻¹)	Raman/IR shift cm⁻¹ (^{18/16}O shift cm⁻¹)	<i>d</i> (Fe–O_{bridge}) (Å) <i>d</i> (Fe···Cr) (Å)
1	397 (3700), 446 (3000), 558 (720)	773 (-43)	1.81 3.65
1-NCS	390 (7500), 442 (6300), 560 (1400)	800 (-32)	1.85 3.67
1-NCO	380 (6000), 438 (4200), 560 (850)	888 (-49)	N.A.
2	381 (3800), 451 (3200), 558 (920)	760 (-40)	1.84 3.65
4	390 (3900), 440 (3500), 545 (920)	780 (-44)	N.A.
5	362 (5200), 382 (5000), 434 (2600), 520 (640)	886 (-42)	1.78 3.56
6	370 (5200), 438 (2400), 538 (720)	877 (-53)	N.A.

Chapter 4

Characterization and Reactivity Studies of a

Linear Fe–O–Mn Species Obtained from

Inner-Sphere Electron Transfer

4.1 Introduction

Bimetallic cofactor-containing proteins play an important role in O₂ activation in nature. Among them are the enzymes with Fe/Mn active sites, which belong to a metallocofactor paradigm identified recently.¹⁴⁷⁻¹⁴⁹ One example is the small subunit (R2) of class Ic ribonucleotide reductase (RNR), an enzyme which catalyzes the formation of deoxyribonucleotides from ribonucleotides in *Chlamydia trachomatis*.^{63, 65, 66, 68, 99} Its Fe/Mn cofactor is proposed to bind with O₂ to generate a transient Fe^{III}-O-Mn^{IV} species, which initiates the redox cascade in the R1 subunit. The other example is the R2-like ligand-binding oxidase (R2lox), which performs a two-electron oxidation reaction and generates a covalent cross-link between a tyrosine and an abnormally inert valine residue in the protein scaffold, and a μ -hydroxo, bis- μ -carboxylato bridged Fe^{III}Mn^{III} cofactor is found in its resting state.¹⁵⁰⁻¹⁵²

Chemists have long been interested in the Fe/Mn metallocofactors not only for their rich spectroscopic properties, but also for the versatile oxidation states on both atoms, which endow the Fe/Mn core with the capability of performing redox chemistry. Different approaches have been applied to make synthetic Fe/Mn models for decades. For example, the Que group utilized the dinucleating ligand BPMP (BPMP = 2,6-bis[(bis(2-pyridylmethyl)-amino)methyl]-4-methylphenolate) to make Fe^{II}Mn^{II} and Fe^{III}Mn^{II} complexes *via* phenolate oxygen bridging.⁸⁸ Also, the Wieghardt group synthesized the

carboxylate-bridged $(\text{TACN})\text{Fe}^{\text{III}}-\text{O}-\text{Mn}^{\text{III}}(\text{Me}_3\text{TACN})$ complexes (TACN: 1,4,7-triazacyclononane, Me_3TACN : 1,4,7-trimethyl-1,4,7-triazacyclononane) by the hydrolysis of $\text{FeCl}_3(\text{TACN})$ and $\text{MnCl}_3(\text{Me}_3\text{TACN})$ precursors.⁸⁷ Recently, the Nordlander group reported the synthesis and characterization of a mixed-valence complex $[\text{Fe}^{\text{III}}\text{Mn}^{\text{II}}(\text{ICIMP})(\text{OAc})_2\text{Cl}]$ ($\text{H}_2\text{ICIMP} = 2\text{-}(\text{N-carboxylmethyl})\text{-}[\text{N}(\text{N-methylimidazolyl-2-methyl})\text{aminomethyl}]\text{-}[\text{6}(\text{N-isopropylmethyl})\text{-}[\text{N}(\text{N-methylimidazolyl-2-methyl})\text{aminomethyl-4-methylphenol}]$), in which the two pockets of the ligand differ both in terms of the number of donor moieties and their identities, so as to allow for the selective binding of Fe^{III} and Mn^{II} ions.¹⁵³ The structures of these three complexes are shown in Figure 4.1. The correlated synthesis strategies either have difficulties in selectively binding the two metals at specific sites while avoiding mixtures and homodinuclear side products, or require complicated unsymmetrical ligand synthesis. This has inspired me to investigate alternative approaches to synthesize Fe/Mn bimetallic complexes.

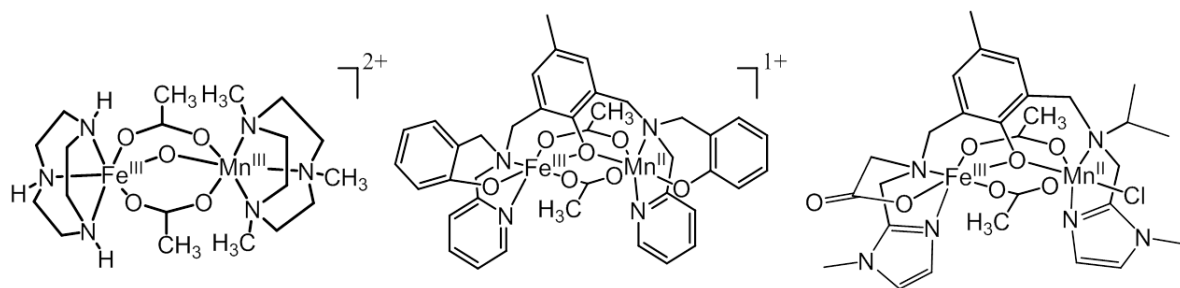


Figure 4.1 (Left) Structure of $[(\text{TACN})\text{Fe}^{\text{III}}-\text{O}-\text{Mn}^{\text{III}}(\text{Me}_3\text{TACN})]^{2+}$.⁸⁷ (Middle) $[\text{Fe}^{\text{III}}\text{Mn}^{\text{II}}\text{BPMP}(\text{O}_2\text{CCH}_2\text{CH}_3)_2]^+$.⁸⁸ (Right) $[\text{Fe}^{\text{III}}\text{Mn}^{\text{II}}(\text{ICIMP})(\text{OAc})_2\text{Cl}]$.¹⁵³

Recently we have reported the synthesis of a pair of (TMC)Fe^{III}-O-Cr^{III} isomers by the inner-sphere electron transfer reaction between [(TMC)Fe^{IV}(O_{anti/syn})](OTf)₂ and Cr^{II}(OTf)₂ (Chapter 2).^{104, 136} The strategy has been then extended to make a series of (L)Fe^{III}-O-Cr^{III} complexes when different oxoiron(IV) species were used (Chapter 3). Herein the reaction between [(N4Py)Fe^{IV}(O)](OTf)₂ (N4Py = N,N-bis(2-pyridylmethyl)-N-bis(2-pyridyl)methylamine) and [Mn^{II}(dpaq)](OTf) (dpaq = 2-[bis(pyridin-2-ylmethyl)]amino-N-quinolin-8-yl-acetamidate) to form a new species **1** with a 1:1 stoichiometric ratio was reported. UV-vis absorption, resonance Raman, EPR, X-ray absorption spectroscopic methods, as well as electrospray mass spectrometry, were utilized to identify **1** with a [(N4Py)Fe^{III}-O-Mn^{III}(dpaq)]³⁺ core. In parallel, the reaction between [(BnTPEN)Fe^{IV}(O)](OTf)₂ (BnTPEN = N-benzyl-N,N',N'-tris(2-pyridylmethyl)-ethylene-diamine) and [Mn^{II}(dpaq)](OTf) was also explored, yielding a complex **2** with a [(BnTPEN)Fe^{III}-O-Mn^{III}(dpaq)]³⁺ core. For reactivity studies, **1** can not only be hydrolyzed by water which leads to the dissociation of the Fe^{III}-O-Mn^{III} core, but also can be reduced by one electron from dcamethylferrocene to generate a metastable species, which is proposed to be [(N4Py)Fe^{II}-O-Mn^{III}(dpaq)]²⁺. The intermediate will consequently decay to generate corresponding (N4Py)Fe(II) and (dpaq)Mn(III) species. The synthesis and characterization of **1** and **2** together with the reactivity study of **1** further broaden the horizon of Fe/Mn synthetic molecules. What's more, the results demonstrate a wider application of the inner-sphere electron transfer reaction to build versatile types of μ -oxo heterobimetallic complexes.

4.2 Experimental details

4.2.1 Materials

All reagents and solvents were purchased from commercial sources and used as received unless specified. The preparations for N4Py ligand,¹⁵⁴ [(N4Py)Fe^{II}(NCCH₃)](OTf)₂,¹⁴⁵ BnTPEN,¹⁴⁵ [(BnTPEN)Fe^{II}(OTf)](OTf),¹⁴⁵ iodosylbenzene (C₆H₅IO),¹⁰⁶ ¹⁸O labeled iodosylbenzene (C₆H₅I¹⁸O)¹⁴³ were carried out following published procedures. The [(N4Py)Fe^{IV}(O)](OTf)₂ and [(BnTPEN)Fe^{IV}(O)](OTf)₂ solution were prepared in a universal procedure as follows: Fe(II) complex in CH₃CN was stirred with 3 eq. solid PhIO at room temperature for 30 min. The turbid liquid was kept at -40 °C for 20 mins and then filtered by the PTFE syringe filter for use. All moisture- and oxygen-sensitive compounds were prepared using standard Schlenk–line techniques.

Synthesis of H-dpaq¹⁵⁵ (i) A solution of 2-chloroacetyl chloride (1.06 g, 9.39 mmol) was dissolved in CH₂Cl₂ (20 ml) and then added dropwise to a cooled stirred solution of 8-aminoquinoline (1.12 g, 7.77 mmol) and Et₃N (0.78 g, 7.7 mmol) in CH₂Cl₂ (20 ml) within 1 h. After being stirred for 2 h at room temperature, the mixture was removed under reduced pressure to obtain a white solid, which was purified by silica gel column chromatography using ethyl acetate and petroleum ether (3:1, v/v) as the eluent to afford the product 2-chloro-N-(quinol-8-yl)-acetamide 1.20 g (yield = 70%). (ii) 2-

chloro-N-(quinol-8-yl)-acetamide (1.18 g, 5.35 mmol), di(picoly)amine (0.88 g, 4.4 mmol), Et₃N (0.47 g, 4.7 mmol), and potassium iodide (30 mg) were dissolved in acetonitrile (40 ml), and the mixture was stirred under reflux for 14 h under a nitrogen atmosphere. The mixture was cooled to room temperature, and the solvent was removed to obtain a yellow oil, which was purified by alumina column chromatography using ethyl acetate as eluent to afford 1.33 g product (yield = 73 %). ¹H NMR (500 MHz, CDCl₃): δ 3.56 (s, 2H), 4.02 (s, 4H), 7.15–7.19 (m, 2H), 7.51–7.55 (m, 3H), 7.66 (d, 2H), 8.00 (d, 2H), 8.21 (d, 1H), 8.54 (d, 2H), 8.77–8.80 (m, 1H), 8.96 (d, 1H), 11.62 (s, 1H). ESI-MS (in CH₃OH): m/z = 384. Predicted: m/z = 384.

Synthesis of [Mn(dpaq)](OTf)¹⁵⁶ H-dpaq (0.270 g, 0.705 mmol) ligand was reacted with Mn(OTf)₂·2CH₃CN (0.306 g, 0.703 mmol) in the presence of KO^tBu (0.079 g, 0.70 mmol) in 7 mL CH₃OH under an inert atmosphere. The orange-colored resultant solution was stirred overnight, then the solvent was evaporated to dryness under vacuum. The solid product was recrystallized using CH₃OH/Et₂O to yield orange-colored crystals of [Mn^{II}(dpaq)](OTf). Crystals were obtained by subsequent recrystallization of the final solid product in the CH₃OH/Et₂O solvent system. [Mn^{II}(dpaq)](OTf) was further characterized by ESI-MS and showed m/z = 437 ([Mn(dpaq)]⁺) and 1123 ([Mn₂(dpaq)₂(OTf)]⁺). Elementary analysis calc. (%): C 49.15, H 3.44, N 11.94; found (%): C 49.01, H 3.49, N 11.83.

4.2.2 Instrumentation

Elemental analysis was carried out by Atlantic Microlab (Norcross, GA). UV-vis absorption spectra were recorded on an HP 8453A diode array spectrometer. Low-temperature visible spectra were obtained using a cryostat from UNISOKU Scientific Instruments, Japan. Electrospray mass spectrometry was performed on a Finnigan LCQ ion trap mass spectrometer. Raman spectra were collected with an Acton AM-506 monochromator equipped with a Princeton LN/CCD data collection system, with 514.5/568.2-nm excitation from a Spectra-Physics model 2060 argon-ion by Cobolt Lasers, Inc. Spectra in acetonitrile were obtained at 77 K using a 135 ° backscattering geometry. The detector was cooled to -120 °C prior to the experiments. Spectral calibration was performed using the Raman spectrum of acetonitrile/toluene 50:50 (v:v). The collected data was processed using Spekwin32 and a multipoint baseline correction was performed for all spectra. X-band EPR spectra were collected on a Bruker Elexsys E-500 spectrometer equipped with an Oxford ESR-910 cryostat. EPR spectral integrations were carried out using a Windows software package (SpinCount v3.1.2).

4.2.3 X-ray absorption spectroscopy (XAS)

Iron K-edge X-ray absorption spectra of complex **1** and **2** were collected on SSRL beam line 7-3 using a 30 element solid state Ge detector (Canberra) with a SPEAR storage ring current of ~500 mA at a power of 3.0 GeV. The incoming X-rays were unfocused using a Si(220) double crystal monochromator, which was detuned by 40% of the maximal flux to attenuate harmonic X-rays. Seven scans were collected from 6882 eV

to 8000 eV at a temperature (10 K) that was controlled by an Oxford Instruments CF1208 continuous flow liquid helium cryostat. An iron foil was placed in the beam pathway prior to I_0 and scanned concomitantly for an energy calibration, with the first inflection point of the edge assigned to 7112.0 eV. A 3 μm Mn filter and a Soller slit were used to increase the signal to noise ratio of the spectra. Photoreduction was monitored by scanning the same spot on the sample twice and comparing the first derivative peaks associated with the edge energy during collection.

The detector channels from the scans were examined, calibrated, averaged, and processed for EXAFS analysis using EXAFSPAK to extract $\chi(k)$. Theoretical phase and amplitude parameters for a given absorber-scatterer pair were calculated using FEFF 8.40¹⁵⁷ and were utilized by the “opt” program of the EXAFSPAK package during curve fitting. Parameters for each species were calculated using a model derived from the crystal structures of $[\text{Fe}^{\text{III}}(\text{OCH}_3)(\text{N4Py})]^{2+}$ ¹⁵⁸ and $[\text{Mn}^{\text{III}}(\text{OH})(\text{dpaq})]^+$.¹⁵⁶ In all analyses, the coordination number of a given shell was a fixed parameter and was varied iteratively in integer steps, while the bond lengths (R) and mean-square deviation (σ^2) were allowed to freely float.

Pre-edge analysis was performed on data normalized in the “process” program of the EXAFSPAK package, and pre-edge features were fit as described elsewhere¹²² between 7108 eV to 7118 eV using the Fityk¹¹³ program with pseudo-Voigt functions composed of 50:50 Gaussian/Lorentzian functions.

4.3. Results and discussion

4.3.1. Generation of [(N4Py)Fe^{III}-O-Mn^{III}(dpaq)]³⁺ (**1**)

At room temperature a 0.3 mM solution of [(N4Py)Fe^{IV}(O)](OTf)₂ was first prepared in acetonitrile. The titration of [Mn^{II}(dpaq)](OTf) into the [(N4Py)Fe^{IV}(O)](OTf)₂ solution at -40 °C resulted in the decay of the 695-nm band characteristic for [(N4Py)Fe^{IV}(O)]²⁺ moiety with concomitant growth of absorption band at 440 nm. An isosbestic point at 620 nm in this transformation indicates a clean conversion to a new species (complex **1**, Figure 4.2).

Further titration experiment demonstrated a 1:1 ratio between Fe and Mn, which is consistent with a 1:1 stoichiometry between [Fe^{IV}(O)(TMC)(NCCH₃)](OTf)₂ and Cr(OTf)₂.^{104, 136} Since in the latter case a (TMC)Fe-O-Cr species was unambiguously identified as the reaction product, it is reasonable to propose that this new species **1** has a similar Fe-O-Mn core.

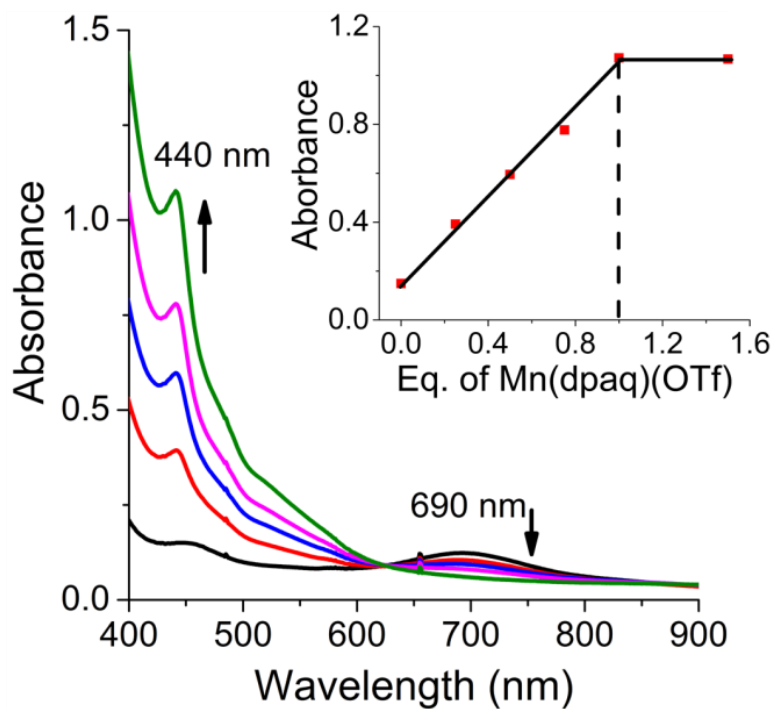


Figure 4.2 UV-vis absorption spectral titration of 0.3 mM $[\text{Fe}^{\text{IV}}(\text{O})(\text{N4Py})(\text{NCCH}_3)]^{2+}$ in CH_3CN at $-40\text{ }^\circ\text{C}$ with $[\text{Mn}^{\text{II}}(\text{dpaq})](\text{OTf})$. Black, 0 eq.; red, 0.25 eq.; blue: 0.5 eq.; magenta, 0.75 eq.; green, 1 eq. (Inset) Absorbance at 440 nm indicating formation of **1** vs eq. $[\text{Mn}^{\text{II}}(\text{dpaq})](\text{OTf})$ added into 0.3 mM $[\text{Fe}^{\text{IV}}(\text{O})(\text{N4Py})(\text{NCCH}_3)](\text{OTf})_2$ in CH_3CN at $-40\text{ }^\circ\text{C}$.

The electrospray ionization mass spectrometry (ESI-MS) experiment of **1** was then explored. In the ESI-MS spectrum a dominant peak at $m/z +1174.0$ was observed, which is assigned as $[(\text{N4Py})\text{FeOMn}(\text{dpaq})(\text{OTf})_2]^+$ based on its mass and isotope distribution pattern, consistent with the μ -oxo heterobimetallic conjecture (Figure 4.3).

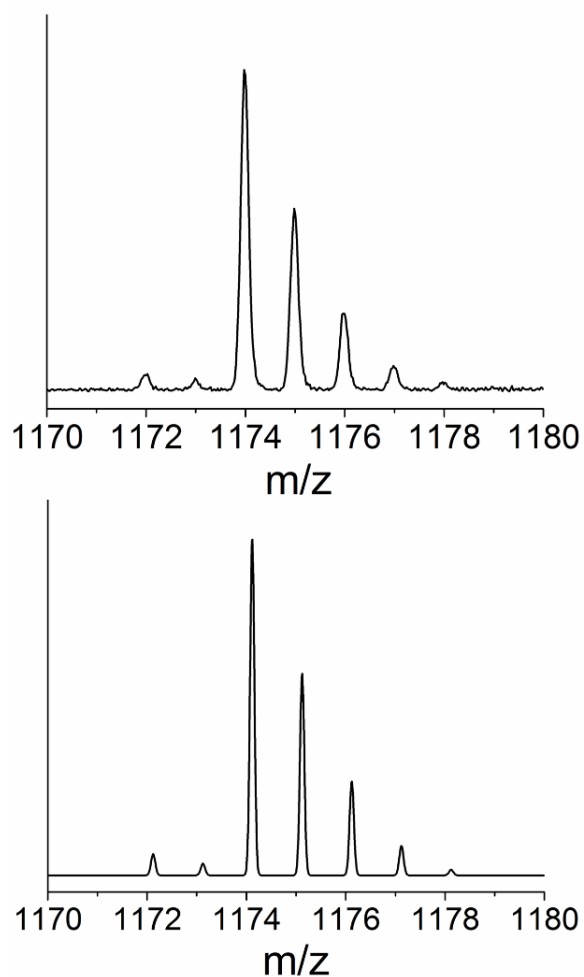


Figure 4.3 (Up) ESI-MS spectrum of $m/z = 1174.0$ peak; (Bottom) Simulated peak based on $[(N4Py)FeOMn(dpaq)(OTf)_2]^+$ formula.

With the idea that **1** contains an Fe–O–Mn core in mind, the control experiment between PhIO and $[Mn^{II}(dpaq)](OTf)$ was conducted. The purpose is to verify that when $[(N4Py)Fe^{IV}(O)](OTf)_2$ reacts with $[Mn^{II}(dpaq)](OTf)$, the reaction is not just a simple oxygen atom transfer (since PhIO is an oxygen atom transfer reagent).

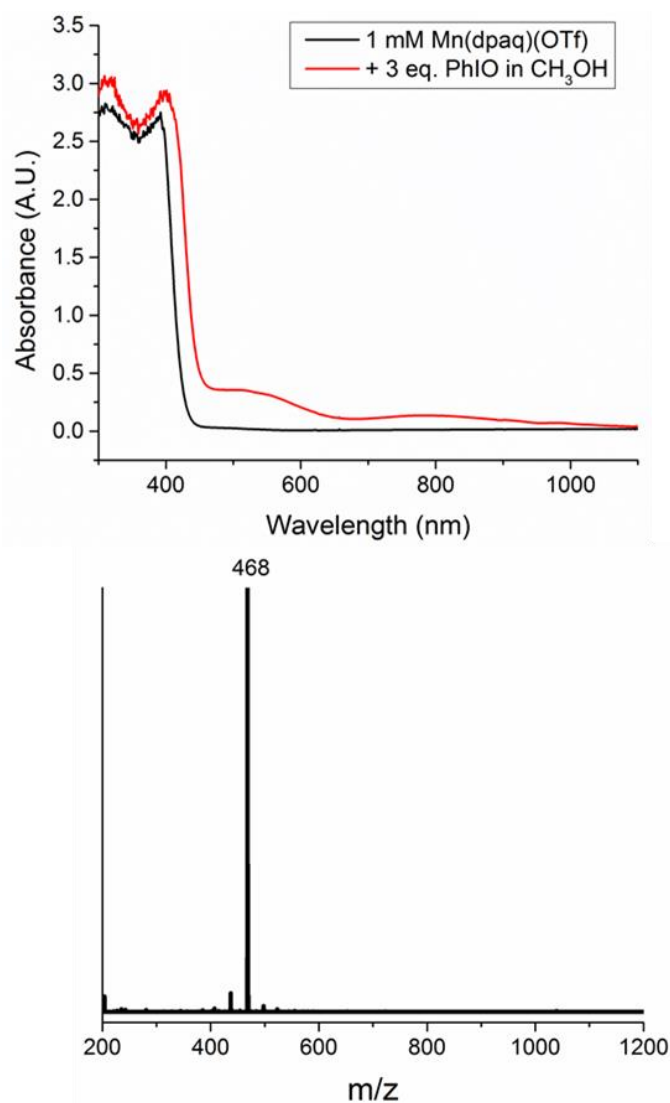


Figure 4.4 (Top) UV-vis spectra of 1 mM $[\text{Mn}^{\text{II}}(\text{dpaq})](\text{OTf})$ in CH_3CN (black) and after the addition of 3 eq. PhIO dissolved in CH_3OH (red) at $-40\text{ }^\circ\text{C}$. (Bottom) ESI-MS spectrum of the reaction between $[\text{Mn}^{\text{II}}(\text{dpaq})](\text{OTf})$ and 3 eq. PhIO dissolved in CH_3OH .

The reaction was monitored by UV-vis spectroscopic method. When 3 eq. of PhIO (dissolved in CH_3OH) was added into 1 mM $[\text{Mn}(\text{dpaq})](\text{OTf})$ solution in CH_3CN

at -40 °C, the growth of bands at 550 nm and 800 nm was observed (Figure 4.4), significantly different compared with the band in **1** ($\lambda_{\text{max}} = 440$ nm, Figure 4.2). This result suggests that unlike PhIO, [(N4Py)Fe^{IV}(O)](OTf)₂ acts more than an oxygen atom transfer reagent towards [Mn^{II}(dpaq)](OTf).

The product from reaction between PhIO and [Mn^{II}(dpaq)](OTf) was injected into ESI-MS spectrometer. Interestingly, A molecular peak at $m/z = 468$ was observed, and is assigned as [Mn(dpaq)(OCH₃)]⁺ based on its mass and isotope pattern (Figure 4.4). It has been reported that PhIO can react with CH₃OH to form PhI(OCH₃)₂,¹⁴³ this result indicates that the PhI(OCH₃)₂ further reacts with [Mn^{II}(dpaq)](OTf) to generate [Mn^{III}(dpaq(OCH₃))]⁺ species.

4.3.2 Resonance Raman Spectrum of **1**

The 0.5 mM frozen sample of **1** was further studied by the Raman spectroscopy to gain insight into its structure. A band at 846 cm⁻¹ was observed upon 514.5-nm laser excitation (Figure 4.5). This assignment is corroborated by the observed downshift of the peak from 846 cm⁻¹ to 805 cm⁻¹ upon substitution of ¹⁸O into the oxo bridge. It is important to note that, although [Fe^{IV}(O)(N4Py)(NCCCH₃)]²⁺ has an Fe^{IV}=O vibrational band at 843 cm⁻¹, this $\nu(\text{Fe}^{\text{IV}}=\text{O})$ peak has not been observed by Raman with the 514.5-nm laser excitation at 0.5 mM concentration. The 846 cm⁻¹ band of **1** falls within the 700 – 900 cm⁻¹ range, typically found for the $\nu_{\text{as}}(\text{Fe}-\text{O}-\text{Fe})$ of nearly linear Fe–O–Fe complexes.¹¹⁶ Also, the 846 cm⁻¹ band of **1** is comparable with $\nu_{\text{as}}(\text{Fe}-\text{O}-\text{Cr})$ in

(N4Py)Fe–O–Cr(OTf)₄(NCCH₃) (870 cm⁻¹, reported in Chapter 3). All these results associate the 846 cm⁻¹ band in **1** with $\nu_{as}(\text{Fe–O–Mn})$.

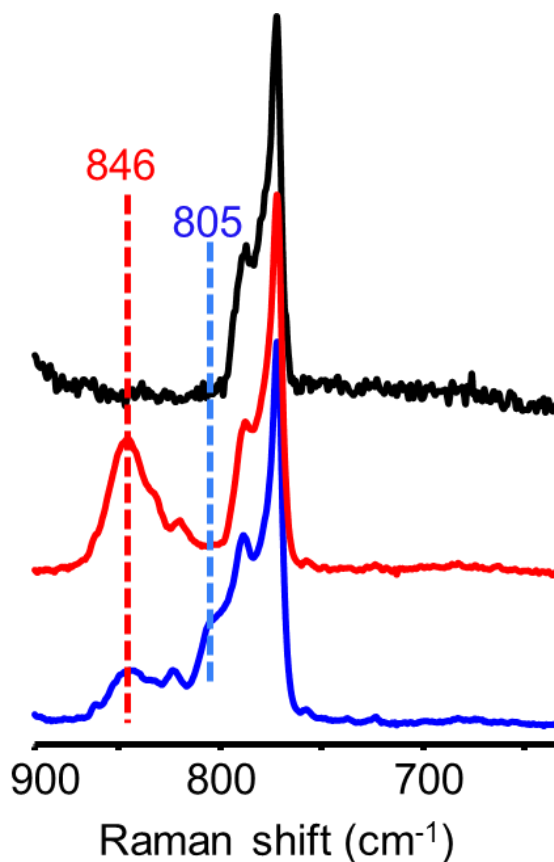


Figure 4.5 Resonance Raman spectra of **1** (0.5 mM) in CH₃CN at λ_{ex} 514.5 nm at 77 K. (Black) CH₃CN. (Red) ¹⁶O-labeled **1**. (Blue) ¹⁸O-labeled **1**.

4.3.3 EPR Spectrum of **1**

The X-band EPR spectrum of 0.5 mM **1** in CH₃CN is shown in Figure 4.6. The $T = 30$ K spectrum exhibits a resonance at $g = 2$, consistent with the antiferromagnetic

coupling between an $S = 5/2$ Fe(III) and an $S = 2$ Mn(III) complex. Integration of the EPR spectrum revealed that the concentration of the signal is 0.48 mM, confirming the $g = 2$ peak does originate from complex **1**. Also, the presence of a 6-line hyperfine pattern ($A = 100$ G) is consistent with the single electron coupling with a Mn nucleus ($I = 5/2$), which is also observed in the the class Ic RNR R2 with an Fe^{III}Mn^{III} core.⁶³ The EPR spectrum of **1** further confirms the structural assignment of an Fe^{III}-O-Mn^{III} core.

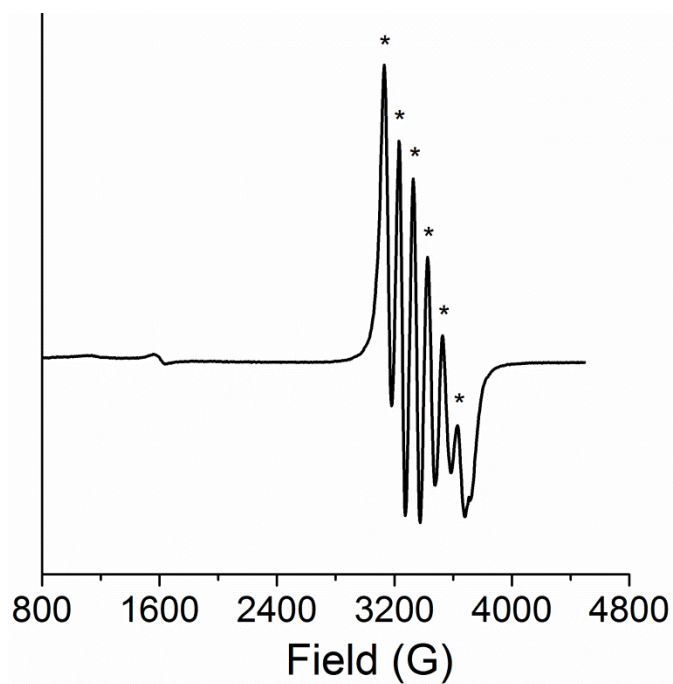


Figure 4.6 X-band EPR spectrum of 0.5 mM **1** in frozen CH₃CN. Conditions: $T = 30$ K; microwave power attenuation: 30 dB. Asterisks indicate hyperfine pattern.

4.3.4 XAS Analysis on **1**

Fe K-edge X-ray absorption spectroscopy (XAS) measurements were conducted in order to obtain more structural information on **1**. The K-edge energy is 7123.7 eV, which is very similar to the K-edge energy (7124.0 eV) found for the previously reported (TMC)Fe^{III}-O-Cr^{III} species¹⁰⁴ and ~1 eV higher in energy (7122.6 eV) than for the Sc bound (TMC)Fe^{III}(O)Sc^{III}(OTf)₄(NCCH₃).¹⁰² The pre-edge analysis shows a peak with a maximum at 7114.0 eV and a calculated area of 12.7 units (Figure 4.7). This value is slightly higher than that found for the six-coordinate Fe^{III}-O-Cr^{III} complex with an area of 11 units. The five-coordinate Fe^{III}-O-Sc^{III} complex had a much higher pre-edge area (32 units), so **1** is more consistent with a six-coordinate Fe^{III} center assignment.

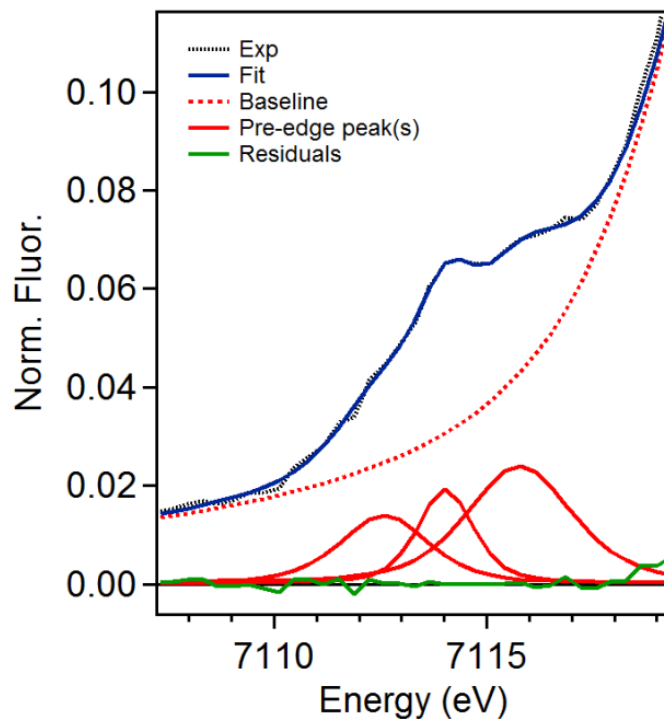


Figure 4.7 Pre-edge region of the Fe K-edge XAS spectrum of **1** (grey line): baseline fit (red dot), pre-edge peaks (red lines), pre-edge fit (blue line), Residuals (green line).

The EXAFS data was collected between $k = 2\text{--}15 \text{ \AA}^{-1}$ ($\Delta R = 0.12 \text{ \AA}$) to provide bonding metrics for complex **1**, and the fitting results are summarized in Figure 4.8 and Table 4.1. The best fit of **1** gives scattering pair distances that correspond to 1 Fe–O/N at 1.80 \AA , 5 Fe–N/O at 2.16 \AA , 5 Fe•••C at 3.06 \AA , and 1 Fe•••Mn at 3.56 \AA , which involves multiple scattering pathways. The 1.80- \AA Fe–O/N distance and 2.16- \AA Fe–O/N distance are assigned to the μ -oxo bridge and the five nitrogen donors of the N4Py ligand, respectively. This assignment is consistent with the Fe^{III}–O–Cr^{III} adduct, which has Fe–N/O distances at 1.81 \AA , 2.17 \AA . The carbon shells are slightly different between these two species, as TMC uses aliphatic carbon atoms in the ligand framework versus pyridine carbons used in N4Py. The Fe^{III}–O–Cr^{III} and **1** also differ in the Fe•••M distances, for which **1** is 0.09 \AA shorter than the Fe^{III}–O–Cr^{III} species (3.65 \AA). Two models were used to accommodate the Fe•••Mn distance in **1**, one that was near linear ($\angle\text{Fe–O–Mn} = \sim 180^\circ$) and one that was bent ($\angle\text{Fe–O–Mn} = 155^\circ$). The best model for **1** was linear which was necessary to fit the Fe•••Mn distance with a mean squared deviation (σ^2) that was positive, whereas the bent model resulted in unreasonable fit parameters. The linear Fe–O–Mn required the inclusion of a double scattering pathway (Fe–O) as well as a triple scattering pathway (Fe–O–Mn). This linear geometry implies that the Fe–O and Mn–O bond lengths cannot be the same, as this would result in a 3.6 \AA distance, similar to the Fe^{III}–O–Cr^{III} species. By deduction from the Fe•••M and Fe–O distances, the Cr–O

distance is 1.84 Å, whereas the Mn–O distance would be 1.76 Å. A Mn–O distance of 1.76 Å is slightly shorter than the Mn^{III}–OH distance of 1.80 Å observed in the crystal structure of [(dpaq)Mn^{III}(OH)]⁺,¹⁵⁶ however, in the (TMC)Fe^{III}–O–Sc adduct the Fe–O distance was found to be 1.74 Å by EXAFS analysis (with an Fe•••Sc distance of 3.69Å).¹⁰²

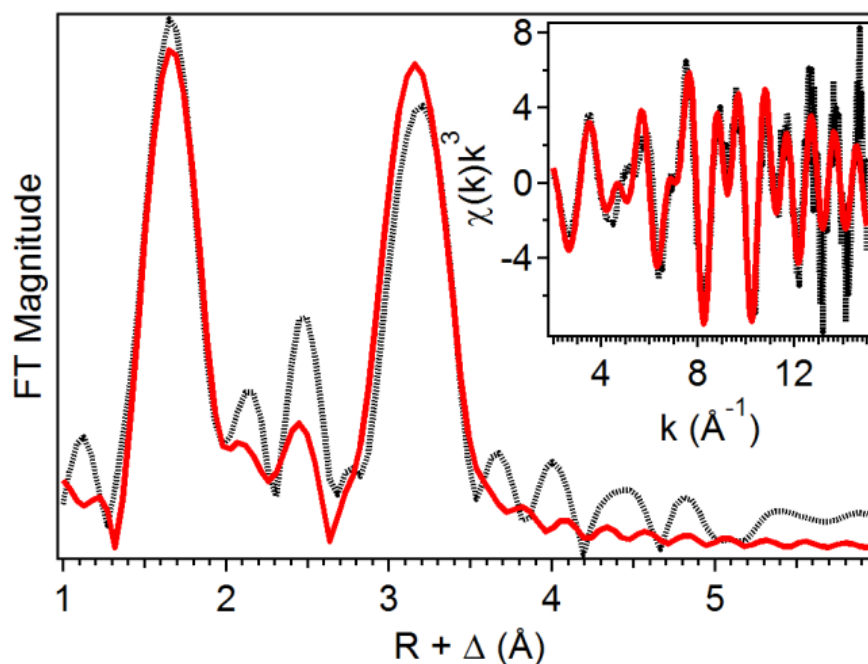


Figure 4.8 Fourier-transformed Fe K-edge EXAFS data for **1** (black) and the corresponding best fit (red, fit #15 in Table 4.1). (Inset) unfiltered k -space data (black) and its fit (red).

Table 4.1 Fit Parameters for **1** unfiltered from $k = 2 - 15 \text{ \AA}^{-1}$.

Fit	Fe–N			Fe–O			Fe••C			Fe••Mn			GOF		
	N	R(Å)	$\sigma^2(10^{-3})$	N	R(Å)	$\sigma^2(10^{-3})$	N	R(Å)	$\sigma^2(10^{-3})$	N	R(Å)	$\sigma^2(10^{-3})$	E_o	F	F'
1	6	2.14	5.26										-5.15	1541	817
2	5	2.14	4.23										-5.21	1513	809
3	4	2.14	3.20										-5.14	1516	810
4	3	2.14	2.05										-5.69	1561	822
5	5	2.15	4.42	1	1.80	2.03							-2.41	1334	760
6	5	2.13	4.15	2	1.80	6.90							-4.86	1378	772
7	4	2.13	3.11	2	1.79	7.70							-5.43	1445	791
8	5	2.17	4.59	1	1.81	1.83	5	3.15	0.54				2.04	1327	758
9	5	2.15	4.48	1	1.80	2.08	5	3.01	9.30				-2.19	1275	742
10	5	2.13	4.28	1	1.79	2.41	5	2.96	7.54	1	3.61	-1.70	-7.91	597	508
11	5	2.15	4.18	1	1.80	2.41	5	2.96	-1.00	1	3.64	-1.20	-2.92	498	464

12	5	2.14	4.28	1	1.80	2.17	7	2.95	1.27	1	3.63	-1.20	-3.52	630	522
							8	3.11	1.47						
13	5	2.15	4.20	1	1.80	2.25	7	2.97	0.98	1	3.59	2.70	-1.88	554	490
							8	3.12	1.17	2	\3.59	\2.70			
14	5	2.15	4.47	1	1.80	1.92	5	3.01	8.41	1	3.58	2.09	-2.33	629	521
										2	\3.58	\2.09			
15	5	2.16	4.56	1	1.80	1.75	5	3.06	8.99	1	3.56	1.90	-0.11	585	503
										2	\3.56	\1.90			
										1	\ 3.56	\ 1.90			
16	5	2.17	4.70	1	1.81	1.59	7	3.16	2.64	1	3.51	3.23	3.53	877	616
										2	\ 3.51	\ 3.23			

\ = double scattering pathway, \| = triple scattering pathway

4.3.5 Generation of $[(\text{BnTPEN})\text{Fe}^{\text{III}}-\text{O}-\text{Mn}^{\text{III}}(\text{dpaq})]^{3+}$ (**2**)

In parallel with the generation of **1**, the reaction between $[(\text{BnTPEN})\text{Fe}^{\text{IV}}(\text{O})](\text{OTf})_2$ and $[\text{Mn}^{\text{II}}(\text{dpaq})](\text{OTf})$ was explored. Addition of $[\text{Mn}^{\text{II}}(\text{dpaq})](\text{OTf})$ into $[(\text{BnTPEN})\text{Fe}^{\text{IV}}(\text{O})](\text{OTf})_2$ solution at $-40\text{ }^\circ\text{C}$ resulted in the decay of the 740-nm band characteristic for $[(\text{BnTPEN})\text{Fe}^{\text{IV}}(\text{O})]^{2+}$ moiety, with concomitant growth of absorption band at 446 nm, indicating the formation of a new species (complex **2**, Figure 4.9). The 446-nm band is close to the 440-nm band in **1**, indicating the similar electronic structures in both complexes.

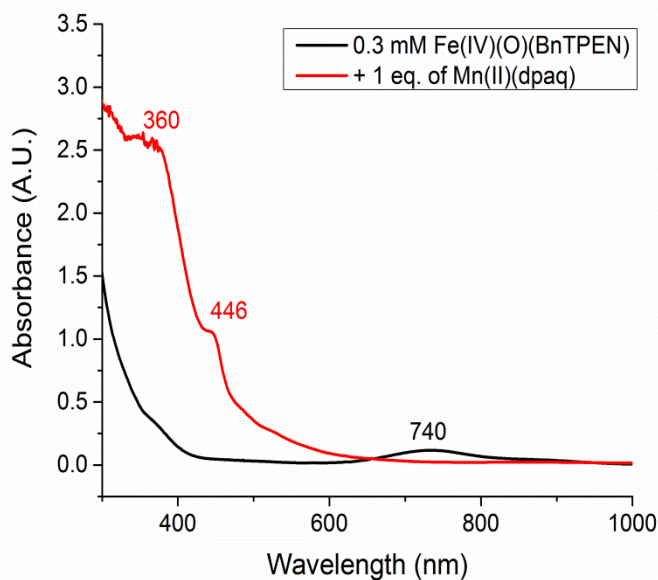


Figure 4.9 UV-vis absorption spectra of 0.3 mM $[\text{Fe}^{\text{IV}}(\text{O})(\text{BnTPEN})(\text{NCCH}_3)](\text{OTf})_2$ in CH_3CN at $-40\text{ }^\circ\text{C}$ (black) with 1 eq. of $[\text{Mn}^{\text{II}}(\text{dpaq})](\text{OTf})$ (red).

To test whether **2** also contains an Fe–O–Mn core, an aliquot of **2** solution in CH₃CN was injected into electrospray ionization mass spectrometer, and a dominant peak at m/z +1230.0 was observed, which is assigned as [(BnTEPN)FeO[Mn(dpaq)](OTf)₂]⁺ based on its mass and isotope distribution pattern (Figure 4.10). This further confirmed that similar as **1**, **2** also possesses a Fe–O–Mn motif.

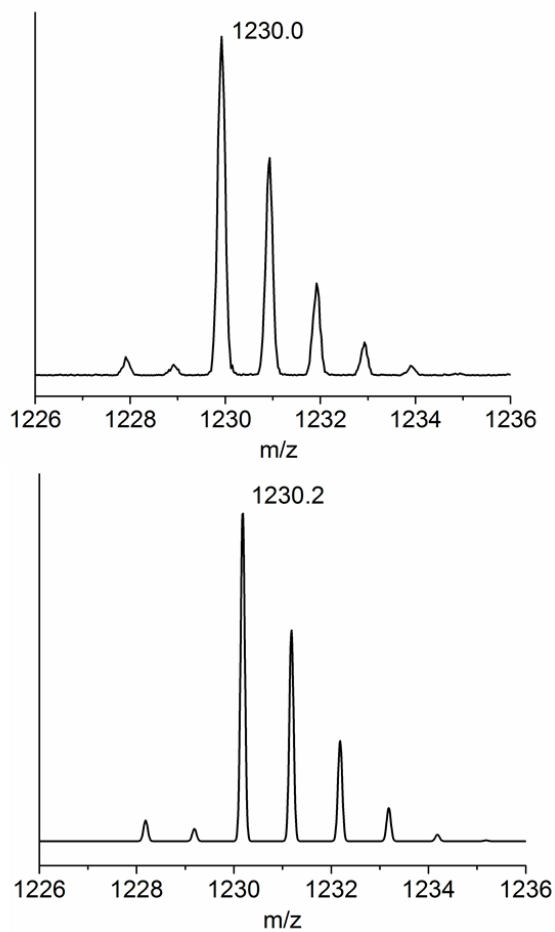


Figure 4.10 (Up) ESI-MS spectra of m/z = 1123.0 peak; (Bottom) Simulated peak of m/z = 1230.2 based on [(BnTPEN)FeOMn(dpaq)](OTf)₂⁺ formula.

The X-band EPR spectrum of 0.5 mM **2** in CH₃CN is shown in Figure 4.11. The $T = 30$ K spectrum exhibits a resonance at $g = 2$, consistent with the antiferromagnetically coupling between the $S = 5/2$ Fe(III) and the $S = 2$ Mn(III), giving a system $S = 1/2$ ground state. Also, the presence of a 6-line hyperfine pattern ($A = 100$ G) can be rationalized by the single electron coupling with a Mn nucleus ($I = 5/2$), and is consistent with what is observed in the EPR spectrum of **1**. The results from UV-vis, ESI-MS and EPR further confirm that complex **2** is also with an Fe^{III}-O-Mn^{III} core as **1**.

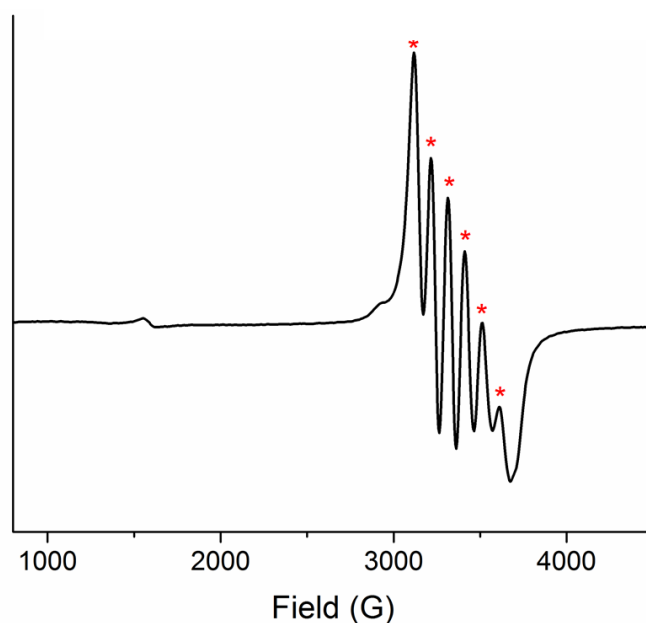


Figure 4.11 X-band EPR spectrum of 0.5 mM **2** in frozen CH₃CN. Conditions: $T = 30$ K; microwave power attenuation: 30 dB. Asterisks indicate hyperfine pattern.

4.3.6 XAS Analysis on **2**

Fe K-edge XAS measurements on **2** was also conducted. The K-edge energy is 7124.0 eV, which is very similar to the K-edge energy (7123.7 eV) found for complex **1**. The pre-edge analysis (Figure 4.12) shows a peak with a maximum at 7115.1 eV and a calculated area of 11.1 units. This value is also close to that in **1** (12.7 units), suggesting the great structural similarities between the two complexes.

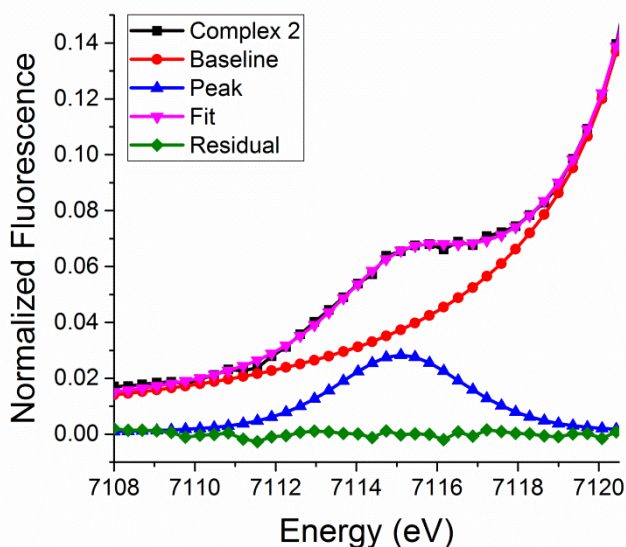


Figure 4.12 Pre-edge region of the Fe K-edge XAS spectrum of **2** (black): baseline fit (red), pre-edge peak (blue), pre-edge fit (magenta), Residual (green).

The EXAFS data was collected between $k = 2\text{--}15 \text{ \AA}^{-1}$ ($\Delta R = 0.12 \text{ \AA}$) to provide bonding metrics for complex **2**, and the fitting results are summarized in Figure 4.13 and Table 4.2. The best fit of **2** gives scattering pair distances that correspond to 1 Fe–O/N at 1.80 \AA , 5 Fe–N/O at 2.16 \AA , 7 Fe•••C at 3.04 \AA , and 1 Fe•••Mn at 3.58 \AA with double

scattering pathway. The 1.80-Å Fe–O/N distance and 2.16-Å Fe–N/O distance are assigned to the μ -oxo bridge and the nitrogen donors of the BnTPEN ligand respectively. This assignment is very close with that in complex **1**, which has 1 Fe–O/N distance at 1.80 Å and 5 Fe–N/O at 2.16 Å. The Fe•••Mn distance differs a little in **1** and **2**, in which the former is 0.2 Å shorter (3.56 Å) than that in the later (3.58 Å). The strong double scattering pathway in the best fit for **2** implies a linear Fe–O–Mn core as that in **1**. Deducted from the Fe•••M and Fe–O distances, the Mn–O distance in **2** is 1.78 Å, also comparable with the Mn^{III}–OH distance of 1.80 Å in the crystal structure of [(dpaq)Mn^{III}(OH)]⁺.¹⁵⁶ In conclusion, the EXAFS derived model of **2** agrees well with EXAFS model of **1**, suggesting high structural similarity between them.

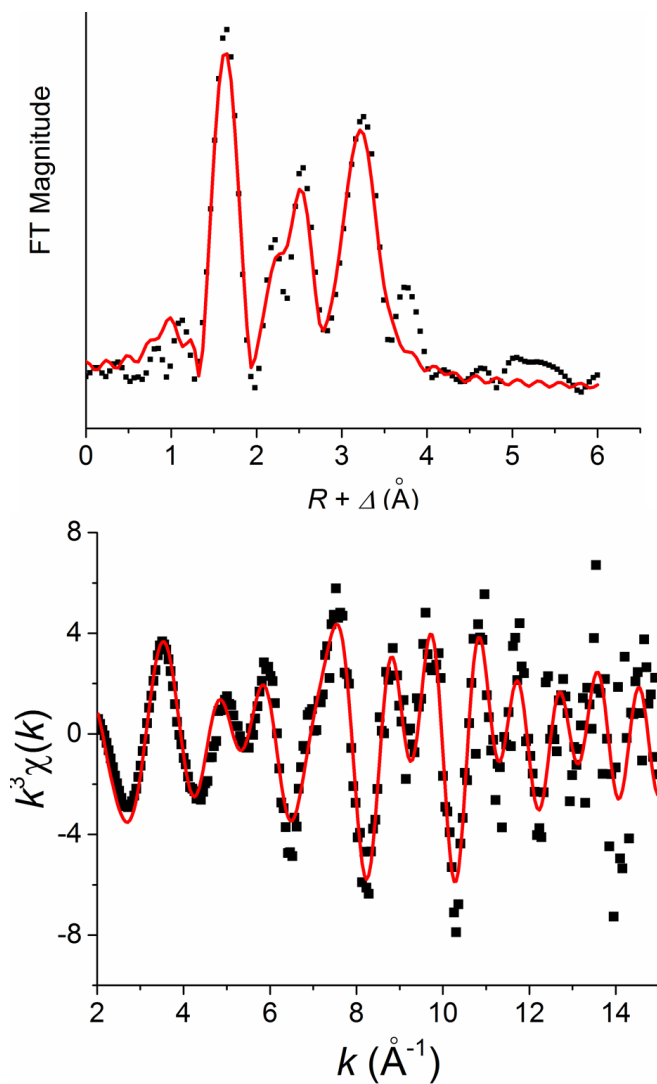


Figure 4.13 (Top) Fourier-transformed Fe K-edge EXAFS data for **2** (black) and the corresponding best fit (red, fit #9 in Table 4.2). (Bottom) unfiltered k -space data (black) and fit (red).

Table 4.2 Fit Parameters for **2** unfiltered from $k = 2 - 15 \text{ \AA}^{-1}$.

Fit	Fe–N/O			Fe–O/N			Fe•••C			Fe•••Mn			E_o	GOF	
	N	R(Å)	$\sigma^2(10^{-3})$	N	R(Å)	$\sigma^2(10^{-3})$	N	R(Å)	$\sigma^2(10^{-3})$	N	R(Å)	$\sigma^2(10^{-3})$		F	F'
1	5	2.15	6.24										-9.67	1296	846
2	6	2.15	7.57										-9.39	1312	851
3	4	2.14	4.76										-11.33	1301	847
4	5	2.14	6.26	1	1.80	2.01							-9.07	1138	792
5	5	2.12	5.47	2	1.79	7.11							-13.21	1178	806
6	5	2.15	6.80	1	1.80	1.82	6	3.03	4.38				-7.11	968	731
7	5	2.15	6.83	1	1.80	1.83	7	3.03	5.15				-7.05	966	730
8	5	2.14	6.79	1	1.80	1.59	7	3.03	4.02	1	3.64	-0.80	-8.19	482	516
9	5	2.16	7.01	1	1.80	1.57	7	3.04	3.80	\1	\3.58	\0.22	-5.76	446	496

\ indicates double scattering pathway

4.3.7 Reactivity of Complex 1

With detailed characterization of **1**, its reactivity property was then explored. **1** is stable even at room temperature, but quite accidentally, it is found that the addition of water will induce **1** to decay. As shown in Figure 4.14, when 50 μL H_2O was added into 1.5 mL 0.4 mM **1** at 25 $^\circ\text{C}$, it decayed in 20 mins.

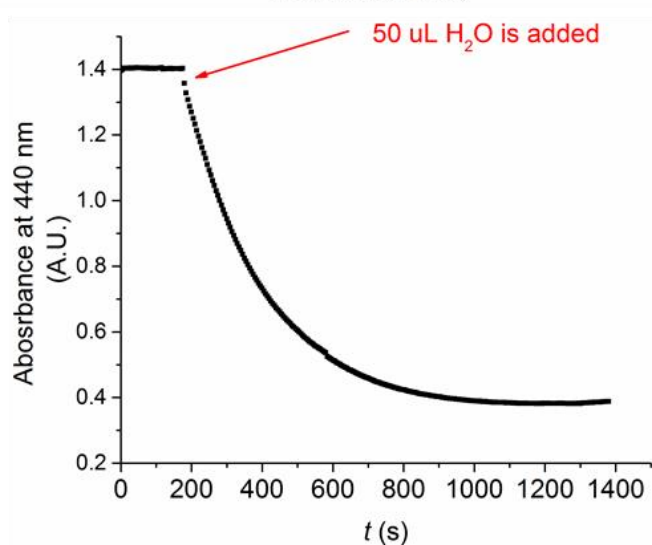
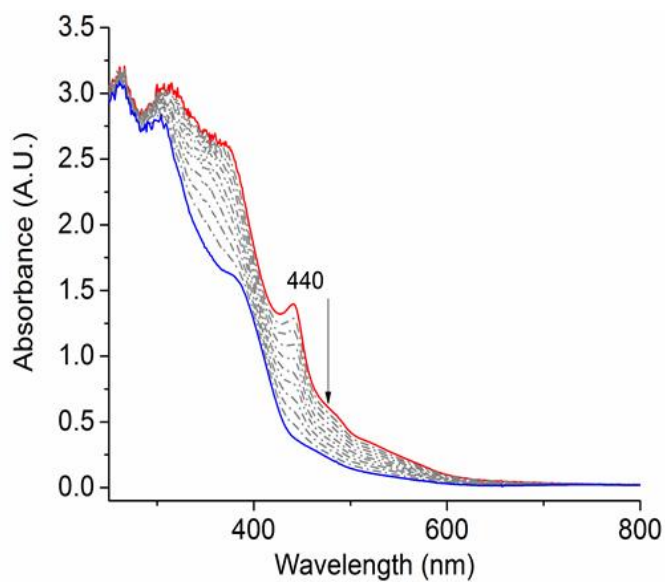


Figure 4.14 (Top) In 1.5 mL 0.4 mM **1** in CH₃CN at 25 °C (red), 50 uL H₂O was added (blue). (Bottom) UV-vis absorption change of the 440-nm peak.

To identify the product, an aliquot of the reaction solution between **1** and water was injected into ESI-MS spectrometer. With the disappearance of the molecular peak at $m/z = 1174.0$ ($[(N4Py)FeOMn(dpaq)(OTf)_2]^+$), two new peaks, $m/z = 454.1$ and $m/z = 589.0$, were observed and assigned as $[(dpaq)Mn(OH)]^+$ and $[(N4Py)Fe(OH)(OTf)]^+$ respectively. The oxidation states of Mn and Fe are proposed to be +3 and +3 based on the total charge of the two ions. This result indicates that a non-redox hydrolysis happens as shown in Figure 4.15.

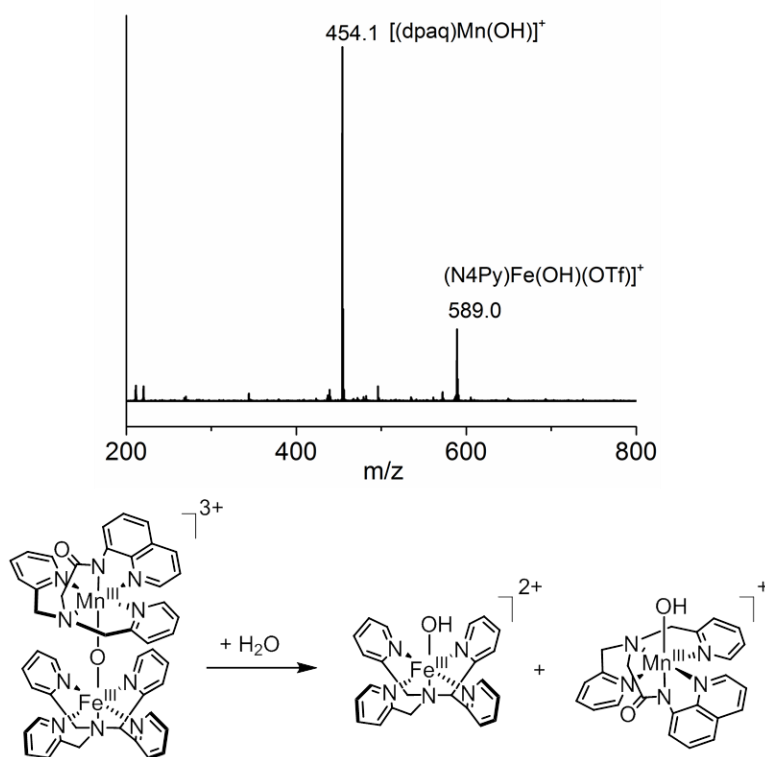


Figure 4.15 (Top) ESI-MS results on **1** +H₂O. (bottom) Proposed hydrolysis reaction between **1** and H₂O.

Furthermore, the redox reaction of **1** was explored. Different oxidant, including cerium ammonium nitrate, WCl₆ and H₂O₂, were tried to oxidize **1**. No changes in neither UV-vis nor EPR spectra were detected, indicating no reaction happens. However, **1** can be reduced by decamethylferrocene, a one-electron reducing reagent, and the newly formed species with an absorption maxima at 560 nm was observed (Figure 4.16). Titration revealed the stoichiometry between **1** and decamethylferrocene is 1:1, suggesting that it is a one-electron transfer reaction. The 560-nm intermediate was meta-stable at -40 °C, and can decay to generate a new species with a 458-nm absorption band, which is characteristic of [Fe^{II}(N₄Py)(NCCH₃)]²⁺ (Figure 4.16). To support the observation, in ESI-MS spectra the formation of [Fe(N₄Py)(OTf)]⁺ and [Mn^{III}(dpaq)(OTf)]⁺ were also detected in the decay product of 560-nm intermediate. Based on these information, the meta-stable species is proposed as an Fe^{II}-O-Mn^{III} complex, after **1** being reduced by the decamethylferrocene.

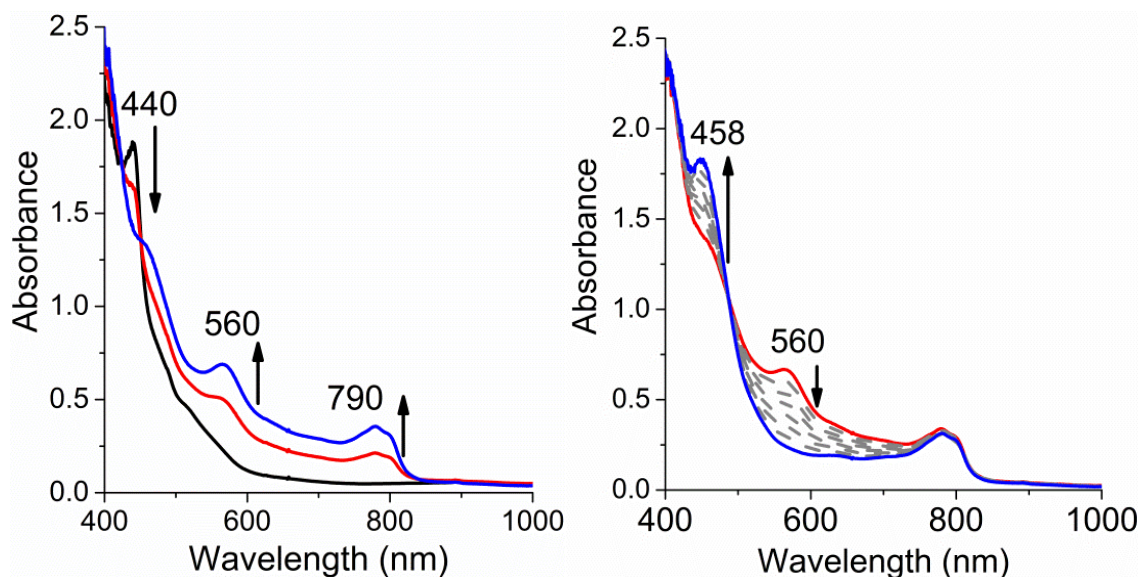


Figure 4.16 (Left) Titration of decamethylferrocene (Fc^*) into **1** at $-40\text{ }^\circ\text{C}$ in CH_3CN . Black: 0.5 mM **1**; Red: **1** + 0.5 eq. Fc^* ; Blue: **1** + 1.0 eq. Fc^* . (Right) decay of 560 nm species.

The resonance Raman experiment was sequentially conducted on the frozen solution of 560-nm intermediate by using the 568.2-nm laser. If it contains an $\text{Fe}^{\text{II}}\text{-O-Mn}^{\text{III}}$ core, its $\nu_{\text{as}}(\text{Fe}^{\text{II}}\text{-O-Mn}^{\text{III}})$ value should be smaller than in **1**, which has $\nu_{\text{as}}(\text{Fe}^{\text{III}}\text{-O-Mn}^{\text{III}}) = 846\text{ cm}^{-1}$. The spectra are shown in Figure 4.17.

The 560-nm intermediate showed three peaks in the Raman spectrum: 780 cm^{-1} , 749 cm^{-1} and 730 cm^{-1} , which are all lower than the 846 cm^{-1} in **1**. To test whether one or more of these bands belong to the $\text{Fe}^{\text{II}}\text{-O-Mn}^{\text{III}}$ species, its ^{18}O labeled isotopomer was prepared. No shift in the Raman spectra was observed, meaning all these three bands are not ^{18}O sensitive. However, in the Raman spectrum of the decayed species of the 560-nm

intermediate, the three bands, (780 cm^{-1} , 749 cm^{-1} and 730 cm^{-1}) have all disappeared. It can be thus concluded that these three vibrations are associated with the 560-nm intermediate, but they are not correlated with the Fe–O–Mn vibration, due to the lack of ^{18}O labeling shift.

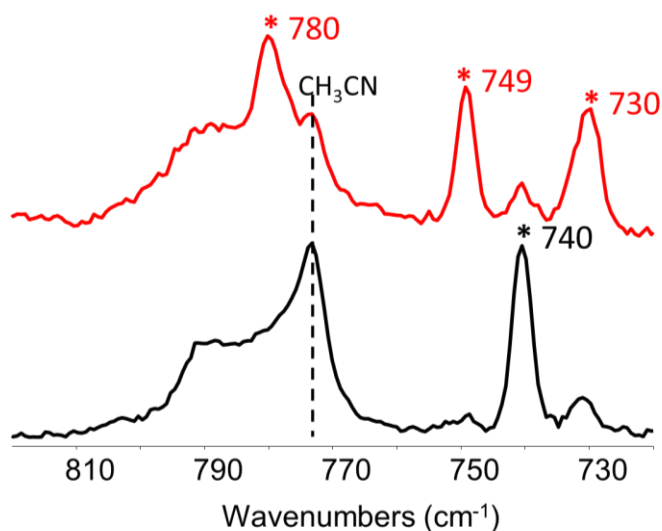


Figure 4.17 (Red) 560-nm intermediate. (Black) decay of 560-nm intermediate $\lambda_{\text{ex}} = 568.2\text{ nm}$, 20 mW, 77 K.

4.4 Conclusion

In this chapter, I have expanded the application of inner-sphere electron transfer reaction to make two Fe–O–Mn complexes, **1** and **2**. Unlike $\text{Cr}(\text{OTf})_2$ used in the previous two chapters, manganese salts generally have higher oxidation potentials, thus proper oxoiron(IV) and Mn(II) species have to be chosen. Herein $[(\text{N4Py})\text{Fe}^{\text{IV}}(\text{O})](\text{OTf})_2$ and $[(\text{BnTPEN})\text{Fe}^{\text{IV}}(\text{O})](\text{OTf})_2$ are able to oxidize $[\text{Mn}^{\text{II}}(\text{dpaq})](\text{OTf})$, while

$[(\text{TMC})\text{Fe}^{\text{IV}}(\text{O})](\text{OTf})_2$ is not, indicating its oxidation potential is not high enough. Also, $[\text{Mn}^{\text{II}}(\text{dpaq})](\text{OTf})$ is chosen because it can be oxidized by O_2 to generate a stable $[\text{Mn}^{\text{III}}(\text{dpaq})(\text{OH})](\text{OTf})$ complex, reflecting its relatively strong reducing capabilities.¹⁵⁶

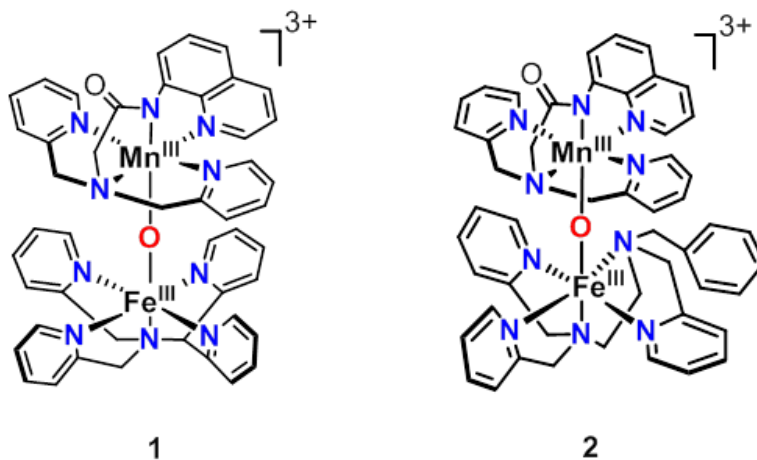


Figure 4.18 Proposed structures of **1** and **2**.

The proposed structures of **1** and **2** are shown in Figure 4.18. With detailed characterization results from UV-vis absorption, resonance Raman, EPR, X-ray absorption spectroscopic methods, as well as electrospray mass spectrometry, **1** and **2** present great similarities in their structures. The water hydrolysis reaction of complex **1** including the disassociation of $\text{Fe}^{\text{III}}\text{-O-Mn}^{\text{III}}$ core to $\text{Fe}^{\text{III}}\text{-OH}$ and $\text{Mn}^{\text{III}}\text{-OH}$ species is reported. The reduction of **1** by decamethylferrocene was found to generate a metastable intermediate with a 560-nm UV-vis band, and is proposed to have an $\text{Fe}^{\text{II}}\text{-O-Mn}^{\text{III}}$ core. However, I could not generate the one electron oxidized species *i.e.*, $\text{Fe}^{\text{III}}/\text{Mn}^{\text{IV}}$, which is proposed as the active intermediate in class 1c RNR. The Fe-O-Mn cores in both **1** and **2**

are in linear motif, both Fe and Mn ions are coordinately saturated. This makes it impossible for the addition of other bridging ligands in between the two metal centers, such as carboxylate or peroxo unit. However, the success of synthesizing and characterizing **1** and **2** definitely demonstrates a wider application of inner-sphere electron transfer reaction to make biomimetic μ -oxo heterobimetallic species.

Chapter 5

From Linear to Nonlinear: A Synthetic Model for

Class Ic Ribonucleotide Reductase

5.1 Introduction

In Chapter 4 the synthesis and characterization of two $\text{Fe}^{\text{III}}\text{-O-Mn}^{\text{III}}$ species: $[(\text{N4Py})\text{Fe-O-Mn}(\text{dpaq})]^{3+}$ and $[(\text{BnTPEN})\text{Fe-O-Mn}(\text{dpaq})]^{3+}$, have been discussed. Both complexes were prepared from the inner-sphere electron transfer reaction between the correlated oxoiron (IV) species and $[\text{Mn}^{\text{II}}(\text{dpaq})](\text{OTf})$, illustrating a wider application of this strategy in making the μ -oxo heterobimetallic molecules. However, compared with the Fe/Mn species in the class 1c RNR, there are two significant structural differences in the synthetic analogues.

Firstly, the resting state of class 1c RNR contains a μ -oxo/ μ -aqua/ μ -carboxylato $\text{Fe}^{\text{III}}/\text{Mn}^{\text{III}}$ core based on the XRD results,^{62, 147, 149, 159} while in the active $\text{Fe}^{\text{III}}/\text{Mn}^{\text{IV}}$ complex a μ -oxo/ μ -hydroxo/ μ -carboxylato Fe/Mn core is proposed,⁶⁸ and in its precursor an $\text{Fe}^{\text{IV}}/\text{Mn}^{\text{IV}}$ intermediate with a bis- μ -oxo/ μ -carboxylato Fe/Mn core is proposed.⁶⁹ In contrast, in both $[(\text{N4Py})\text{Fe-O-Mn}(\text{dpaq})]^{3+}$ and $[(\text{BnTPEN})\text{Fe-O-Mn}(\text{dpaq})]^{3+}$, the μ -oxo is the only bridging ligand, due to the lack of coordination sites on both metal centers. Secondly, in nature the $\text{Fe}^{\text{III}}/\text{Mn}^{\text{III}}$ complexes in class 1c RNR has an $\text{Fe}\cdots\text{Mn}$ distance of 3.3 Å based on XRD results,⁶² while the $\text{Fe}^{\text{III}}/\text{Mn}^{\text{IV}}$ and $\text{Fe}^{\text{IV}}/\text{Mn}^{\text{IV}}$ intermediates are proposed with $d(\text{Fe}\cdots\text{Mn})$ of 2.92 Å and 2.75 Å respectively based on EXAFS analysis.⁶⁸ ⁶⁹ In comparison, the $\text{Fe}\cdots\text{Mn}$ distances in $[(\text{N4Py})\text{Fe-O-Mn}(\text{dpaq})]^{3+}$ and $[(\text{BnTPEN})\text{Fe-O-Mn}(\text{dpaq})]^{3+}$ are close to 3.6 Å based on EXAFS analysis, indicating a linear Fe-O-Mn motif in both complexes. Based on the strategy of constructing μ -oxo heterobimetallic species discussed in the previous chapters, can we apply this method to make better Fe/Mn synthetic complexes, which can overcome these two shortfalls?

To fulfill this goal, neither oxoiron(IV) complex nor Mn(II) species can be supported by the pentadentate ligands. Instead, tetradentate ligands are preferred to coordinating with each metal atom to provide two extra binding positions. Also, in order to make the Fe–O–Mn core non-linear, these two binding sites should be able to be linked through a bridging ligand. Taking the two points into account, the ligand I used is TPA (TPA = tris(2-pyridylmethyl)amine). One reason is that TPA ligand and its derivatives are well known for their application in supporting high valent metal centers. For example, the $[\text{Fe}^{\text{IV}}(\text{O})(\text{TPA})(\text{NCCH}_3)](\text{OTf})_2$ is one of the first synthetic oxoiron(IV) species reported,⁷ the $[\text{Fe}^{\text{III}}\text{Fe}^{\text{IV}}(\mu\text{-O})_2(5\text{-Et}_3\text{-TPA})_2](\text{ClO}_4)_3$ is the first iron(III)iron(IV) complex that has been crystallographically characterized,¹⁶¹ and the $[\text{Fe}^{\text{IV}}\text{Fe}^{\text{IV}}(\mu\text{-O})_2(3,5\text{-Me}_2\text{-4-MeO})_3\text{-TPA})_2]^{4+}$ is the first diiron(IV) synthetic complexes that has been characterized.^{162,}

¹⁶³ The structures of the three synthetic complexes are shown in Figure 5.1.

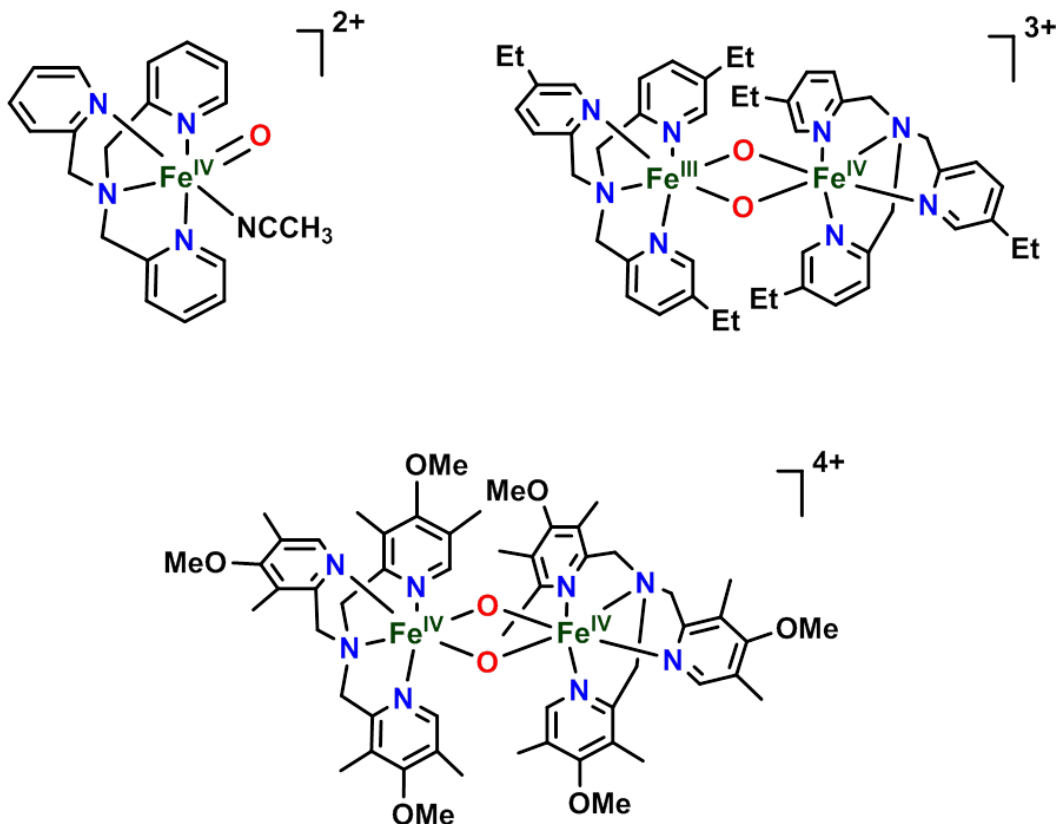


Figure 5.1 Structures of $[\text{Fe}^{\text{IV}}(\text{O})(\text{TPA})(\text{NCCH}_3)]^{2+}$ (top left), $[\text{Fe}^{\text{III}}\text{Fe}^{\text{IV}}(\mu\text{-O})_2(5\text{-Et}_3\text{-TPA})_2]^{3+}$ (top right), $[\text{Fe}^{\text{IV}}\text{Fe}^{\text{IV}}(\mu\text{-O})_2(3,5\text{-Me}_2\text{-4-MeO})_3\text{-TPA})_2]^{4+}$ (bottom).

Compared with the TPA supported diiron complexes in Figure 5.1, in $(\text{CH}_3\text{CN})(\text{TMC})\text{Fe}^{\text{III}}\text{-O-Cr}(\text{OTf})_4(\text{NCCH}_3)$,^{104, 136} it is impossible for the bridging ligand to link between Fe and Cr. Also, in $[(\text{N}4\text{Py})\text{Fe-O-Mn}(\text{dpaq})]^{3+}$ and $[(\text{BnTPEN})\text{Fe-O-Mn}(\text{dpaq})]^{3+}$, there is no vacant site for an extra bridging ligand to bind between the Fe and Mn center. Moreover, the $\text{Mn}^{\text{II}}(\text{TPA})(\text{OTf})_2$ has been reported in literature and is easy to synthesize.¹⁶⁴ Based on all of these reasons, the reaction between $\text{Fe}^{\text{IV}}(\text{O})(\text{TPA})(\text{OTf})_2$ and $\text{Mn}^{\text{II}}(\text{TPA})(\text{OTf})_2$ was first explored. As shown in Figure 5.2, ideally if there is no direct oxygen atom transfer from $\text{Fe}^{\text{IV}}(\text{O})(\text{TPA})(\text{OTf})_2$ complex to

the $\text{Mn}^{\text{II}}(\text{TPA})(\text{OTf})_2$ complex, then a $(\text{TPA})\text{Fe}^{\text{III}}\text{-O-Mn}^{\text{III}}(\text{TPA})$ species is proposed to be generated, similar as the ways of forming $(\text{CH}_3\text{CN})(\text{TMC})\text{Fe}^{\text{III}}\text{-O-Cr}(\text{OTf})_4(\text{NCCH}_3)$ and $[(\text{N4Py})\text{Fe-O-Mn}(\text{dpaq})]^{3+}$. The two *cis*-labile coordinating sites will not only apply asymmetric force to make Fe-O-Mn non-linear, but also provide positions for the bridge ligand binding.

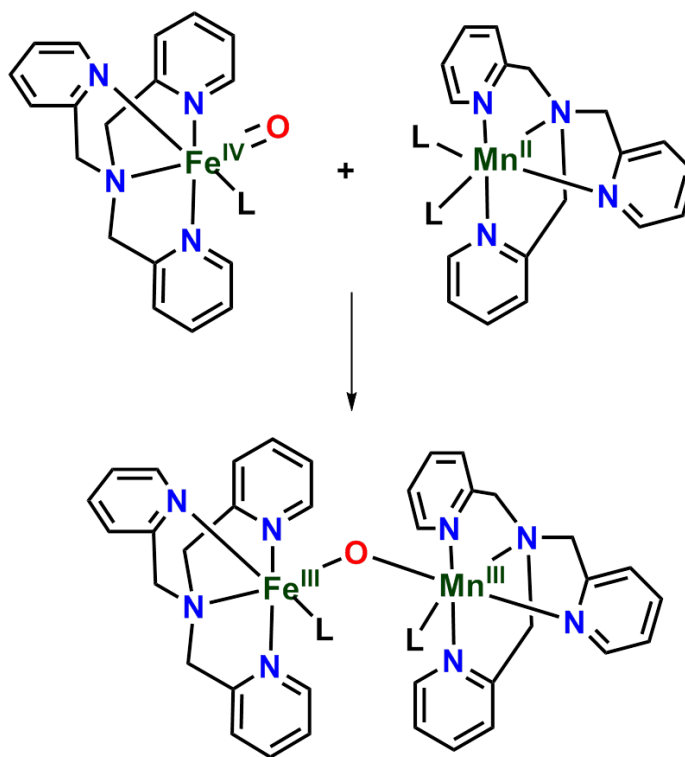


Figure 5.2 Proposed reaction between $[\text{Fe}^{\text{IV}}(\text{O})(\text{TPA})](\text{OTf})_2$ and $\text{Mn}^{\text{II}}(\text{TPA})(\text{OTf})_2$ to generate $(\text{TPA})\text{Fe}^{\text{III}}\text{-O-Mn}^{\text{III}}(\text{TPA})$ species. L represents OTf^- or CH_3CN .

After the successful synthesis of $(\text{TPA})\text{Fe}^{\text{III}}\text{-O-Mn}^{\text{III}}(\text{TPA})$, the correlated characterization results from UV-vis and EPR spectroscopy will be presented. Reaction of adding NBu_4OAc /hydrogen peroxide into **1** will be discussed as shown in Figure 5.3.

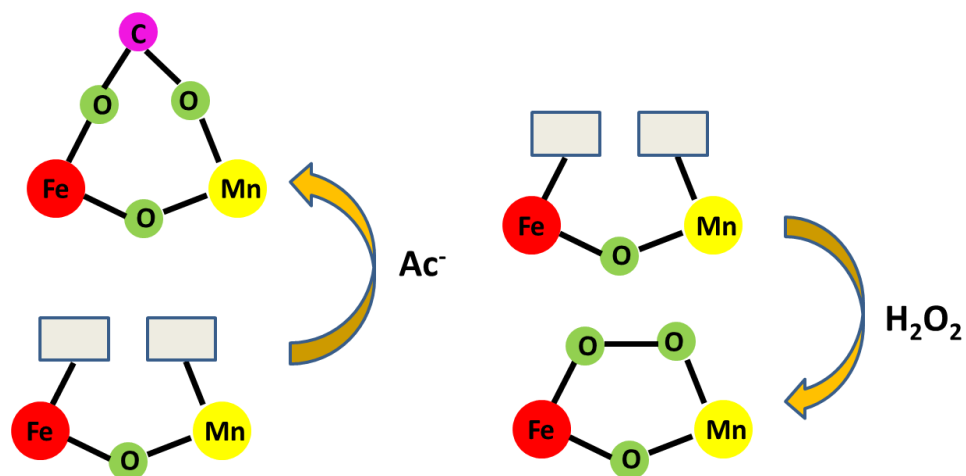


Figure 5.3 Proposed reactions between $\text{OAc}^-/\text{H}_2\text{O}_2$ with **1**.

5.2 Experimental details

5.2.1 Materials

All reagents and solvents were purchased from commercial sources and used as received unless specified. The preparations for TPA ligand,¹⁶⁵ $\text{Fe}^{\text{II}}(\text{TPA})(\text{OTf})_2 \cdot 2\text{CH}_3\text{CN}$,¹⁶⁰ $(2\text{-}^t\text{BuSO}_2\text{-C}_6\text{H}_4\text{IO})$ ^{107, 108} were carried out following published procedures. (*Caution: An injury was recently reported while attempting to synthesize $2\text{-}^t\text{BuSO}_2\text{-C}_6\text{H}_4\text{IO}$,¹⁰⁹ so this synthetic procedure should be carried out with the appropriate safety precautions and protective equipment*)¹¹⁰ All moisture- and oxygen-sensitive compounds were prepared using standard Schlenk–line techniques.

Synthesis of $\text{Mn}^{\text{II}}(\text{TPA})(\text{OTf})_2$ ¹⁶⁴ A solution of TPA (0.224 g, 0.758 mmol) in 10 mL of CH_3CN was added to the solution of $\text{Mn}(\text{OTf})_2 \cdot 2\text{CH}_3\text{CN}$ (0.273 mg,

0.627 mmol) in 10 mL of CH₃CN to produce a pale yellow solution. After stirring at room temperature for 12 h, the reaction mixture was filtered to yield a yellow solution. The filtrate was concentrated until it became viscous, and Et₂O was carefully layered on top to give colorless blocks *via* diffusion induced precipitation over 24 h (0.282 g, 70% yield).

5.2.2 Instrumentation

UV-vis absorption spectra were recorded on an HP 8453A diode array spectrometer. Low-temperature visible spectra were obtained using a cryostat from UNISOKU Scientific Instruments, Japan. Electrospray mass spectrometry was performed on a Finnigan LCQ ion trap mass spectrometer. X-band EPR spectra were collected on a Bruker Elexsys E-500 spectrometer equipped with an Oxford ESR-910 cryostat. EPR spectral integrations were carried out using a Windows software package (SpinCount v3.1.2).

5.2.3 X-ray Absorption Spectroscopy (XAS)

Iron K-edge X-ray absorption spectroscopy experiment were collected on SSRL beam line 9-3 using a 100 element solid state Ge detector (Canberra) with a SPEAR storage ring current of ~500 mA at a power of 3.0 GeV. The incoming X-rays were unfocused using a Si(220) double crystal monochromator, which was detuned by 40% of

the maximal flux to attenuate harmonic X-rays. Seven scans were collected from 6882 eV to 8000 eV at a temperature (10 K) that was controlled by an Oxford Instruments CF1208 continuous flow liquid helium cryostat. An iron foil was placed in the beam pathway prior to I_0 and scanned concomitantly for an energy calibration, with the first inflection point of the edge assigned to 7112.0 eV. A 3 μm Mn filter and a Soller slit were used to increase the signal to noise ratio of the spectra. Photoreduction was monitored by scanning the same spot on the sample twice and comparing the first derivative peaks associated with the edge energy during collection.

The detector channels from the scans were examined, calibrated, averaged, and processed for EXAFS analysis using EXAFSPAK to extract $\chi(k)$. Theoretical phase and amplitude parameters for a given absorber-scatterer pair were calculated using FEFF 8.40 and were utilized by the “opt” program of the EXAFSPAK package during curve fitting). In all analyses, the coordination number of a given shell was a fixed parameter and was varied iteratively in integer steps, while the bond lengths (R) and mean-square deviation (σ^2) were allowed to freely float. The amplitude reduction factor S_0 was fixed at 0.9, while the edge-shift parameter E_0 was allowed to float as a single value for all shells.

Pre-edge analysis was performed on data normalized in the “process” program of the EXAFSPAK package, and pre-edge features were fit as described elsewhere¹²² between 7108 eV to 7118 eV using the Fityk¹¹³ program with pseudo-Voigt functions composed of 50:50 Gaussian/Lorentzian functions.

5.3 Results and Discussion

5.3.1 Reaction Between and $\text{Fe}^{\text{IV}}(\text{O})(\text{TPA})(\text{OTf})_2$ and $\text{Mn}^{\text{II}}(\text{TPA})(\text{OTf})_2$

In 2003 the Que group reported quantitative formation of $\text{Fe}^{\text{IV}}(\text{O})(\text{TPA})(\text{OTf})_2$ by reacting $\text{Fe}^{\text{II}}(\text{TPA})(\text{OTf})_2$ with 1 eq. of peracetic acid.¹⁶⁰ However since the byproduct of this reaction is acetic acid, which can potentially bind to the Fe center, herein I generated $\text{Fe}^{\text{IV}}(\text{O})(\text{TPA})(\text{OTf})_2$ with the addition of 1 eq. of 2-^tBuSO₂-C₆H₄IO into $\text{Fe}^{\text{II}}(\text{TPA})(\text{OTf})_2$, and the byproduct 2-^tBuSO₂-C₆H₄I will not bind with the metal center. As shown in Figure 5.4, after the formation of 1 mM $\text{Fe}^{\text{IV}}(\text{O})(\text{TPA})(\text{OTf})_2$ at -40 °C, $\text{Mn}^{\text{II}}(\text{TPA})(\text{OTf})_2$ was gradually added into oxoiron(IV) solution. The near-IR 724 nm band which belongs to the ferryl species decreased together with the formation of a shoulder band at 500 nm, and an isosbestic point at 644 nm was detected (Figure 5.4, left).

Further quantitative analysis suggests that 1 eq. of $\text{Mn}^{\text{II}}(\text{TPA})(\text{OTf})_2$ was needed to fully react with the $\text{Fe}^{\text{IV}}(\text{O})(\text{TPA})(\text{OTf})_2$ in solution, implying the 1:1 stoichiometry in generating the new species (complex **1**) (Figure 5.4, right). This stoichiometric result resembles that from the reaction between $\text{Fe}^{\text{IV}}(\text{O})(\text{N4Py})(\text{OTf})_2$ and $\text{Mn}^{\text{II}}(\text{dpaq})(\text{OTf})$. To conclude, the strategy of inner-sphere electron transfer to construct heterobimetallic μ -oxo species works here, and the tetradentate tripodal TPA ligand is supporting both metals.

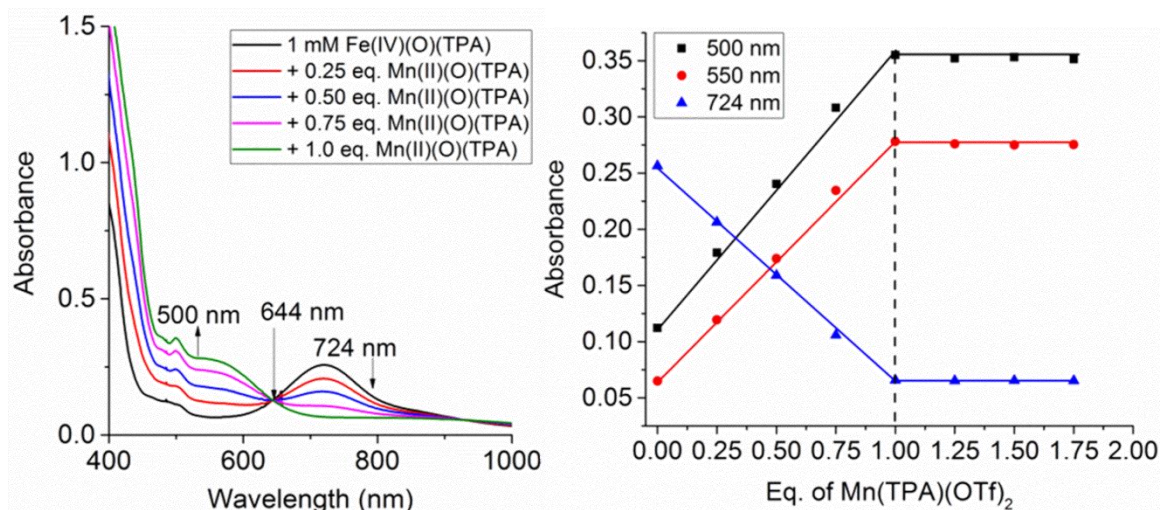


Figure 5.4 (Left) UV-vis spectra of 1 mM $\text{Fe}^{\text{IV}}(\text{O})(\text{TPA})(\text{OTf})_2$ and $\text{Mn}^{\text{II}}(\text{TPA})(\text{OTf})_2$ in CH_3CN at $-40\text{ }^\circ\text{C}$. Black, 0 eq.; red, 0.25 eq.; blue: 0.5 eq.; magenta, 0.75 eq.; green, 1 eq. (Right) Titration between $\text{Fe}^{\text{IV}}(\text{O})(\text{TPA})(\text{OTf})_2$ and $\text{Mn}^{\text{II}}(\text{TPA})(\text{OTf})_2$.

Although it is logical to propose **1** with a $(\text{TPA})\text{Fe}-\text{O}-\text{Mn}(\text{TPA})$ core, unlike $[(\text{N4Py})\text{Fe}^{\text{III}}-\text{O}-\text{Mn}^{\text{III}}(\text{dpaq})]^{3+}$, I was not able to obtain the evidence for its existence from ESI-MS spectra. However, the EPR experiment was carried out on **1**, and in its spectrum a six-line splitting pattern at $g = 2$ range was presented (Figure 5.5). The $g = 2$ signal can be rationalized by the antiferromagnetic coupling between the $\text{Fe}(\text{III})$ and $\text{Mn}(\text{III})$ center. The six-line splitting pattern is due to the the unpaired electron coupling with Mn nucleus ($I = 5/2$), and is consistent with that in $[(\text{N4Py})\text{Fe}-\text{O}-\text{Mn}(\text{dpaq})]^{3+}$ reported in Chapter 4.

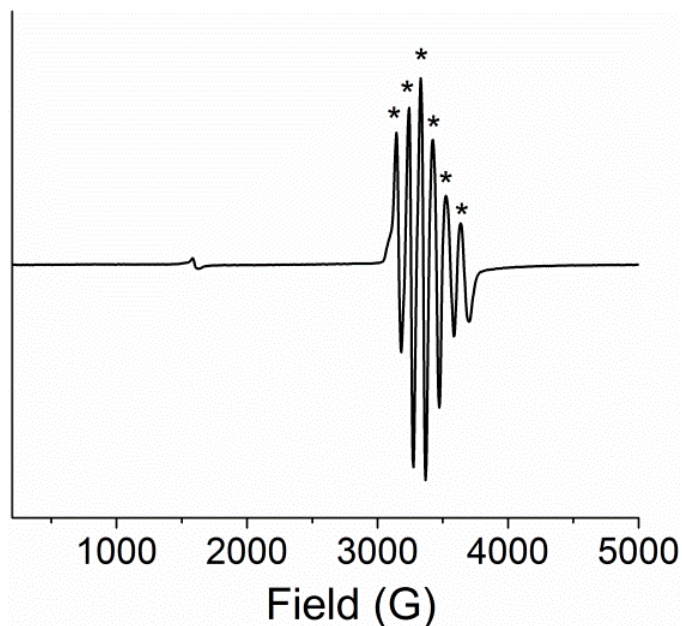


Figure 5.5 X-band EPR spectrum of 0.5 mM **1** in CH₃CN. Conditions: $T = 2$ K; microwave power attenuation: 30 dB. Asterisk indicates hyperfine pattern.

5.3.2 XAS Analysis on **1**

Fe K-edge X-ray absorption spectroscopy (XAS) measurements were conducted in order to obtain more structural information on **1**. The K-edge energy is 7124.6 eV, which is a little higher to the K-edge energy found for the previously reported (CH₃CN)(TMC)Fe^{III}-O-Cr^{III}(OTf)₄(NCCH₃) (7124.0 eV)¹⁰⁴ and [(N4Py)Fe-O-Mn(dpaq)]³⁺ (7123.7 eV). The pre-edge analysis (Figure 5.6) shows a peak with a maximum at 7115.1 eV and a calculated area of 15.0 units, close to that in [(N4Py)Fe-O-Mn(dpaq)]³⁺ (12.7 units), in which Fe center is 6-coordinated. The results above indicate that **1** contains a six coordinate Fe^{III} center.

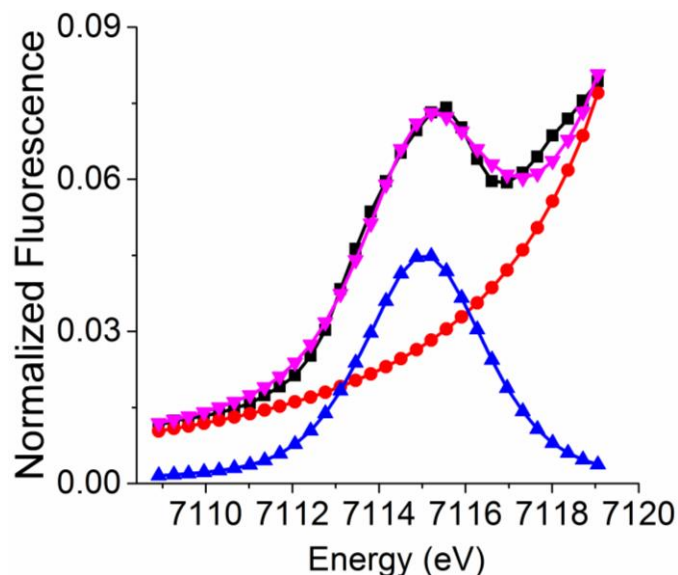


Figure 5.6 Pre-edge region of the Fe K-edge XAS spectrum of **1** (black line): baseline fit (pink dot), pre-edge peak (red lines), pre-edge fit (blue line).

An EXAFS analysis was done between $k = 2\text{--}14 \text{ \AA}^{-1}$ ($\Delta R = 0.13 \text{ \AA}$) to provide bonding metrics for complex **1**, and the fitting results are summarized in Figure 5.7 and Table 5.1. The best fit of **1** gives scattering pair distances that correspond to the following single-scattering shells: 5 Fe–N/O at 2.13 \AA , 1 Fe–O/N at 1.81 \AA , 6 Fe•••C at 3.04 \AA , 0.7 Fe•••Mn at 3.34 \AA . The atoms 2.13- \AA and 1.80- \AA away are assigned to the nitrogen donors of the TMC ligand and a μ -oxo bridge, respectively. In the Fourier-transformed figure of **1**, an 3.6- \AA $d(\text{Fe}\bullet\bullet\bullet\text{Mn})$ cannot be fitted, which is the $d(\text{Fe}\bullet\bullet\bullet\text{Mn})$ in $[(\text{N4Py})\text{Fe}^{\text{III}}\text{--O--Mn}^{\text{III}}(\text{dpaq})]^{3+}$. This suggests that **1** has a different $\text{Fe}^{\text{III}}\text{--O--Mn}^{\text{III}}$ core motif compared with that in $[(\text{N4Py})\text{Fe}^{\text{III}}\text{--O--Mn}^{\text{III}}(\text{dpaq})]^{3+}$.

The most interesting finding from the EXAFS fitting is the 3.34-Å Fe•••Mn distance. Firstly, it is a single-scattering pathway instead of a multiple scattering pathway. The multiple scattering pathway fitting is widely associated with the linear μ -oxo heterobimetallic species, such as $(\text{CH}_3\text{CN})(\text{TMC})\text{Fe}^{\text{III}}-\text{O}-\text{Cr}^{\text{III}}(\text{OTf})_4(\text{NCCH}_3)$, $(\text{CH}_3\text{CN})(\text{TMCPy})\text{Fe}^{\text{III}}-\text{O}-\text{Cr}^{\text{III}}(\text{OTf})_4(\text{NCCH}_3)$, $[(\text{N4Py})\text{Fe}^{\text{III}}-\text{O}-\text{Mn}^{\text{III}}(\text{dpaq})]^{3+}$ and $[(\text{BnTPEN})\text{Fe}^{\text{III}}-\text{O}-\text{Mn}^{\text{III}}(\text{dpaq})]^{3+}$. Thus the 3.34-Å Fe•••Mn single scattering pathway fitting suggests a bent $\text{Fe}^{\text{III}}-\text{O}-\text{Mn}^{\text{III}}$ core instead of a linear one.

Secondly, the 3.34 Å Fe•••Mn distance is significantly shorter than $d(\text{Fe}\cdots\text{Cr})$ in $(\text{L})\text{Fe}-\text{O}-\text{Cr}$ in Chapter 3, or $d(\text{Fe}\cdots\text{Mn})$ in $(\text{L})\text{Fe}-\text{O}-\text{Mn}$ in Chapter 4, which are close to 3.6 Å. This difference further indicates that the Fe–O–Mn motif is not linear in **1**. If $d(\text{Mn}-\text{O})$ in **1** is the same as that in $[(\text{N4Py})\text{Fe}^{\text{III}}-\text{O}-\text{Mn}^{\text{III}}(\text{dpaq})]^{3+}$ (1.82 Å), the Fe–O–Mn angle is estimated to be 134° based on Cosine law. The bent Fe–O–Mn core in **1** is exactly as expected from the beginning and proposed in Figure 5.2.

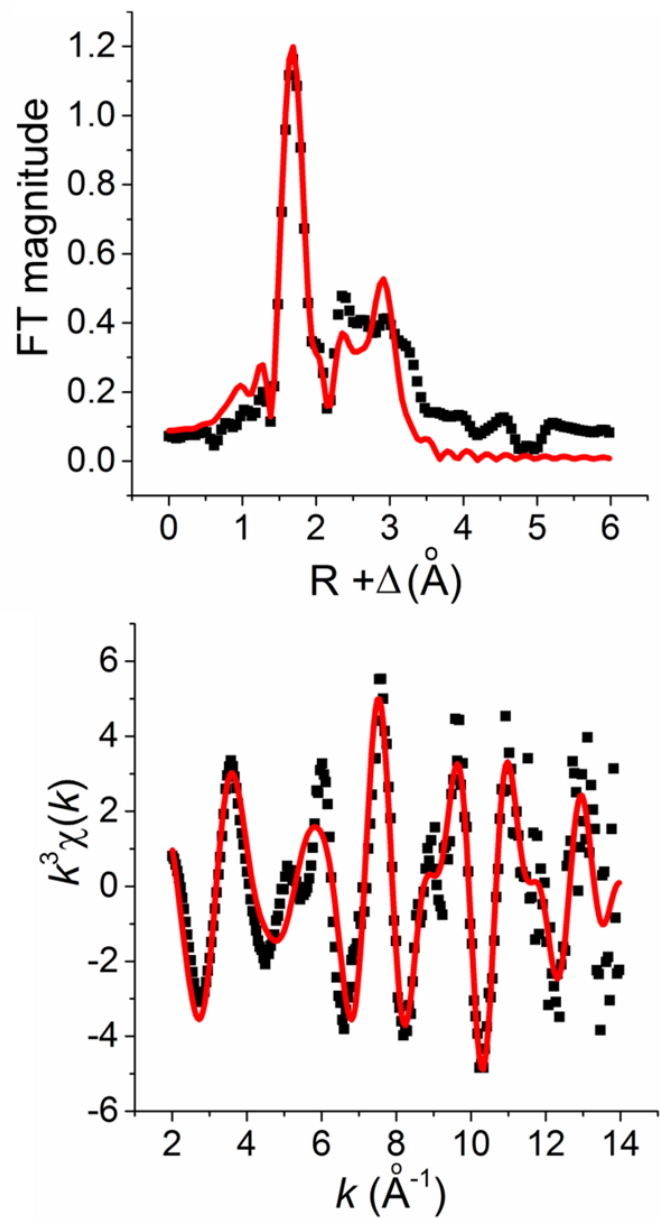


Figure 5.7 (Top) Fourier-transformed Fe K-edge EXAFS data for **1** (black) and the corresponding best fit (red, fit #7 in Table 5.1).

Table 5.1 Fit Parameters for **1** unfiltered from $k = 2 - 14 \text{ \AA}^{-1}$.

Fit	Fe-N			Fe-O			Fe•••C			Fe•••Mn			E_0	GOF	
	N	R (Å)	$\sigma^2 (10^{-3})$	N	R (Å)	$\sigma^2 (10^{-3})$	N	R (Å)	$\sigma^2 (10^{-3})$	N	R (Å)	$\sigma^2 (10^{-3})$		F	F'
1	5	2.13	4.18										-7.75	594	696
2	4	2.13	2.79										-7.62	542	665
3	4	2.12	2.88	1	1.81	4.25							-8.40	454	609
4	5	2.12	4.30	1	1.81	3.10							-5.71	453	608
5	5	2.11	4.31	1	1.81	2.82				0.7	3.33	0.46	-9.86	336	524
6	5	2.13	4.58	1	1.81	2.67	4	3.04	3.97	0.7	3.34	1.14	-6.71	239	442
7	5	2.13	4.64	1	1.81	2.57	6	3.04	6.36	0.7	3.34	1.12	-9.71	229	432

5.3.3 Reaction Between **1** and NBu₄OAc

The success of synthesis and characterization of **1** with a bent Fe–O–Mn core gives hope of its further reaction with other coordinate ligand L to form a Fe(μ -oxo)(L)Mn species, as shown in Figure 5.3. To start, 1 eq. of NBu₄OAc was added into 0.5 mM **1** solution in CH₃CN, and the reaction was monitored by the UV-vis spectrometer. The addition of Ac⁻ into **1** will induce the change of the UV-vis spectrum of **1**, with the formation of a 577 nm peak (Figure 5.8). The UV-Vis spectra changes suggest that acetate lead to the electronic structure changes of **1**, possibly due to the binding to the metal centers.

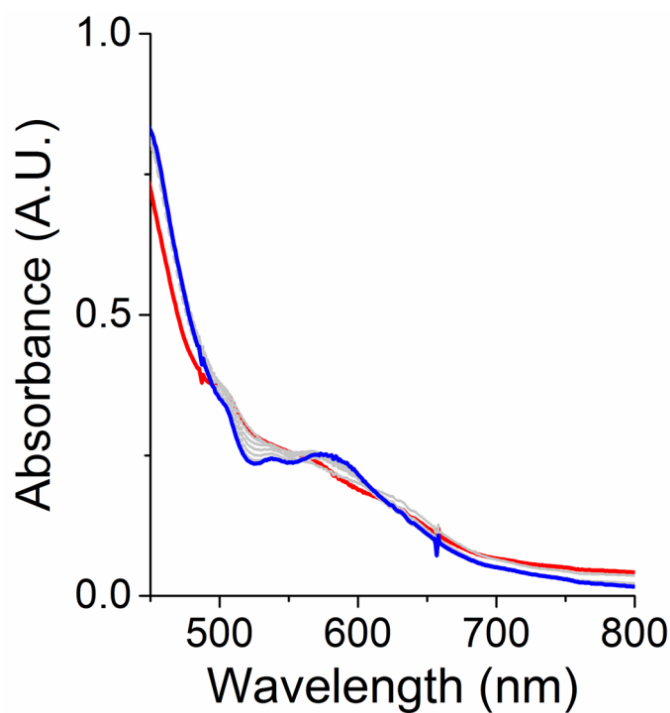


Figure 5.8 At -40 °C in CH₃CN, UV-vis spectra of 0.5 mM **1** (red) and after the addition 1 eq. of NBu₄OAc (blue).

The conclusion that acetate ion is binding to the Fe–O–Mn core in **1** is further confirmed by the EPR spectroscopic results. As shown in Figure 5.9, the spectrum of reaction between **1** and 1 eq. of NBu₄OAc produced a six-line splitting pattern at $g = 2$. The six line splitting at $g = 2$ is consistent with what is observed in **1**, indicating that Fe(III) and Mn(III) center are antiferromagnetic coupled with each other, and the unpaired electron is coupled with Mn nucleus ($I = 5/2$). However, the splitting pattern in Figure 5.9 is slightly different with that in **1** (Figure 5.5). In Figure 5.9 the second from left peak has the highest intensity, while in Figure 5.5 the third from left peak has the highest intensity. This change in the shape of EPR spectra of **1** after the addition of NBu₄OAc further indicates that acetate is binding to the Fe–O–Mn core.

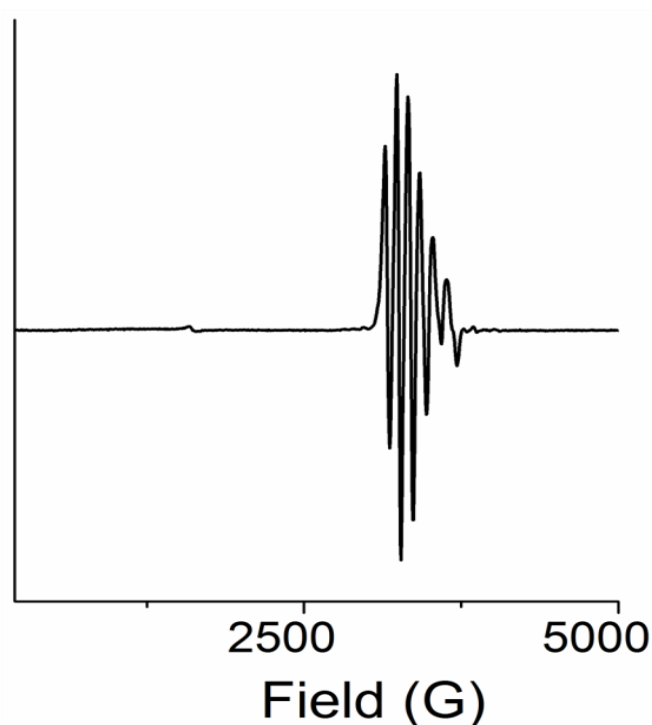


Figure 5.9 EPR spectrum of the reaction of **1** and 1 eq. of NBu₄OAc. Conditions: $T = 2$ K; microwave power attenuation: 30 dB.

5.3.4 Reaction Between **1** and H₂O₂

In the enzymes with diiron active site such as class Ia RNR,^{44, 48, 49} soluble methane monooxygenases,^{67, 166, 167} human deoxyhypusine hydroxylase (hDOHH),^{168, 169} the O₂ activation proceeds *via* the binding of O₂ to the diferrous active site to form a peroxodiferric intermediate. Many synthetic peroxodiferric molecules have been spectroscopically characterized from the reactions of diiron(II) precursors with O₂ or diiron(III) complexes with H₂O₂.^{75, 77, 81, 170-172} Although there is no direct evidence that the Fe(peroxo)Mn intermediate is involved in the reaction mechanism in class 1c RNR catalytic cycle, the success of reaction between **1** and NBu₄OAc suggests that such Fe(peroxo)Mn synthetic complexes may be obtained, which has not been reported in the literature so far.

Based on the discussion above the reaction between **1** and H₂O₂ was explored, with the hope to obtain the Fe(peroxo)Mn species. 0.75 mM complex **1** was first prepared using the procedure mentioned above at -40 °C in CH₃CN. Then 90% H₂O₂ was diluted in CH₃CN for use. 1 eq. of H₂O₂ in 10 uL CH₃CN was added into solution of **1**, the shoulders at 500 nm and 550 nm slowly increased, the bands plateaued at 2700 s (Figure 5.10). Adding more eq. of H₂O₂ further increased the absorption of the 500 nm and 550 nm bands, and at 4 eq. of H₂O₂ in total there was no further change on the spectra (Figure 5.11). Based on the UV-vis results the reaction between H₂O₂ and **1** is confirmed,

however the reaction product could not be identified based on the peaks in the low temperature ESI-MS results.

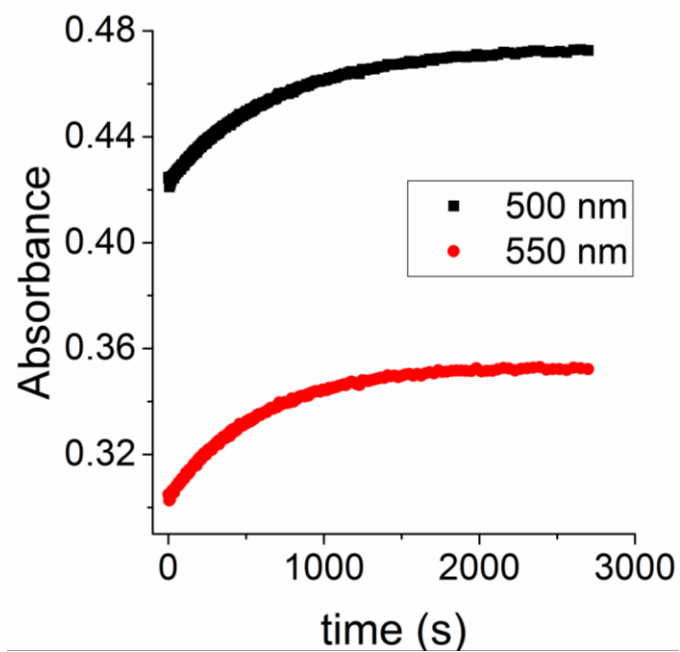


Figure 5.10 Time trace of 0.75 mM **1** + 1 eq of H₂O₂ at -40 °C in CH₃CN.

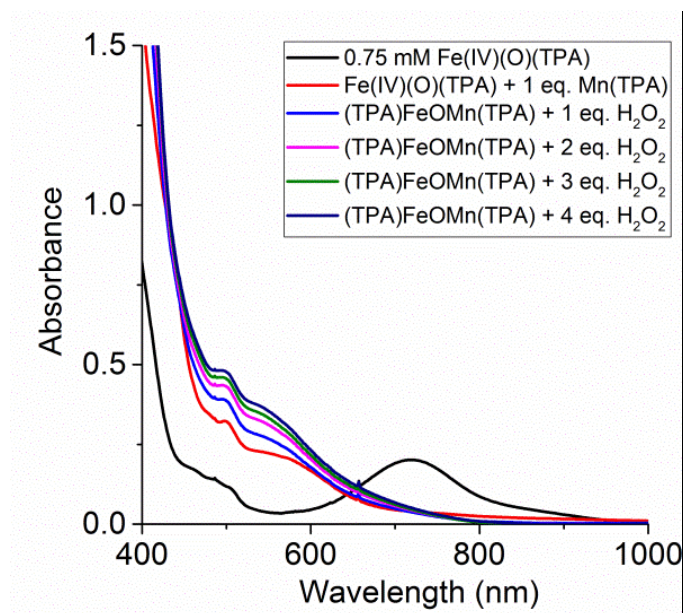


Figure 5.11 Reaction between 0.75 mM **1** and different eq. of H₂O₂.

Fe K-edge X-ray absorption spectroscopy (XAS) measurements were conducted in order to obtain more structural information on the product from reaction between **1** and H₂O₂ as described above in the UV-vis section. The K-edge energy is 7124.4 eV, which is a little higher than the K-edge energy found for the previously reported (CH₃CN)(TMC)Fe^{III}-O-Cr^{III}(OTf)₄(NCCH₃) (7124.0 eV)¹⁰⁴ and [(N4Py)Fe-O-Mn(dpaq)]³⁺ reported in Chapter 4 (7123.7 eV), but comparable to 7124.6 eV in **1**. The pre-edge analysis (Figure 5.12) shows two peaks with a maximum at 7113.0 eV and 7114.5 eV, with a calculated area of 12.1 units, very close to that in [(N4Py)Fe-O-Mn(dpaq)]³⁺ (12.7 units) and **1** (15.0 units). The results above indicate the product from **1** with H₂O₂ possesses a six coordinate Fe^{III} center.

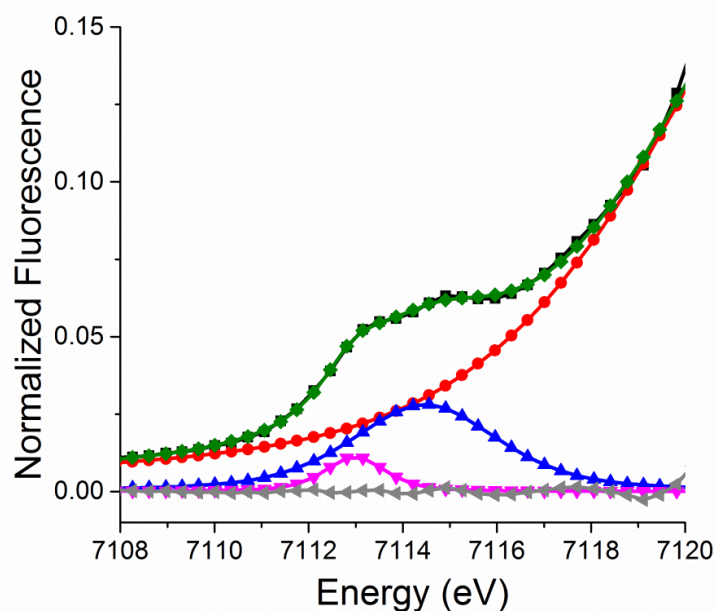


Figure 5.12 Pre-edge region of the Fe K-edge XAS spectrum of **1** + 4 eq. of H₂O₂ (black line): baseline fit (red line), pre-edge peak 1 (magenta line), pre-edge peak 2 (blue line), pre-edge fit (green line), residuals (gray line).

An EXAFS analysis was done between $k = 2\text{--}14 \text{ \AA}^{-1}$ ($\Delta R = 0.13 \text{ \AA}$) to provide bonding metrics for the product from the reaction between **1** and H₂O₂, and the fitting results are summarized in Figure 5.13 and Table 5.2. The best fit gives scattering pair distances that correspond to the following single-scattering shells: 4 Fe–N/O at 2.09 Å, 2 Fe–O/N at 1.87 Å, 4 Fe•••C at 2.93 Å, 1 Fe•••Mn at 3.40 Å. 4 2.09-Å N/O can be attributed to the four nitrogen atoms on the TPA ligand, and for 2 1.80-Å O/N atoms, one can be assigned as the μ -oxo bridge, and the other can be assigned as the μ -1 oxygen atom from the μ -1,2 peroxo anion bridging between Fe and Mn. This Fe–O₂ distance is comparable to those in the reported Fe^{III}₂(μ -oxo)(μ -1,2-peroxo) structures.^{75, 81} The

Fe•••Mn at 3.40 Å is a little longer than 3.34-Å $d(\text{Fe}\bullet\bullet\bullet\text{Mn})$ in **1**, but much shorter than 3.58-Å $d(\text{Fe}\bullet\bullet\bullet\text{Mn})$ in $[(\text{N4Py})\text{Fe}^{\text{III}}-\text{O}-\text{Mn}^{\text{III}}(\text{dpaq})]^{3+}$, which has a linear Fe–O–Mn core. Based on the EXAFS fitting results, the reaction between **1** and H_2O_2 is proposed to form a $\text{Fe}^{\text{III}}(\mu\text{-oxo})(\mu\text{-1,2-peroxo})\text{Mn}^{\text{III}}$ species (complex **2**).

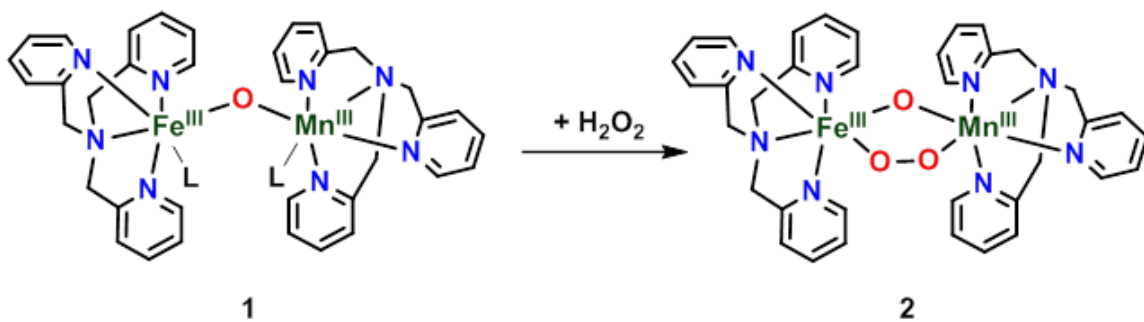


Figure 5.13 Proposed reaction mechanism between **1** and H_2O_2 to form **2**.

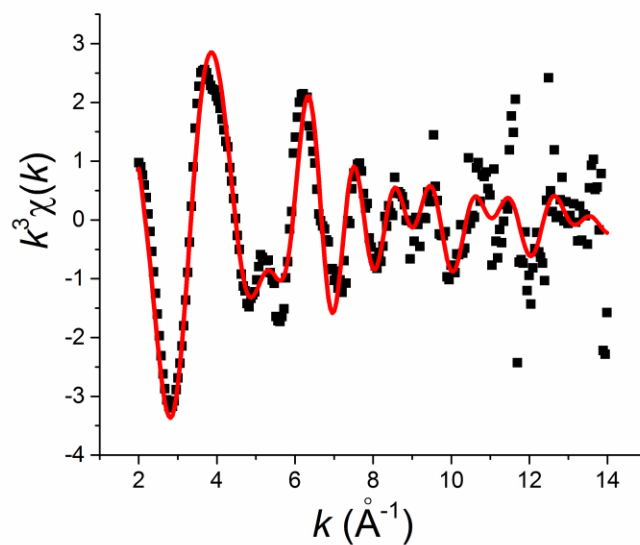
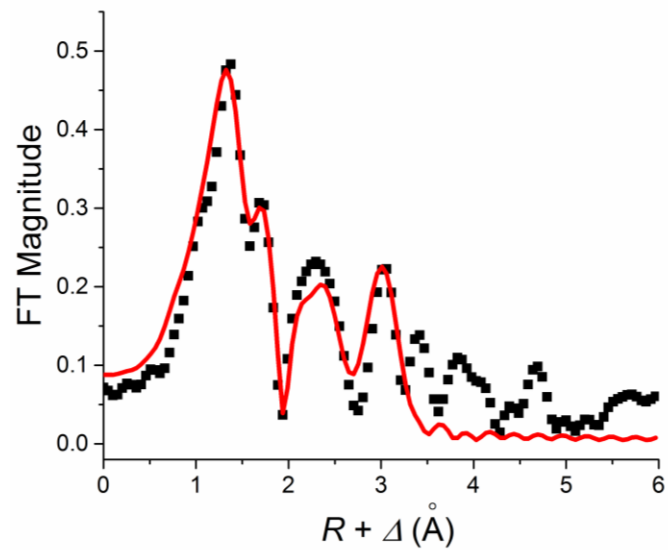


Figure 5.14 (Top) Fourier-transformed Fe K-edge EXAFS data for **2** (black) and the corresponding best fit (red, fit #7 in Table 5.2). (Bottom) Unfiltered k -space data (black) and its fit (red).

Table 5.2 Fit Parameters for **2** unfiltered from $k = 2 - 14 \text{ \AA}^{-1}$

Fit	Fe-O/N			Fe-N/O			Fe•••Mn			Fe•••C			E_0	GOF	
	N	R (Å)	$\sigma^2 (10^{-3})$		F	F'									
1	2	1.98	12.68										-8.10	1880	730
2	1	1.97	8.58										-8.28	2420	831
3	2	1.88	8.70	4	2.10	11.10							-8.29	1158	575
4	2	1.87	9.75	5	2.09	14.41							-8.24	1177	579
5	1	1.86	4.41	4	2.08	11.87							-7.14	1136	569
6	2	1.87	8.61	4	2.09	11.15	1	3.39	6.55				-8.90	920	512
7	2	1.87	9.04	4	2.09	11.71	1	3.40	7.01	4	2.93	13.39	-8.11	708	450

5.4 Conclusion

In this chapter the stoichiometric reaction between $\text{Fe}^{\text{IV}}(\text{O})(\text{TPA})(\text{OTf})_2$ and $\text{Mn}^{\text{II}}(\text{TPA})(\text{OTf})_2$ was explored. Based on results from UV-vis and EPR spectroscopy, a $(\text{TPA})\text{Fe}^{\text{III}}-\text{O}-\text{Mn}^{\text{III}}(\text{TPA})$ (species **1**) was generated with two *cis*-labile coordinating sites on the Fe and Mn centers. This geometry leads to the asymmetric force to make Fe–O–Mn non-linear, which is confirmed by the 3.34- Å Fe...Mn distance from EXAFS analysis. This result indicates that the inner-sphere electron transfer strategy can be applied to synthesize the non-linear μ -oxo heterobimetallic complexes.

What is more exciting is that **1** can further react with NBu_4OAc and H_2O_2 . From the spectroscopic evidence it is proposed that the acetate and peroxide anion are bridging between the Fe and Mn centers respectively, which lead to a better biosynthetic models for the analogues in class 1c RNR.

Chapter 6

Conclusion and Perspective

6.1 Introduction

In 2003, the Que group reported the first crystal structure of the nonheme Fe(IV)-oxo species, $[\text{Fe}^{\text{IV}}(\text{O})(\text{TMC})(\text{NCCH}_3)](\text{OTf})_2$ (complex **1**) (TMC, 1,4,8,11-tetramethyl-1,4,8,11-tetraazacyclotetradecane), which was generated quantitatively from the reaction between $\text{Fe}^{\text{II}}(\text{TMC})(\text{OTf})_2$ and 1 eq. of iodosylbenzene at 233K in CH_3CN .¹⁰⁵ **1** has a characteristic 824-nm absorption band in its UV-vis spectrum, which is proposed to originate from the d-d transition of Fe(IV) center based on the variable-temperature magnetic circular dichroism (VT-MCD) spectroscopic studies.^{173, 174}

The single crystal of **1** was obtained due to its unexpected stability ($t_{1/2} = 10$ h at room temperature and 1 month at -40 °C), showing a 1.646-Å Fe-O bond length, which is comparable with the Fe-O bond lengths in the nonheme oxoiron(IV) species in the enzymatic systems.^{13, 175} The TMC ligand coordinates to the Fe center in the equatorial plane, while the oxo ligand and solvent CH_3CN molecule occupy the two axial positions. It is noticeable that all four methyl groups on TMC molecule are oriented in the same direction with respect to the FeN₄ plane and *anti* to the oxo ligand (Figure 6.1).

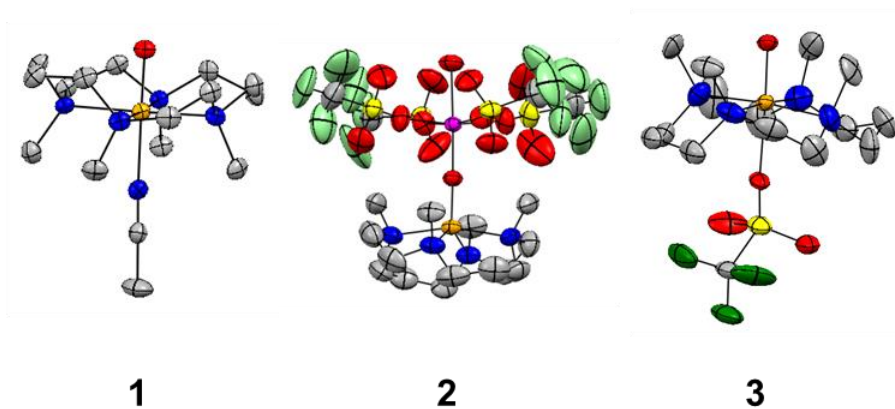


Figure 6.1 XRD structures of **1**¹⁰⁵, **2**¹⁷⁶, **3**¹⁰³.

In 2008, Dr. Kallol Ray in the Que group reported an unexpected conversion of **1** to its inverted isomer in the presence of iodosobenzene and tetrafluoroborate anion.¹⁷⁷ Compared with the structure of **1**, in its inverted isomer the oxoiron moiety is pointed to the same direction to the four methyl groups on the TMC molecule. Instead of the characteristic 824-nm band in **1**, its inverted isomer is observed with the bands at 806 nm and 1026 nm. The fact that simple position interchange of the axial oxo and CH₃CN ligands between **1** and its inverted isomer can lead to significant difference in their electronic structures is intriguing. The conversion is proposed to take place *via* a transient dioxoiron(VI) species, which has yet been confirmed experimentally.

The flip of the TMC-supported oxoiron moiety is also observed by other researchers. In 2010, the Nam group reported the evidence concerning the binding of the Sc(III) ion to the [(TMC)Fe^{IV}(O)]²⁺.¹⁷⁶ In the paper, complex **1** solution was added with 1

eq. of $\text{Sc}(\text{OTf})_3$, from which the single crystals were grown from a CH_3CN /diethyl ether mixture at $-15\text{ }^\circ\text{C}$. The researchers have solved the structures (Figure 6.1) and identify the formula as $[(\text{TMC})\text{Fe}^{\text{IV}}(\text{O})\text{Sc}(\text{OTf})_4(\text{OH})]$ (**2**), in which an oxo-Sc interaction leads to a structural distortion of the oxoiron(IV) moiety from an octahedral six-coordinated geometry to a distorted square pyramidal five-coordinated geometry. Interesting, all four N-methyl groups of the TMC ligand in **2** point to the same side of the oxo moiety, whereas those in **1** orient away from the oxo ligand. Five years later, Dr. Jai Prakash in the Que group re-examined the structure of **2**. Based on its Mössbauer and EPR spectra, **2** was re-assigned with a high-spin iron(III) center, contrary to the earlier assignment of a +4 oxidation state for the iron center.¹⁰² The mechanism of oxo flipping is yet to be clarified.

In 2015, Dr. Jai Prakash from the Que group found out that by treating $\text{Fe}^{\text{II}}(\text{TMC})(\text{OTf})_2$ with $2\text{-}^t\text{BuSO}_2\text{-C}_6\text{H}_4\text{IO}$ instead of $\text{C}_6\text{H}_4\text{IO}$, an oxoiron(IV) product (complex **3**) with the 815-nm absorption band in its UV-vis spectrum can be generated. Although the 815-nm band of **3** is only slightly different compared to the 824-nm band in **1**, the distinction between the two complexes is most starkly manifested in their $^1\text{H-NMR}$ spectra. The single crystal of **3** was obtained from $\text{CH}_2\text{Cl}_2/\text{Et}_2\text{O}$ diffusion, and it reveals a complex with the formulation of $[\text{Fe}^{\text{IV}}(\text{O})(\text{TMC})(\text{OTf})](\text{OTf})$, in which the oxo ligand is on the same side of the four methyl groups on the TMC ligand (Figure 6.1).

The clarification on the structures of **1** and **3** illustrate that how simple position interchange of the oxo ligand can affect the electronic structures of the oxoiron moieties. However, the mechanism of the oxo flip between **1** and **2** is not clear. Since in **2** the Fe^{III} –

O–Sc moiety is *syn* to the four methyl groups on the TMC ligand, is the topology of Fe^{III}–O–Sc moiety *anti* to the to the four methyl groups on the TMC ligand accessible? This is a fundamental question to help interpret the relationship between coordination geometry and the electronic structures of the organometallic complexes.

6.2 The Two Faces of Tetramethylcyclam in Iron Chemistry: Distinct Fe–O–M Complexes Derived from [Fe^{IV}(O_{*anti/syn*})(TMC)]²⁺ Isomers

As discussed above, complex **2** with the (TMC)Fe^{III}–O–Sc core is formed by recrystallization from the solution of **1** with the addition of 1 eq. Sc(OTf)₃. One electron is needed to reduce the Fe(IV) center in **1** to Fe(III) in **2**, and it cannot come from Sc(OTf)₃ which is a redox inactive salt. This causes difficulty in the preparation of (TMC)Fe^{III}–O–Sc complex *in situ*. In my thesis, the Cr(OTf)₂ salt was used to react with [(TMC)Fe(O)]²⁺ species. Unlike Sc(OTf)₃, Cr(OTf)₂ is a strong reducing reagent, and while been oxidized from Cr(II) to Cr(III) an immediate color change from blue to green happens, indicating the reaction occurs. Also, Cr(II) has been well known for its property of inducing inner sphere electron transfer reactions identified by Prof. Henry Taube. Based on this idea, the reactions between [Fe^{IV}(O_{*anti/syn*})(TMC)]²⁺ isomers and Cr(OTf)₂ were explored. It has to be mentioned here that the Cr(OTf)₂ is not commercially available. At first CrCl₂ was used, however it appears that the Cl⁻ could lead to the decay of the [(TMC)Fe(O)]²⁺ by binding to the axial position. Also, CrCl₂ cannot be dissolved

in CH₃CN, which is the solvent for the reaction. Because of these two reasons, Cr(OTf)₂ was synthesized as the way of making Fe(OTf)₂,¹⁰⁴ and worked well for the reaction.

When [Fe^{IV}(O_{anti/syn})(TMC)]²⁺ isomers were used to react with 1 eq. of Cr(OTf)₂ in CH₃CN at -40 °C, the correlated Fe–O–Cr complexes **4** and **5** were formed respectively (Figure 6.2). The structures of **4** and **5** have been unambiguously assigned based on results from UV-vis, resonance Raman, Mössbauer, and X-ray absorption spectroscopic data, as well as electrospray mass spectrometry. In addition, the crystal structures of (Cl)(TMC)Fe–O_{anti}–FeCl₃ and [(TMC)Fe–O_{syn}–FeCl₃](OTf) have been determined by X-ray crystallography to further support the structural identification of **4** and **5**.

In **4** the Fe–O–Cr moiety orients in the opposite direction of the four methyl groups on the TMC ligand, while in **5** the Fe–O–Cr moiety orients in the same direction of the four methyl groups on the TMC ligand. There are several consequences caused by this orientation difference. Firstly, the Fe center is 6-coordinate in **4**, but 5-coordinate in **5**. It can be explained by the longer distance of the Fe from the mean N₄ plane of the TMC framework in **5** than in **4**, which causes the dissociation of the axial binding ligand. Secondly, the $\nu_{\text{as}}(\text{Fe–O–Cr})$ in **4** is 100 cm⁻¹ lower than that in **5**, and this can be explained by the extra ligand binding to the Fe in the former, which counteracts the positive charge of the Fe center. These results emphasize the importance of the ligand topology in determining the coordination sphere of the iron center.

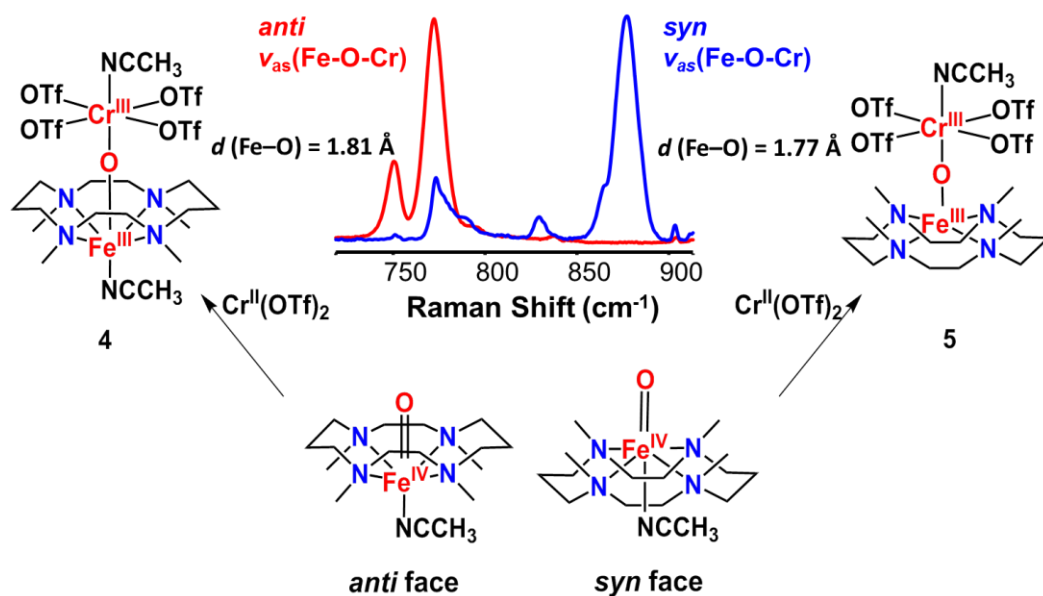


Figure 6.2 Structural comparison between **4** and **5**.

As the future work of this part, the reactivity studies of **4** and **5** will be investigated. Although it has been demonstrated that both complexes are inert to the common hydrogen atom transfer (HAT) reagents (xanthene and 2,4,6-tri-(tert-butyl)phenol) or oxygen atom transfer reagents (OAT) (4-methoxythioanisole or PPh_3), it will still be interesting to explore their electron transfer reaction to compare their redox potentials. Complex **2** can quantitatively react with 1 eq. of ferrocene, indicating the Fe(III) is reduced to Fe(II). Thus the reaction between ferrocene (and its derivatives) with **4** / **5** will be interesting to be tested, as it can reveal the information about how the redox potential of the Fe(III) center is affected by the coordination sphere.

The other direction is focus on the consequences of replacing the methyl groups of the TMC ligand with other R groups, such as the benzyl groups introduced by Nam¹³⁵ on the relative stabilities of the *syn* and *anti* isomers. Part of this work is completed and discussed in Chapter 3, and will be discussed in section 6.3.

6.3 Coordination Effects on Structures of (L)Fe^{III}-O-Cr^{III} Species

In Chapter 2, a pair of (TMC)Fe^{III}-O-Cr^{III} isomers **4** and **5**, synthesized from the reaction between Cr(OTf)₂ and the corresponding [(TMC)Fe^{IV}O_{*anti/syn*}]²⁺ complexes, are characterized in detail by UV-vis, resonance Raman, Mössbauer, and X-ray absorption spectroscopic methods, as well as electrospray mass spectrometry. The results demonstrate the application of the inner sphere electron transfer reaction between the Cr(OTf)₂ and [(TMC)Fe^{IV}O]²⁺ species. One advantage of studying synthetic molecules compared with its corresponding nature intermediates is that, in principle, the coordination sphere of the synthetic molecules can be systematically modulated to determine how the local coordination geometry governs electronic structure and reactivity.¹³⁷ Based on this idea a variety of oxoiron(IV) complexes, including [Fe^{IV}(O)(TMCPy)](OTf)₂, [Fe^{IV}(O)(TMCdma)](OTf)₂, [Fe^{IV}(O)(N4Py)](OTf)₂ and [Fe^{IV}(O)(BnTPEN)](OTf)₂, were utilized to react with Cr(OTf)₂ to generate (L)Fe^{III}-O-Cr^{III} complexes **6**, **7**, **8**, **9** (Figure 6.3).

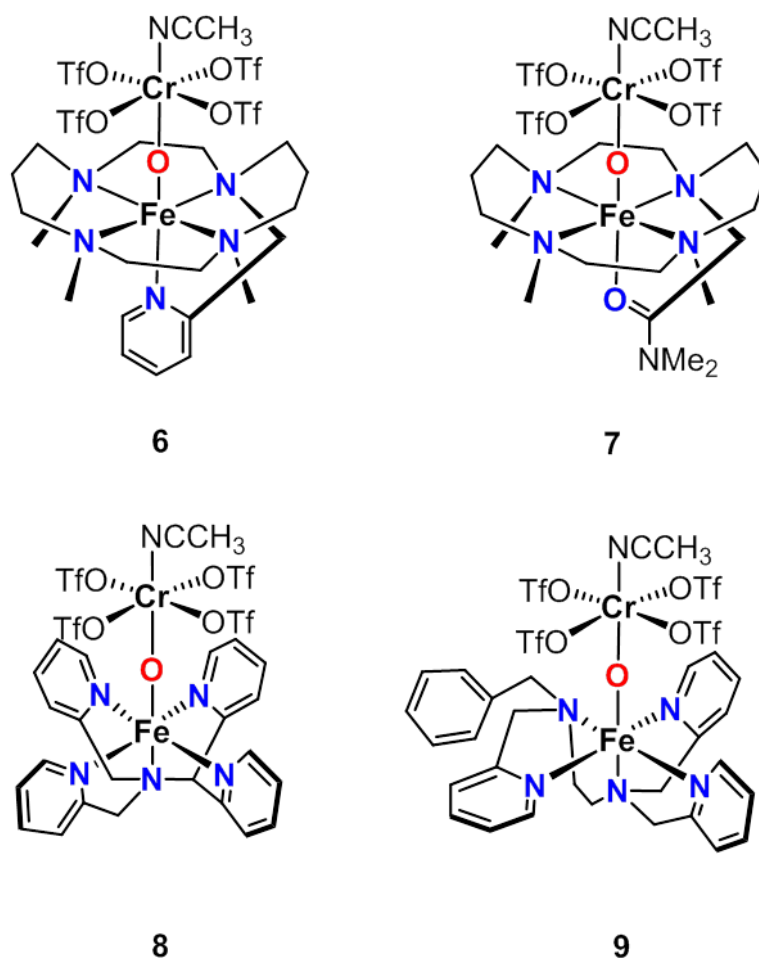


Figure 6.3 Proposed structures of **6-9**.

All these four complexes have been identified to have the $\text{Fe}^{\text{III}}\text{-O-Cr}^{\text{III}}$ core as discussed in detailed in Chapter 3. However, it has been found that different supporting ligands to iron play an important role on the vibrational number of $\text{Fe}^{\text{III}}\text{-O-Cr}^{\text{III}}$ core. In **6** and **7**, the $\nu_{\text{as}}(\text{Fe}^{\text{III}}\text{-O-Cr}^{\text{III}})$ value identified by the Raman technique is around 770 cm^{-1} , while in **8** and **9** the $\nu_{\text{as}}(\text{Fe}^{\text{III}}\text{-O-Cr}^{\text{III}})$ value identified by the Raman technique is around

870 cm^{-1} . In **6-9** the iron supporting ligands are all pentadentate molecules, so the 100 cm^{-1} $\nu_{\text{as}}(\text{Fe}^{\text{III}}-\text{O}-\text{Cr}^{\text{III}})$ difference is attributed to the different ligand structure.

There are two ways to interpret the effect. The first view is from the basicity of the nitrogen donor. In **6** and **7**, the Fe center is coordinated by four alkyl amines in the equatorial position and one ligand at the axial position. In **8**, the Fe center is coordinated by four pyridines in the equatorial position and one amine at the axial position. In **9**, the Fe center is coordinated by three pyridines, one amine in the equatorial position and one amine in the axial position. Since alkyl amine is a strong Lewis base than pyridine, more numbers of alkyl amines in **6** and **7** leads to a stronger electron donation effect, which can counteract the positive charge of the Fe center, thus elongate the Fe–O and Fe \cdots Cr distances.

The second view is from the steric characters. Although the accurate metric information of **6-9** are not accessible beyond EXAFS analysis, XRD data on some correlated complexes have been reported in literature. In $[\text{Fe}^{\text{IV}}(\text{O})(\text{TMCdma})](\text{OTf})_2$, which is the oxoiron(IV) precursor of **6**, the $d(\text{Fe}-\text{N}_{\text{amine}})$ is 2.060 Å, while $d(\text{Fe}-\text{O}_{\text{amide}})$ is 1.981 Å.¹⁴² In the crystal structure of $[(\text{N4Py})\text{Fe}^{\text{III}}-\text{O}-\text{Fe}^{\text{III}}(\text{N4Py})]^{4+}$, an analogue of **7**, $d(\text{Fe}-\text{N}_{\text{py}}) = 2.151$ Å, and $d(\text{Fe}-\text{N}_{\text{amine}}) = 2.255$ Å¹⁷⁸. It can be seen that the axial oxygen in **6** has much shorter $d(\text{Fe}-\text{O})$ than the $d(\text{Fe}-\text{N}_{\text{amine}})$ in **7**, suggesting in **6** the positive charge of the Fe center is counteracted at a higher level, which lead to the weaker $\nu_{\text{as}}(\text{Fe}^{\text{III}}-\text{O}-\text{Cr}^{\text{III}})$ value.

In this section, the inner sphere electron transfer reaction is extended to a wider application, and a series of (L)Fe–O–Cr species were synthesized and characterized. The effect of coordination sphere to the $\nu_{\text{as}}(\text{Fe}^{\text{III}}\text{--O--Cr}^{\text{III}})$ value may be further clarified from theoretical calculation as the future research direction. Also, it will be interesting to explore other reducing metals instead of Cr(II) in reacting with the oxoiron(IV) complexes. Mn(II) salt was utilized to make a series of Fe^{III}/Mn^{III} complexes as synthetic models for the metallocofactors in class Ic RNR, and will be discussed in details in the following two sections.

6.4 Characterization and Reactivity Studies of a Linear Fe–O–Mn Species Obtained from Inner-Sphere Electron Transfer

With the success of synthesizing a series of Fe^{III}–O–Cr^{III} complexes by inner-sphere electron transfer, other heterobimetallic species are expected to be made by the same strategy. The Fe^{III}/Mn^{III} complexes attract my interest. Unlike Fe^{III}/Cr^{III} complex, which does not have any biological relevance, the Fe^{III}/Mn^{III} metallocofactor plays an important role in O₂ activation among the proteins such as class 1c RNR.^{63, 65, 66, 68, 99, 147-149} Its Fe/Mn cofactor is proposed to bind with O₂ to generate a transient Fe^{III}–O–Mn^{IV} species, which initiates the redox cascade in the R1 subunit. In comparison, the reported synthetic Fe^{III}/Mn^{III} complexes are quite rare, and the correlated synthesis strategies either have difficulties in selectively binding the two metals at specific sites while

avoiding mixtures and homodinuclear side products,^{87, 88} or require complicated unsymmetrical ligand synthesis.¹⁵³

Herein the synthesis of complex **10** and **11** were reported from the reaction between their correlated oxoiron(IV) species [(N4Py)Fe^{IV}(O)](OTf)₂ and [(BnTPEN)Fe^{IV}(O)](OTf)₂ with [(dpaq)Mn^{II}(OTf)] with a 1:1 stoichiometric ratio. The structures of **10** and **11** are proposed in Figure 6.4, which are supported by the data from UV-vis absorption, resonance Raman, EPR, X-ray absorption spectroscopic methods, as well as electrospray mass spectrometry. Similar as **4-9**, both complexes **10** and **11** have linear μ -oxo heterobimetallic motif.

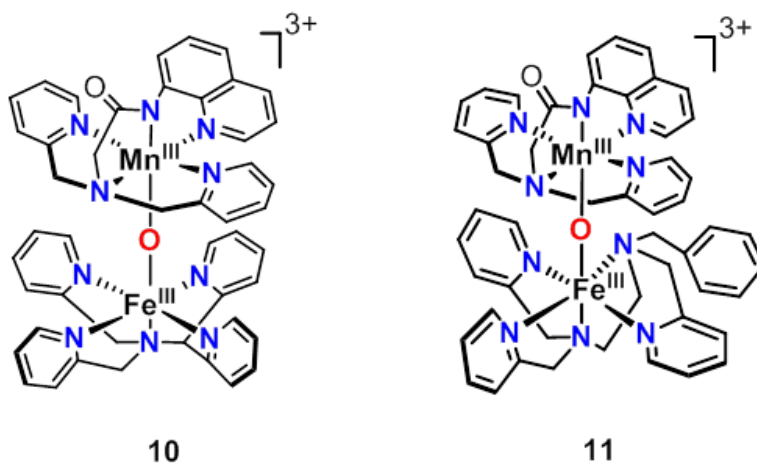


Figure 6.4 Proposed structures of **10-11**.

The synthesis of **10** and **11** has further demonstrated the application of the inner-sphere reaction strategy to build versatile types of μ -oxo heterobimetallic complexes. **10** is able to react with not only H₂O to break the Fe^{III}-O-Mn^{III} core, but also

decamethylferrocene to generate a metastable intermediate, which is proposed to be an Fe^{II}-O-Mn^{III} complex. However, **10** cannot be further oxidized to generate the Fe^{III}/Mn^{IV} species, which is proposed as the active intermediate in class 1c RNR. Future work will be focused on the modification of supporting ligand of Mn in **10**, so as to lower the Mn^{IV}/Mn^{III} redox potential for easier oxidation.

6.5 From Linear to Nonlinear: A Synthetic Model for Class 1c Ribonucleotide Reductase

Although **10** and **11** with linear Fe-O-Mn core were synthesized and well characterized, in nature there are no Fe^{III}/Mn^{III} metallocofactors with the linear Fe-O-Mn motif reported to date. Also, the μ -oxo bond is the only bridging ligand in **10** and **11** due to the lack of coordination sites on both Fe and Mn ions, while in the Fe/Mn intermediates in class 1c RNR the other ligands, such as acetate are found to bridge between the Fe and Mn center.

In this section the tetradentate ligand TPA is used to coordinate with Fe and Mn atom. the Fe^{IV}(O)(TPA) OTf)₂ can react with Mn^{II}(TPA)(OTf)₂ to generate complex **12** with an Fe^{III}-O-Mn^{III} core. Based on XAS results, the $d(\text{Fe}\cdots\text{Mn})$ in **12** is 3.34 Å, much shorter than 3.56 Å $d(\text{Fe}\cdots\text{Mn})$ in **10**. The much shorter Fe^{III}⋯Mn^{III} distance reflects a bent Fe-O-Mn structure in **12**, indicating the inner-sphere electron transfer can be used to synthesize nonlinear heterobimetallic complexes. Also, the bent Fe-O-Mn motif allows a second ligand to bridge between the two metal centers. Acetate and peroxide anions were

used respectively, and the spectroscopic results indicate they can bind between the Fe and Mn atoms.

As the future direction, the reactivity of **12** will be explored. What is really exciting is that TPA and its derivatives are known as versatile ligands to support the high valent diiron complexes. Examples include the $[\text{Fe}^{\text{III}}\text{Fe}^{\text{IV}}(\mu\text{-O})_2(5\text{-Et}_3\text{-TPA})_2](\text{ClO}_4)_3$, the first iron(III)iron(IV) complex that has been crystallographically characterized,¹⁶¹ also the $[\text{Fe}^{\text{IV}}\text{Fe}^{\text{IV}}(\mu\text{-O})_2(3,5\text{-Me}_2\text{-4-MeO})_3\text{-TPA})_2]^{4+}$, the first diiron(IV) synthetic complexes that has been characterized. By introducing the electron donation groups on the pyridine rings of TPA ligand can stabilize the high valent Fe center. Inspired by this, the TPA derivatives can be used in **12**, with the expectation to generate $\text{Fe}^{\text{III}}/\text{Mn}^{\text{IV}}$ and $\text{Fe}^{\text{IV}}/\text{Mn}^{\text{IV}}$ species as analogues in class Ic RNR.

6.6 Conclusion

In conclusion, a series of Fe–O–Cr and Fe–O–Mn complexes were synthesized and characterized from the reaction between oxoiron(IV) species and correlated Cr(II)/Mn(II) salt via the inner-sphere electron transfer. This method can not only selectively bind the two metals at specific sites while avoiding mixtures and homodinuclear side products, but also avoid the complicated unsymmetrical ligand synthesis. With the more than 100 oxoiron(IV) complexes to select, more Fe–O–M complexes can be expected to be generated using this method, so as to greatly enrich the

synthetic Fe–O–M complexes. This can also help us to better understand the effect of M ions to the Fe–O moiety.

References

1. Hayaishi, O.; Katagiri, M.; Rothberg, S. *J. Am. Chem. Soc.* **1955**, *77*, 5450-5451.
2. Que, L., Jr. *J. Biol. Inorg. Chem.* **2017**, *22*, 171-173.
3. Groves, J. T. *Proc. Natl. Acad. Sci. U.S.A.* **2003**, *100*, 3569-3574.
4. Nam, W. *Acc. Chem. Res.* **2007**, *40*, 522-531.
5. Sono, M.; Roach, M. P.; Coulter, E. D.; Dawson, J. H. *Chem. Rev.* **1996**, *96*, 2841-2888.
6. Maines, M. D. *FASEB J.* **1988**, *2*, 2557-2568.
7. de Visser, S. P.; Rohde, J.-U.; Lee, Y.-M.; Cho, J.; Nam, W. *Coord. Chem. Rev.* **2013**, *257*, 381-393.
8. Hegg, E. L., Que, L., Jr. *J. Eur. J. Biochem.* **1997**, *250*, 625-629.
9. Koehntop, K. D.; Emerson, J. P.; Que, L., Jr. *J. Biol. Inorg. Chem.* **2005**, *10*, 87-93.
10. Bruijninx, P. C. A.; van Koten, G.; Gebbink, R. J. M. K. *Chem. Soc. Rev.* **2008**, *37*, 2716-2744.
11. Price, J. C.; Barr, E. W.; Glass, T. E.; Krebs, C.; Bollinger, J. M. *J. Am. Chem. Soc.* **2003**, *125*, 13008-13009.
12. Price, J. C.; Barr, E. W.; Tirupati, B.; Bollinger, J. M.; Krebs, C. *Biochemistry* **2003**, *42*, 7497-7508.
13. Krebs, C.; Galonic Fujimori, D.; Walsh, C. T.; Bollinger Jr, J. M. *Acc. Chem. Res.* **2007**, *40*, 484-492.

14. de Visser, S. P. *Coord. Chem. Rev.* **2009**, *253*, 754-768.
15. Galonic Fujimori, D.; Barr, E. W.; Matthews, M. L.; Koch, G. M.; Yonce, J. R.; Walsh, C. T.; Bollinger, J. M.; Krebs, C.; Riggs-Gelasco, P. J. *J. Am. Chem. Soc.* **2007**, *129*, 13408-13409.
16. Galonić, D. P.; Barr, E. W.; Walsh, C. T.; Bollinger, J. M.; Krebs, C. *Nat. Chem. Biol.* **2007**, *3*, 113-116.
17. Panay, A. J.; Lee, M.; Krebs, C.; Bollinger Jr, J. M.; Fitzpatrick, P. F. *Biochemistry* **2011**, *50*, 1928-1933.
18. Ferguson-Miller, S.; Babcock, G. T. *Chem. Rev.* **1996**, *96*, 2889-2908.
19. Qin, L.; Sharpe, M. A.; Garavito, R. M.; Ferguson-Miller, S. *Curr. Opin. Struct. Bio.* **2007**, *17*, 444-450.
20. Yoshikawa, S.; Shimada, A. *Chem. Rev.* **2015**, *115*, 1936-1989.
21. Bosetti, F.; Brizzi, F.; Barogi, S.; Mancuso, M.; Siciliano, G.; Tendi, E. A.; Murri, L.; Rapoport, S. I.; Solaini, G. *Neurobiol. Aging* **2002**, *23*, 371-376.
22. Tsukihara, T.; Aoyama, H.; Yamashita, E.; Tomizaki, T.; Yamaguchi, H.; Shinzawa-Itoh, K.; Nakashima, R.; Yaono, R.; Yoshikawa, S. *Science* **1996**, *272*, 1136-1144.
23. Tsukihara, T.; Aoyama, H.; Yamashita, E.; Tomizaki, T.; Yamaguchi, H.; Shinzawa-Itoh, K.; Nakashima, R.; Yaono, R.; Yoshikawa, S. *Science* **1995**, *269*, 1069-1074.

24. Yoshikawa, S.; Shinzawa-Itoh, K.; Nakashima, R.; Yaono, R.; Yamashita, E.; Inoue, N.; Yao, M.; Fei, M. J.; Libeu, C. P.; Mizushima, T. *Science* **1998**, *280*, 1723-1729.
25. Yano, N.; Muramoto, K.; Shimada, A.; Takemura, S.; Baba, J.; Fujisawa, H.; Mochizuki, M.; Shinzawa-Itoh, K.; Yamashita, E.; Tsukihara, T. *J. Bio. Chem.* **2016**, *291*, 23882-23894.
26. Quist, D. A.; Diaz, D. E.; Liu, J. J.; Karlin, K. D. *J. Biol. Inorg. Chem.* **2016**, 1-36.
27. Van Gelder, B. F.; Beinert, H. *BBA-Biogergetics* **1969**, *189*, 1-24.
28. Tweedle, M. F.; Wilson, L. J. *J. Bio. Chem.* **1978**, *253*, 8065-8071.
29. Aoyama, H.; Muramoto, K.; Shinzawa-Itoh, K.; Hirata, K.; Yamashita, E.; Tsukihara, T.; Ogura, T.; Yoshikawa, S. *Proc. Natl. Acad. Sci. U.S.A.* **2009**, *106*, 2165-2169.
30. Sucheta, A.; Szundi, I.; Einarsdóttir, Ó. *Biochemistry* **1998**, *37*, 17905-17914.
31. Varotsis, C.; Woodruff, W. H.; Babcock, G. T. *J. Am. Chem. Soc.* **1989**, *111*, 6439-6440.
32. Han, S.; Ching, Y.-c.; Rousseau, D. L. *Proc. Natl. Acad. Sci. U.S.A.* **1990**, *87*, 2491-2495.
33. Ogura, T.; Takahashi, S.; Shinzawa-Itoh, K.; Yoshikawa, S.; Kitagawa, T. *J. Bio. Chem.* **1990**, *265*, 14721-14723.
34. Proshlyakov, D. A.; Ogura, T.; Shinzawa-Itoh, K.; Yoshikawa, S.; Appelman, E. H.; Kitagawa, T. *J. Bio. Chem.* **1994**, *269*, 29385-29388.

35. Ogura, T.; Hirota, S.; Proshlyakov, D. A.; Shinzawa-Itoh, K.; Yoshikawa, S.; Kitagawa, T. *J. Am. Chem. Soc.* **1996**, *118*, 5443-5449.
36. Reichard, P. *Annu. Rev. Biochem.* **1988**, *57*, 349-374.
37. Stubbe, J.; Van Der Donk, W. A. *Chem. Rev.* **1998**, *98*, 705-762.
38. Herrick, J.; Sclavi, B. *Mol. Microbiol.* **2007**, *63*, 22-34.
39. Cotruvo Jr, J. A.; Stubbe, J. *Annu. Rev. Biochem.* **2011**, *80*, 733-767.
40. Cerqueira, N. M.; Fernandes, P. A.; Eriksson, L. A.; Ramos, M. J. *J. Comput. Chem.* **2004**, *25*, 2031-2037.
41. Booker, S.; Licht, S.; Broderick, J.; Stubbe, J. *Biochemistry* **1994**, *33*, 12676-12685.
42. Sintchak, M. D.; Arjara, G.; Kellogg, B. A.; Stubbe, J.; Drennan, C. L. *Nat. Struct. Mol. Biol.* **2002**, *9*, 293-300.
43. Fontecave, M.; Mulliez, E.; Logan, D. T. *Prog. Nucleic. Acid. Res. Mol.* **2002**, *72*, 95-127.
44. Minnihan, E. C.; Nocera, D. G.; Stubbe, J., *Acc. Chem. Res.* **2013**, *46*, 2524-2535.
45. Uhlin, U.; Eklund, H. *Nature* **1994**, *370*, 533-539.
46. Seyedsayamdost, M. R.; Stubbe, J. *J. Am. Chem. Soc.* **2006**, *128*, 2522-2523.
47. Yokoyama, K.; Smith, A. A.; Corzilius, B. r.; Griffin, R. G.; Stubbe, J. *J. Am. Chem. Soc.* **2011**, *133*, 18420-18432.
48. Yun, D.; Garc á-Serres, R.; Chicalese, B. M.; An, Y. H.; Huynh, B. H.; Bollinger, J. M. *Biochemistry* **2007**, *46*, 1925-1932.

49. Baldwin, J.; Krebs, C.; Saleh, L.; Stelling, M.; Huynh, B. H.; Bollinger, J. M.; Riggs-Gelasco, P. *Biochemistry* **2003**, *42*, 13269-13279.
50. Bollinger Jr, J.; Edmondson, D.; Huynh, B.; Filley, J.; Norton, J.; Stubbe, J. *Science* **1991**, *253*, 292-299.
51. Han, W.-G.; Liu, T.; Lovell, T.; Noodleman, L. *J. Am. Chem. Soc.* **2005**, *127*, 15778-15790.
52. Ravi, N.; Bollinger Jr, J. M.; Huynh, B. H.; Stubbe, J.; Edmondson, D. E. *J. Am. Chem. Soc.* **1994**, *116*, 8007-8014.
53. Riggs-Gelasco, P. J.; Shu, L.; Chen, S.; Burdi, D.; Huynh, B. H.; Que, L., Jr.; Stubbe, J. *J. Am. Chem. Soc.* **1998**, *120*, 849-860.
54. Han, W.-G.; Liu, T.; Lovell, T.; Noodleman, L. *J. Inorg. Biochem.* **2006**, *100*, 771-779.
55. Mitić, N.; Clay, M. D.; Saleh, L.; Bollinger, J. M.; Solomon, E. I. *J. Am. Chem. Soc.* **2007**, *129*, 9049-9065.
56. Dassama, L. M.; Silakov, A.; Krest, C. M.; Calixto, J. C.; Krebs, C.; Bollinger Jr, J. M.; Green, M. T. *J. Am. Chem. Soc.* **2013**, *135*, 16758-16761.
57. Doan, P. E.; Shanmugam, M.; Stubbe, J.; Hoffman, B. M. *J. Am. Chem. Soc.* **2015**, *137*, 15558-15566.
58. Cotruvo Jr, J. A.; Stubbe, J. *Biochemistry* **2010**, *49*, 1297-1309.
59. Cotruvo Jr, J. A.; Stich, T. A.; Britt, R. D.; Stubbe, J. *J. Am. Chem. Soc.* **2013**, *135*, 4027-4039.
60. Cotruvo Jr, J. A.; Stubbe, J. *Metallomics* **2012**, *4*, 1020-1036.

61. Roshick, C.; Iliffe-Lee, E. R.; McClarty, G. *J. Bio. Chem.* **2000**, *275*, 38111-38119.
62. Högbom, M.; Stenmark, P.; Voevodskaya, N.; McClarty, G.; Gräslund, A.; Nordlund, P. *Science* **2004**, *305*, 245-248.
63. Jiang, W.; Yun, D.; Saleh, L.; Barr, E. W.; Xing, G.; Hoffart, L. M.; Maslak, M.-A.; Krebs, C.; Bollinger, J. M. *Science* **2007**, *316*, 1188-1191.
64. Jiang, W.; Hoffart, L. M.; Krebs, C.; Bollinger, J. M. *Biochemistry* **2007**, *46*, 8709-8716.
65. Jiang, W.; Bollinger, J. M.; Krebs, C. *J. Am. Chem. Soc.* **2007**, *129*, 7504-7505.
66. Bollinger, J. M.; Jiang, W.; Green, M. T.; Krebs, C., *Curr. Opin. Struct. Bio.* **2008**, *18*, 650-657.
67. Tinberg, C. E.; Lippard, S. J. *Acc. Chem. Res.* **2011**, *44*, 280-288.
68. Younker, J. M.; Krest, C. M.; Jiang, W.; Krebs, C.; Bollinger Jr, J. M.; Green, M. T. *J. Am. Chem. Soc.* **2008**, *130*, 15022-15027.
69. Martinie, R. J.; Blaesl, E. J.; Krebs, C.; Bollinger, J., J Martin; Silakov, A.; Pollock, C. J. *J. Am. Chem. Soc.* **2017**, *139*, 1950-1957.
70. Ghiladi, R. A.; Ju, T. D.; Lee, D.-H.; Moenne-Loccoz, P.; Kaderli, S.; Neuhold, Y.-M.; Zuberbühler, A. D.; Woods, A. S.; Cotter, R. J.; Karlin, K. D. *J. Am. Chem. Soc.* **1999**, *121*, 9885-9886.
71. Chishiro, T.; Shimazaki, Y.; Tani, F.; Tachi, Y.; Naruta, Y.; Karasawa, S.; Hayami, S.; Maeda, Y., *Angew. Chem. Int. Ed.* **2003**, *115*, 2894-2897.

72. Kim, E.; Helton, M. E.; Wasser, I. M.; Karlin, K. D.; Lu, S.; Huang, H.-w.; Moënne-LoCcOz, P.; Incarvito, C. D.; Rheingold, A. L.; Honecker, M., *Proc. Natl. Acad. Sci. U.S.A.* **2003**, *100*, 3623-3628.
73. Kim, E.; Shearer, J.; Lu, S.; Moënne-LoCcOz, P.; Helton, M. E.; Kaderli, S.; Zuberbühler, A. D.; Karlin, K. D. *J. Am. Chem. Soc.* **2004**, *126*, 12716-12717.
74. Kim, E.; Shearer, J.; Lu, S.; Moënne-LoCcOz, P.; Helton, M. E.; Kaderli, S.; Zuberbühler, A. D.; Karlin, K. D. *J. Am. Chem. Soc.* **2004**, *126*, 12716-12717.
75. Dong, Y.; Yan, S.; Young, V. G.; Que, L., Jr. *Angew. Chem. Int. Ed.* **1996**, *35*, 618-620.
76. Fiedler, A. T.; Shan, X.; Mehn, M. P.; Kaizer, J.; Torelli, S.; Frisch, J. R.; Kodera, M.; Que, L., Jr. *J. Phys. Chem. A* **2008**, *112*, 13037-13044.
77. Frisch, J. R.; Vu, V. V.; Martinho, M.; Münck, E.; Que, L., Jr. *Inorg. Chem.* **2009**, *48*, 8325-8336.
78. Tshuva, E. Y.; Lippard, S. J. *Chem. Rev.* **2004**, *104*, 987-1012.
79. Que, L., Jr.; Dong, Y. *Acc. Chem. Res.* **1996**, *29*, 190-196.
80. Dong, Y.; Ménage, S.; Brennan, B. A.; Elgren, T. E.; Jang, H. G.; Pearce, L. L.; Que, L., Jr. *J. Am. Chem. Soc.* **1993**, *115*, 1851-1859.
81. Kim, K.; Lippard, S. J. *J. Am. Chem. Soc.* **1996**, *118*, 4914-4915.
82. Dong, Y.; Fujii, H.; Hendrich, M. P.; Leising, R. A.; Pan, G.; Randall, C. R.; Wilkinson, E. C.; Zang, Y.; Que, L., Jr. *J. Am. Chem. Soc.* **1995**, *117*, 2778-2792.
83. MacMurdo, V. L.; Zheng, H.; Que, L., Jr. *Inorg. Chem.* **2000**, *39*, 2254-2255.
84. Kovacs, J. A. *Acc. Chem. Res.* **2015**, *48*, 2744-2753.

85. Coggins, M. K.; Sun, X.; Kwak, Y.; Solomon, E. I.; Rybak-Akimova, E.; Kovacs, J. A. *J. Am. Chem. Soc.* **2013**, *135*, 5631-5640.
86. Leto, D. F.; Chattopadhyay, S.; Day, V. W.; Jackson, T. A. *Dalton Trans.* **2013**, *42*, 13014-13025.
87. Hotzelmann, R.; Wieghardt, K.; Floerke, U.; Haupt, H. J.; Weatherburn, D. C.; Bonvoisin, J.; Blondin, G.; Girerd, J. J. *J. Am. Chem. Soc.* **1992**, *114*, 1681-1696.
88. Holman, T. R.; Wang, Z.; Hendrich, M. P.; Que, L., Jr. *Inorg. Chem.* **1995**, *34*, 134-139.
89. Nanthakumar, A.; Fox, S.; Murthy, N. N.; Karlin, K. D.; Ravi, N.; Huynh, B. H.; Orosz, R. D.; Day, E. P.; Hagen, K. S.; Blackburn, N. J. *J. Am. Chem. Soc.* **1993**, *115*, 8513-8514.
90. Ogo, S.; Wada, S.; Watanabe, Y.; Iwase, M.; Wada, A.; Harata, M.; Jitsukawa, K.; Masuda, H.; Einaga, H. *Angew. Chem. Int. Ed.* **1998**, *37*, 2102-2104.
91. MacBeth, C. E.; Golombek, A. P.; Young, V. G., Jr.; Yang, C.; Kuczera, K.; Hendrich, M. P.; Borovik, A. S. *Science* **2000**, *289*, 938-941.
92. MacBeth, C. E.; Gupta, R.; Mitchell-Koch, K. R.; Young, V. G.; Lushington, G. H.; Thompson, W. H.; Hendrich, M. P.; Borovik, A. *J. Am. Chem. Soc.* **2004**, *126*, 2556-2567.
93. England, J.; Guo, Y.; Farquhar, E. R.; Young Jr, V. G.; Münck, E.; Que, L., Jr. *J. Am. Chem. Soc.* **2010**, *132*, 8635-8644.
94. McDonald, A. R.; Que, L., Jr. *Coord. Chem. Rev.* **2013**, *257*, 414-428.

95. Sastri, C. V.; Oh, K.; Lee, Y. J.; Seo, M. S.; Shin, W.; Nam, W. *Angew. Chem. Int. Ed.* **2006**, *45*, 3992-3995.
96. Suga, M.; Akita, F.; Hirata, K.; Ueno, G.; Murakami, H.; Nakajima, Y.; Shimizu, T.; Yamashita, K.; Yamamoto, M.; Ago, H. *Nature* **2015**, *517*, 99-103.
97. Pérez-Navarro, M.; Neese, F.; Lubitz, W.; Pantazis, D. A.; Cox, N. *Curr. Opin. Chem. Biol.* **2016**, *31*, 113-119.
98. Jiang, W.; Yun, D.; Saleh, L.; Barr, E. W.; Xing, G.; Hoffart, L. M.; Maslak, M.-A.; Krebs, C.; Bollinger, J. M., Jr. *Science* **2007**, *316*, 1188-1191.
99. Jiang, W.; Yun, D.; Saleh, L.; Bollinger, J. M., Jr.; Krebs, C. *Biochemistry* **2008**, *47*, 13736-13744.
100. Fukuzumi, S.; Morimoto, Y.; Kotani, H.; Naumov, P.; Lee, Y.-M.; Nam, W. *Nat. Chem.* **2010**, *2*, 756-759.
101. Swart, M. *Chem. Commun.* **2013**, *49*, 6650-6652.
102. Prakash, J.; Rohde, G. T.; Meier, K. K.; Jasniewski, A. J.; Van Heuvelen, K. M.; Münck, E.; Que, L., Jr. *J. Am. Chem. Soc.* **2015**, *137*, 3478-3481.
103. Prakash, J.; Rohde, G. T.; Meier, K. K.; Münck, E.; Que, L., Jr. *Inorg. Chem.* **2015**, *54*, 11055-11057.
104. Zhou, A.; Kleespies, S. T.; Van Heuvelen, K. M.; Que, L., Jr. *Chem. Commun.* **2015**, *51*, 14326-14329.
105. Rohde, J.-U.; In, J. H.; Lim, M. H.; Brennessel, W. W.; Bukowski, M. R.; Stubna, A.; Münck, E.; Nam, W.; Que, L., Jr. *Science* **2003**, *299*, 1037-1039.
106. Havare, N.; Plattner, D. A. *Org. Lett.* **2012**, *14*, 5078-5081.

107. Macikenas, D.; Skrzypczak-Jankun, E.; Protasiewicz, J. D. *J. Am. Chem. Soc.* **1999**, *121*, 7164-7165.
108. Macikenas, D.; Skrzypczak-Jankun, E.; Protasiewicz, J. D. *J. Am. Chem. Soc.* **2011**, *133*, 4151-4151.
109. Hupp, J. T.; Nguyen, S. T. *C&EN* **2011**, *89*, 2.
110. Song, F.; Wang, C.; Falkowski, J. M.; Ma, L.; Lin, W. *J. Am. Chem. Soc.* **2010**, *132*, 15390-15398.
111. Puri, M.; Biswas, A. N.; Fan, R.; Guo, Y.; Que, L., Jr. *J. Am. Chem. Soc.* **2016**, *138*, 2484-2487.
112. Petasis, D. T.; Hendrich, M. P. *Methods Enzymol.* **2015**, *563*, 171-208.
113. Wojdyr, M. *J. Appl. Cryst.* **2010**, *43*, 1126-1128.
114. Hübschle, C. B.; Sheldrick, G. M.; Dittrich, B. *J. Appl. Cryst.* **2011**, *44*, 1281-1284.
115. Sheldrick, G. M. *J. Appl. Cryst.* **2015**, *71*, 3-8.
116. Sanders-Loehr, J.; Wheeler, W. D.; Shiemke, A. K.; Averill, B. A.; Loehr, T. M. *J. Am. Chem. Soc.* **1989**, *111*, 8084-8093.
117. Koehntop, K. D.; Rohde, J.-U.; Costas, M.; Que, L., Jr. *Dalton Trans.* **2004**, 3191-3198.
118. Kurtz Jr, D. M. *Chem. Rev.* **1990**, *90*, 585-606.
119. Lee, S. C.; Holm, R. *J. Am. Chem. Soc.* **1993**, *115*, 11789-11798.
120. Berry, J. F.; Bill, E.; García-Serres, R.; Neese, F.; Weyhermüller, T.; Wieghardt, K. *Inorg. Chem.* **2006**, *45*, 2027-2037.

121. Liston, D. J.; Kennedy, B. J.; Murray, K. S.; West, B. O. *Inorg. Chem.* **1985**, *24*, 1561-1567.
122. Westre, T. E.; Kennepohl, P.; DeWitt, J. G.; Hedman, B.; Hodgson, K. O.; Solomon, E. I. *J. Am. Chem. Soc.* **1997**, *119*, 6297-6314.
123. Roe, A.; Schneider, D.; Mayer, R.; Pyrz, J.; Widom, J.; Que, L., Jr. *J. Am. Chem. Soc.* **1984**, *106*, 1676-1681.
124. Shan, X.; Rohde, J.-U.; Koehntop, K. D.; Zhou, Y.; Bukowski, M. R.; Costas, M.; Fujisawa, K.; Que, L., Jr. *Inorg. Chem.* **2007**, *46*, 8410-8417.
125. Cho, J.; Jeon, S.; Wilson, S. A.; Liu, L. V.; Kang, E. A.; Braymer, J. J.; Lim, M. H.; Hedman, B.; Hodgson, K. O.; Valentine, J. S.; Solomon, E. I.; Nam, W. *Nature* **2011**, *478*, 502-505.
126. Sastri, C. V.; Park, M. J.; Ohta, T.; Jackson, T. A.; Stubna, A.; Seo, M. S.; Lee, J.; Kim, J.; Kitagawa, T.; Münck, E. *J. Am. Chem. Soc.* **2005**, *127*, 12494-12495.
127. Fiedler, A. T.; Halfen, H. L.; Halfen, J. A.; Brunold, T. C. *J. Am. Chem. Soc.* **2005**, *127*, 1675-1689.
128. McDonald, A. R.; Bukowski, M. R.; Farquhar, E. R.; Jackson, T. A.; Koehntop, K. D.; Seo, M. S.; De Hont, R. F.; Stubna, A.; Halfen, J. A.; Münck, E. *J. Am. Chem. Soc.* **2010**, *132*, 17118-17129.
129. Cho, J.; Woo, J.; Nam, W. *J. Am. Chem. Soc.* **2010**, *132*, 5958-5959.
130. Fukuzumi, S. *Coord. Chem. Rev.* **2013**, *257*, 1564-1575.
131. Siegbahn, P. E. M. *Acc. Chem. Res.* **2009**, *42*, 1871-1880.
132. Tsui, E. Y.; Kanady, J. S.; Agapie, T. *Inorg. Chem.* **2013**, *52*, 13833-13848.

133. Young, K. J.; Brennan, B. J.; Tagore, R.; Brudvig, G. W. *Acc. Chem. Res.* **2015**, *48*, 567-574.
134. Codolà Z.; Gómez, L.; Kleespies, S. T.; Que, L., Jr.; Costas, M.; Lloret-Fillol, J. *Nat. Commun.* **2015**, *6*, 5865-5874.
135. Wilson, S. A.; Chen, J.; Hong, S.; Lee, Y.-M.; Clémancey, M.; Garcia-Serres, R.; Nomura, T.; Ogura, T.; Latour, J.-M.; Hedman, B. *J. Am. Chem. Soc.* **2012**, *134*, 11791-11806.
136. Zhou, A.; Prakash, J.; Rohde, G. T.; Klein, J. E. M. N.; Kleespies, S. T.; Draksharapu, A.; Fan, R.; Guo, Y.; Cramer, C. J.; Que, L., Jr. *Inorg. Chem.* **2016**, *56*, 518-527.
137. Jackson, T. A.; Rohde, J.-U.; Seo, M. S.; Sastri, C. V.; DeHont, R.; Stubna, A.; Ohta, T.; Kitagawa, T.; Munck, E.; Nam, W.; Que, L., Jr. *J. Am. Chem. Soc.* **2008**, *130*, 12394-12407.
138. Bernasconi, L.; Louwarse, M. J.; Baerends, E. J. *Eur. J. Inorg. Chem.* **2007**, *2007*, 3023-3033.
139. Sastri, C. V.; Lee, J.; Oh, K.; Lee, Y. J.; Lee, J.; Jackson, T. A.; Ray, K.; Hirao, H.; Shin, W.; Halfen, J. A.; Kim, J.; Que, L., Jr.; Shaik, S.; Nam, W. *Proc. Natl. Acad. Sci. U.S.A.* **2007**, *104*, 19181-19186.
140. Bukowski, M. R.; Koehntop, K. D.; Stubna, A.; Bominaar, E. L.; Halfen, J. A.; Münck, E.; Nam, W.; Que, L., Jr. *Science* **2005**, *310*, 1000-1002.

141. Thibon, A.; England, J.; Martinho, M.; Young, V. G.; Frisch, J. R.; Guillot, R.; Girerd, J. J.; Münck, E.; Que, L., Jr.; Banse, F. *Angew. Chem. Int. Ed.* **2008**, *47*, 7064-7067.
142. England, J.; Bigelow, J. O.; Van Heuvelen, K. M.; Farquhar, E. R.; Martinho, M.; Meier, K. K.; Frisch, J. R.; Münck, E.; Que, L., Jr. *Chem. Sci.* **2014**, *5*, 1204-1215.
143. Schardt, B. C.; Hill, C. L. *Inorg. Chem.* **1983**, *22*, 1563-1565.
144. Thibon, A.; England, J.; Martinho, M.; Young, V. G., Jr.; Frisch, J. R.; Guillot, R.; Girerd, J.-J.; Muenck, E.; Que, L., Jr.; Banse, F. *Angew. Chem. Int. Ed.* **2008**, *47*, 7064-7067.
145. Klinker, E. J.; Kaizer, J.; Brennessel, W. W.; Woodrum, N. L.; Cramer, C. J.; Que, L., Jr. *Angew. Chem. Int. Ed.* **2005**, *44*, 3690-3694.
146. Scarrow, R. C.; Trimitsis, M. G.; Buck, C. P.; Grove, G. N.; Cowling, R. A.; Nelson, M. J. *Biochemistry* **1994**, *33*, 15023-15035.
147. Högbom, M. *J. Biol. Inorg. Chem.* **2010**, *15*, 339-349.
148. Carboni, M.; Latour, J.-M. *Coord. Chem. Rev.* **2011**, *255*, 186-202.
149. Griese, J. J.; Srinivas, V.; Högbom, M. *J. Biol. Inorg. Chem.* **2014**, *19*, 759-774.
150. Andersson, C. S.; Högbom, M. *Proc. Natl. Acad. Sci. U.S.A.* **2009**, *106*, 5633-5638.
151. Shafaat, H. S.; Griese, J. J.; Pantazis, D. A.; Roos, K.; Andersson, C. S.; Popović-Bijelić, A.; Gräslund, A.; Siegbahn, P. E.; Neese, F.; Lubitz, W. *J. Am. Chem. Soc.* **2014**, *136*, 13399-13409.

152. Miller, E. K.; Trivelas, N. E.; Maugeri, P. T.; Blaesi, E. J.; Shafaat, H. S. *Biochemistry* **2017**, *56*, 3369-3379.
153. Das, B.; Daver, H.; Singh, A.; Singh, R.; Haukka, M.; Demeshko, S.; Meyer, F.; Lisensky, G.; Jarenmark, M.; Himø, F. *Eur. J. Inorg. Chem.* **2014**, *2014*, 2204-2212.
154. Sahu, S.; Widger, L. R.; Quesne, M. G.; De Visser, S. P.; Matsumura, H.; Moënne-Loccoz, P.; Siegler, M. A.; Goldberg, D. P. *J. Am. Chem. Soc.* **2013**, *135*, 10590-10593.
155. Wang, Z.-W.; Chen, Q.-Y.; Liu, Q.-S. *Transition Met. Chem.* **2014**, *39*, 917-924.
156. Wijeratne, G. B.; Corzine, B.; Day, V. W.; Jackson, T. A. *Inorg. Chem.* **2014**, *53*, 7622-7634.
157. Ankudinov, A.; Ravel, B.; Rehr, J.; Conradson, S. *Phys. Rev. B* **1998**, *58*, 7565.
158. Roelfes, G.; Lubben, M.; Chen, K.; Ho, R. Y.; Meetsma, A.; Genseberger, S.; Hermant, R. M.; Hage, R.; Mandal, S. K.; Young, V. G. *Inorg. Chem.* **1999**, *38*, 1929-1936.
159. Högbom, M.; Galander, M.; Andersson, M.; Kolberg, M.; Hofbauer, W.; Lassmann, G.; Nordlund, P.; Lendzian, F. *Proc. Natl. Acad. Sci. U.S.A.* **2003**, *100*, 3209-3214.
160. Lim, M. H.; Rohde, J. U.; Stubna, A.; Bukowski, M. R.; Costas, M.; Ho, R. Y. N.; Munck, E.; Nam, W.; Que, L., Jr. *Proc. Natl. Acad. Sci. U.S.A.* **2003**, *100*, 3665-3670.
161. Hsu, H.-F.; Dong, Y.; Shu, L.; Young, V. G.; Que, L., Jr. *J. Am. Chem. Soc.* **1999**, *121*, 5230-5237.

162. Xue, G.; Wang, D.; De Hont, R.; Fiedler, A. T.; Shan, X.; Münck, E.; Que, L., Jr. *Proc. Natl. Acad. Sci. U.S.A.* **2007**, *104*, 20713-20718.
163. Xue, G.; Fiedler, A. T.; Martinho, M.; Münck, E.; Que, L., Jr. *Proc. Natl. Acad. Sci. U.S.A.* **2008**, *105*, 20615-20620.
164. Ward, A. L.; Elbaz, L.; Kerr, J. B.; Arnold, J. *Inorg. Chem.* **2012**, *51*, 4694-4706.
165. Gafford, B. G.; Holwerda, R. A. *Inorg. Chem.* **1989**, *28*, 60-66.
166. Liu, K. E.; Wang, D.; Huynh, B. H.; Edmondson, D. E.; Salifoglou, A.; Lippard, S. J. *J. Am. Chem. Soc.* **1994**, *116*, 7465-7466.
167. Valentine, A. M.; Stahl, S. S.; Lippard, S. J. *J. Am. Chem. Soc.* **1999**, *121*, 3876-3887.
168. Vu, V. V.; Emerson, J. P.; Martinho, M.; Kim, Y. S.; Münck, E.; Park, M. H.; Que, L., Jr. *Proc. Natl. Acad. Sci. U.S.A.* **2009**, *106*, 14814-14819.
169. Jasniewski, A. J.; Engstrom, L. M.; Vu, V. V.; Park, M. H.; Que, L., Jr. *J. Biol. Inorg. Chem.* **2016**, *21*, 605-618.
170. Kitajima, N.; Tamura, N.; Amagai, H.; Fukui, H.; Moro-oka, Y.; Mizutani, Y.; Kitagawa, T.; Mathur, R.; Heerwegh, K. *J. Am. Chem. Soc.* **1994**, *116*, 9071-9085.
171. Zhang, X.; Furutachi, H.; Fujinami, S.; Nagatomo, S.; Maeda, Y.; Watanabe, Y.; Kitagawa, T.; Suzuki, M. *J. Am. Chem. Soc.* **2005**, *127*, 826-827.
172. Cranswick, M. A.; Meier, K. K.; Shan, X.; Stubna, A.; Kaizer, J. s.; Mehn, M. P.; Münck, E.; Que, L., Jr. *Inorg. Chem.* **2012**, *51*, 10417-10426.
173. Decker, A.; Rohde, J. U.; Que, L., Jr.; Solomon, E. I. *J. Am. Chem. Soc.* **2004**, *126*, 5378-5379.

174. Decker, A.; Rohde, J.-U.; Klinker, E. J.; Wong, S. D.; Que, L., Jr.; Solomon, E. I. *J. Am. Chem. Soc.* **2007**, *129*, 15983-15996.
175. Riggs-Gelasco, P. J.; Price, J. C.; Guyer, R. B.; Brehm, J. H.; Barr, E. W.; Bollinger, J. M.; Krebs, C. *J. Am. Chem. Soc.* **2004**, *126*, 8108-8109.
176. Fukuzumi, S.; Kotani, H.; Suenobu, T.; Hong, S.; Lee, Y.-M.; Nam, W. *Chem. - Eur. J.* **2010**, *16*, 354-361.
177. Ray, K.; England, J.; Fiedler, A. T.; Martinho, M.; Munck, E.; Que, L., Jr. *Angew. Chem. Int. Ed.* **2008**, *47*, 8068-8071.
178. Roelfes, G.; Lubben, M.; Chen, K.; Ho, R. Y. N.; Meetsma, A.; Genseberger, S.; Hermant, R. M.; Hage, R.; Mandal, S. K.; Young, V. G. *Inorg. Chem.* **1999**, *38*, 1929-1936.

Bibliography

Publications

- **Zhou, A.**; Prakash, J.; Rohde, G. T.; Klein, J. E. M. N.; Kleespies, S. T.; Draksharapu, A.; Fan, R.; Guo, Y.; Cramer, C. J.; Que, L., Jr. The Two Faces of Tetramethylcyclam in Iron Chemistry: Distinct Fe–O–M Complexes Derived from $[\text{Fe}^{\text{IV}}(\text{O}_{\text{syn/anti}})(\text{TMC})]^{2+}$ Isomers, *Inorg. Chem.* **2017**, *56*, 518-527.
- **Zhou, A.**; Kleespies, S.; Heuvelen, K.; Que, L. Jr. Characterization of a Heterobimetallic Nonheme Fe(III)–O–Cr(III) Species Formed by O₂ Activation. *Chem. Commun.* **2015**, *51*, 14326-14329.
- Schreiber, R. E.; Cohen, H.; Leitus, G.; Wolf, Sharon G.; **Zhou, A.**; Que, L. Jr.; Neumann, R. Reactivity and O₂ Formation by Mn(IV) and Mn(V) Hydroxo Species Stabilized within in a Polyfluoroxometalate Framework. *J. Am. Chem. Soc.* **2015**, *137*, 8738–8748.

Presentations

- **Zhou, A.**; Prakash, J.; Rohde, G. T.; Klein, J. E. M. N.; Kleespies, S. T.; Draksharapu, A.; Fan, R.; Guo, Y.; Cramer, C. J.; Que, L., Jr. Characterization of a (μ-oxo) Heterobimetallic Pair: How does Ligand Topology Affect Metal Coordination Environment. **253rd American Chemical Society, San Francisco, CA.** April 2– 6, 2017. (Poster presentation)

- **Zhou, A.**; Kleespies, S.; Heuvelen, K.; Que, L. Jr. Characterization of a

- Heterobimetallic Nonheme Fe(III)–O–Cr(III) Species Formed by O₂ Activation. **17th International Conference on Bioinorganic Chemistry, Beijing, China**. July 21 – 25, 2015. (Presented as slam poster to the conference participants)
- **Zhou, A.**; Kleespies, S.; Heuvelen, K.; Que, L. Jr. Characterization of a Heterobimetallic Nonheme Fe(III)–O–Cr(III) Species Formed by O₂ Activation. **CIGS International Graduate Research Showcase**, Minneapolis, MN. April 22, 2016. (Poster presentation)
- **Zhou, A.**; Kleespies, S.; Heuvelen, K.; Que, L. Jr. Characterization and Reactivity of a Heterobimetallic Nonheme Fe(III)–O–Cr(III) Species Formed by O₂ Activation. **14th Annual Graduate Student Research Symposium**, Minneapolis, MN, June 2, 2015. (Poster presentation)